UNIVERSITY OF SOUTHAMPTON

STABILITY AND PERFORMANCE OF ACTIVE VIBRATION ISOLATION SYSTEMS

by

Kanapathipillai Arunachalam ANANTHAGANESHAN
(Ganesh)

A thesis submitted for the degree of

Doctor of Philosophy

INSTITUTE OF SOUND AND VIBRATION RESEARCH
FACULTY OF ENGINEERING AND APPLIED SCIENCE

December 2002

UNIVERSITY OF SOUTHAMPTON

ABSTRACT

FACULTY OF ENGINEERING AND APPLIED SCIENCE
INSTITUTE OF SOUND AND VIBRATION RESEARCH

Doctor of Philosophy

STABILITY AND PERFORMANCE OF ACTIVE VIBRATION ISOLATION SYSTEMS

By K. A. Ananthaganeshan

Active vibration isolation techniques can be used to avoid some of the compromises inherent in using a passive system to isolate delicate equipment from base vibration. In active control, a secondary force, which can be proportional to equipment acceleration, velocity or displacement, is introduced between the base and the equipment to reduce the overall response by destructive interference. In this thesis the stability and performance of active vibration isolation of equipment using acceleration, velocity or displacement feedback control with a decentralised control strategy is investigated.

Previous experimental work on active vibration isolation systems has shown that the gain in the feedback loop is limited because of the stability of the system. However, theoretical analyses of these systems showed that they are unconditionally stable. These discrepancies are investigated in this thesis and it is demonstrated that the instrumentation plays a crucial role in the stability and performance of an active isolation system. A holistic analysis of decentralised vibration isolation control systems integrating (a) the structural dynamics (b) the signal conditioning devices and (c) the actuators, to assess the stability and performance of the systems is adopted. In addition, the effect of losing control of one of the decentralised loops is also investigated.

In the stability analysis two frequency regimes are identified; (a) a low frequency regime and (b) a high frequency regime. In the low frequency regime, the phase advance of the high-pass filters, which are inherent in the control system, causes the instability. In the high frequency regime instability is caused by time delay, or phase lag (from low-pass filters). Simple formulae are derived for simplified systems, which give the frequencies at which the systems become unstable and the maximum gains that can be applied to each system. These formulae can be used as simple rules of thumb for the analysis of stability of more complex systems.

Considering the three control strategies, it is established that the acceleration feedback control system has the lowest maximum gain, and velocity and displacement feedback control systems have good low frequency stability. With time delay in the feedback systems, the displacement feedback control strategy is the most susceptible to instability. Similarly, with low-pass filters in the system, the displacement feedback control strategy is again the most susceptible. Thus velocity feedback control is proven to be most attractive.

Uncertainty due to component failure is also investigated in a two-channel velocity feedback system and it is found that failure does not affect the stability of the system, but it does degrade the performance significantly. It is observed that in a system with failure, only a small improvement on performance is possible from the system with no control. Thus, with respect to component failure, increasing gain in a system with failure does not cause the system to become unstable but does not improve the performance significantly.

Contents list

List of Figures

List of Tables

Acknowledgements

Appreciation with gratitude goes to my supervisor Prof. Michael John Brennan, for his continuing guidance, patience and strict attention to the details throughout this project. His encouragement and supervision greatly contributed to the progress of this project.

Many suggestions from Prof. Stephen Elliott and Dr David Thompson to improve the quality of my work are gratefully acknowledged.

I would like to thank the Dynamics group secretary Ms Anne Marie McDonnell and the ISVR librarian Ms Alison Gunn for their help. I would also like to express my gratitude to Dr. Richard Grice, Dr. S. M. Kim and Mr. Tristan Armstrong for their assistance to start the experimental work in this project.

I have reserved a special mention for my wife Subo, friends Logan, Suren and Niranjan and cousins Siva, Arul and Thushy who have continually supported me throughout the time I have spent in the UK.

Glossary of symbols

$\mathbf{a}$	Equipment mass centre velocity vector
c	Damping of a single mount
c_a	Internal damping of an accelerometer
E_k	Kinetic energy
f_c	Control force
$\mathbf{f_c}$	Control force vector
$\mathrm{F_c}$	Control force in frequency domain
f_m	Mount force (active and passive)
$\mathbf{f_m}$	Mount force vector (active and passive)
f_p	Primary disturbance force
$\mathbf{f_p}$	Primary disturbance force vector
$\mathrm{F_p}$	Primary disturbance force infrequency domain
f_{pm}	Collocated disturbance force
$\mathbf{f_{pm}}$	Collocated disturbance force vector
$\mathrm{g_a}$	Gain in acceleration feedback control
$\mathrm{g_v}$	Gain in velocity feedback control
$\mathrm{g_d}$	Gain in displacement feedback control
g_{na}	Normalised gain in acceleration feedback control
g_{nv}	Normalised gain in velocity feedback control
g_{nd}	Normalised gain in displacement feedback control
$\mathrm{g_{a\_max}}$	Maximum gain in acceleration feedback control
$\mathrm{g_{v\_max}}$	Maximum gain in velocity feedback control
$\mathrm{g_{d\_max}}$	Maximum gain in displacement feedback control
$G(j\omega)$	Plant frequency response function
$\mathbf{G}(j\omega)$	Plant frequency response matrix
$H(j\omega)$	Feedback frequency response function
$\mathbf{H}(j\omega)$	Feedback frequency response matrix
J	Moment of inertia of equipment about the mass centre
$\mathbf{J}$	Inertia matrix of equipment
k	Stiffness of a single mount

k_a	Internal stiffness of an accelerometer
l	Disturbance between mounts
l_p	Length of the plate
m	Mass of the isolation system
m,n	Integers representing number of modal lines
m_p	Mass of the equipment (plate)
m_s	Mass of the shaker
m_{st}	Mass per unit area of the flexible base structure
N_{mn}	Normalising factor
$\mathbf{Q}$	Transfer matrix
r	Ratio
v_b	Velocity of the base at the location of mount
$\mathbf{v_b}$	Velocity of the base at the location of mount
v_e	Velocity of the equipment at the location of the mount
$\mathbf{v_e}$	Velocity of the equipment at the location of the mount
x,y	Coordinate system
Y_{bp}	Transfer mobility between the disturbance force and mount locations
$\mathbf{Y_b}$	Mobility matrix of base
Z_b	Impedance of the base at the location of mount
Z_e	Impedance of the unconnected equipment
Z_m	Impedance of the mount
$\mathbf{Z_b}$	Impedance matrix of the base at the location of mount
$\mathbf{Z_e}$	Impedance matrix of the unconnected equipment
$\mathbf{Z_m}$	Impedance matrix of the mount
ω	Frequency
ω_n	Natural frequency
ω_{mn}	Resonance frequency of mn^{th} mode
ω_h	-3dB corner frequency of high-pass filter
ω_i	-3dB corner frequency of integrator
ω_l	-3dB corner frequency of low-pass filter
τ_h	Time constant for high-pass filters
τ_i	Time constant for integrator

τ_l	Time constant for low-pass filters
Ω	Non-dimensional frequency
Ω_c	Critical frequency
ζ	Damping ratio
ζ_a	Damping ratio of an accelerometer model
θ	Beam function for a free-free beam‘
ϕ	Beam function for a clamped-clamped beam
α	Ratio of natural frequency of the system to the corner frequency of the high pass filter
β	Ratio of natural frequency of the system to the corner frequency of the integrator filter
γ	Ratio of natural frequency of the system to the corner frequency of the low pass filter
Π	Power

Chapter 1

Introduction

1.1 Background

All structures possessing mass and elasticity are capable of vibrating. Among the various problems and issues associated with this vibration, the isolation of a piece of equipment from a vibrating base is a common one in the field of mechanical engineering [1-3]. Often, very little can be done to reduce the vibration of the base, which in general has complex dynamics and is subject to design constraints [4]. Traditionally, engineers have solved the problem of vibration isolation by designing passive systems based on compliant materials, such as rubber, to decouple the equipment dynamics from the base dynamics [5]. Typically the base vibration has an unpredictable waveform and the passive isolators have to deal with broadband excitation spectra [1,6]. However, the conventional passive form of isolation is generally a compromise between (a) high frequency isolation, which requires low values of damping, and (b) limited excitation of rigid body modes that requires high values of isolator damping [7-12]. This inherent trade-off in performance of a passive isolation system can be enhanced by coupling an active system to a passive isolation system [13,14].

The essential components of an active system are (a) sensors (to detect the vibration), (b) an electronic controller and the associated signal conditioning devices and (c) actuators [13,15,16]. Sensors and actuators, together with associated signal conditioning equipment, play an important role in active vibration (isolation) control and often introduce limitations on the performance of the system [15,16]. The problem is further aggravated by the stability problems, (inherent in control systems), which are often difficult to identify by analysis. Because of these reasons, performance and stability are two crucial factors found in the general literature on control systems [17,18]. However, there is a necessity for a holistic analysis integrating (a) the structural dynamics (b) the dynamics of the sensors (c) the signal conditioning devices and (d) the dynamics of the actuators, to assess the stability and performance. The main aim of this thesis is to investigate this performance and stability in feedback active isolation systems integrating structural dynamics, dynamics of signal

conditioning devices and actuators. In addition, a system under control could perform unexpectedly and affect the system to be isolated when one of the active channels fails. This uncertainty in performance due to a component failure is an associated issue and therefore investigated with the main aim of the thesis.

1.2 Literature review

Published literature on active vibration isolation discusses (a) the methods (b) control strategies, (c) applications and (d) analysis of performance and stability. This can be structured for easy comprehension in the manner shown in Figure 1.1

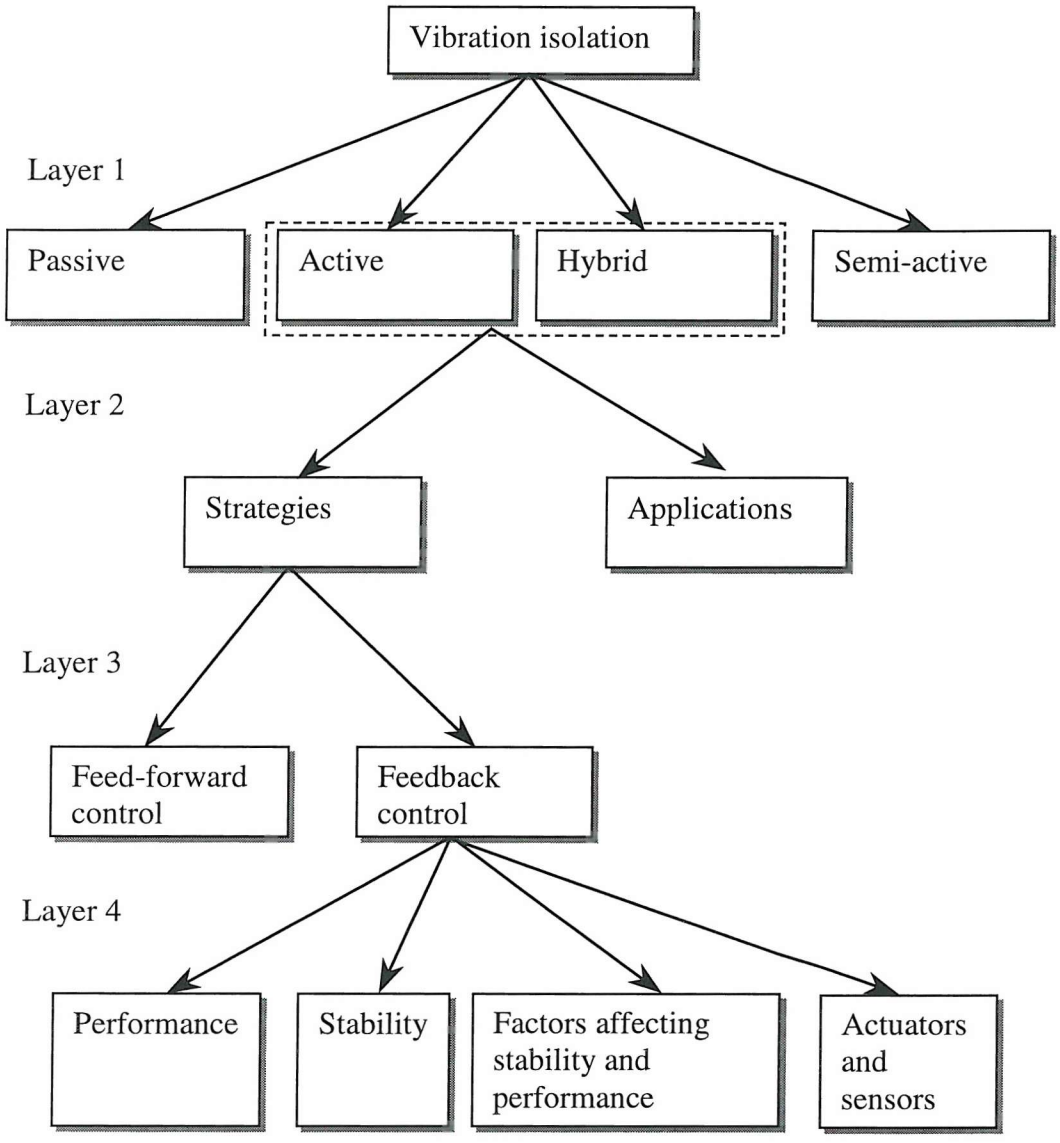

Figure 1.1 Overview of vibration isolation methods in the literature

Layer 1 in Figure 1.1 consists of the different methods used for vibration isolation. In the recent literature the terms active and hybrid are used synonymously. Layer 2 shows

strategies and applications. The control strategies can either be feed-forward or feedback, and should be considered in conjunction with the applications. Layer 4 describes the components of feedback control with respect to performance and stability. The following sub sections describe the elements of Figure 1.1 in some detail.

1.2.1 Vibration isolation methods

Isolation of sensitive equipment from the base structure to which it is attached is a common problem that arises in several application areas [3]. As shown in layer 1 in Figure 1.1, there are four types of vibration isolation methods, which can be adapted to this kind of problem. They are passive [3,5], fully-active [19], hybrid [20] and adaptive-passive (or semi-active control) [21]. Figure 1.2 illustrates the characteristics of these methods.

Passive control devices impart forces that are developed in response to the motion of the base structure by means of resilience and energy dissipation [3]. These control devices cannot supply energy to the system (which includes the structure and the passive devices). In addition a passive system does not make any real-time changes in the system and hence cannot destabilise a conservative system. The conventional passive system consists of compliant mounts (with stiffness and damping properties) positioned between the base and the equipment to be isolated. This can provide good isolation at high frequencies, above the resonance caused by the mass of the equipment and stiffness of the mount [22]. Thus, a passive system, although stable, has an inherent drawback in performance. An active system can be coupled to a dynamic system to enhance the performance of the passive system [13,14].

The way in which an active control system works is to reduce the overall response of a system by destructive interference using an external secondary vibration source [13]. An active system is constructed to give performance, which is not possible by passive means. In the past this was not greatly explored due to its inherent cost and complexity. However, with the development of computers fast enough to run control algorithms in real-time and more 'smart' materials such as piezo ceramics and shape memory alloys, active control of vibration has become prevalent in the last two decades [23].

A Hybrid isolation system combines the benefits of both passive and active isolation. In a hybrid isolation system, active control may be used to supplement and improve the

performance of a passive scheme or alternatively, a passive control system may be added to an active scheme to decrease its energy requirements [20].

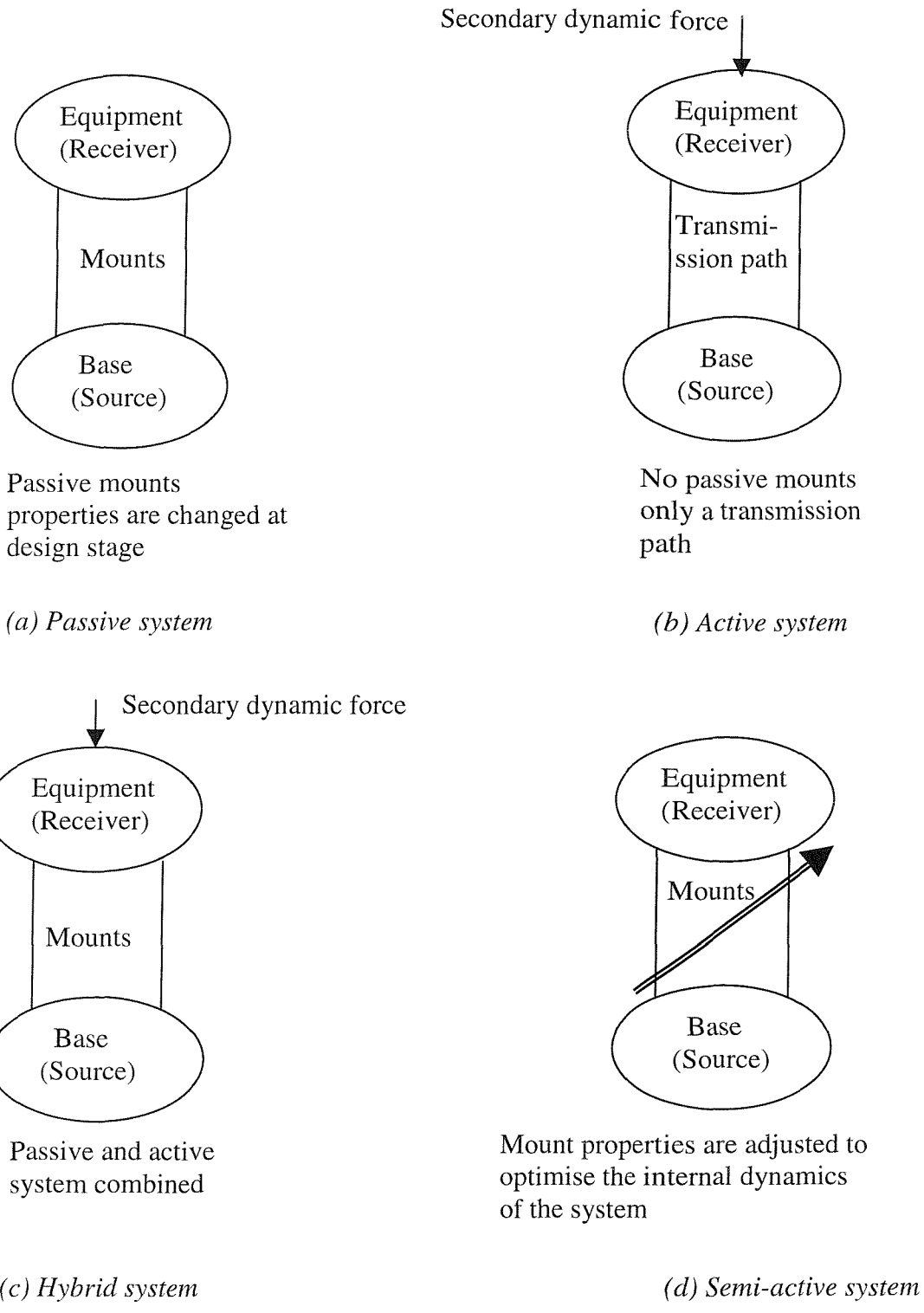

Figure 1.2 Schematic diagrams of different isolation methods.

It should be noted that the major difference between an active and a hybrid isolation scheme is generally the amount of external energy used to implement control. A hybrid isolation system can sometimes alleviate some of the limitations that exist in either a passive or active

isolation system alone. For example, in the event of a power failure, the passive element in the hybrid system still offers some degree of protection. Since a hybrid system consists of an active element, many researchers generally refer to it simply as an active system.

Semi-active isolation is essentially equivalent to a passive system with variable mount properties. One type employs an energy dissipating mechanism by means of a controllable damper [24-27] and another type employs stiffness control [21]. A semi-active system is generally considered less costly compared to an active system and its performance is better than a passive system [28,29]. However, it requires some switching mechanisms or modulated dissipating elements to adjust the mount properties [27]. Although semi-active systems require only signal processing and low-level power supplies (thus suitable for earthquake applications where power failure is a common phenomenon), they are generally non-linear and their performance is generally not as good as an active system [29].

1.2.2 Control strategies

In active isolation, an external source supplies the power to control actuator(s) that apply force(s) to the structure. These forces, generally referred to as control or secondary forces, are applied in a prescribed manner. The prescribed manner, in this context, is defined as the control strategy. These strategies are applied to a physical system with the objective of keeping the output, (force, acceleration, velocity, displacement etc) at a specified set of locations within the structure, below a specified level in the presence of any disturbances [21]. In control theory these physical systems are categorised in two groups (a) without mathematical models and (b) with mathematical models.

In the first group one can choose structural and control design parameters intuitively and try them on a physical system. This is generally referred to as intelligent control. Two main methodologies related to intelligent control have been well developed. They are (a) artificial neural networks and (b) Fuzzy logic control; they have recently been applied to dynamic structures for vibration control, for example Kwak and Sciulli [30] and Kidner [23]. However, since they are rule based, there could be a number of solutions to the physical design problem and the designer has to choose one intuitively.

The second class of problems (i.e. with mathematical models) mathematical models of the physical system and its control environment are constructed. However most of the problems

have to be mathematically idealised for investigation. This gives a set of mathematical models (equations), which can only approximate the actual dynamical behaviour of the physical system. Due to lack of available mathematical techniques, mathematical idealization of a physical system is, in general, only possible if the system is linear [20]. There are many strategies proposed by researchers for this class of problem and there are several methods in which these strategies can be classified: open-loop and closed-loop control [17,31], analogue [32] and digital control [33], feedback and feed-forward control [34] etc. Most closed-loop systems can be broadly classified into feedback and feed-forward control systems. Feed-forward control has generally been used for harmonic disturbances, where a reference signal can easily be obtained. Feedback control is generally used for random disturbances where reference signal is not available [34] or in situations where it is not possible to sample the incoming disturbance soon enough for a feed-forward control system to be effective. Since typical base vibration has an unpredictable waveform, with broadband random excitation [1,6], feedback control is favoured in this project.

There are two other terminologies commonly found in control literature, which are (a) optimal control, for example Sungsoo et al [35] and Khulief [36] and (b) robust control, for example Damaren et al [37]. In this context optimal feedback control means minimising or maximising a performance measure and robust control focuses on the issues of performance and stability in the presence of uncertainty. Optimal control gives more consideration to performance while the robust control gives more consideration to stability

Although an active isolator can be constructed by feeding back the full state variables as seen in references [37-40], a more straightforward and simple way may be direct output feedback control. Although the output can be acceleration, velocity, displacement, force etc, most of the work of this kind tends to favour velocity feedback [2,6,34,38,41,42]. The advantage of using velocity feedback control is that for collocated force actuators and sensors, a multichannel control system is proven to be unconditionally stable [41,43]. In multichannel feedback control system of this type, the decentralised velocity feedback control technique, where each actuator is operated independently by feeding back the equipment velocity response at the same location, has been shown to be effective [2,6,31,44].

For mathematical convenience, most of the structures can be modelled as a discrete parameter system or a continuous (or distributed parameter) system [9]. Although velocity feedback control is widely used in discrete systems for its simplicity and stability

characteristics, it has some problems for distributed parameter systems. Distributed parameter systems such as large space structures have a very high number of vibration modes. The presence of un-modelled modes within the bandwidth of a closed-loop system results in the phenomenon of spillover, which could potentially destabilise the system [45,46,47,48]. Balas [41] showed that collocated direct velocity feedback control provides a stable system, which is insensitive to spillover. However the system could be destabilised by the inclusion of actuator dynamics [46, 47], which are essential components in the control system. Goh and Caughey [47] proposed positive position Feedback (PPF) as a viable alternative. In situations, where the structure does not have a high enough roll-off or if a finite bandwidth actuator/ sensor is used, the system could potentially become unstable [48]. Under these circumstances PPF can be used, and stability (it is not unconditionally stable [46]) can be guaranteed by considering only the stiffness properties of the structure [45].

1.2.3 Applications

Applications of active vibration control found in the literature are summarised in this section. Active control of vibrations has been growing interest for applications to aircraft and helicopters [19,49,50], space structures [41,46,47, 51, 52], automobiles [53,54], ships [55], band saw [37] etc. Pearson et al [49] identified that active vibration control in a helicopter can be applied in three main areas (a) at the rotor, (b) at the main gear box to the fuselage interface (active isolation) and (c) within the fuselage itself. The main source of interior noise in a helicopter is due to the gearbox. Maier et al [50] applied active vibration control to isolate the fuselage from the gearbox using smart gearbox struts in-order to reduce the interior noise. They used peizoceramic patches, which were glued onto the conventional gearbox struts and were used as actuators. Sutton et al [19] considered the active isolation of multiple structural waves on a helicopter gearbox support strut. They identified that tonal vibration due to the meshing of gear teeth in the main drive unit is the main source of high frequency noise in the fuselage and used magnetostrictive actuators clamped to the strut to introduce the required secondary forces.

Vaillon et al [52] used active (micro) vibration isolation to isolate micro-vibration from equipment through the primary structure of a satellite to sensitive payloads. They achieved this by incorporating active elements in all struts of the satellite. Thus isolation of the payload from the source was achieved.

Successful noise control often depends on effective isolation of vibrating machine from its support structure. Jenkins et al [56] used active feed-forward control techniques for the isolation of periodic machinery vibrations. The requirement of a reference signal in feed-forward control was achieved by sensing the rotation of the machine. They showed that the kinetic energy of the machine could be reduced at harmonics of the firing frequency of the test engine.

Esmailzadeh and Fahimi [53] studied active suspensions for a car. They compared the available passive and active suspension and concluded the performance of active suspension is much superior than that of passive system. They discussed that this superior performance can be achieved when the actuators are controlled with optimal full state-vector feedback.

Winberg et al [55] showed that the sound level in the cabin of a ship could be minimised by actively isolating the hull from the engine. Nevala and Jarviluoma [57] considered active isolation for driver's seat for off-road vehicles. They showed that the performance of an active system is better in comparison with a passive system.

General-purpose vibration isolation tables, which are intended to isolate a payload from floor motion (base excitation), find application in optical experiments, semiconductor manufacturing, scanning probe microscopes, commercial interferometers, electro-physiology recording, precise measurement etc. Erin and Wilson [58] proposed a pneumatic vibration isolator employing active controller for the vibration isolation purposes.

Although this review on the applications of active isolation is not comprehensive, it shows the wide range of applications available for active vibration isolation. In addition a brief survey of commercial companies producing active isolation system and solutions is given in appendix A (based on Internet search).

1.2.4 Performance and related issues

The primary objective in active isolation is the reduction of the vibratory response or kinetic energy of the structure considered, and is often referred to as the performance (or objective) of the system in the active control literature. Although stability is a prerequisite for good performance, it is not necessarily true that all stable systems exhibit good performance [59].

In this section, methods to access the performance of active control systems, which are found in literature, are discussed.

The effective evaluation of an active control system depends on the choice of the performance measure and how well the parameter(s) used as a performance measure(s) represent the actual physical vibration [60]. Sometimes the most meaningful performance measure can be calculated in a theoretical model, but may be difficult to measure directly in practice, and hence a compromise often is required. To a certain extent this also depends on the type of structure. These performance measures include total kinetic energy [2,19, 60] where the structure is generally considered rigid, minimising highest modal energy [61] where the structure is a large flexible one, power transmission or power flow [62-64], flexural energy level [65], sum of squares of translational velocity components [60,66], magnitude of velocity or point mobility [67], vibration amplitude [68] etc. Although there is no obvious criterion for the choice of performance measure, it is the complexity and nature of the vibration of the structure, which determines the performance measure. The most commonly found performance measures are summarised in Table 1.1.

Performance measure	Limitations
Magnitude of velocity per unit disturbance, vibration amplitude	This can be applied to systems that can be modelled as single degree of freedom system [67,68] or lumped mass-spring-damper systems. The advantage is that the cost function is easy to measure.
Total kinetic energy (i.e. the sum of kinetic energy in heave, pitch and role motion)	This is applicable for systems that can be modelled as rigid bodies for example [2,19]. Most distributed systems can only be modelled as rigid bodies at low frequencies [69]
Power transmission	Minimisation of power transmission is a good strategy [70]. However the difficulty in measuring such parameter and the effects produced by flanking paths makes this approach practically difficult.
Sum of squares of translational velocity components	If the structure being controlled is flexible then it is difficult and inappropriate to consider total kinetic energy or point mobility etc. Under theses circumstances this method has proven to be good [60,66].

Table 1.1 Summary of performance measures

Another important term, which has some similarity with the performance measure in the active vibration control literature, is the parameter being controlled. This is sometimes referred to as the cost function. This parameter can sometimes be used as the performance measure as well, for example magnitude of velocity can be the cost function and the performance measure. The cost function must reflect the nature of the dynamic system for active control to be a success [60]. Brennan et al [64] compared three cost functions to control flexural vibration on a beam namely (a) suppression of the incident propagating wave, (b) maximizing the power absorbed by the secondary force and (c) minimizing the total power supplied to the beam. They used power as the performance measure to evaluate these strategies and concluded that the power minimization strategy was the most appropriate for their application.

Gardonio et al [70] considered a rigid mass acting as a source and a receiver plate connected through a pair of active mounts to study the effectiveness of different control strategies. They considered (a) cancellation of velocities at the receiver junctions, (b) cancellation of forces at the receiver junctions, (c) power due to out-of-plane velocities and forces measured at the receiver junctions and (d) sum of squared out-of-plane velocities and weighted sum of squared out-of-plane forces at receiver junctions. They compared the strategies against the benchmark of minimization of total power transmission and used total power as the performance measure to evaluate the strategies. They concluded that the cancellation of velocity or force and minimising axial power generally gives poor results compared with the benchmark, whereas minimisation of sum of squared out-of-plane velocities and weighted squared out-of-plane forces at receiver junctions gives a better result which is comparable with the benchmark. Anthony and Elliott [60] considered a similar comparison for a lightweight cantilever beam (2D cantilever beam-like truss structure). They considered (a) total vibrational energy (b) the flexural vibration energy level, (c) sum of squares of translational velocity components and (d) weighted sum of all velocity components (i.e. translational and rotational) and used total vibrational energy to evaluate the other three and concluded that weighted sum of all velocity components was more suitable. These analyses thus show that the strategies are system dependent and should be considered carefully.

1.2.5 stability and related issues

Stability of a feedback control system can be judged using several methods such as the root-locus method, Nyquist stability criterion, gain and phase margin etc [18, 31]. For a multi-input multi-output system the Nyquist criterion states that a control system is stable if and only if none of the eigenvalue loci of the corresponding open-loop system enclose (-1,0) in the Nyquist plane [31]. The advantage of using this criterion is that, in a feedback control system the open-loop response can be measured and easily compared with mathematical predictions [2].

As mentioned previously, the characteristic difference between passive and active control is that passive control does not make any real-time changes in the system and hence cannot destabilise a conservative system [20]. There can be un-modelled dynamic characteristics (which are difficult to capture in a model), which could make the behaviour of the real system fall short of the designed active system. In control theory this kind of error is categorised into four groups (a) parameter error (b) errors in model order (c) neglected disturbance and (d) neglected nonlinearities. No single control theory can treat all four types of errors [59].

Balas [41] showed that for collocated actuators and sensors, a multi-input and multi-output system is unconditionally stable. Such stability guarantees fall short in practice, in the presence of real hardware and non-negligible dynamics of actuators and sensors. Thus, even an error-free design poses serious problems when it comes to practice. In addition, unavoidable time delays frequently appear in controlled structural systems [71]. The characteristic equation of a linear system with time delays is a transcendental equation involving exponential functions and potentially has an infinite number of roots [13, 71]. Thus stability analysis of a multi-degree of freedom system with time delay is usually difficult.

1.2.6 Factors affecting stability and performance

As mentioned in section 1.2.5 sensors and actuators together with associated signal conditioning equipment and time delay affect the stability and performance. In this section additional factors affecting the performance and stability of active vibration isolation are reviewed in conjunction with them.

When a secondary force is created that is proportional to absolute velocity of the equipment, the system will control the basic resonance without compromising high frequency performance. This is termed 'skyhook damping' [72]. Elliott et al [67] pointed out that this 'skyhook' phenomenon can be practically realised using two actuator arrangements (a) reactive actuator and (b) inertial actuator. In these cases the secondary force generated by the actuator must either (a) react off the base structure or (b) react off an inertial mass. They showed that the stability of the reactive system is tolerant of the additional contribution to the plant response from the reactive force. However for an inertial configuration to be stable with high feedback gain, the natural frequency of the actuator must be well below that of the equipment on its resilient mount.

Most practical structures are multi-degree of freedom systems and they require more than one sensor-actuator pair to control their vibration. The overall performance of an active control system can be greatly improved by choosing proper sensors and sensor positions [73]. However the robustness of such an optimal system for uncertainties is not guaranteed. Kashani and Kiriczi [74] considered unstructured and structured uncertainties of an active suspension system and showed that robust stability of an active suspension system could be obtained. In addition to these uncertainties there exists a class of uncertainty due to component failure in an active system and this is an area that requires further research.

As mentioned previously, time delay in the controller is another parameter, which could affect the performance and stability. Most of the analyses of the stability of feedback systems with time delay establish some necessary and sufficient conditions for stability for example [71,75]. However these conditions do not show any explicit relationship between the time delay and the system parameters for a stable system.

In practice there exists another difficulty due to the inability to generate control forces exactly as desired due to the non-ideal characteristics of the components in the control system. Ren et al [33] analysed the effect of phase lag introduced by A/D and D/A converters and electromagnetic actuators. They argued that in a velocity feedback system, phase lag of a little over ninety degrees could potentially cause instabilities. However in an active control system there are other components such as an integrator, high-pass filters, low-pass filters, time delays etc in addition to A/D, D/A converters and actuators. For a thorough analysis they also have to be investigated.

1.2.7 Sensors and actuators in active isolation

An active vibration control system consists of actuators, sensors and an electronic controller together with signal conditioning devices. Although there have been significant advances in controller design, in terms of software, hardware and control algorithms, the developments in the design of transducers have not matched in pace [76]. The ability to stabilise the active isolation system and achieve performance objectives using feedback control is highly dependent on the location, quality, type and number of control actuators and sensors. This section presents a brief survey on sensors and actuators used in active vibration isolation that can be found in the literature.

Garcia-Bonito et al [76] summarise the type of actuators and their relative merits and demerits as follows. Actuators used in active control, in general employ four mechanisms. They are (a) electromagnetic (b) hydraulic (c) piezoelectric and (d) magnetostrictive. Electromagnetic vibration actuators work on the solenoid principle. They are normally cheap and quite large for the amount of force they generate. Hydraulic actuators can provide very high force but are expensive, heavy and inefficient at high frequencies. On the other hand, the vibration actuators based on piezoelectric or magnetostrictive elements are small, compact and produce comparatively large forces. This leaves a requirement for a selection criterion for actuators. This is achieved by (a) matching the stiffness of the actuator to the stiffness of the external load or (b) the actuator should be able to generate enough force to produce a free displacement equal to or greater than the source displacement [76].

Accelerometers together with electromagnetic actuators are generally used as sensors and actuators for active vibration isolation, for example [2,6]. Malowicki and Leo [78] used a peizoceramic actuator for active isolation of automotive seats. They showed that pre-stressed, curved peizoceramic actuators with feedback control techniques can be employed to achieve the force and displacement levels required for active isolation of automotive seats.

One of the basic requirements of actuators for active isolation in space applications is that they are lightweight. This requirement renders electromagnetic actuators largely redundant for space applications. Bohannan et at [79] investigated the use of a piezoelectric polymer actuator for active vibration isolation in space applications. This actuator employs a leaf-spring configuration and the electromechanical properties can be adjusted to meet the requirements for isolation by changing the number of layers (or leafs).

Most of the piezoelectric actuators used in smart structure applications are either stiff-stacks, which produce high force and small deflections or compliant benders, which produce small force and high displacement. This leaves a mid operating range; Garcia-Bonito et al [76] designed a high displacement piezoelectric actuator, which essentially uses a PZT (lead Zirconate/titanate) ring as an active component driving a piston hydraulically.

Piezoelectric materials can transform mechanical energy into electrical energy and *vice versa.* The first property allows one to use it as a sensor, as described for example by Yang et al [77], while the other property allows it to be used as an actuator, as described for example, by Baz et al [61].

1.3 State of the art within the scope of the project

The technologies available to tackle vibration isolation have been briefly reviewed in the preceding sections. Figure 1.1 shows how the various facets scattered in the literature can be structured within the perspective of this project. In this section each layer of Figure 1.1 discussed in the proceeding sections are assessed.

In layer one, methods of vibration isolation are given and briefly reviewed in section 1.2.1. As pointed out by Ungar [22], there is an inherent problem associated with good high and low frequency isolation with passive systems. This problem can be overcome by coupling an active system to the passive system [14] known as a hybrid (or sometimes as an active system). The advantage of this method is that it not only eliminates the inherent problem associated with passive methods but also reduces the external power requirement if only active methods are to be used. In addition it gives some additional protection in the event of power failure, which is not available with a purely active system. Thus this hybrid active-passive system is the one studied in this thesis.

Considering the strategies given in layer 3, feedback control is considered appropriate for vibration isolation since typical base vibration has an unpredictable waveform with broadband random excitation [1,6]. Performance and stability are two main issues with the design of a control system. Both of these criteria have to be analysed separately.

All active systems consist of sensors, actuators and an electronic controller together with signal conditioning devices, which often place limitations on the available performance as pointed out by Brennan et al [15]. Thus using decentralised feedback control in this thesis, is an holistic analysis of a vibration isolation system integrating (a) the structural dynamics (b) signal conditioning devices and (c) actuators, to assess the stability and performance of the system. In addition uncertainty due to component failure is also analysed.

1.4 Objective and contribution of the thesis

The feasibility of active vibration isolation using decentralised velocity feedback control techniques was investigated on a two-mount system by Serrand and Elliott [6] and on a four-mount system by Kim et al [2]. They showed that there is a significant difference between theoretical prediction and measurement due to low frequency phase advance introduced by external instruments. As discussed by Brennan et al [15], sensors, actuators and signal conditioning devices, which are essential components in active vibration isolation, often place limitations on the available performance. The objectives of this thesis are to,

- Investigate the performance and stability of an active isolation system, which uses decentralised acceleration, velocity and displacement feedback control strategies.
- Investigate the stability limitations on the above three control strategies by integrating (a) structural dynamics (b) signal conditioning devices (c) actuators and (d) time delay in the feedback loop.
- Identify the sources, which have significant effect at (a) low and (b) high frequencies, and derive simple formulae for the maximum gains for a stable system and identify the best strategy among acceleration, velocity and displacement feedback control strategies.
- On the chosen strategy, investigate the performance due to the uncertainty arising from component failure.

The main contributions of this thesis are,

- The sources of instability at low frequencies have been identified, and the limitations they place on the stability have been established by integrating their characteristics

together with the structural dynamics. Simple formulae for maximum gain have been derived for all three-control strategies.

- The sources of instability at high frequencies have been identified and their limitation on the stability has been established by integrating their characteristic together with structural dynamics. Simple formulae for maximum gain have also been derived for all three strategies.
- The limitation on performance due to component failure in a decentralised feedback control has been established.

Additionally two analytical derivations relating the stability of (a) a base excited single degree of freedom system and (b) a multi-input-multi-output system have been established. They are,

- Base excited SDOF system for the three control strategies - Appendix B
- Stability of a MIMO system on a rigid foundation for the three control strategies - Appendix F

1.5 Layout of this thesis

To conduct a theoretical and experimental study on active vibration isolation, a two-mount (active/passive mount) system is considered throughout this thesis. Following this introduction, active vibration isolation using decentralised acceleration, velocity and displacement feedback control strategy is investigated for its performance and stability in Chapter 2. In this Chapter, isolation of a two-mount system from both a moving inelastic and a flexible base is investigated. A clamped-free-clamped-free (CFCF) base is considered as the flexible base. The predictions provided by the idealised model are compared with measured data in this chapter, where a large discrepancy between predicted and observed behaviour is noted. This discrepancy requires modification of the idealised model, and is described in Chapter 3 and 4. In addition Chapter 3 describes the stability issues at low frequency in all three control strategies. Simple formulae for maximum gain integrating structural dynamics, and characteristics of signal conditioning devices are derived in this Chapter. Theoretical models are validated by experimental work. Chapter 4 describes the stability issues at high frequencies. Simple formulae are also derived for maximum gain with time delay for acceleration, velocity and displacement feedback control strategies. In Chapter

5, the performance of the active isolation system with uncertainty due to component failure (in a single loop) is investigated. The theoretical models are validated by experimental work. Finally conclusions are summarised and further work is suggested in chapter 6. Nine appendixes have also been included to support the main body of the thesis.

Chapter 2

The concept of active vibration isolation and decentralised feedback control

2.1 Introduction

As discussed in Chapter 1 conventional passive vibration isolation systems, which consist of compliant mounts positioned between the base and the equipment to be isolated, can provide good isolation at high frequencies, above the resonance frequency of the system [6]. In order to achieve this high frequency performance, damping present in the mounts must be small, which degrades the low frequency performance. One way to overcome this problem is to introduce an active element into each existing passive mount [13,14]. The active system considered in these papers involves feeding back the full state variables, as commonly seen in work on active suspensions [53, 54]. However a more simple and straightforward way may be to use direct output feedback [2,6]. In this approach the required secondary force is proportional to the output, which, can in general, be acceleration, velocity or displacement of the equipment.

The work in this thesis describes a theoretical and experimental investigation into an active isolation system with two-mounts in which electromagnetic actuators are installed in parallel with each passive mount. These active/passive mounts are placed between a piece of equipment (such as the instrument boxes in aeroplanes and telescopes in satellites etc.) and a vibrating base. As discussed in Chapter 1, feedback control is the best control strategy for this kind of problem, where the base vibration is often random. Each actuator is operated independently by feeding back the signal proportional to the corresponding output (acceleration, velocity or displacement) at the same location [2]. This is generally known as decentralised feedback control with collocated sensors and actuators [31].

In general, equipment is three-dimensional in nature and is supported on four active/passive mounts. These mounts are placed close to the four geometric corners of the equipment in

such a way to maintain static balance. Kim et al [2] studied such a four-mount system, which had a decentralised feedback control strategy. They encountered instability at about 1Hz (for a high gain) using velocity feedback control.

Because the two-mount isolator system is relatively simple compared to the four-mount system, it has the advantage of being able to give more insight into the stability and performance issues and factors affecting them (rather than the effect by the structural dynamics). Acceleration, velocity and displacement feedback control strategies are applied and assessed.

The objectives of this chapter are to:

- Describe the concept of active vibration isolation using a base excited SDOF system and feedback control strategy.
- Describe the concept of decentralised feedback control using a two-mount system.
- Establish that there is a considerable discrepancy between the system that is commonly used for closed-loop performance and stability analysis, and a real system (using acceleration, velocity and displacement feedback control).

The inherent stability issues related to the feedback control systems are also studied for the SDOF system model and presented in Appendix B. An analytical study on stability and performance of a two-mount feedback control system is compared with some experimental work and finally conclusions are given.

2.2 Concept of active vibration isolation

Consider an active vibration isolation system shown in Figure 2.1a, where an equipment structure of mass m is supported upon a single mount with stiffness k and damping c. A controller with frequency response function $H(j\omega)$ is used to produce the required secondary control force, which can be proportional to acceleration, velocity or displacement of the equipment. This control force is applied between the base and the equipment in such a way to give negative feedback control. The impedance method described by Kim et al [2] is used for the analysis of the system.

A simplified impedance representation of the system is shown in Figure 2.1b, where Z_e is the impedance of the unconnected equipment and $Z_m = \frac{k}{j\omega} + c$ represents the impedance of the mount. Similarly Z_b is the impedance of the base at the mount location. The equipment velocity V_e $\left(v_e(t) = V_e(j\omega)e^{j\omega t}\right)$ is related to the mount force F_m $\left(f_m(t) = F_m(j\omega)e^{j\omega t}\right)$ as follows,

$$F_m = Z_e V_e \tag{2.1}$$

where F_m is the force generated by the mount (both active and passive) and is given by,

$$F_m = F_c + Z_m(V_b - V_e) \tag{2.2}$$

where $f_c(t) = F_c(j\omega)e^{j\omega t}$ is the control force and V_b $\left(v_b(t) = V_b(j\omega)e^{j\omega t}\right)$ is the velocity of the base at the location of the mount. The base velocity can be expressed as,

$$Z_b V_b = F_{pm} - F_m \tag{2.3}$$

where F_{pm} is the collocated disturbance force. (Note that the effect of any non-collocated force can be transferred as an equivalent collocated force using $F_{pm} = Z_b Y_{bp} F_p$, where Y_{bp} is the transfer mobility between the disturbance force and the mount location and F_p is the primary force). From equations (2.1), (2.2) and (2.3), in the absence of the disturbance force, F_{pm}, the equipment velocity is related to the control force by,

$$V_e = \frac{1}{Z_m + Z_e + Z_m Y_b Z_e} F_c \tag{2.4}$$

Now consider Figure 2.1c, which describes the typical feedback control block diagram representation of a single-input (for example disturbance force) and single-output (for example velocity of the equipment) system. In the absence of the primary force (i.e. $F_{pm} = 0$), the secondary/control force F_c is related to the equipment velocity V_e by [6],

$$V_e = G(j\omega)F_c \tag{2.5}$$

where $G(j\omega)$ is the plant frequency response function, which from equations (2.4) and (2.5) is given by,

$$G(j\omega) = \frac{1}{Z_e + Z_m + Z_m Y_b Z_e} \tag{2.6}$$

The control forces for acceleration, velocity and displacement feedback control are given by $F_c = j\omega g_a V_e$, $F_c = g_v V_e$ and $F_c = \frac{1}{j\omega} g_d V_e$ respectively, where g_a, g_v and g_d are the feedback gains for acceleration, velocity and displacement feedback control respectively. Comparing

the control forces and Figure 2.1c the feedback frequency response functions for acceleration, velocity and displacement feedback control can receptively be written as,

$$H(j\omega) = j\omega g_a \tag{2.7a}$$

$$H(j\omega) = g_v \tag{2.7b}$$

$$H(j\omega) = \frac{1}{j\omega} g_d \tag{2.7c}$$

The open-loop and closed-loop frequency response functions are given by $G(j\omega)H(j\omega)$ and $\frac{V_e}{F_{pm}} = \frac{G(j\omega)}{1+G(j\omega)H(j\omega)}$ respectively.

2.2.1 stability and performance of the active isolation system

Feedback control systems are susceptible to instability and hence need assessment. The Nyquist criterion is generally used for stability analysis [59], which states that a closed-loop feedback control system is stable if and only if the plot of the real part against the imaginary part of the open-loop frequency response function does not enclose the critical point (-1,0) on the Nyquist plane [59]. For a single input and single output (SISO) system this can be interpreted as; when the imaginary part of open-loop frequency response function is zero $\left(\text{i.e. } \text{Im}\{G(j\omega)H(j\omega)\} = 0\right)$, the real part of the open-loop frequency response function is greater than -1 $\left(\text{i.e. } \text{Re}\{G(j\omega)H(j\omega)\} > -1\right)$ then the system is stable. It is said to be unconditionally stable, when the imaginary part is zero, and the real part is greater than or equal to zero $\left(\text{i.e. } \text{Re}\{G(j\omega)H(j\omega)\} \geq 0\right)$.

A stability analysis of a SDOF isolation system with acceleration, velocity and displacement feedback control is given in the Appendix B. Active isolation using acceleration, velocity and displacement feedback control system is unconditionally stable when the equipment is mass-like.

The closed-loop responses for acceleration, velocity and displacement feedback control are given by, $\frac{V_e}{F_{pm}} = \frac{G(j\omega)}{1+j\omega g_a G(j\omega)}$, $\frac{V_e}{F_{pm}} = \frac{G(j\omega)}{1+g_v G(j\omega)}$ and $\frac{V_e}{F_{pm}} = \frac{G(j\omega)}{1+\frac{g_d}{j\omega}G(j\omega)}$

respectively. It should be noted that the feedback gains are always positive and appear in the denominator. These equations suggest that as the gain is increased to a very large value (say infinity) the equipment velocity tends to zero. Thus the equipment is dynamically decoupled from the base and hence is isolated in all three cases.

2.2.2 Simulations

Some simulations are presented in this section in-order to illustrate the stability and performance of the active isolation systems discussed above. For simplicity consider a SDOF system on a moving inelastic base. Equations (2.1) and (2.2) give,

$$Z_e V_e = F_c + Z_m (V_b - V_e) \tag{2.8}$$

Since the base has a prescribed motion, the primary disturbance is the prescribed motion of the base. Thus in the absence of primary disturbance $(i.e\ Z_m V_b = 0)$ the control force is related to the equipment velocity as,

$$V_e = \frac{1}{(Z_e + Z_m)} F_c \tag{2.9}$$

Thus the plant frequency response function is given by,

$$G(j\omega) = \frac{1}{Z_e + Z_m} \tag{2.10}$$

where $Z_e = j\omega m$.

From equation (2.10), substituting for Z_e and Z_m the plant frequency response function can be written as,

$$G(j\omega) = \frac{j\omega}{k - \omega^2 m + j\omega c} \tag{2.11}$$

Substituting $\omega_n = \sqrt{\frac{k}{m}}$ and $\zeta = \frac{c}{2\sqrt{mk}}$ (System natural frequency and damping ratio) into equation (2.11) and writing in non-dimensional from gives,

$$G(j\Omega) = \frac{cV_e(j\Omega)}{F_c(j\Omega)} = \frac{j2\zeta\Omega}{(1 - \Omega^2 + j2\zeta\Omega)} \tag{2.12}$$

where $\Omega = \frac{\omega}{\omega_n}$, is the forcing frequency normalised by the natural frequency of the system.

Letting the controller frequency response function be $H(j\Omega)$ the non-dimensional closed-loop frequency response is given by:

$$\frac{V_e(j\Omega)}{V_b(j\Omega)} = \left(\frac{G(j\Omega)}{1+G(j\Omega)H(j\Omega)}\right)\left(\frac{Z_m}{c}\right) \tag{2.13}$$

From equations (2.7a), (2.7b) and (2.7c), feedback frequency response functions are given by, for acceleration feedback control $H(j\Omega) = j\Omega\frac{g_a}{m}\frac{1}{2\zeta}$, for velocity feedback control $H(j\Omega) = \frac{g_v}{c}$ and for displacement feedback control $H(j\Omega) = \frac{1}{j\Omega}\frac{g_d}{k}\frac{1}{2\zeta}$, where $\frac{g_a}{m}$, $\frac{g_v}{c}$ and $\frac{g_d}{k}$ are the normalised feedback gains. Substituting for $G(j\Omega)$ and the appropriate $H(j\Omega)$ into equation (2.13), the non-dimensionalised closed-loop frequency response function can be derived for acceleration, velocity and displacement feedback control:

ACCELERATION FEEDBACK CONTROL

$$\frac{V_e(j\Omega)}{V_b(j\Omega)} = \frac{1+j2\zeta\Omega}{1-\left(1+\frac{g_a}{m}\right)\Omega^2 + j2\zeta\Omega} \tag{2.14}$$

VELOCITY FEEDBACK CONTROL

$$\frac{V_e(j\Omega)}{V_b(j\Omega)} = \frac{1+j2\zeta\Omega}{1-\Omega^2 + j2\zeta\Omega\left(1+\frac{g_v}{c}\right)} \tag{2.15}$$

DISPLACEMENT FEEDBACK CONTROL

$$\frac{V_e(j\Omega)}{V_b(j\Omega)} = \frac{1+j2\zeta\Omega}{\left(1+\frac{g_d}{k}\right)-\Omega^2 + j2\zeta\Omega} \tag{2.16}$$

Figure 2.2a shows the closed-loop non-dimensional transmissibility for acceleration, velocity and displacement feedback control as a function of non-dimensional frequency for non-dimensional gain of 10, and a damping ratio of 0.05. It can be seen that acceleration feedback reduces the response at the original resonance frequency and produces a resonance frequency lower than that of the original system. Thus acceleration feedback control effectively adds mass to the system. It can also be seen from Figure 2.2a that velocity feedback effectively adds damping to the system, and that displacement feedback effectively adds stiffness to the system [13]. It is also noted that acceleration and displacement feedback tend to reduce the damping in the system, which results in narrower peaks. The reason for

this is evident from the expression for the damping ratio given by $\zeta = \frac{c}{2\sqrt{mk}}$, because if either m or k is increased the damping ratio is reduced.

To assess the overall performance of the control strategies the mean-square response of the system normalised to the mean-square response in the absence of control is plotted for the three control strategies. Figure 2.2b shows this for the frequency range $0 \leq \Omega \leq 100$. It can be seen that there is little difference in the performance of the three control strategies for non-dimensional gains up to 60.

The Nyquist plot for acceleration, velocity and displacement feedback control are shown in Figure 2.2c. It can be seen that none of the plots crosses the negative real axis and therefore does not encloses the critical (-1,0) point. In addition, for acceleration feedback control when Ω tends to infinity, the real part tends to $\frac{g_a}{m}$. For velocity feedback control, the Nyquist plot is completely in the right half of the Nyquist plane, and thus the system is unconditionally stable. It crosses the real axis when the real part of the open-loop response is zero and $\frac{g_v}{c}$. Unlike acceleration feedback control, when Ω tends to infinity the real and imaginary parts of the open-loop frequency response function tend to zero. The Nyquist plot for the displacement feedback given in Figure 2.2c shows that displacement feedback control strategy gives a stable system. When Ω tends to infinity the real and imaginary parts of the open-loop frequency response function tend to zero.

2.2.3 Summary

A SDOF system with acceleration, velocity and displacement feedback control has been considered to explain the concept of active vibration isolation. Acceleration, velocity and displacement feedback control strategies give a stable system (as shown in Appendix B). For the systems on moving inelastic base, the Nyquist plots for all three strategies begin at the origin and follow a clockwise direction back to or closer to the origin as the frequency is increased. In the acceleration feedback control strategy, the critical point (-1,0) is closer to the low frequency part of the plot. For velocity feedback control the entire Nyquist plot lies far away from the critical point (-1,0). In displacement feedback control the critical point is closer to the high frequency part of the plot.

It can be seen that all three strategies reduce the resonance peak response of the original passive system. Their overall performance is also comparable.

Thus all the three strategies considered, which provide a stable system with comparable performance, can dynamically decouple/isolate the equipment from the base.

2.3 Decentralised feedback control for vibration isolation

Consider a two-mount system modelled as a lumped mass-spring-damper system with independent (decentralised) feedback control applied as shown in Figure 2.3a. Two-control forces f_{c1} and f_{c2} act between the equipment and the base in parallel with the passive mounts. The control system employs a direct negative output feedback control such that the signal measured by each sensor mounted on the equipment is used to generate a control force at that mount location. These forces are produced via the controllers, which have equal gain and are proportional to output (acceleration, velocity or displacement) at the mount. In this chapter the performance and stability of this system is investigated and compared with measurement. Two situations are considered, namely the two-mount system (a) on a moving inelastic base and (b) on a flexible base. In-order to ensure that the system on a moving inelastic base behaves as a two-degrees-of freedom system an asymmetric equipment structure is considered as shown in Figure 2.3a.

2.3.1 Impedance representation of the two-mount system

Figure 2.3b shows the impedance representation of the physical system shown in Figure 2.3a, where $\mathbf{Z}_e$ is the impedance matrix of the unconnected rigid equipment and $\mathbf{Z}_m$ represents the impedance matrix of the mounts. Similarly $\mathbf{Z}_b$ is the impedance matrix of the base. The vector of velocities of the equipment $\mathbf{v}_e$ is related to the vector of mount forces as follows,

$$\mathbf{f}_m = \mathbf{Z}_e \mathbf{v}_e \tag{2.17}$$

where $\mathbf{f}_m$ is the mount force vector (both active and passive) and is given by,

$$\mathbf{f}_m = \mathbf{f}_c + \mathbf{Z}_m(\mathbf{v}_b - \mathbf{v}_e) \tag{2.18}$$

where the impedance matrix $\mathbf{Z}_m$ is diagonal, whose diagonal terms are the impedance of each mount, which are given by $Z_m = \frac{k}{j\omega} + c$. In addition $\mathbf{f}_c$ is the vector of control forces and $\mathbf{v}_b$ is the vector of velocities of the base at the location of mounts.

The base velocity vector can be written as,

$$\mathbf{Z}_b \mathbf{v}_b = \mathbf{f}_{pm} - \mathbf{f}_m \tag{2.19}$$

where $\mathbf{f}_{pm}$ is the vector of collocated disturbance forces. If the disturbance force(s) are non-collocated force(s) then their effect can be expressed in terms of equivalent collocated forces as,

$$\mathbf{f}_{pm} = \mathbf{Z}_b \mathbf{Y}_{bp} \mathbf{f}_p \tag{2.20}$$

where $\mathbf{Y}_{bp}$ is the transfer mobility of the base between the locations of mounts and the vector of primary forces $\mathbf{f}_p$. Combining equations (2.18), (2.19) and (2.20) give the compact description of the system in terms of impedances.

$$\begin{bmatrix} \mathbf{Z}_e + \mathbf{Z}_m & -\mathbf{Z}_m \\ -\mathbf{Z}_m & \mathbf{Z}_b + \mathbf{Z}_m \end{bmatrix} \begin{bmatrix} \mathbf{v}_e \\ \mathbf{v}_b \end{bmatrix} = \begin{bmatrix} \mathbf{f}_c \\ \mathbf{f}_{pm} - \mathbf{f}_c \end{bmatrix} \tag{2.21}$$

From equation (2.20) and in the absences of primary forces $\left(\text{i.e. } \mathbf{f}_p = 0\right)$, the equivalent collocated primary disturbance vector $\mathbf{f}_{pm} = 0$. The equipment velocity and control force can then be related by,

$$\mathbf{v}_e = \left[\mathbf{Z}_e + \mathbf{Z}_m + \mathbf{Z}_m \mathbf{Y}_b \mathbf{Z}_e\right]^{-1} \mathbf{f}_c \tag{2.22}$$

where $\mathbf{Y}_b = \mathbf{Z}_b^{-1}$

Similar to the single mount system, Figure 2.3c, describes a typical feedback control block diagram representation of a multi-input (for example disturbance forces) and multi-output (for example velocity at mount locations) system. The secondary/control force vector $\mathbf{f}_c$ is related to the mount location velocity vector $\mathbf{v}_e$ by,

$$\mathbf{v}_e = \mathbf{G}(j\omega)\mathbf{f}_c \tag{2.23}$$

From equations (2.22) and (2.23) the plant frequency response matrix is given by,

$$\mathbf{G}(j\omega) = \left[\mathbf{Z}_e + \mathbf{Z}_m + \mathbf{Z}_m \mathbf{Y}_b \mathbf{Z}_e\right]^{-1} \tag{2.24}$$

which is a compact impedance representation of the plant.

2.3.2 Formulation of performance measure

So far little or no attention is paid specifically to the type of feedback (i.e. acceleration, velocity or displacement). For analytical simplicity the output of the block diagram is kept as velocity. This means that the plant response matrix can be expressed in terms of mobility or impedance, which is relatively easy to interpret [83].

The feedback frequency response matrix can be adjusted so that acceleration, velocity and displacement feedback control can be achieved as desired (similar to the single mount case considered previously). These give three formulations for the feedback frequency response matrix. They are, $\mathbf{H}(j\omega)= j\omega\begin{bmatrix} g_a & 0 \\ 0 & g_a \end{bmatrix}$, $\mathbf{H}(j\omega)=\begin{bmatrix} g_v & 0 \\ 0 & g_v \end{bmatrix}$ and $\mathbf{H}(j\omega)=\frac{1}{j\omega}\begin{bmatrix} g_d & 0 \\ 0 & g_d \end{bmatrix}$ for acceleration, velocity and displacement feedback control respectively.

Considering Figure 2.3c, the closed-loop velocity vector $\mathbf{v}_e$ (i.e. velocity vector in the presence of the primary disturbance) can be written as,

$$\mathbf{v}_e = \left[\mathbf{I}+\mathbf{G}(j\omega)\mathbf{H}(j\omega)\right]^{-1}\mathbf{G}(j\omega)\mathbf{f}_{pm} \qquad (2.25)$$

where $\mathbf{I}$ is the identity matrix of size (2 x 2)

Letting the velocity vector at the mass centre be $\mathbf{a}=\begin{bmatrix} v \\ l\dot{\theta} \end{bmatrix}$ and $\mathbf{Q}$ be the transformation matrix which transforms the mount location velocity vector $\mathbf{v}_e$ to the mass centre velocity vector $\mathbf{a}$, then these velocity vectors are related as,

$$\mathbf{v}_e = \mathbf{Q}\mathbf{a} \text{ and hence } \mathbf{a} = \mathbf{Q}^{-1}\mathbf{v}_e \qquad (2.26a,b)$$

Thus using equation (2.26b) the velocity vector at the mass centre can be found provided $\mathbf{Z}_e$, $\mathbf{Z}_m$ and $\mathbf{Q}$ are known. As discussed in Chapter 1, since the equipment is rigid, the kinetic energy of the equipment mass may be used as the performance measure. This is given by,

$$E_k = \frac{1}{2}\mathbf{a}^H\mathbf{J}\mathbf{a} \qquad (2.27)$$

where $\mathbf{a}^H$ is the Hermitian transpose of velocity vector $\mathbf{a}$ and $\mathbf{J}$ is the inertia matrix of the equipment, which is given by,

$$\mathbf{J} = \begin{bmatrix} m & 0 \\ 0 & \frac{J}{l^2} \end{bmatrix} \qquad (2.28)$$

where J is the moment of inertia about the mass centre.

Using equation (2.27) the kinetic energy that may be used to investigate the closed-loop performance of a two-mount isolation system can be found. The stability of the system can be studied using the Nyquist criterion. For a multi-input-multi-output (MIMO) system the Nyquist criterion states that a closed-loop MIMO system is stable if and only if none of the eigenvalue loci of the open-loop frequency response matrix $\mathbf{G}(j\omega)\mathbf{H}(j\omega)$ encloses the critical (-1,0) point in the Nyquist plane [31].

2.4 Simulations

Simulations and experiments are carried out on a physical system (shown in Figure 2.4) whose main properties are given in Table 2.1 [4]. The system shown in Figure 2.4 is a symmetric system, where an aluminium plate (which represents some rigid equipment and behaves as a rigid body at frequencies up to 1kHz [4]) is supported on two-rubber mounts placed beneath the plate. Two electromagnetic shakers are also installed in parallel to the passive mounts to produce the control forces. The main properties given in Table 2.1 are used for simulations.

2.4.1 Two-mount system on a moving inelastic base

In this section the two-mount system on a moving inelastic base with acceleration, velocity and displacement feedback control is considered. Both stability and performance are discussed. When a moving inelastic base is considered, the disturbance is the prescribed motion of the base. Thus the plant response function is modified. From equation (2.17) and (2.18)

$$\mathbf{Z}_e\mathbf{v}_e = \mathbf{f}_c + \mathbf{Z}_m(\mathbf{v}_b - \mathbf{v}_e) \tag{2.29}$$

In the absence of primary disturbances $\left(\text{i.e. } \mathbf{Z}_m\mathbf{v}_b = 0\right)$, the equipment velocity vector can be related to control force vector as,

$$\mathbf{v}_e = \left[\mathbf{Z}_e + \mathbf{Z}_m\right]^{-1}\mathbf{f}_c \tag{2.30}$$

Similar to the previous definition, from (2.30) the plant response matrix is given by,

$$\mathbf{G}(j\omega) = \left[\mathbf{Z}_e + \mathbf{Z}_m\right]^{-1} \tag{2.31}$$

The open-loop frequency response matrix is $\mathbf{G}(j\omega)\mathbf{H}(j\omega)$ and the closed-loop response is given by,

$$\mathbf{v}_e = \left[\mathbf{I} + \mathbf{G}(j\omega)\mathbf{H}(j\omega)\right]^{-1} \mathbf{G}(j\omega)\mathbf{Z}_m \mathbf{v}_b \qquad (2.32)$$

Setting $\mathbf{v}_b = [1 \quad 1]^T v_b$ (because both the mounts experience the same velocity on a moving inelastic base) equation (2.32) becomes,

$$\frac{\mathbf{v}_e}{v_b} = \left[\mathbf{I} + \mathbf{G}(j\omega)\mathbf{H}(j\omega)\right]^{-1} \mathbf{G}(j\omega)\mathbf{Z}_m [1 \quad 1]^T \qquad (2.33)$$

Substituting equation (2.33) in equation (2.26b) the mass centre velocities can be found. Since the two-mount system shown in Figure 2.4 is a symmetric, on a moving inelastic base this system would behave as a SDOF system. In this case a decentralised feedback control is not required (A single input and single output control is sufficient in this case). Thus a mass of 0.69 kg is lumped on one of the shakers so that the system becomes asymmetric. Simulations and experiments for the moving inelastic base case are done using this asymmetric system. In this case the mass centre is at *rl* from the left end of the mount where *l* is the distance between the mounts and *r* (= 0.404) is the ratio of the lengths between the left hand end of the mount and mass centre to the length between the mounts.

2.4.1.1 Acceleration feedback control

The closed-loop response and corresponding mass centre velocities can be obtained from equations (2.31) and (2.26b) respectively provided $\mathbf{Q}$, $\mathbf{Z}_e$, $\mathbf{Z}_m$ and $\mathbf{H}(j\omega)$ are known. From equation (2.27) the total kinetic energy can also be determined to investigate the performance. Similarly these matrices are also required to find the plant response function given in equation (2.31) and hence to find the open-loop frequency response matrix. The feedback frequency response matrix for acceleration feedback control is given by

$$\mathbf{H}(j\omega) = j\omega m \begin{bmatrix} \frac{g_a}{m} & 0 \\ 0 & \frac{g_a}{m} \end{bmatrix} = j\omega m \begin{bmatrix} g_{na} & 0 \\ 0 & g_{na} \end{bmatrix}$$ where g_{na} is the normalised gain for acceleration feedback control. The matrices $\mathbf{Q}$, $\mathbf{Z}_e$ and $\mathbf{Z}_m$ are derived in Appendix C for the system considered and are given by, $\mathbf{Q} = \begin{bmatrix} 1 & -r \\ 1 & 1-r \end{bmatrix}$,

$$\mathbf{Z}_e = j\omega\begin{bmatrix} (1-r)^2 m+\frac{J}{l^2} & (1-r)rm-\frac{J}{l^2} \\ (1-r)rm-\frac{J}{l^2} & r^2 m+\frac{J}{l^2} \end{bmatrix}$$ and $\mathbf{Z}_m = \begin{bmatrix} Z_m & 0 \\ 0 & Z_m \end{bmatrix}$ where $Z_m = \frac{k}{j\omega}+c$. For the system considered (i.e. when a mass of 0.69 kg is lumped on the left end of one of the control shakers) $r = 0.404$.

Figure 2.5 shows the simulations for active vibration isolation using acceleration feedback control. In Figure 2.5a the open-loop plot of eigenvalues are given for a normalised gain $\frac{g_a}{m} = 5$. One eigenvalue is given by the solid line and other by the dashed line. It can be seen from this figure that the eigenvalues do not cross the negative real axis and thus the system is unconditionally stable. Figure 2.5b shows the total kinetic energy of the equipment mass for normalised gains of 0, 5, 10 and 15. It can be seen that when the gain is increased the performance at the original resonance peaks improve. However the peaks appear at lower frequencies. Although active vibration isolation using acceleration feedback control gives a narrower peak with higher magnitude than the original system, the overall performances, which is measured by the change in the kinetic energy of the equipment mass integrated over a frequency range $(0 \le freq \le 250 \text{ Hz})$ shows that the overall performance improves as the gain is increased. The change in kinetic energy, shown in Figure 2.5c is defined as the ratio of area of total kinetic energy curve for a specific band of frequencies $(\text{e.g } 0 \le freq \le 250 \text{ Hz})$ when the gain is some value g to the area when the gain is zero. Considering the total kinetic energy as well as the change in kinetic energy, the isolation of the two-mount system using acceleration feedback control strategy gives a stable system with reasonable performance.

2.4.1.2 Velocity feedback control

Similar to the system with acceleration feedback control, open-loop eigenvalues, total kinetic energy and the change in kinetic energy plots are considered for velocity feedback control. The feedback frequency response matrix for active isolation using velocity feedback control is given by $\mathbf{H}(j\omega) = c\begin{bmatrix} \frac{g_v}{c} & 0 \\ 0 & \frac{g_v}{c} \end{bmatrix} = c\begin{bmatrix} g_{nv} & 0 \\ 0 & g_{nv} \end{bmatrix}$, where g_{nv} is the normalised gain for

velocity feedback control. Figure 2.6 shows the simulations for active isolation using velocity feedback control. The open-loop eigenvalue plots for a normalised gain $\frac{g_v}{c}=5$ are given in Figure 2.6a. One eigenvalue is given by the solid line and other by the dashed line. It shows that the plots do not cross the negative real axis and are entirely on the right half of the Nyquist plane. Thus the system is unconditionally stable. Figure 2.6b shows the total kinetic energy of the equipment mass. It can be seen from this figure that as the gain is increased the resonance peaks improve while low and high frequency parts of the plot remain largely unchanged due to the sky-hook damping effect. The overall performance is judged using the change in kinetic energy of the equipment mass integrated over a frequency range $(0 \le freq \le 250 \text{ Hz})$. This is shown in Figure 2.6c where it can be seen that the system continued to improve as the gain is increased. Thus isolation using velocity feedback control also gives a stable system with reasonable performance.

2.4.1.3 displacement feedback control

In this section simulations for active isolation using displacement feedback control are presented. The feedback frequency response matrix for displacement feedback control is given by $\mathbf{H}(j\omega)=\frac{k}{j\omega}\begin{bmatrix}\frac{g_d}{k} & 0\\ 0 & \frac{g_d}{k}\end{bmatrix}=\frac{k}{j\omega}\begin{bmatrix}g_{nd} & 0\\ 0 & g_{nd}\end{bmatrix}$, where g_{nd} is the normalised gain for displacement feedback control. Figure 2.7a shows the simulations for the open-loop eigenvalue plots for the system with normalised gain $\frac{g_d}{k}=5$. One eigenvalue is given by the solid line and other by the dashed line. It can be seen that these plots also do not cross the negative real axis and hence give an unconditionally stable system. Figure 2.7b shows the total kinetic energy of the equipment mass for various gains. It can be seen that as the gain is increased the response at the original resonance peaks reduces considerably, however the peaks appear at a higher frequency. In addition Figure 2.7c shows that the displacement feedback control system also gives a reasonable overall performance. The simulations reveal that active vibration isolation using displacement feedback gives a stable system with reasonable performance.

2.4.2 Two-mount system on a flexible base

In this section the two-mount system on a clamped-free-clamped-free (CFCF) flexible base with acceleration, velocity and displacement feedback control is considered. Both stability and performance of these systems are discussed. If the base mobility matrix is known, the closed-loop velocities at the mount location can be calculated using equation (2.25). The collocated mount location disturbance force vector is given by equation (2.20). Note that the vector $\mathbf{f}_p$ becomes a single force if the excitation is only a point force. Once the closed-loop velocities at the mount locations are determined the mass centre velocities can also be found using equation (2.26b). From equation (2.27) the total kinetic energy can also be calculated.

2.4.2.1 Clamped-free-clamped-free (CFCF) flexible base

A flexible base structure with a pair of opposite edges are free and other pair is clamped (a clamped-free-clamped-free – CFCF) was considered. This base structure is relatively easy to realise in practice. Figure 2.8 shows a schematic diagram of the flexible base and the position of the mounts of the two-mount system. Figure 2.9 shows the physical CFCF base. The geometric and martial properties are given in Table 2.2. The coordinate system considered for the geometric properties is also shown in Figure 2.8.

The mobility of the base plate is derived in Appendix D and is given by,

$$Y_{ij} = \frac{V(x_i, y_i)}{F(x_j, y_j)} = \frac{j\omega}{m_{st}} \sum_{m=2}^{M} \sum_{n=0}^{N} \frac{\theta_m(x_i)\phi_n(y_i)\theta_m(x_j)\phi_n(y_j)}{N_{mn}(\omega_{mn}^2 - \omega^2 + j2\zeta_s\omega_{mn}\omega)} \qquad (2.34)$$

where, Y_{ij} is the mobility of a CFCF base described by the ratio of velocity at (x_i, y_i) to the force at (x_j, y_j). The integers m and n are number of modal lines. N_{mn} is called the normalising factor and m_{st} is the mass per unit area.

In addition, $\theta(x)$ and $\phi(y)$ are characteristic beam functions in the x and y directions respectively. These functions are chosen to satisfy the plate boundary conditions in the direction they represent. The factors ζ_s and ω_{mn} are the damping ratio and the natural frequency corresponding to mn^{th} mode respectively. A validation of this model is given in Appendix E.

2.4.2.2 Acceleration feedback control

The properties of the two-mount system considered previously are used for the simulations. The plant response matrix of the system is given by equation (2.24), which includes the base structure mobility. Using the base mobility given by equation (2.34) and the same feedback response matrix used for the corresponding case in the moving inelastic base, the open-loop frequency response matrix can be found. The excitation point on the base and the mounts location are given in Table 2.2. The stability of the system can be assessed using the Nyquist criterion for a MIMO system discussed previously.

The open-loop eigenvalue plots for a normalised gain $\frac{g_a}{m} = 5$ are given in Figure 2.10a. One eigenvalue is given by the solid line and other by the dashed line. It can be seen that the eigenvalues of the open-loop frequency response matrix do not cross the negative real axis and hence the system is unconditionally stable. The effects of base dynamics can also be seen in the eigenvalue plots. Total kinetic energy of the equipment mass for normalised gains 0, 5, 10 and 15 are given in Figure 2.10b. It can be seen that the kinetic energy of the equipment mass at the original resonance frequency reduces considerably while the peak appears at lower frequencies, which is similar to the moving inelastic base case. Similar to the SDOF system discussed previously, the acceleration feedback control system effectively adds mass and hence attenuates the response at higher frequencies. The change in kinetic energy of the equipment mass integrated over a frequency range $(0 \leq freq \leq 250 \text{ Hz})$ is given in Figure 2.10c. It shows that as the gain is increased the overall performance of active isolation with acceleration feedback continued to improve and thus provides a system with reasonable performance.

2.4.2.3 Velocity feedback control

Simulations of active vibration isolation using velocity feedback are given in Figure 2.11. The open-loop eigenvalue plot is given in Figure 2.11a, where one eigenvalue is given by the solid line and other by the dashed line. It can be seen that the system is unconditionally stable. The kinetic energy (of the equipment mass) plot is shown in Figure 2.11b for normalised gains 0, 5, 10 and 15. It shows that as the gain is increased the kinetic energy at the resonance peak reduces. Figure 2.11c shows the change in kinetic energy of the

equipment mass integrated over a frequency range $(0 \leq freq \leq 250 \text{ Hz})$ plot as a function of gain. It shows as the gain is increased the system continued to improve.

2.4.2.4 Displacement feedback control

Figure 2.12a shows the open-loop eigenvalue plots for a normalised gain $\frac{g_d}{k} = 5$ of an active isolation system using displacement feedback control. It can be seen that the system exhibits unconditional stability. Figure 2.12b shows the plot of kinetic energy of the equipment mass for normalised gains 0, 5, 10 and 15. It can be seen that as the gain is increased the kinetic energy at the original resonance reduces while the resonance peak appears at higher frequencies as seen in the SDOF system considered previously. A displacement feedback control system effectively adds stiffness to the system and hence alters the dynamic characteristics of the system. Figure 2.12c shows the plot of change in kinetic energy of the equipment mass integrated over a frequency range $(0 \leq freq \leq 250 \text{ Hz})$. It shows that as the gain is increased the system improves.

2.4.3 Summary

A two-mount system with acceleration, velocity and displacement feedback has been considered for active isolation from a moving inelastic base and from a CFCF flexible base. The simulations show that the system is unconditionally stable in all three cases. The performance of the system has been assessed considering kinetic energy of the equipment mass, which shows that in all three strategies the kinetic energy reduces at the original resonance frequency of the passive system. The overall performance assessed by considering the change in kinetic energy of the equipment mass integrated over a frequency range shows that all three strategies give a reasonable overall performance.

2.5 Experiments

Some experimental work was conducted to validate and evaluate the theoretical findings presented in section 2.4. The two-mount system considered for the simulations was considered for the experimental investigation as well. Two situations were considered similar to the previous cases:

(a) Two-mount system on a moving inelastic base

(b) Two-mount system on a CFCF flexible base

These are described in the following sections.

2.5.1 Two-mount system on a moving inelastic base

Figure 2.13 shows the two-mount system described earlier on a moving inelastic base (A large shaker provides the moving inelastic base – Derritron vibrator type VP4). As mentioned previously a mass of 0.69kg was lumped on one of the shakers to give an asymmetric system. A decentralised feedback arrangement used for the experimental investigation is shown in Figure 2.14 and a list of instruments used is given in Table 2.3.

Two accelerometers (B&K type 4375) attached to the equipment, close to the centre of the mounts were used to sense the acceleration of the equipment. The outputs of these accelerometers were conditioned separately by two charge amplifiers (B&K type 2635). These charge amplifiers also provided single and double integration required to produce velocity and displacement signals. Thus the signals required for acceleration, velocity and displacement feedback control could be obtained. A two-channel power amplifier (type V200 Mos Fet) was used as a controller. The outputs of the charge amplifiers were used, as the inputs to the power amplifier. The outputs of the power amplifier were fedback to the secondary shakers so as to produce decentralised negative feedback control. The outputs from the charge amplifiers were also connected to the HP analyser (Hewlett Packard type 35650) for data collection (a frequency resolution of 0.5 Hz was used). Two different configurations were used for open-loop and closed-loop measurements.

The following approach was used measure the open-loop frequency response matrix; in the absence of primary force the control force is related to the equipment velocity by equation (2.23). If the closed-loop is opened then the velocity, which is now the open-loop velocity

and the secondary force can be related as $\mathbf{v}_{eo} = \mathbf{G}(j\omega)\mathbf{H}(j\omega)\mathbf{f}_{co}$ (Note that controller frequency response matrix also included and $\mathbf{v}_{eo}$ and $\mathbf{f}_{co}$ represent the open-loop velocity vector and corresponding control force vector). This can be expanded for a two-mount system to give,

$$\begin{bmatrix} v_{eo1} \\ v_{eo2} \end{bmatrix} = \begin{bmatrix} GH_{11} & GH_{12} \\ GH_{21} & GH_{22} \end{bmatrix} \begin{bmatrix} f_{co1} \\ f_{co2} \end{bmatrix} \tag{2.35}$$

where v_{eo1} and v_{eo2} represent open-loop velocities at mount locations 1 and 2. Similarly f_{co1} and f_{co2} are the secondary forces of the control shaker when the loop is opened. GH_{11}, GH_{12} etc represent the elements of open-loop frequency response matrix. When the system is excited only by the control shaker at mount location 1 $(\text{i.e.} f_{co2} = 0)$, equation (2.35) becomes, $v_{eo1} = GH_{11} f_{co1}$ and $v_{eo2} = GH_{21} f_{co1}$. Similarly when the system is excited by the shaker at mount location 2, equation (2.35) becomes, $v_{eo2} = GH_{22} f_{co2}$ and $v_{eo1} = GH_{12} f_{co2}$. Thus, the elements of open loop frequency response matrix can be found by exciting them at mount locations (by the control shaker), and measuring the response per unit disturbance of the control shaker. (Property of reciprocity can be used to reduce the number of measurement i.e. $GH_{12} = GH_{21}$).

Using this approach, the elements of open-loop frequency response matrix were measured and the open-loop frequency response matrix was constructed (random signal was used too excite the secondary shaker). Figure 2.15a shows the open-loop eigenvalue plots for acceleration feedback control with a power amplifier gain 0.06. In Figure 2.15a one eigenvalue is given by the solid line and other by the dashed line. It can be seen that these eigenvalue plots enclose the Nyquist critical point (-1,0). Thus, the acceleration feedback control system becomes unstable for a relatively low gain.

For closed-loop measurements a rigid plate attached to a large shaker (Derritron Vibrator type VP4) was used as moving inelastic base. A signal from a third accelerometer attached to the moving inelastic base was used as the reference signal for closed loop measurements. A schematic diagram of the experimental set-up is given in Figure 2.14. The kinetic energy can be obtained from closed-loop velocities in a similar manner considered for simulations. From measured closed-loop mount location velocities, mass centre velocities can be calculated using equation (2.26b). Using equation (2.27) the kinetic energy can be found. The kinetic energy thus obtained is given in Figure 2.15b. The plot shows the kinetic energy of the

equipment mass with no control and with a power amplifier gain 0.02. Only a small reduction in kinetic energy (or improvement in performance) can be seen from these measurements (Also note that increasing next gain step (which is amplifier gain 0.06) in the power amplifier makes the system unstable –Figure 2.15a, which includes the critical point). These two plots show that the acceleration feedback control system becomes unstable with a small gain and the performance is also very poor compared the corresponding simulations. This is a considerable deviation from the findings of simulations.

The open and closed-loop velocities of the two-mount system with velocity feedback control were measured in a similar manner to acceleration feedback control. Figure 2.16a shows the open-loop eigenvalue plots of the two-mount system with velocity feedback control. A power amplifier gain of 0.12 was used. It can be seen that the system exhibits good stability characteristics compared to acceleration feedback control. The total kinetic energy plot for various gains of the power amplifier is shown in Figure 2.16b. It can be seen that as the gain is increased the system gives a better performance than acceleration feedback control. It can also be seen in Figure 2.16c, that as the gain is increased the system improves.

Figure 2.17a shows the open-loop eigenvalue plots of the two-mount system with displacements feedback control for a power amplifier gain 0.12. Although the system exhibits relatively better stability compared to the other two strategies, the performance is not so as seen in Figure 2.17b.

The power amplifier gain used can be non-dimensionalised by dividing them by mass, damping and stiffness. However, the true non-dimensional gain depends on gains introduced by other instruments such as charge-amplifier, shaker etc,. In addition the non-dimensional gain thus obtained would differ from each other because of different denominator (i.e. mass, damping and stiffness). Hence for easy comparison the power amplifier gain was used.

Measurements show that acceleration feedback control becomes unstable with a small gain; displacements feedback control exhibits poor performance.

2.5.2 Two-mount system on a CFCF flexible base

The two-mount system on the CFCF base structure is shown in Figure 2.9. The base was excited by a random signal at the excitation point shown in Figure 2.8 (and the co-ordinates are given in Table 2.2) and the two-mount system was placed in the position shown in Figure 2.8 (the co-ordinates are given in Table 2.2). The experimental set up was similar to the one discussed for the moving inelastic base and is shown in Figure 2.18. The acceleration measured at each mounts location fed in to a two-channel power amplifier after conditioning by a charge amplifier so as to produce acceleration feedback in a similar way to that described previously.

The elements of the open-loop frequency response matrix were measured in a similar way to that described in section 2.5.1. From the measurements the open-loop frequency response matrix was constructed and the eigenvalues were calculated. The open-loop eigenvalue plot for acceleration feedback control is shown in Figure 2.19a for a power amplifier gain of 0.02, where one eigenvalue is given by the solid line and other by the dashed line. It can be seen that the Nyquist plot encloses the negative real axis for a small gain and thus the system does not have good stability characteristics. It was observed during the measurement that as the gain was adjusted from zero to the next available gain step (0.02) in the power amplifier, the system became unstable, which is evident from Figure 2.19a. Since this is the smallest non-zero gain available in the power amplifier (V200 Mos Fet) used, the closed-loop response could not be measured. Thus, although the system showed good stability and performance for simulations with a flexible CFCF base, when implemented the stability and performance with acceleration feedback is very poor.

Figure 2.20a shows the open-loop eigenvalue plot of the two-mount system with velocity feedback control for a power amplifier gain 0.12. The open-loop frequency response matrix was constructed from measurement in a similar way to that described previously. It can be seen that the eigenvalue plot includes the negative axis closer to the origin. As the gain is increased it could potentially grow to include the critical (-1,0) point and becomes unstable. Figure 2.20b shows the total kinetic energy of the equipment mass for various gains. Figure 2.20c shows the change in kinetic energy as a function of power amplifier gain. It shows as the gain is increased the overall performance improves. It can also be seen that the velocity feedback control give better stability and better performance compared to the acceleration feedback control. However even velocity feedback control system, which showed

unconditional stability in the simulations is susceptible to instability when implemented on a flexible base.

Figure 2.21a shows the open-loop eigenvalue plots of the two-mount active isolation system with displacement feedback. It can be seen that the system includes the negative real axis closer to the origin. However it shows better stability than the other two systems considered. However the performance shown in Figure 2.20b suggest that although there is a little improvement in performance at the original resonance frequency, the improvement is not significant.

2.5.3. Summary

Measured open-loop and closed-loop characteristics of a two-mount system have been presented in the preceding sections. The open-loop characteristic of acceleration feedback system showed that the system becomes unstable with a small power amplifier gain (for both moving inelastic and flexible CFCF bases). The performance of acceleration feedback system is also not significant. Thus, stability and performance characteristics of acceleration feedback system are insignificant compared to the simulations for the same cases.

Although the measured open-loop eigenvalue plot for velocity feedback control system exhibits reasonable stability property with moving inelastic base, it crosses the negative real axis closer to the origin for the CFCF base case. Thus, for CFCF case as the gain is increased this system potentially becomes unstable, which is against the conclusion arrived at based on the simulations.

Although the measured open-loop characteristics of displacement feedback control system exhibited better stability characteristics compared to the other two strategies, the performance is not very good. This is again contradicts the conclusions arrived at based on simulations.

2.6 Conclusions

In this chapter the concept of active vibration isolation has been described using a SDOF system. This concept was applied to a two-mount system using decentralised feedback control. Simulations and measurements were conducted on this two-mount system. Simulations show that all three strategies provide a stable system and a better performance than the original passive system (which are evident from the change in kinetic energy plots). Two base conditions were considered and the stability analyses (Nyquist plots) showed that they are all unconditionally stable. However the measurements show that all three strategies provide an active system, which is only conditionally stable.

Hence there is a difference between the simulations and measurements of the system in terms of its stability and performance characteristics. In active isolation using the velocity feedback technique, this discrepancy is minimal compared to the other two.

Thus, the conventional analytical tool is inadequate in judging the performance and especially the stability of active isolation systems. This demands an improvement in the analytical model incorporating structural as well as the sensor, signal conditioning devices and actuator dynamics into the analytical models. This improved analytical model by including the characteristics of electrical instruments, sensor and actuator dynamics is discussed in the next two chapters.

Mass of the equipment plate – m_p (kg)	1.08
Mass of each shaker – m_s (kg)	0.91
Plate length – l_p (mm)	200
Distance between mounts – l (mm)	134
Axial stiffness of each mounts (*N/m*)	$2.4e^4$
Damping of each mounts (*Ns/m*)	18
External diameter of the mount (*mm*)	60
Internal diameter of the mount (*mm*)	40
Height of the mount (*mm*)	60

Table 2.1 Characteristic properties of the two-mount active isolation system

Density of the base plate	$7800kg/m^3$
Young modulus	207×10^{11} Nm^{-2}
Poisson's ratio	0.3
Dimensions of plate (L_x, L_y, t)	520 mm, 700 mm, 2 mm
Damping ratio	0.01
Excitation point	410 mm, 200 mm
Location of mount 1	184 mm, 312 mm
Location of mount 2	296 mm, 385 mm

Table 2.2 Geometric and material properties of the CFCF base

Name	Type	Serial number or Department serial number
Accelerometers (3 Numbers)	B&K 4375	987173, 987169 and 1760059
Single channel power amplifier	TPA 50-D (H/H Electronics)	3633 (Dept. No.)
Two channel power amplifier	V200 Mos Fet	4493
Charge amplifiers (3 Numbers)	B&K 2635	0782, 2688 and 943130 (Dept. No.)
Force gauge	B&K 8200	688893
Large shaker (Derritron vibrator)	Type VP4	325
Analyser (HP analyser)	Hewlett Packard 35650	2911A02485

Table 2.3 List of instrument used in the active isolation experiments

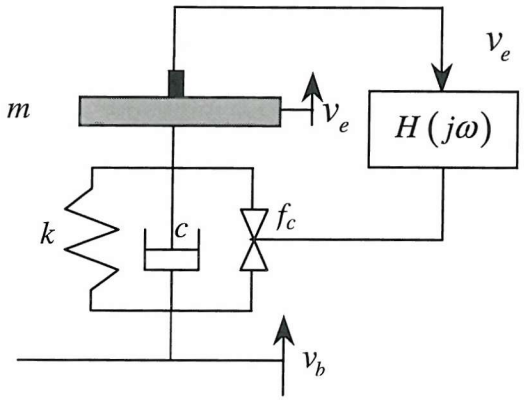

(a) Physical representation

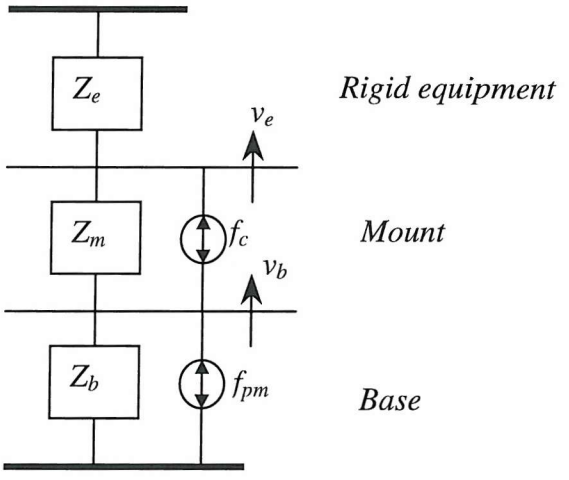

(b) Impedance representation of a single mount system

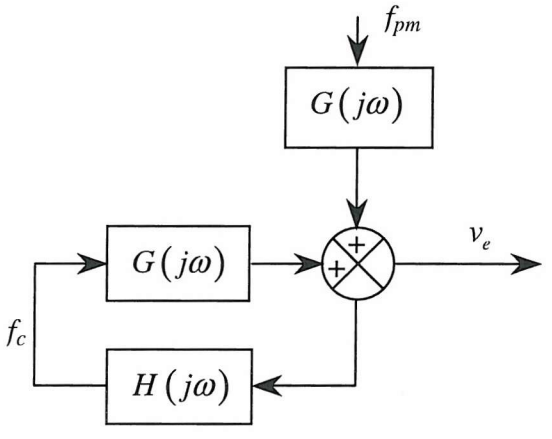

(c) Block diagram representation

Figure 2.1 Single mount active isolation system

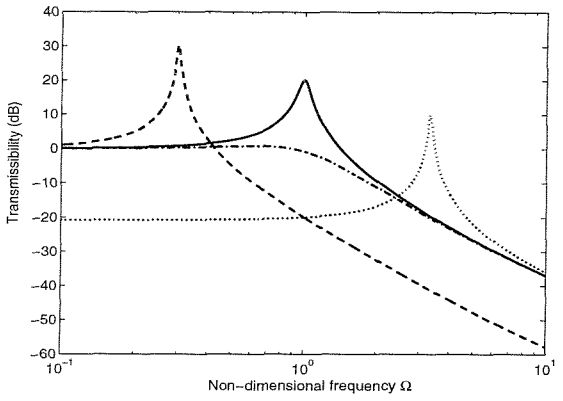

(a) Closed-loop frequency response (Non-dimensional gain 10 *and damping ratio* $\zeta = 0.05$ *) No control: _____, acceleration feedback: ----------, velocity feedback: -.-.-.-.-.-.-.-.-, displacement feedback:.....*

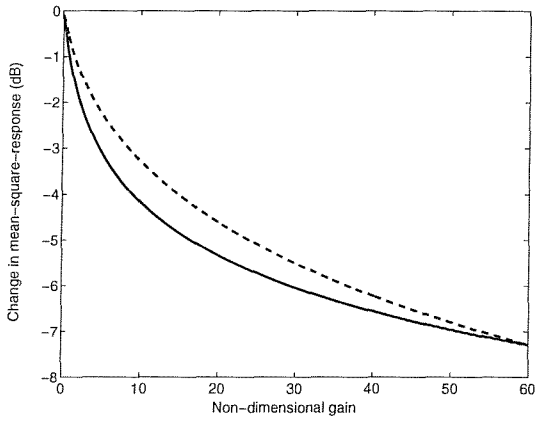

(b) Change in mean square response in the frequency range $0 \leq \Omega \leq 100$ *; (damping ratio* $\zeta = 0.05$ *) velocity feedback: ----------, acceleration and displacement feedback:_____*

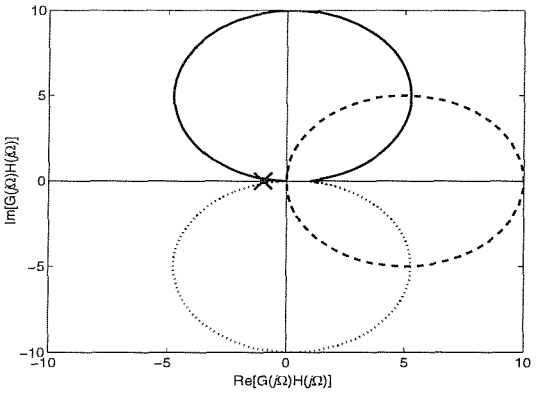

(c) Open-loop frequency response (damping ratio $\zeta = 0.05$ *); acceleration feedback:_____, velocity feedback:----------, displacement feedback:.....*

Figure 2.2 SDOF system response with acceleration, velocity and displacement feedback control.

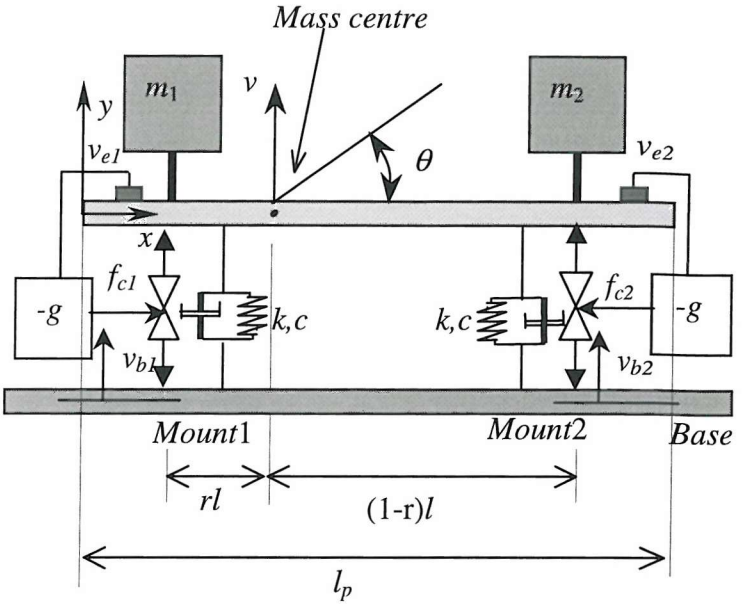

(a) Physical representation of two-mount system with decentralised feedback control

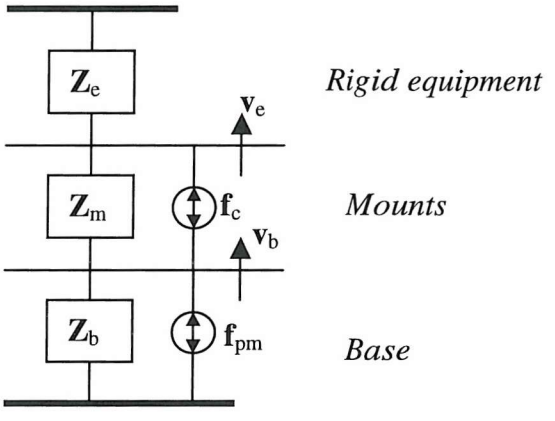

(b) Impedance representation of the two-mount system

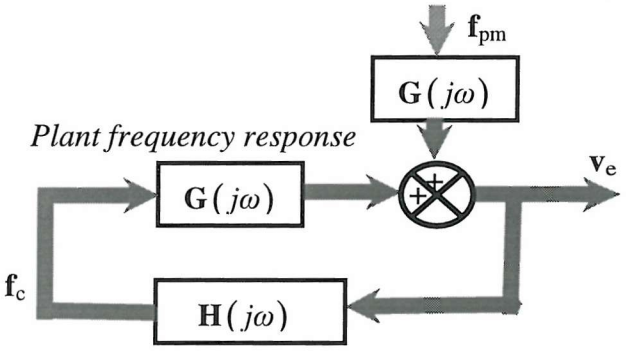

Feedback path frequency response

(c) Control block diagram representation

Figure 2.3 Two-mount active isolation system with decentralised feedback control

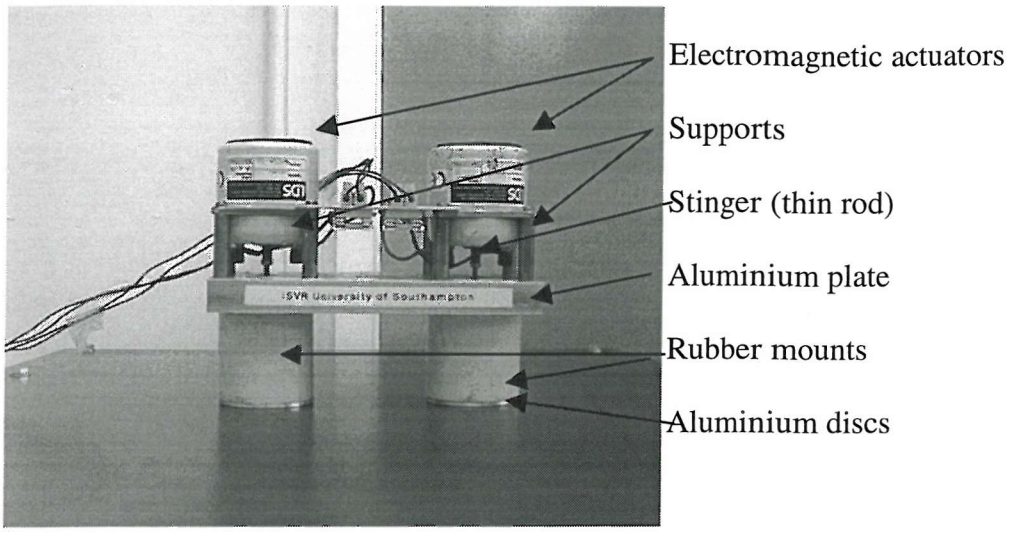

Figure 2.4 Two-mount active isolation system

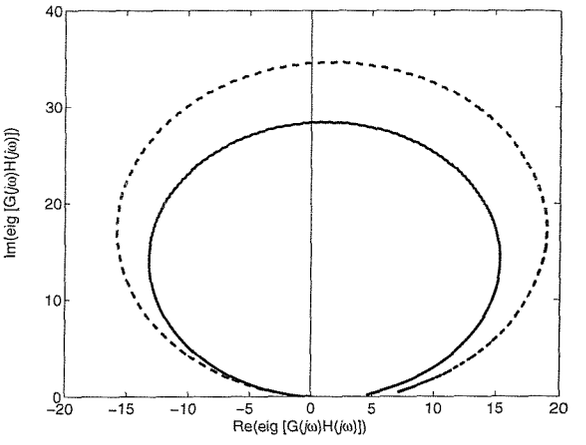

(a) Open loop eigenvalue plots for a normalised gain $\frac{g_a}{m} = 5$

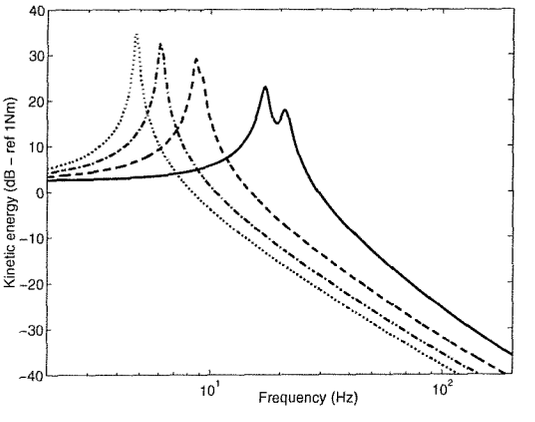

(b) Total kinetic energy, normalised gain 0:_____,normalised gain 05: ----------, normalised gain 10: -.-.-.-.-.-, normalised gain 15: .....

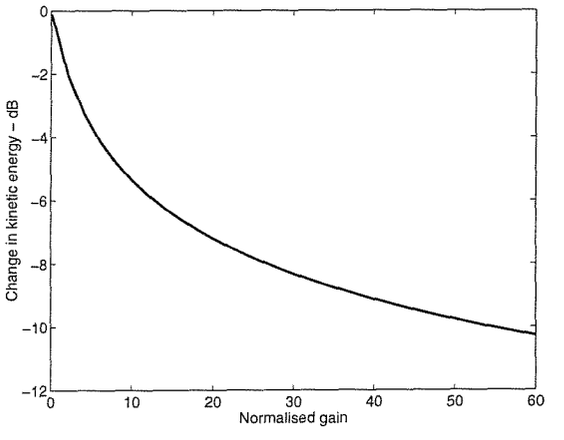

(c) Change in kinetic energy for frequency range $0 \leq freq \leq 250$ Hz

Figure 2.5 Active isolation of a two-mount system from a moving inelastic base using acceleration feedback control.

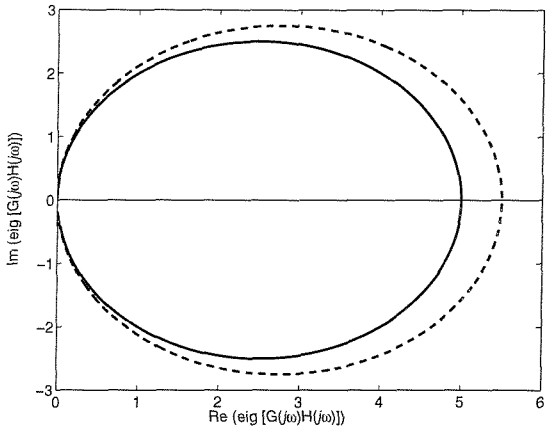

(a) Open loop eigenvalue plots for a normalised gain $\frac{g_v}{c} = 5$

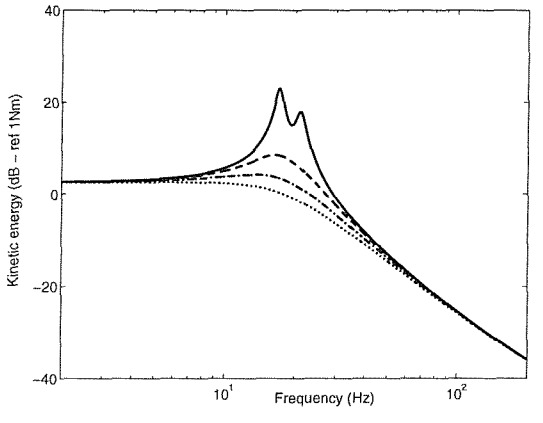

(b) Total kinetic energy, normalised gain 0:_____,normalised gain 05: ----------, normalised gain 10: -.-.-.-.-.-, normalised gain 15: .....

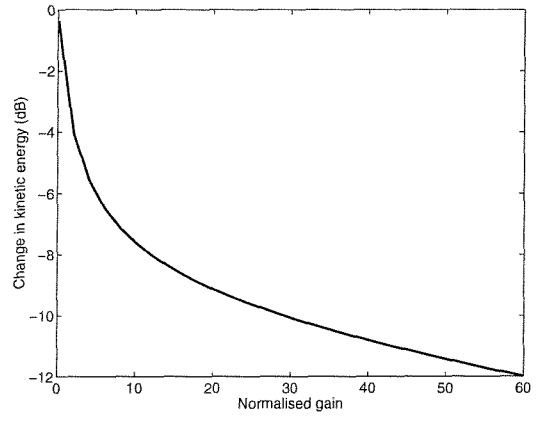

(c) Change in kinetic energy for frequency range $0 \leq freq \leq 250$ Hz

Figure 2.6 Active isolation of a two-mount system from a moving inelastic base using velocity feedback control.

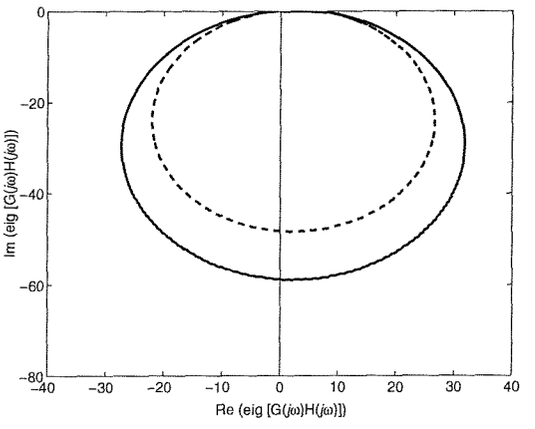

(a) Open loop eigenvalue plots for a normalised gain $\frac{g_d}{k} = 5$

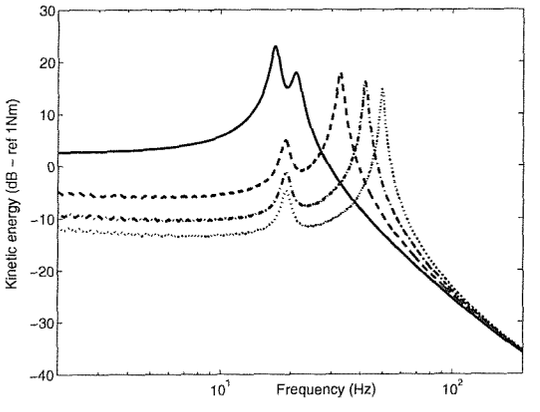

(b) Total kinetic energy, normalised gain 0:_____,normalised gain 0.5: ----------, normalised gain 1.0: -.-.-.-.-.-, normalised gain 1.5: .....

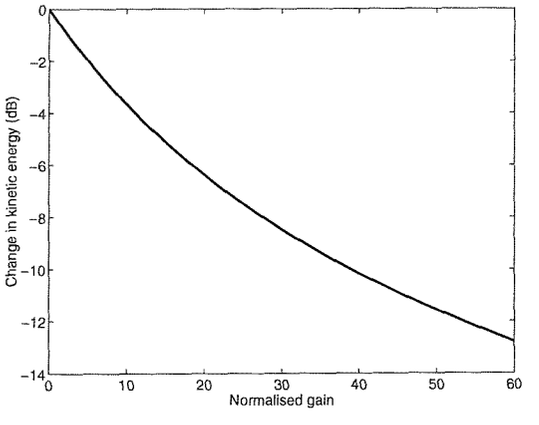

(c) Change in kinetic energy for frequency range $0 \leq freq \leq 250$ Hz

Figure 2.7 Active isolation of a two-mount system from a moving inelastic base using displacement feedback control.

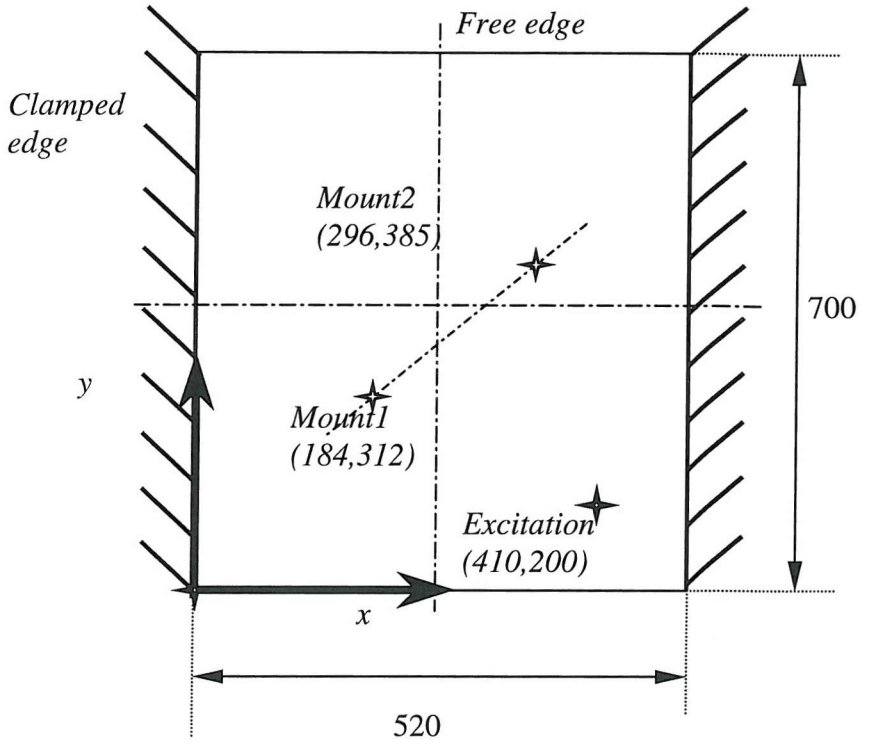

Figure 2.8 Schematic plan view diagram of the flexible base and mount positions (Co-ordinates of mounts location and excitation are given in parenthesis - all dimension are in mm,)

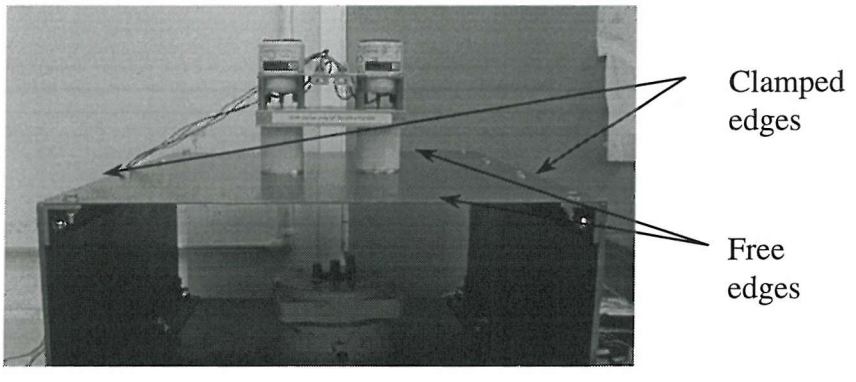

Figure 2.9 Two-mount active isolation system on CFCF flexible base structure

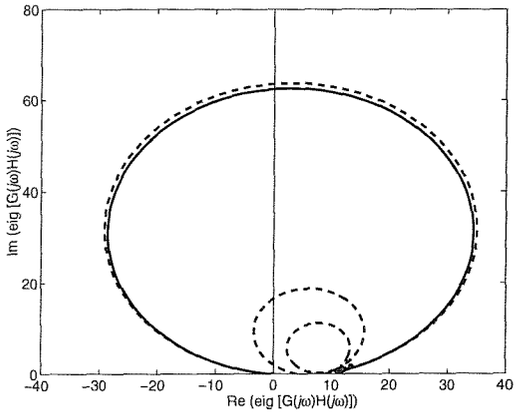

(a) Open loop eigenvalue plots for a normalised gain $\frac{g_a}{m} = 5$

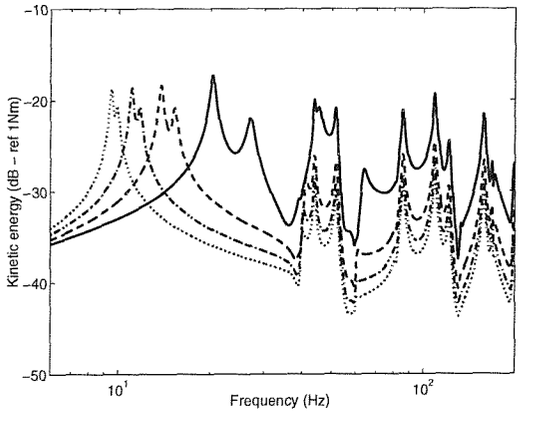

(b) Total kinetic energy, normalised gain 0:_____,normalised gain 5: **----------**, *normalised gain 10:* **-.-.-.-.-.-**, *normalised gain 15:* **.....**

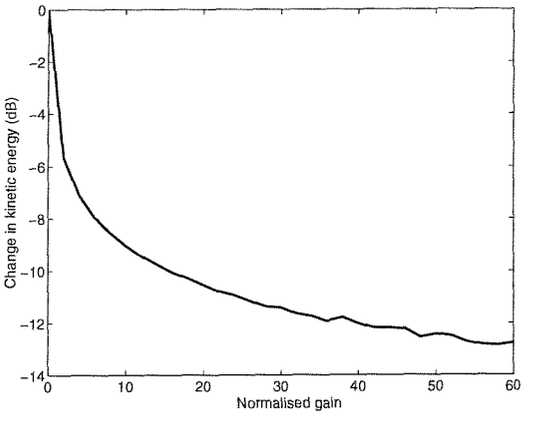

(c) Change in kinetic energy for frequency range $0 \leq freq \leq 250$ Hz

Figure 2.10 Active isolation of a two-mount system from a CFCF flexible base using acceleration feedback control

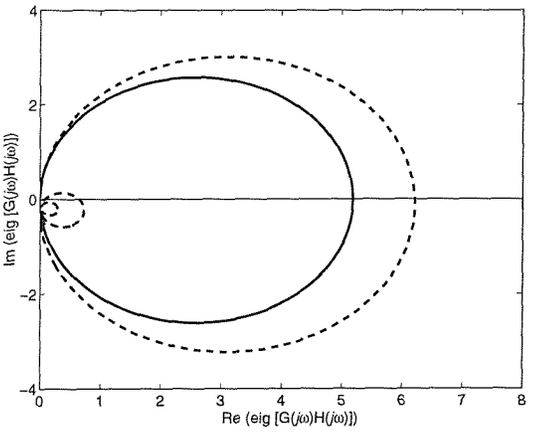

(a) Open loop eigenvalue plots for a normalised gain $\frac{g_v}{c} = 5$

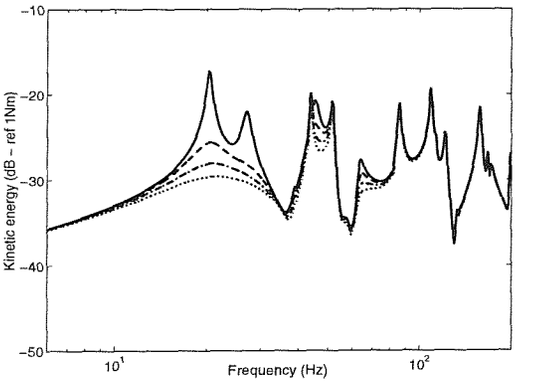

(b) Total kinetic energy, normalised gain 0:_____,normalised gain 5: ----------, normalised gain 10: -.-.-.-.-.-, normalised gain 15: .....

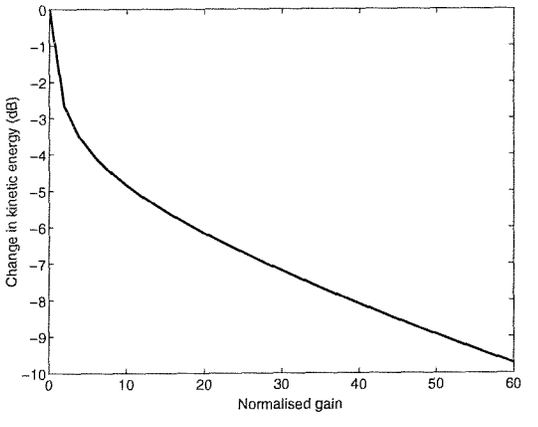

(c) Change in kinetic energy for frequency range $0 \leq freq \leq 250$ Hz

Figure 2.11 Active isolation of a two-mount system from a CFCF flexible base using velocity feedback control

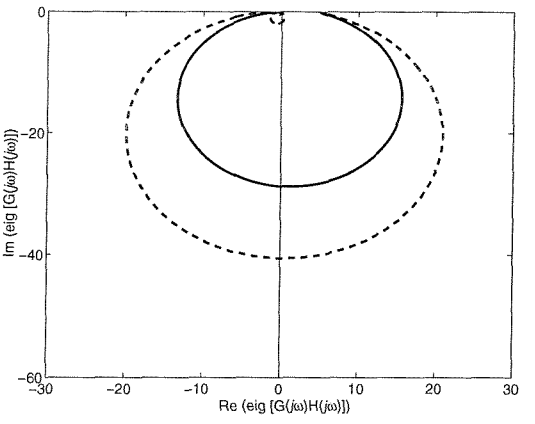

(a) Open loop eigenvalue plots for a normalised gain $\frac{g_d}{k} = 5$

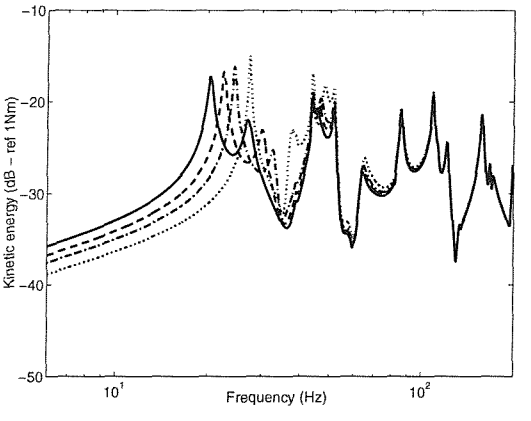

(b) Total kinetic energy, normalised gain 0:_____,normalised gain 5: **----------**, *normalised gain 10:* **-.-.-.-.-.-**, *normalised gain 15:* **.....**

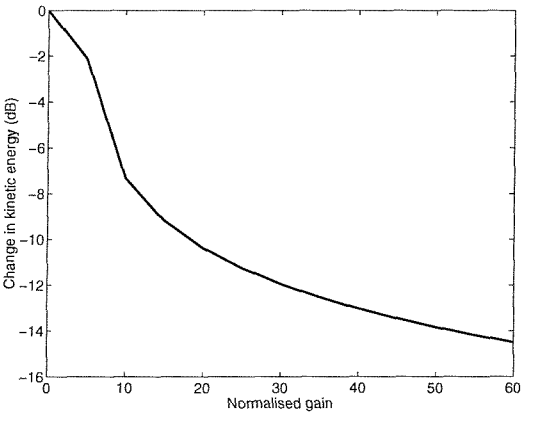

(c) Change in kinetic energy for frequency range $0 \leq freq \leq 250$ Hz

Figure 2.12 Active isolation of a two-mount system from a CFCF flexible base using displacement feedback control

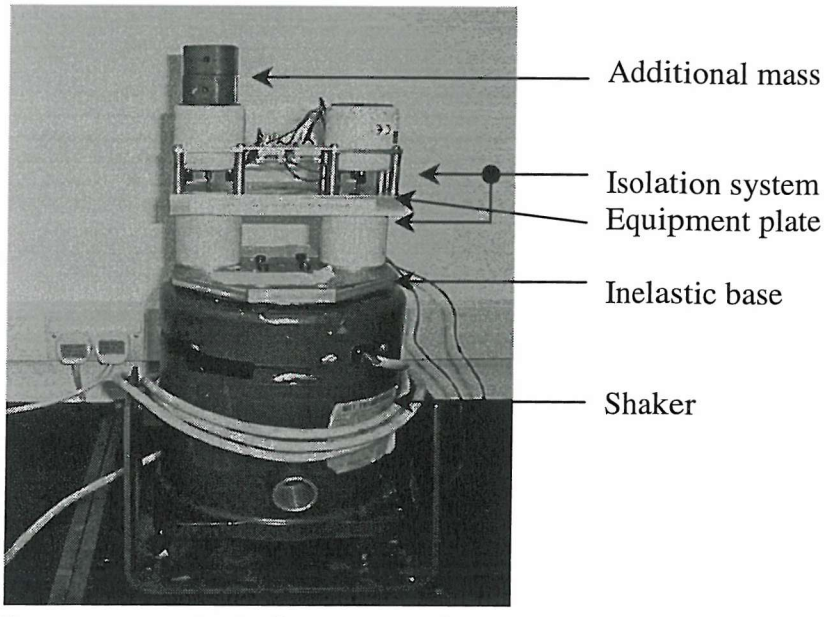

Figure 2.13 Two-mount active isolation control system on a moving inelastic base (A large shaker- Derritron vibrator type VP4 provides the moving inelastic base)

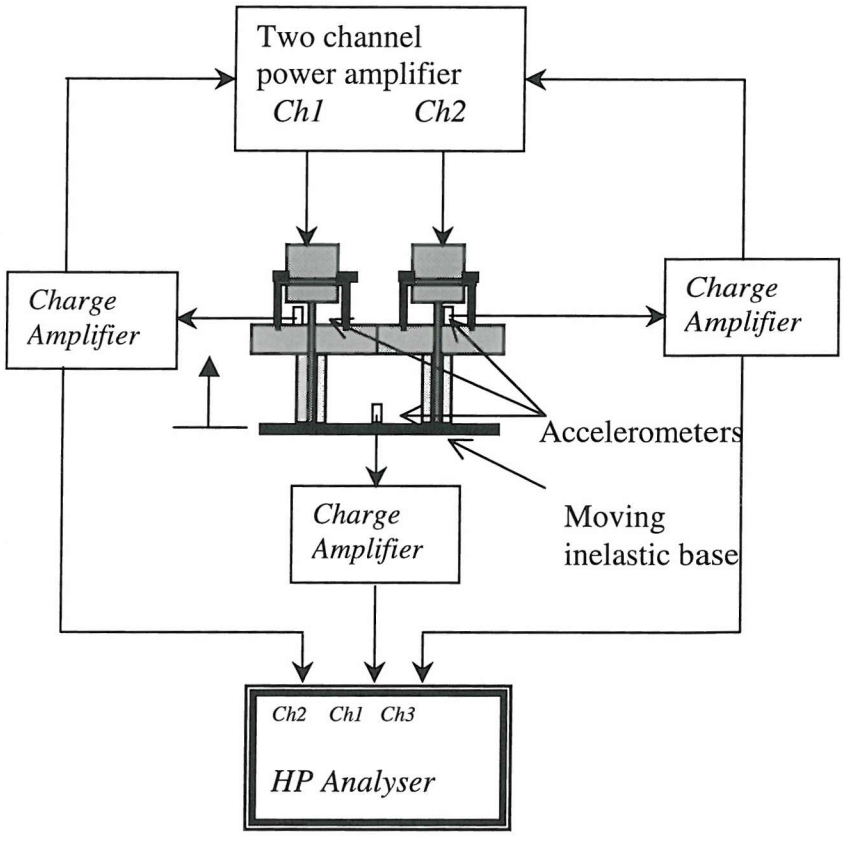

Figure 2.14 Experimental set-up for feedback control of a two-mount system on a moving inelastic base with decentralised feedback control applied.

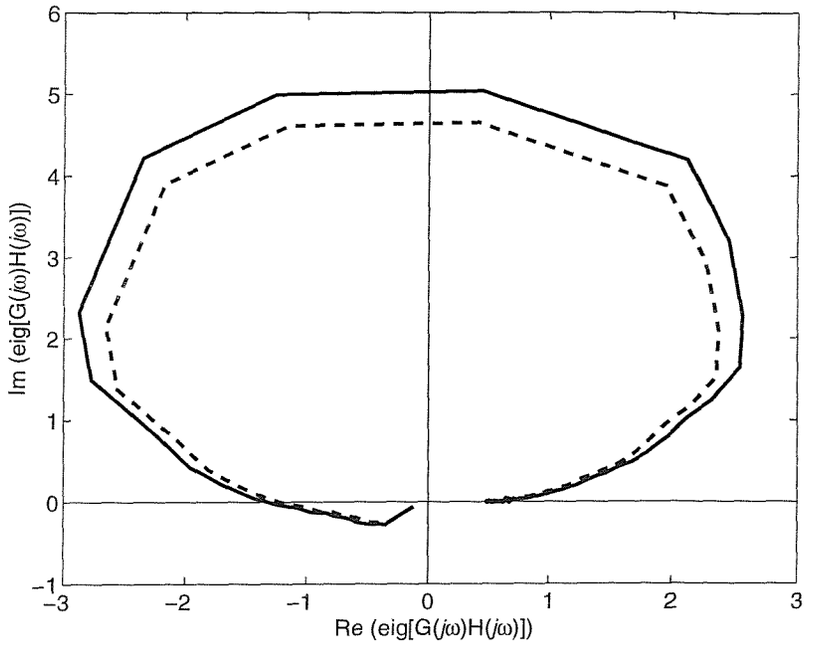

(a) Open-loop eigenvalue plots – power amplifier gain 0.06

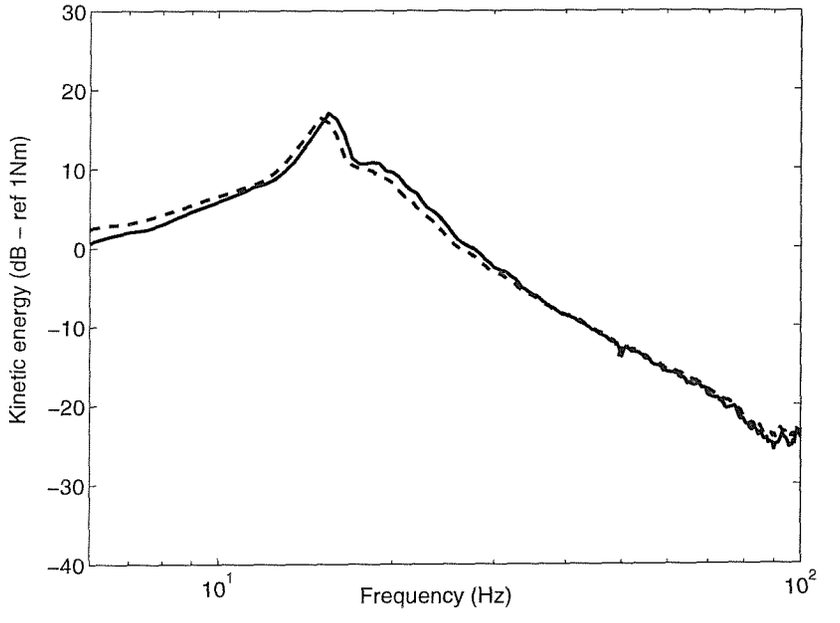

(b) Total kinetic energy – Power amplifier gains g_a= 0_____, g_a =0.02 ----------

Figure 2.15 Active isolation of a two-mount system from a moving inelastic base using acceleration feedback control

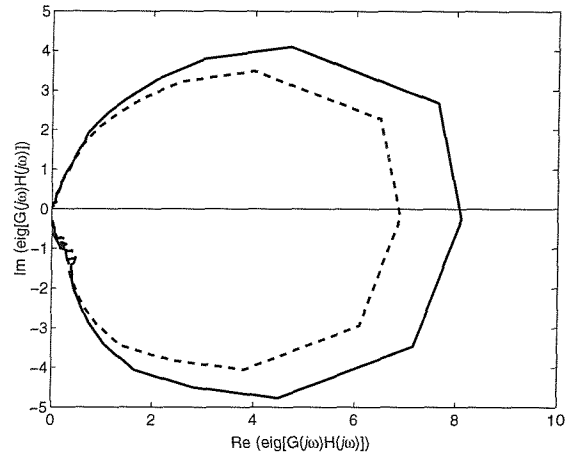

(a) Open-loop eigenvalue plots – power amplifier gain 0.12

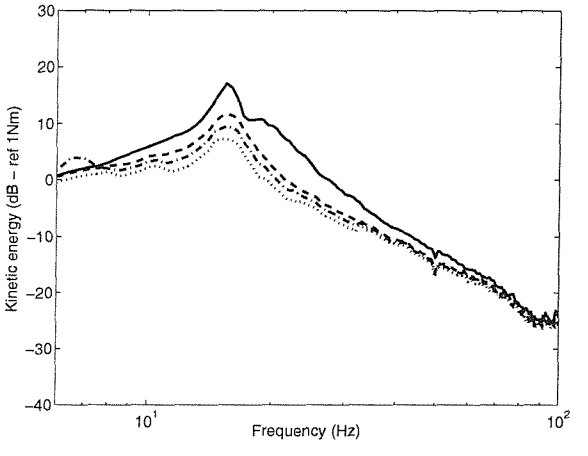

(b) Total kinetic energy – Power amplifier gains g_a= 0_____, g_a =0.02 ---------- g_a =0.06 -.-.-.-.-, g_a =0.12 .....

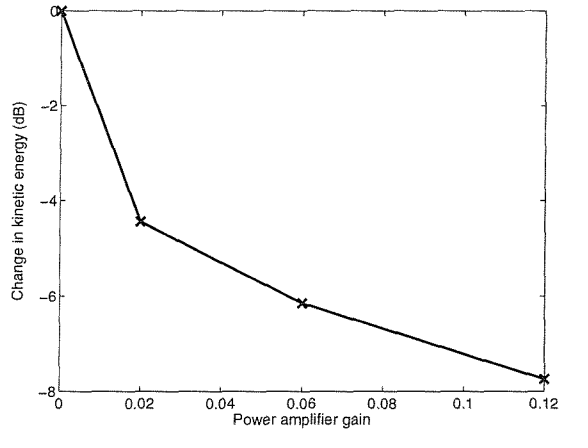

(c) Change in kinetic energy - 4 ≤ freq ≤ 200 Hz

Figure 2.16 Active isolation of a two-mount system from a moving inelastic base using velocity feedback control

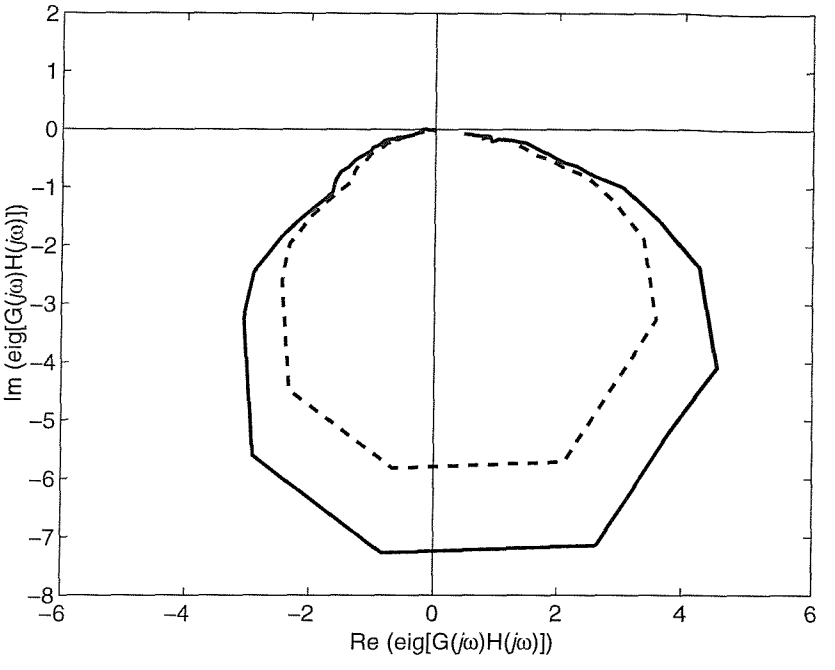

(a) Open-loop eigenvalue plots – power amplifier gain 0.12

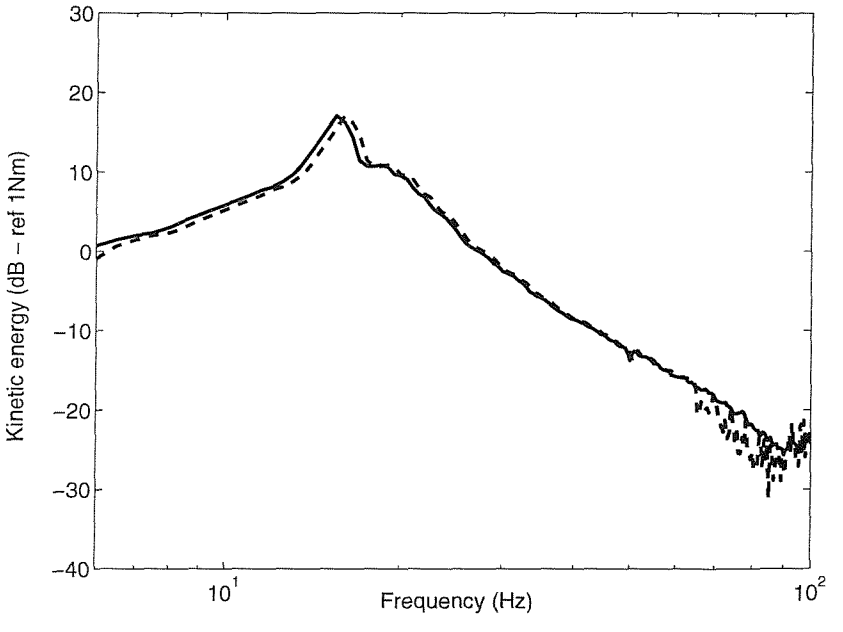

(b) Total kinetic energy – Power amplifier gains g_a= 0_____, g_a =0.06 ----------

Figure 2.17 Open-loop eigenvalue plots (for power amplifier gain 0.12) for active isolation of a two-mount system from a moving inelastic base using displacement feedback control.

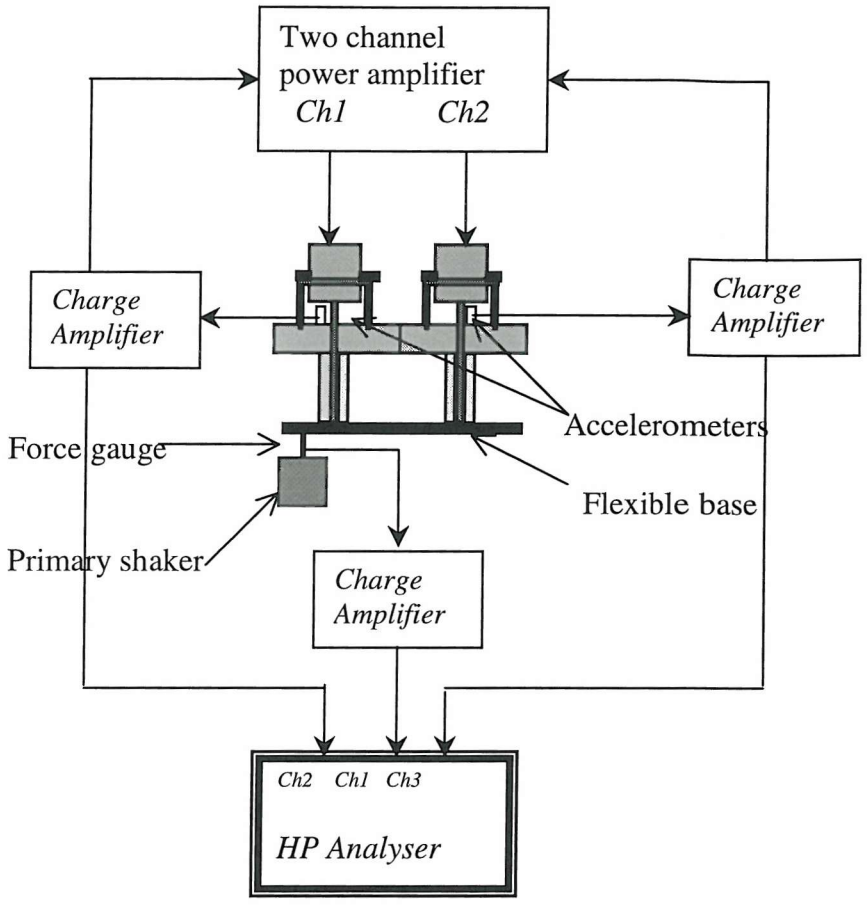

Figure 2.18 Experimental set-up for feedback control of a two-mount system on a CFCF flexible base with decentralised feedback control applied.

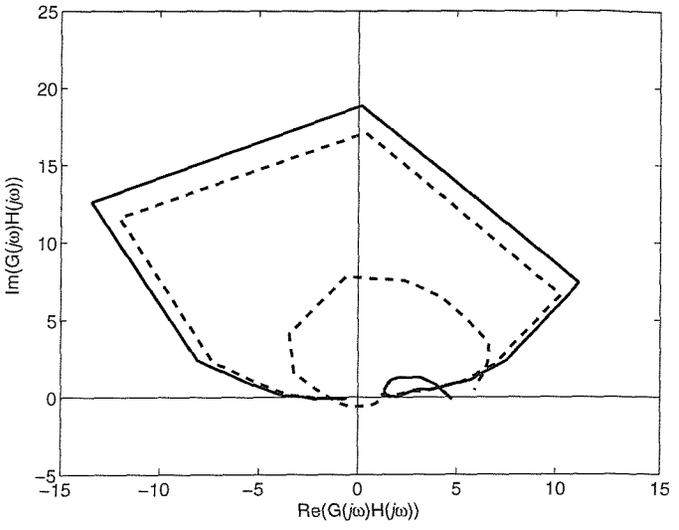

(a) Open loop eigenvalue plots- power amplifier gain 0.02

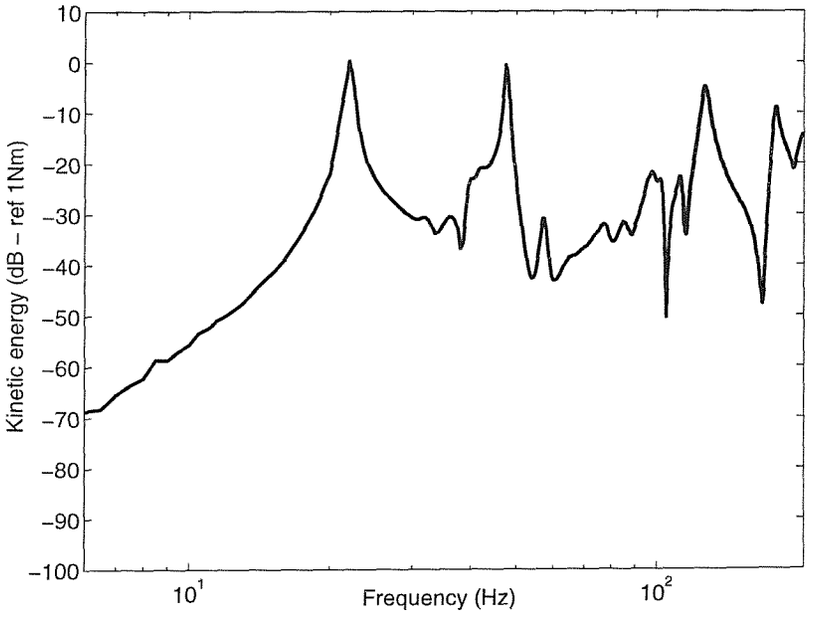

(b) Total kinetic energy - power amplifier gain 0

Figure 2.19 Active isolation of a two-mount system from a CFCF flexible base using acceleration feedback control (Measurement)

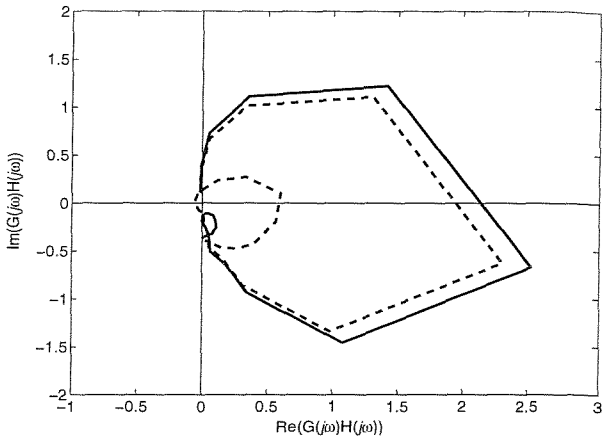

(a) Open-loop eigenvalue plots – power amplifier gain 0.12

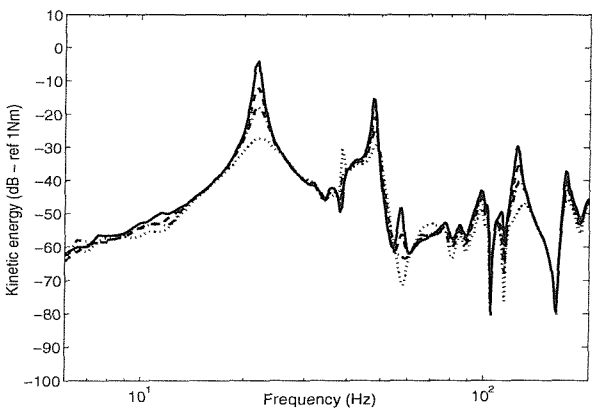

(b) *Total kinetic energy - Power amplifier gains* g_{na}*= 0*____ g_{na} *=0.06* ----------, g_{na} *=0.12* -.-.-.-.-, g_{na} *=0.25* .....

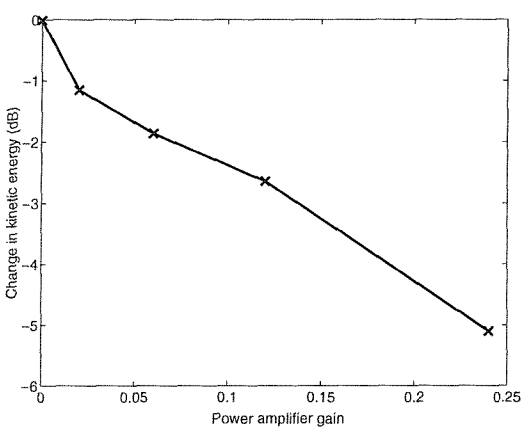

(d) Change in kinetic energy - $4 \leq freq \leq 200$ Hz

Figure 2.20 Active isolation of a two-mount system from a CFCF flexible base using velocity feedback control (Measurement)

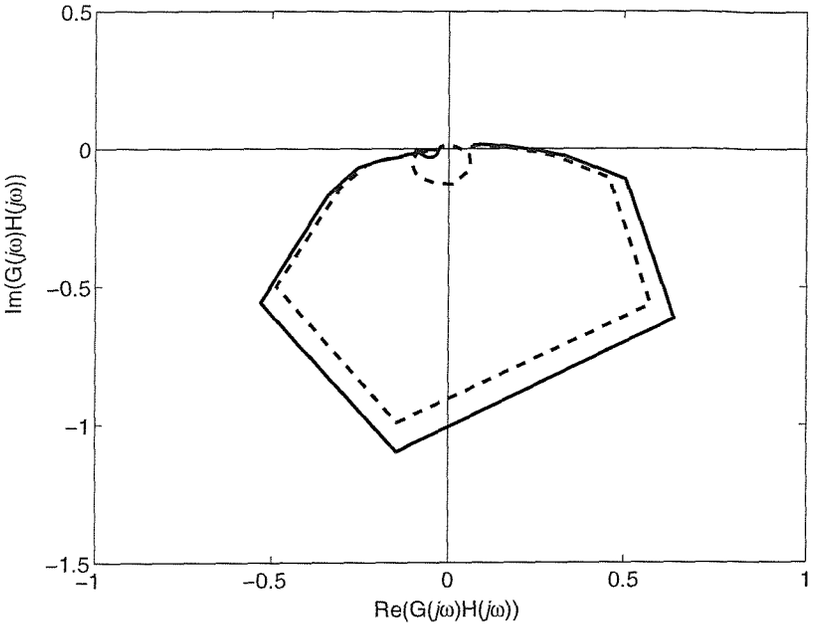

(a) Open-loop eigenvalue plots - power amplifier gain 0.12

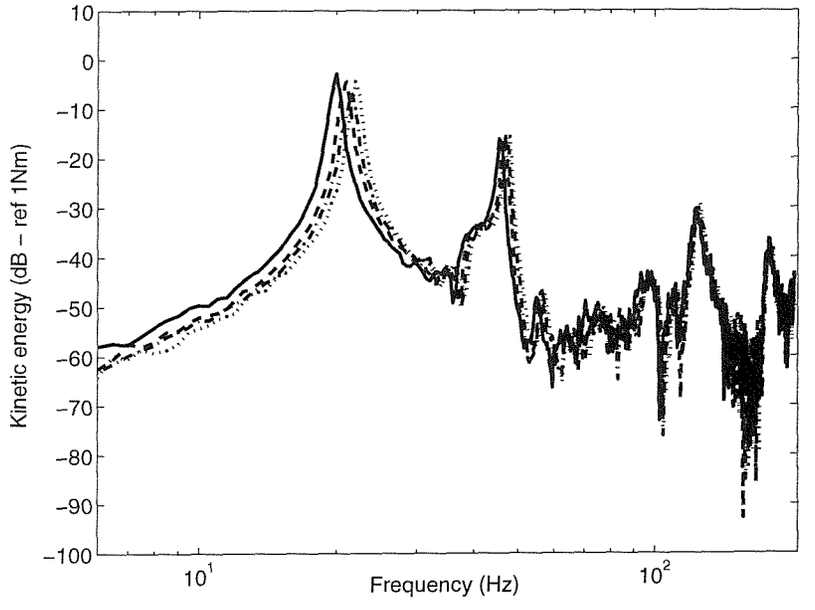

(b) *Total kinetic energy - Power amplifier gains* g_{na}*= 0_____* g_a *=0.06 ----------,* g_a *=0.12 -.-.-.-.-,* g_a *=0.25 .....*

Figure 2.21 Active isolation of a two-mount system from a CFCF flexible base using displacement feedback control (Measurement)

Chapter 3

Low frequency instabilities in feedback control

3.1 Introduction

In Chapter 2 it was shown that there have been considerable discrepancies between the simulations and measurements of active vibration isolation systems for acceleration, velocity and displacement feedback control. The simulations showed that an idealised SDOF system is unconditionally stable when these control strategies are applied. However the experimental results showed that the system is only conditionally stable. The difference between the idealised system and the experimental system is that there are sensors, actuators, signal conditioning devices with integrators and power amplifiers in the experimental system. The characteristics of these devices were assumed to be ideal in the analytical model. These devices are an essential part of an active vibration isolation system.

Accelerometers are generally used as the sensing devices in vibration testing and active vibration control [85]. These devices often use piezoelectric sensing elements to achieve a certain design natural frequency, weight and sensitivity characteristics [85, 86]. They are charge-generating devices, which require high input impedance signal conditioning instruments to interface between them and other instrumentation [85]. These signal-conditioning devices such as charge amplifiers convert the generated charge into voltage and often also have filters to reject unwanted signals [87]. Two kinds of filters are commonly found in these devices, which are high-pass filters and low-pass filters. These filters introduce extra phase shift at certain bands of frequencies, which are some times critical to the system stability [2].

The power amplifier, which controls the gain in the feedback system, often has a high-pass filter incorporated. One other important device in the active control system is the actuator. The characteristics of all these devices generally deviate from the ideal and hence the performance of a realistic system is often quite different from the ideal.

The aim of this chapter is to establish the low frequency sources of instabilities and to quantify their influences on the stability of the feedback control systems. A simple model of a vibration isolation system is considered and later the analysis is extended to a more general multi-input-multi-output system.

3.2 Problem formulation

Consider a simple model of a vibration isolation system as shown in Figure 3.1a. In this model (a SDOF system is set on a moving inelastic base) a passive mount with stiffness k and damping coefficient c supports a rigid mass m. It is assumed that the mounts are mass-less. A control force f_c is also installed between the mass and the base structure in parallel with the passive mount to achieve a reduction in the response of the mass. The control system uses direct negative feedback control. This control force, which can be proportional to acceleration, velocity or displacement, is generated via a controller.

Figure 3.1b, shows a SDOF system set on a rigid foundation. Both of the physical arrangements shown in Figures 3.1a and 3.1b have the same plant frequency response function, which is given by equation (2.6). Since the base is rigid or has a prescribed motion, the base mobility (i.e. $Y_b = 0$) is zero. Thus the plant frequency response function is given by,

$$G(j\omega) = \frac{1}{Z_e + Z_m} \tag{3.1}$$

where $Z_e = j\omega m$ and $Z_m = \frac{k}{j\omega} + c$.

Since the systems in Figures 3.1a and 3.1b have the same frequency response function (and hence the same open-loop frequency response function), the analysis and subsequent experimental validation are performed on the SDOF system on a rigid foundation (Figure 3.1b) for convenience.

The sources of instabilities for the active isolation system considered in this thesis cause problems at either low frequencies or high frequencies [84]. Thus, two regimes are considered, a low frequency regime and a high frequency regime. In this Chapter, sources of instabilities at low frequencies are identified and their effects on stability and performance

are investigated and compared with an ideal system. The theoretical predictions are subsequently validated by some experiments.

3.3 Stability and performance of an ideal SDOF system on a rigid foundation

In this section the stability and performance of an ideal system is investigated. An ideal system is where an integrator is represented by $\frac{1}{j\omega}$, the control amplifier by a pure gain and signals do not require to be filtered. Because such a system is simple, velocity per unit disturbance force is used as the performance measure.

3.3.1 Performance of ideal system

From equation (3.1) the plant frequency response function can be written as,

$$G(j\omega)=\frac{\dot{X}(j\omega)}{F_c(j\omega)}=\frac{j\omega}{k-\omega^2 m+j\omega c} \tag{3.2}$$

where $\dot{X}(j\omega)$ and $F_s(j\omega)$ are the velocity and secondary or control force respectively.

(i.e. $\dot{x}(t)=\dot{X}(j\omega)e^{j\omega t}$ and $f_c(t)=F_c(j\omega)e^{j\omega t}$)

Substituting $\omega_n=\sqrt{\frac{k}{m}}$ and $\zeta=\frac{c}{2\sqrt{mk}}$ (System natural frequency and damping ratio) into equation (3.2) gives,

$$G(j\omega)=\frac{\dot{X}(j\omega)}{F_c(j\omega)}=\frac{1}{c}\left(\frac{j2\zeta\omega_n\omega}{\omega_n^2-\omega^2+j2\zeta\omega_n\omega}\right) \tag{3.3}$$

Equation (3.3) can be non-dimensionalised to give,

$$G(j\Omega)=\frac{c\dot{X}(j\Omega)}{F_c(j\Omega)}=\frac{j2\zeta\Omega}{(1-\Omega^2+j2\zeta\Omega)} \tag{3.4}$$

where $\Omega=\frac{\omega}{\omega_n}$, is the forcing frequency normalised to the natural frequency of the system. A block diagram representation of the physical system is given in Figure 3.1c. Letting the controller frequency response function be $H(j\Omega)$, which includes the integrators if required, the non-dimensional closed-loop frequency response (mobility) is given by:

$$\frac{c\dot{X}(j\Omega)}{F_p(j\Omega)} = \frac{G(j\Omega)}{1+G(j\Omega)H(j\Omega)} \tag{3.5}$$

where $f_p = F_p e^{j\omega t}$ is the primary disturbance.

From Figure 3.1c the controller frequency response function can be defined as, $H(j\Omega) = \frac{F_c(j\Omega)}{c\dot{X}(j\Omega)}$. For acceleration feedback control $H(j\Omega) = j\Omega \frac{g_a}{m} \frac{1}{2\zeta}$, for velocity feedback control $H(j\Omega) = \frac{g_v}{c}$ and for displacement feedback control $H(j\Omega) = \frac{1}{j\Omega} \frac{g_d}{k} \frac{1}{2\zeta}$, where, as before, $\frac{g_a}{m}$, $\frac{g_v}{c}$ and $\frac{g_d}{k}$ are the normalised feedback gains. Substituting for $G(j\Omega)$ and the appropriate $H(j\Omega)$ into equation (3.5), the non-dimensionalised closed-loop mobility can be derived for acceleration, velocity and displacement feedback control:

ACCELERATION FEEDBACK CONTROL

$$\frac{c\dot{X}(j\Omega)}{F_p(j\Omega)} = \frac{j2\zeta\Omega}{1-\left(1+\frac{g_a}{m}\right)\Omega^2 + j2\zeta\Omega} \tag{3.6}$$

VELOCITY FEEDBACK CONTROL

$$\frac{c\dot{X}(j\Omega)}{F_p(j\Omega)} = \frac{j2\zeta\Omega}{1-\Omega^2 + j2\zeta\Omega\left(1+\frac{g_v}{c}\right)} \tag{3.7}$$

DISPLACEMENT FEEDBACK CONTROL

$$\frac{c\dot{X}(j\Omega)}{F_p(j\Omega)} = \frac{j2\zeta\Omega}{\left(1+\frac{g_d}{k}\right)-\Omega^2 + j2\zeta\Omega} \tag{3.8}$$

Figure 3.2a shows the closed-loop non-dimensional mobility for acceleration, velocity and displacement feedback control as a function of non-dimensional frequency for non-dimensional gains $\frac{g_a}{m}$, $\frac{g_v}{c}$ and $\frac{g_d}{k}$ of 10, and a damping ratio of 0.05. As discussed in Chapter 2, it can be seen that acceleration feedback reduces the response at the original resonance frequency and produces a resonance frequency lower than that of the original system. Acceleration feedback control effectively adds mass to the system. It can also be seen from Figure 3.2a that velocity feedback effectively adds damping to the system, and

that displacement feedback effectively adds stiffness to the system [13]. It is also noted that acceleration and displacement feedback tend to reduce the damping in the system, which results in narrower peaks. The reason for this is evident from the expression for the damping ratio given by $\zeta = \frac{c}{2\sqrt{mk}}$, because if either m or k is increased the damping ratio reduced.

To assess the overall performance of the control strategies the mean-square response of the system normalised to the mean-square response in the absence of control is plotted for the three control strategies in Figure 3.2b for the frequency range $0 \leq \Omega \leq 100$. It can be seen that there is little difference in the performance of the three control strategies for non-dimensional gains up to 60.

3.3.2 Stability of the ideal system

As mentioned in Chapter 2 the Nyquist criterion is used for stability analysis. For a single input single output (SISO) system it states that the system is stable if and only if the Nyquist plot of the open-loop frequency response function $G(j\Omega)H(j\Omega)$ does not enclose the (-1,0) point in the Nyquist plane [59]. Thus the stability of the system can be studied by considering the magnitude of the open-loop frequency response function when it crosses the negative real axis in the complex $G(j\Omega)H(j\Omega)$ plane. This occurs when the imaginary part of $G(j\Omega)H(j\Omega)$ is equal to zero. Substituting $G(j\Omega)$ and the appropriate $H(j\Omega)$, into the open-loop frequency response function for acceleration, velocity and displacement feedback control can be obtained.

3.3.2.1 Acceleration feedback control

The non-dimensional open-loop frequency response function for acceleration feedback control becomes,

$$G(j\Omega)H(j\Omega) = \left(\frac{g_a}{m}\right)\frac{-\Omega^2}{(1-\Omega^2 + j2\zeta\Omega)} \tag{3.9}$$

which can be rearranged into real and imaginary parts to give,

$$G(\,j\Omega)H(\,j\Omega) = -\left(\frac{g_a}{m}\right)\left\{\frac{\Omega^2(1-\Omega^2)}{(1-\Omega^2)^2+(2\zeta\Omega)^2} - j\frac{2\zeta\Omega^3}{(1-\Omega^2)^2+(2\zeta\Omega)^2}\right\} \qquad (3.10)$$

The frequency at which the imaginary part of this open-loop response function is zero can be determined by setting the imaginary part to zero and solving for Ω. This frequency is called as critical frequency and is denoted by Ω_c. From equation (3.10), solving for critical frequency gives $\Omega_c = 0$ and the corresponding magnitude of the real part is also zero $\left(i.e\ \mathrm{Re}\{G(j\Omega_c)H(j\Omega_c)\}=0\right)$. Thus the system is *unconditionally stable.*

The Nyquist plot for acceleration feedback is shown in Figure 3.2c. It can be seen that it does not cross the negative real axis and therefore does not encloses the (-1,0) point. In addition, when Ω tends to infinity, the real part tends to $\frac{g_a}{m}$.

3.3.2.2 Velocity feedback control

With velocity feedback control, the open-loop frequency response function is given by,

$$G(\,j\Omega)H(\,j\Omega) = \left(\frac{2\zeta g_v}{c}\right)\left(\frac{j\Omega}{(1-\Omega^2)+j(2\zeta\Omega)}\right) \qquad (3.11)$$

which can be arranged into real and imaginary parts to give:

$$G(\,j\Omega)H(\,j\Omega) = \left(\frac{2\zeta g_v}{c}\right)\left\{\frac{2\zeta\Omega^2}{\left(1-\Omega^2\right)^2+\left(2\zeta\Omega\right)^2} + j\frac{\Omega\left(1-\Omega^2\right)}{\left(1-\Omega^2\right)^2+\left(2\zeta\Omega\right)^2}\right\} \qquad (3.12)$$

When the imaginary part of this equation is zero, $\Omega_c = 0$ or $\Omega_c = 1$. The corresponding real parts are $\mathrm{Re}\{G(\,j\Omega_c)H(\,j\Omega_c)\}=0$ or $\mathrm{Re}\{G(\,j\Omega_c)H(\,j\Omega_c)\}=\frac{g_v}{c}$ respectively. Since this is either zero or positive the velocity feedback control system is *unconditionally stable.* A more general proof of the unconditional stability of a multi-mount system with multi-channel collocated decentralised feedback control is given in appendix F.

The Nyquist plot for velocity feedback is shown in Figure 3.2c, where it is evident that the Nyquist plot is completely in the right half of the complex plane, and thus the system is unconditionally stable. In addition it crosses the real axis when the open-loop response is

zero and $\frac{g_v}{c}$. When Ω tends to infinity the real and imaginary parts of the open-loop frequency response function tend to zero.

3.3.2.3 Displacement feedback control

For displacement feedback control, the open-loop frequency response function is given by:

$$G(\mathrm{j}\Omega)H(\mathrm{j}\Omega) = \left(\frac{g_d}{k}\right)\left(\frac{1}{(1-\Omega^2)+j(2\zeta\Omega)}\right) \tag{3.13}$$

which can be arranged into real and imaginary parts to give:

$$G(\mathrm{j}\Omega)H(\mathrm{j}\Omega) = \left(\frac{g_d}{k}\right)\left\{\frac{(1-\Omega^2)}{(1-\Omega^2)^2+(2\zeta\Omega)^2} + j\frac{(2\zeta\Omega)}{(1-\Omega^2)^2+(2\zeta\Omega)^2}\right\} \tag{3.14}$$

Setting imaginary part to zero gives, $\Omega_c = 0$ and the corresponding real part is $\mathrm{Re}\{G(\mathrm{j}\Omega_c)H(\mathrm{j}\Omega_c)\} = \frac{g_d}{k}$. Since this is positive the displacement feedback control system is also *unconditionally stable*.

The Nyquist plot for the displacement feedback is also shown in Figure 3.2c. When Ω tends to infinity the real and imaginary parts of the open-loop frequency response function tend to zero.

3.3.2.4 Summary

It is evident that the ideal system is unconditionally stable for acceleration, velocity and displacement feedback control strategies. All three plots begin at the origin and follow a clockwise direction back to or closer to the origin as the frequency is increased. In the acceleration feedback control strategy, the critical point (-1,0) is closer to the low frequency part of the plot. For velocity feedback control the entire Nyquist plot lies far away from the critical point (-1,0). In displacement feedback control the critical point is closer to the high frequency part of the plot.

3.4 Identification of low frequency instability sources

In this section, the characteristics of the components of a real system are described, and the ways in which they differ from the ideal system are discussed. As mentioned previously, accelerometers are generally used to obtain the response of a real system. The output can be integrated once or twice for velocity and displacement signals respectively. Conditioning amplifiers such as B&K charge amplifiers can be used to convert the output charge into voltage and to match the measurement instrumentation sensitivity to that of the accelerometer output. This conditioning amplifier together with the power amplifier (which is used for the feedback gain) contains high-pass filters.

The frequency response function of a high-pass filter has the form of $\frac{j\tau_h\omega}{(1+j\tau_h\omega)}$ and electronic integration has the form of $\frac{1}{(1+j\tau_i\omega)}$ [89, where the constants τ_h and τ_i are time constants. Their inverses are called the –3dB corner frequencies i.e. $\omega_h = \frac{1}{\tau_h}$ and $\omega_i = \frac{1}{\tau_i}$.

Now considering the model of a high-pass filter $hp(j\omega) = \frac{j\tau_h\omega}{(1+j\tau_h\omega)}$, where hp denotes high-pass filter and substituting for $\Omega = \frac{\omega}{\omega_n}$, where ω_n is the resonance frequency of the system and $\alpha = \frac{\omega_n}{\omega_h}$ (α is the ratio of natural frequency of the system to the corner frequency of the high-pass filter) gives,

$$hp(j\Omega) = \frac{j\alpha\Omega}{(1+j\alpha\Omega)} \tag{3.15}$$

The characteristic of a high-pass filter is shown in Figure 3.3a (for α = 1), which shows that it introduces a considerable phase advance at low frequencies. In addition it attenuates the signal at low frequencies. Therefore it generally introduces a low frequency problem.

Considering a model of the integrator $Int(j\omega) = \frac{1}{(1+j\tau_i\omega)}$, where Int denotes the integrator and substituting for $\Omega = \frac{\omega}{\omega_n}$ and $\beta = \frac{\omega_n}{\omega_i}$ gives,

$$Int(j\Omega) = \frac{1}{(1+j\beta\Omega)} \tag{3.16}$$

In terms of non-dimensional frequency an ideal integrator frequency response can be written as $\frac{1}{j\omega_n\Omega}$. Thus from equation (3.16) the real integrator can be considered as an ideal integrator when $\Omega >> 1$.

The characteristic of an integrator is shown in Figure 3.3b, (for $\beta = 1$) which shows that it introduces a considerable phase advance with respect to the ideal integrator at low frequencies. In addition it attenuates the signal with respect to the ideal integrator at low frequencies. Therefore it also generally introduces a low frequency problem. A real integrator can be described by a combination of a high-pass filter and an ideal integrator as, (For simplicity $\alpha = \beta$ is considered here.)

$$Int(j\Omega) = \frac{1}{(1+j\alpha\Omega)} = \left(\frac{\omega_n}{\alpha}\right)\left(\frac{j\alpha\Omega}{(1+j\alpha\Omega)}\right)\left(\frac{1}{j\omega_n\Omega}\right) \qquad (3.17)$$

gain high-pass filter ideal integrator

Thus the analysis can be confined to the analysis of number of high-pass filter components in the feedback loop rather than considering the integrator and high-pass filters separately. For example a velocity feedback system with a real integrator can be considered as a system with one high-pass filter and an ideal integrator. Similarly a system with a real integrator and an amplifier can be considered as a system with two high-pass filters (one each from the real integrator and power amplifier) and an ideal integrator etc. In this model α can be used as a measure of the separation of the corner frequency of the high-pass filter to the natural frequency of the plant.

3.5 Low frequency instabilities

The methodology used to assess the instability is similar to that described in section 3.2. That is the imaginary part of the open-loop frequency response function is set to zero and the resulting equation solved to determine the frequency at which the system becomes unstable (critical frequency). This frequency is then inserted into the real part of the open-loop frequency response function; if this is positive then the system is unconditionally stable and if it is negative then the real part is set to –1 and solved to give the maximum gain that can

be applied before the system becomes unstable. For simplicity it is assumed that each high-pass filter has the same corner frequency and is of first order.

3.5.1 Acceleration feedback control

A system with acceleration feedback control and a single high-pass filter is considered first. The open-loop frequency response function is given by (Note that only a high-pass filter component is added to the open-loop frequency response function for acceleration feedback control given in equation (3.9)),

$$G(j\Omega)H(j\Omega)=\left(\frac{g_a}{m}\right)\left(\frac{-\Omega^2}{1-\Omega^2+j2\zeta\Omega}\right)\left(\frac{j\alpha\Omega}{1+j\alpha\Omega}\right) \tag{3.18}$$

which can be written in terms of its real and imaginary parts as,

$$G(j\Omega)H(j\Omega)=\frac{g_a}{m}\left(\frac{-\alpha\Omega^4\left(2\zeta+\alpha\left(1-\Omega^2\right)\right)}{\left(\left(1-\Omega^2\right)^2+\left(2\zeta\Omega\right)^2\right)\left(1+\alpha^2\Omega^2\right)}+j\frac{\alpha\Omega^3\left(2\alpha\zeta\Omega^2+\Omega^2-1\right)}{\left(\left(1-\Omega^2\right)^2+\left(2\zeta\Omega\right)^2\right)\left(1+\alpha^2\Omega^2\right)}\right) \tag{3.19}$$

Setting the imaginary part to zero gives the critical frequency as $\Omega_c^2=\frac{1}{1+2\zeta\alpha}$. Substituting this into the real part and equating to -1 gives the maximum gain as,

$$\frac{g_{a\_\max}}{m}=\frac{2\zeta}{\alpha}\left(2\zeta\alpha+\alpha^2+1\right) \tag{3.20}$$

For low damping i.e. $\zeta << 1$ and for a high-pass filter corner frequency much less than the resonance frequency of the plant i.e. $\alpha >> 1$ equation (3.20) becomes,

$$\frac{g_{a\_\max}}{m}=2\zeta\alpha \tag{3.21}$$

Note that for systems with low damping i.e. $\zeta << 1$, the maximum gain is very small since it is proportional to system damping.

Figure 3.4 shows the Nyquist plot of the acceleration feedback isolation system with one high-pass filter component. It can be seen that the Nyquist plot includes the critical point (a non-dimensional gain 5 is used). Thus it becomes unstable as the gain is increased.

3.5.2 Velocity feedback control

Now consider a velocity feedback control system with a single high-pass filter, the open-loop response is given by (A high-pass filter component is added to the open-loop frequency response function given in equation (3.11)),

$$G(j\Omega)H(j\Omega)=\frac{2\zeta g_v}{c}\left(\frac{j\Omega}{(1-\Omega^2)+j2\zeta\Omega}\right)\left(\frac{j\alpha\Omega}{1+j\alpha\Omega}\right) \tag{3.22}$$

which can be arranged into real and imaginary parts:

$$G(j\Omega)H(j\Omega)=\frac{g_v}{c}(2\zeta\alpha)\left(\frac{\Omega^2\left(2\zeta\alpha\Omega^2+\left(\Omega^2-1\right)\right)}{\left(\left(1-\Omega^2\right)^2+(2\zeta\Omega)^2\right)\left(1+\alpha^2\Omega^2\right)}+j\frac{\Omega^3\left(2\zeta+\alpha\left(1-\Omega^2\right)\right)}{\left(\left(1-\Omega^2\right)^2+(2\zeta\Omega)^2\right)\left(1+\alpha^2\Omega^2\right)}\right) \tag{3.23}$$

Setting the imaginary part to zero and solving for critical frequency gives $\Omega_c^2=\frac{\alpha+2\zeta}{\alpha}$. Substituting this into the real part of equation (3.23) gives, $\mathrm{Re}\{G(j\Omega_c)H(j\Omega_c)\}=\left(\frac{g_v}{c}\right)(2\zeta\alpha)\frac{2\zeta+\alpha}{2\zeta\left(2\zeta\alpha+\alpha^2+1\right)}$ since this is positive, the Nyquist plot does not cross the negative real axis and so *the system is unconditionally stable.*

Figure 3.4 shows the Nyquist plot of the velocity feedback isolation system with one high-pass filter component. It can be seen that the Nyquist plot does not include the critical point and hence the system is unconditionally stable.

3.5.3 Displacement feedback control

Similarly for a displacement feedback system with a single high-pass filter the open-loop response is given by (A high-pass filter component is added to the open-loop frequency response function given in equation (3.13)),

$$G(j\Omega)H(j\Omega)=\left(\frac{g_d}{k}\right)\left(\frac{1}{(1-\Omega^2)+j2\zeta\Omega}\right)\left(\frac{j\alpha\Omega}{1+j\alpha\Omega}\right) \tag{3.24}$$

which can be expanded into its real and imaginary parts:

$$G(j\Omega)H(j\Omega)=\left(\frac{g_d}{k}\right)\left(\frac{\alpha\Omega^2\left(2\zeta-\alpha\left(\Omega^2-1\right)\right)}{\left(\left(1-\Omega^2\right)^2+\left(2\zeta\Omega\right)^2\right)\left(1+\alpha^2\Omega^2\right)}+j\frac{\alpha\Omega\left(2\zeta\alpha\Omega^2-\left(1-\Omega^2\right)\right)}{\left(\left(1-\Omega^2\right)^2+\left(2\zeta\Omega\right)^2\right)\left(1+\alpha^2\Omega^2\right)}\right) \tag{3.25}$$

Following a similar procedure for a displacement feedback control system gives a critical frequency of $\Omega_c^2=\frac{1}{1+2\zeta\alpha}$ and $\mathrm{Re}\left\{G(j\Omega_c)H(j\Omega_c)\right\}=\left(\frac{g_d}{k}\right)\frac{\alpha(2\zeta\alpha+1)}{2\zeta\left(2\zeta\alpha+\alpha^2+1\right)}$. Since this is also positive *the system is unconditionally stable.*

Figure 3.4 shows the Nyquist plot of the displacement feedback isolation system with one high-pass filter component. It can be seen that the Nyquist plot does not include the critical point and hence the system is unconditionally stable.

3.5.4 Effect of increasing the Number of high-pass filters

The analysis of the systems with up to four high-pass filters can be carried out in a similar manner to that discussed above and the results are shown in Table 3.1 for the approximations of $\zeta<<1$ and $\alpha>>1$ and the corresponding critical frequencies are given in Table 3.2. (Details of the derivations are given in appendix G). It is evident from Table 3.1 that the maximum non-dimensional gain for the acceleration feedback control system is small compared with the corresponding maximum non-dimensional gains for velocity and displacement feedback control. Thus velocity and displacement feedback control have larger stability limits.

The Nyquist plots for acceleration, velocity and displacement feedback control are given in Figure 3.5, for $\alpha=2$ (for clarity), $\zeta=0.05$. This figure shows how the number of high-pass filters components influences stability in each case. It can be seen that with one high-pass filter component the Nyquist plot for acceleration feedback encircles the (-1,0) point and hence this system is only conditionally stable. Conversely with one high-pass filter component the Nyquist plots for velocity and displacement feedback control do not cross the negative real axis and hence the systems are unconditionally stable. As the number of high-pass filter components increases, the system becomes only conditionally stable.

The closed-loop response for the real systems can be calculated by substituting for $G(j\Omega)$ given in equation (3.4) together with the appropriate $H(j\Omega)$, into equation (3.5). The closed-loop mobilities for acceleration feedback control systems with one and two high-pass filters respectively are plotted in Figure 3.6a and 3.6b for 99.9% of the respective maximum gains. Similar plots for velocity feedback are given in Figures 3.6c, 3.6d for systems with two and three high-pass filters respectively for 99.9% of the respective maximum gains. Figures 3.6e and 3.6f show the displacement feedback system with three and four high-pass filters. The closed-loop mobilities with no control and for the ideal systems with realistic maximum gain are also plotted for comparison. The frequencies at which the systems become unstable are evident by narrow peaks and are tabulated in Table 3.2. It is clear from Figure 3.6 that acceleration feedback control is not a realistic practical option as it has a limited effect before it becomes unstable with a single high-pass filter. Displacement feedback introduces a second resonance peak at the critical frequency. It seems that velocity feedback control is, however, a robust and realistic control strategy. To compare the three strategies the mean-square response of the system normalised to mean-square response of the system in the absence of control is plotted for the three control strategies in Figure 3.7 for the frequency range $0 \leq \Omega \leq 100$. It is evident from this graph that velocity feedback is the best control strategy.

3.5.5 Summary

With one high-pass filter in the open-loop frequency response function, acceleration feedback control becomes potentially unstable. It was noted that the critical point is closer to the low frequency part of the Nyquist plot in an ideal acceleration feedback system (section 3.3.2.4). Thus adding one high-pass filter, which is a low frequency source of instability, the unconditionally stable acceleration feedback system becomes a conditionally stable system. The velocity feedback control system becomes conditionally stable with two-high-pass filters and the displacement feedback control becomes conditionally stable with three high-pass filters.

With no high-pass filters, the Nyquist plot for acceleration feedback control is in the upper half of the Nyquist plane. It can be seen that as the high-pass filter components are increased one by one, the low frequency part of the plot crosses the other quadrant of the Nyquist plane in the counter-clockwise direction. However the high frequency part of the plot remains in

the same quadrant as the ideal system. This is because of the 90-degree phase advance introduced by the high-pass filter component, which is dominant at low frequencies. This phenomenon can also be seen in velocity and displacement feedback control as well.

3.6 Experimental work

To validate some of the theoretical predictions, experimental work was carried out on a single-degree-of-freedom system set on a rigid foundation. The system considered is the same as the one shown in Figure 2.4. Since it was a symmetric system with respect to the mass centre of the aluminium plate (representing some equipment), it was possible to treat the system as a single-degree-of-freedom system. Both electromagnetic shakers were driven by the same control signal measured at the mid span of the aluminium plate. The aluminium plate had previously been shown to behave as a rigid mass up to 1000 Hz [4], which is well above the maximum frequency of interest in this experimental study.

In principle the aluminium plate will vibrate under the influence of a primary force that will be counteracted by the secondary force generated by the actuators. Therefore, eventually the aluminium plate will experience the difference of the primary and secondary forces. Hence in this experimental work, the actuators were set to generate both the primary and the secondary forces [4] by exciting them with the difference between the primary and feedback signal as shown in Figure 3.8. A summing box, designed by Serrand [4] was connected as shown in Figure 3.8 to produce the difference between the signals (negative feedback). The output signal from an accelerometer (B&K type 4375) placed in the centre of the plate was fed into the charge amplifier (B&K type 2635), which was again fed through the power amplifier 2 (H/H electronic TPA 100-D) into the summing box ensuring negative feedback. A list of instruments used in the experiments in given in Table 3.3.

The experiments were conducted with the following objectives

- To compare the open-loop and closed-loop responses of acceleration, velocity and displacement feedback control of a single-degree-of-freedom system with theoretical analysis.
- To compare the experimental open-loop and closed-loop response with predictions based on the characteristics of the electrical instruments.

- To investigate the effect of the high-pass filter corner frequency (α) setting in feedback control.

3.6.1 Characteristics of electrical components

Figure 3.8 shows the experimental set-up of the feedback control system. It consists of a summing box, power amplifier 1, two shakers, an accelerometer, a charge amplifier and power amplifier 2 (model and serial numbers are given in Table 3.3). The accelerometer has a unity gain up to 10 kHz. The shaker gain (g_s) is defined as the force generated by the two actuators per unit input voltage. This information was taken from Serrand's work [4]; which is 0.91 N/V. An attempt was made to study the characteristics of the rest of the instrumentation used in the active feedback control of the single-degree-of-freedom system. These results were used to obtain the mathematical models.

White noise from the analyser was fed into the summing box and the output was normalised by the input signal, in a simple experiment to measure the gain (g_b) of the summing box. A pure gain of about 0.67 was observed. Details of the experiments and the technique used to model the characteristics of power amplifier 1, power amplifier 2, the charge amplifier in integration mode with 1 and 10 Hz cut-off frequencies and the charge amplifier characteristics with double integration are given in appendix H. Since the frequency range of interest in this experimental work was 0 to 200 Hz, the characteristics were measured in this range. The low-pass filter of the charge amplifier does not have influence in this frequency range hence it is not included in the mathematical model. The mathematical models are given below,

- Power amplifier 1

$$Pa_1 = \frac{j0.2775\omega}{(1 + j0.0633\omega)} \tag{3.26a}$$

- Power amplifier 2

$$Pa_2 = \frac{-g_{p2}\omega^2}{(1 + j0.0633\omega)^2} \tag{3.26b}$$

where g_{p2} = [0.002, 0.0045, 0.0075, 0.0131, 0.0162, 0.02].

Equation (3.26b) shows the characteristics of power amplifier 2, which is the controller in this experimental work. The gain g_{p2} can take a range of discrete values, hence allowing an increase in the gain in the feedback system. It is seen that it has a second order high-pass filter.

- The charge amplifier with 1 Hz and 10 Hz cut-off frequencies with single integration,

$$Ca_1 = \frac{j4.1539\omega}{(1+j0.159\omega)} \times \frac{1}{(1+j0.251\omega)} \qquad \text{At cut off frequency of 1 Hz.} \qquad (3.27a)$$

$$Ca_{10} = \frac{j0.0567\omega}{(1+j0.0159\omega)} \times \frac{1}{(1+j0.0333\omega)} \qquad \text{At cut off frequency of 10 Hz.} \qquad (3.27b)$$

It was discussed previously that the greater the value of α (ratio of natural frequency of the system to the corner frequency of the electrical components) the better the closed-loop performance of the system. Equations (3.27a) and (3.27b) give the charge amplifier frequency response functions at two cut-off frequencies. It is seen that they are considerably different from each other. This allows the investigation of the effect of the magnitude of α as discussed previously.

- The charge amplifier frequency response function with double integration

$$Ca\_d_1 = \frac{j5.0752\omega}{(1+j0.159\omega)} \times \frac{1}{(1+j0.1757\omega)^2} \qquad \text{At cut off frequency of 1 Hz} \qquad (3.28)$$

Equation (3.28) shows the characteristics of the charge amplifier with double integration, which can be used for displacement feedback control.

3.6.2 Experiments and simulations

Simulations were performed using the measured integrator and high-pass filter characterises and compared with the measurements of the acceleration, velocity and displacement feedback control. The simulated and measured Nyquist plots are shown in Figures 3.9a-d. It can be seen that for acceleration feedback control the Nyquist plot crosses the negative real axis for a very small gain. In Figures 3.9b and 3.9c, it can be seen that for velocity feedback control as the cut-off frequency of the charge amplifier is increased the maximum gain that can be applied is reduced. This is in-line with the prediction given in Table 3.1. In Figure

3.9d it can be seen that with displacement feedback control there is better low frequency stability.

In Figure 3.10 the theoretical and experimental closed-loop responses for the system with velocity feedback are plotted for charge amplifier cut-off frequencies of 1 Hz and 10 Hz. The maximum gain applied in these plots is the gain just before the system becomes unstable. It is clear from this Figure that the cut-off frequency of the charge amplifier has a profound effect on the maximum gain and hence the performance, as discussed previously.
Figure 3.11 shows the theoretical and experimental closed-loop responses for acceleration and displacement feedback control systems. It can be seen that they exhibit poor performance.

3.7 Multi-input-multi-output system

As mentioned previously most mounted equipment has more than one mount and hence generally they cannot be modelled as a SDOF system. Thus the analysis presented above needs to be extended to a general system. In this section a more general system is considered.

Consider a multi-input-multi-output (MIMO) system whose plant frequency response matrix is given by $\mathbf{G}(j\omega)$. This plant response function can be expressed in terms of non-dimensional frequency normalised by its first resonance frequency as $\mathbf{G}(j\Omega)$. For a decentralised feedback control system with equal gains in each loop and identical instruments (i.e. all instruments in each loop are of same type and have the same frequency response function), the feedback frequency response matrix in non-dimensional frequency takes the form $\mathbf{H}(j\Omega)=H(j\Omega)\mathbf{I}$, where $H(j\Omega)$ is same as that in the single-degree-of-freedom system considered previously. The vector of closed-loop frequency responses of the system can be written as,

$$\mathbf{v}=\left[\mathbf{I}+\mathbf{G}(j\Omega)\mathbf{H}(j\Omega)\right]^{-1}\mathbf{G}(j\Omega)\mathbf{f}_p \tag{3.29}$$

This can be expressed as [91],

$$\mathbf{v}=\frac{\mathrm{adj}\left[\mathbf{I}+\mathbf{G}(j\Omega)\mathbf{H}(j\Omega)\right]}{\det\left[\mathbf{I}+\mathbf{G}(j\Omega)\mathbf{H}(j\Omega)\right]}\mathbf{G}(j\Omega)\mathbf{f}_p \tag{3.30}$$

Thus the condition for stability can be written as [31] (noting that $\mathbf{H}(j\Omega)=H(j\Omega)\mathbf{I}$),

$$\det\left[\mathbf{I}+\mathbf{G}(j\Omega)H(j\Omega)\right]\neq 0 \tag{3.31}$$

Letting the eigenvalues of $\mathbf{G}(j\Omega)$be $[\lambda_1,\lambda_2\cdots\lambda_r\cdots\cdots]$, equation (3.31) can be written as,

$$\det\left[\mathbf{I}+\mathbf{G}(j\Omega)H(j\Omega)\right]=\left(1+\lambda_1 H(j\Omega)\right)\left(1+\lambda_2 H(j\Omega)\right)\cdots\left(1+\lambda_r H(j\Omega)\right)\cdots\cdots\neq 0 \tag{3.32}$$

Thus for stability, the plots of the real part against the imaginary part of $\lambda_1 H(j\Omega),\lambda_2 H(j\Omega)$ etc. should not enclose (-1,0) point. It is shown in Appendix F that a multi-channel collocated (i.e. systems with an inelastically moving base or systems on a rigid base) decentralised velocity feedback control is unconditionally stable $\left(i.e.\ \mathrm{Re}\{\lambda_1,\lambda_2,\cdots\lambda_r\cdots\cdots\text{etc}\}\geq 0\right)$. Thus the stability of the system is similar to a SDOF system and depends on the feedback frequency response function as discussed previously. The feedback frequency response function is given by for acceleration feedback control $H(j\Omega)=j\Omega\frac{g_a}{m}\left(\frac{j\alpha\Omega}{1+j\alpha\Omega}\right)^n$, for velocity feedback control $H(j\Omega)=\frac{g_v}{c}\left(\frac{j\alpha\Omega}{1+j\alpha\Omega}\right)^n$ and for displacement feedback control $H(j\Omega)=\frac{1}{j\Omega}\frac{g_a}{k}\left(\frac{j\alpha\Omega}{1+j\alpha\Omega}\right)^n$, where n is the number of high-pass filters (Note that the real integrators are treated as high-pass filters with ideal integrators).

Thus the analytical solutions obtained for the SDOF system can be readily applied to the MIMO system provided collocated decentralised feedback control techniques are applied and the base is inelastic. The condition of collocation cannot be achieved if the base is flexible, which is the subject of further research.

3.8 Conclusions

In this Chapter sources of instability have been investigated. The control strategy used is analogue feedback control. An ideal system (i.e. system with perfect instruments) is found to be unconditionally stable for acceleration, velocity and displacement feedback. When real components are connected, however, it (a real system) becomes only conditionally stable for acceleration, velocity and displacement feedback control. Considering the three configurations, the acceleration feedback control system exhibits the lowest maximum gain.

The velocity feedback control system would be unconditionally stable with one high-pass filter (or with a real integrator) and displacement feedback control system would be unconditionally stable for up to two high-pass filters. Addition of one more high-pass filters makes the system only conditionally stable and when more and more high-pass filters are added the attainable maximum gain reduces. In comparison with velocity feedback, the displacement feedback control system has a higher maximum gain. However the performance, when judged using the attenuation for a given gain, is poor in a realistic displacement feedback system.

Number of high-pass filters	Acceleration feedback	Velocity feedback	Displacement feedback
0	*Unconditionally stable*	*Unconditionally stable*	*Unconditionally stable*
1	$\frac{g_{a\_\max}}{m} \approx 2\zeta\alpha$	*Unconditionally stable*	*Unconditionally stable*
2	$\frac{g_{a\_\max}}{m} \approx \zeta\alpha$	$\frac{g_{v\_\max}}{c} \approx \frac{\alpha}{\zeta}$	*Unconditionally stable*
3	-	$\frac{g_{v\_\max}}{c} \approx \frac{4}{9}\frac{\alpha}{\zeta}$	$\frac{g_{d\_\max}}{k} \approx 8$
4	-	-	$\frac{g_{d\_\max}}{k} \approx 4$

Table 3. 1. Non-dimensional maximum gains for different numbers of high-pass filters $\alpha >> 1 \& \zeta << 1$

Number of high-pass filters	Acceleration feedback	Velocity feedback	Displacement feedback
0	*Unconditionally stable*	*Unconditionally stable*	*Unconditionally stable*
1	$\Omega_c \approx \frac{1}{\sqrt{1+2\zeta\alpha}}$	*Unconditionally stable*	*Unconditionally stable*
2	$\Omega_c \approx \frac{1}{\sqrt{1+\zeta\alpha}}$	$\Omega_c \approx \frac{1}{\alpha}$	*Unconditionally stable*
3	-	$\Omega_c \approx \frac{\sqrt{3}}{\alpha}$	$\Omega_c \approx \frac{1}{\sqrt{3}\alpha}$
4	-	-	$\Omega_c \approx \frac{1}{\alpha}$

Table 3.2. Non-dimensional critical frequencies for different numbers of high-pass filters $\alpha >> 1 \& \zeta << 1$

Name	Type	Serial number
Accelerometer	B&K 4375	1760059
Power amplifier (Power amplifier 1)	H/H electronic TPA 50-D	14415
Power amplifier (Power amplifier 2)	H/H electronic TPA 100-D	15397
Charge amplifier	B&K 2635	1446895
Analyser	Hewlett Packard (*HP* type 35650)	Analyser C (2911A02485)
Shakers	Ling dynamic systems ltd Model V101	40326.21

Table 3.3. List of instruments used for experiments

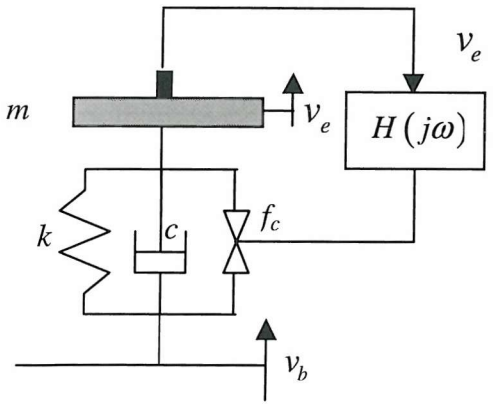

(a) SDOF system on moving inelastic base

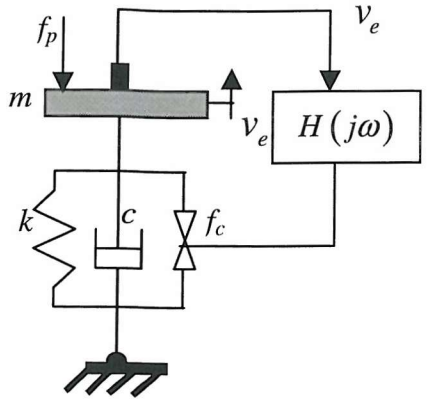

(b) SDOF system on a rigid base

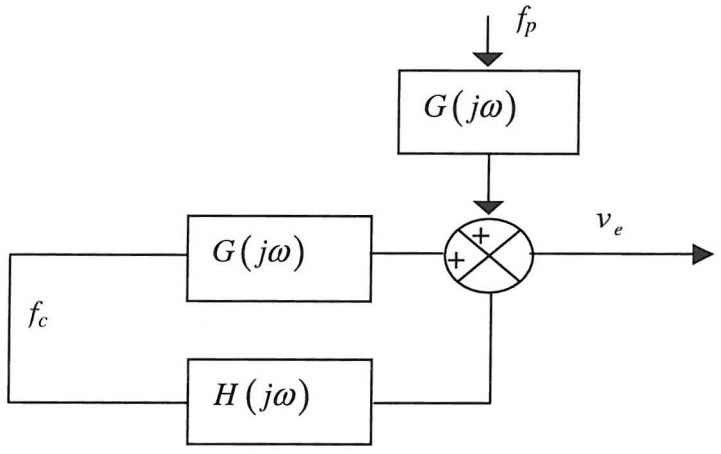

(c) Block diagram representation

Figure 3.1 Feedback control of a single-degree-of-freedom (SDOF) system

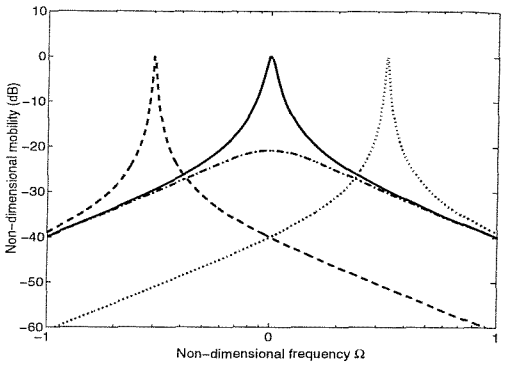

(a) Closed-loop frequency response (Non-dimensional gain 10 *and damping ratio* $\zeta = 0.05$ *) No control: _____, acceleration feedback: ----------, velocity feedback: -.-.-.-.-.-.-.-.-, displacement feedback:.....*

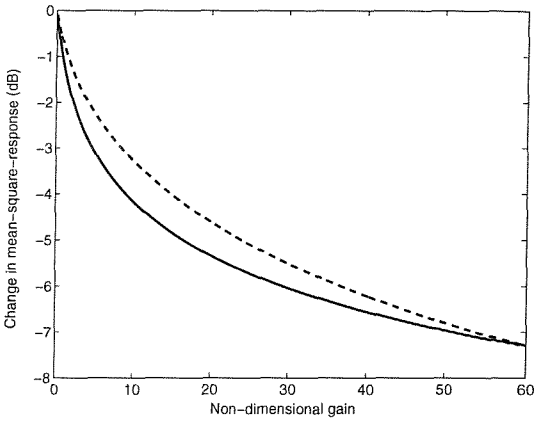

(b) Change in mean square response in the frequency range $0.01 \leq \Omega \leq 100$ *; (damping ratio* $\zeta = 0.05$ *) velocity feedback: ----------, acceleration and displacement feedback:_____*

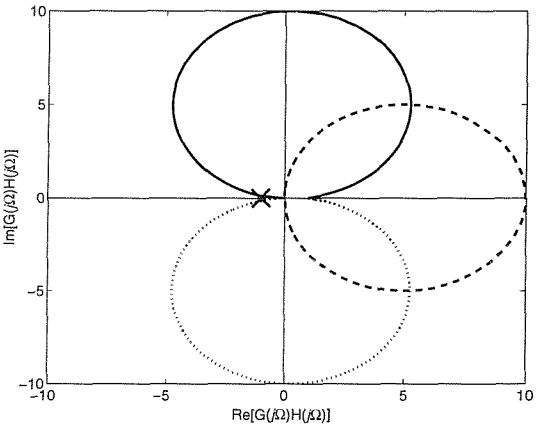

(c) Open-loop frequency response (damping ratio $\zeta = 0.05$ *); acceleration feedback:_____, velocity feedback:----------, displacement feedback:.....*

Figure 3.2 Ideal SDOF system response with acceleration, velocity and displacement feedback control.

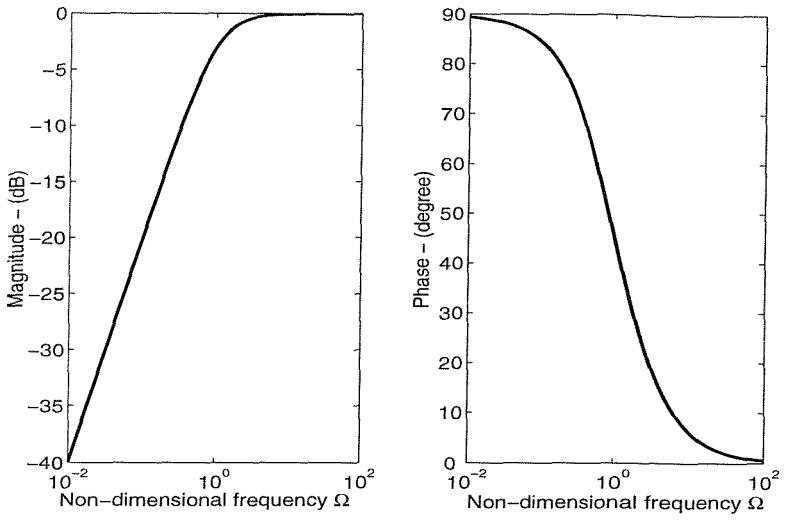

(a) The characteristics of a high pass filter (for $\alpha = 1$)

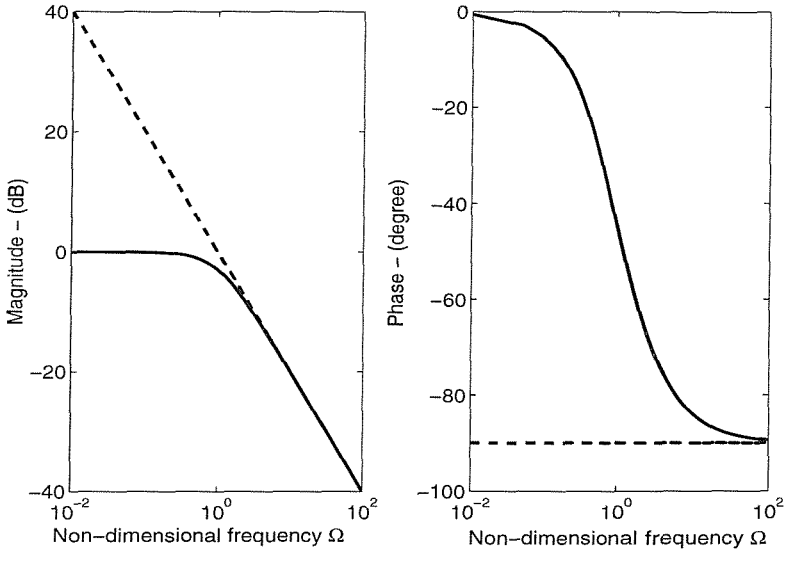

(b) The characteristics of an electronic integrator (for $\beta = 1$) ideal integrator:----------, real integrator:_____

Figure 3.3 Frequency response characteristics of electronic components in the feedback loop

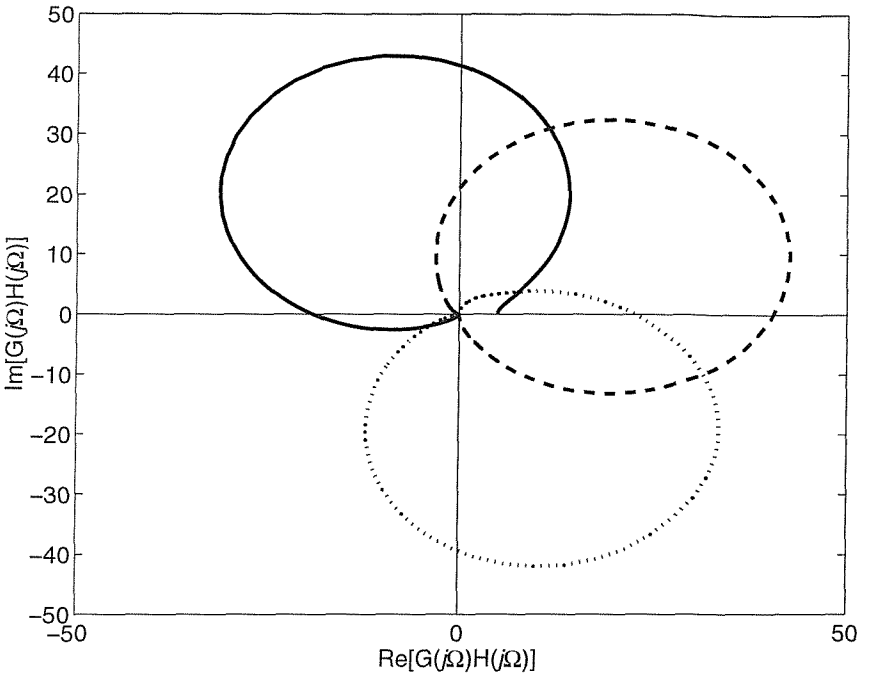

Figure 3.4 Open-loop frequency response function with one first-order high-pass filter with $\alpha = 10$ *for all three control strategies (damping ratio* $\zeta = 0.05$ *and non-dimensional gain* 5*); Acceleration feedback control:*_____*, Velocity feedback control:* ---------- *and displacement feedback control:* .....

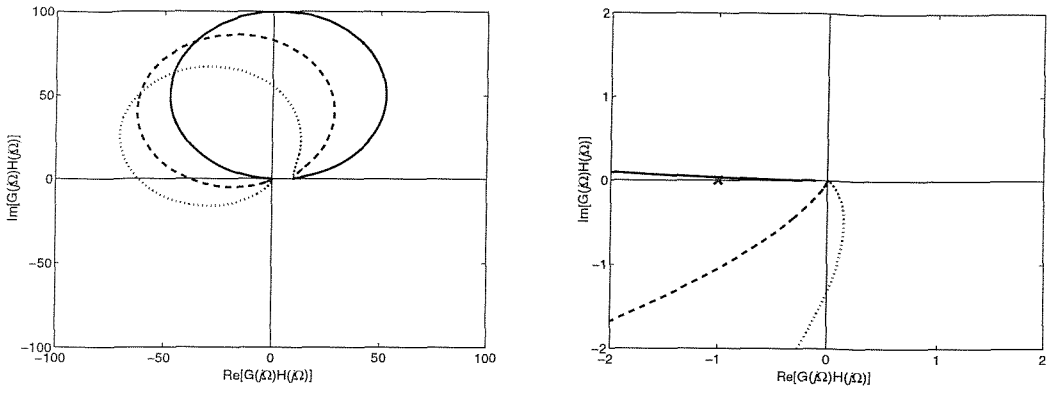

(a) *Acceleration feedback control (both complete and zoomed in the vicinity of the origin)*

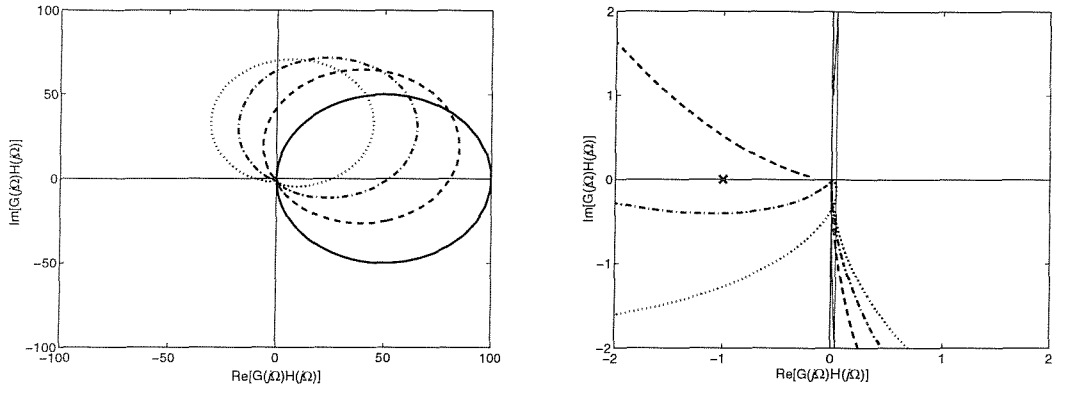

(b) Velocity feedback control (both complete and zoomed in the vicinity of the origin)

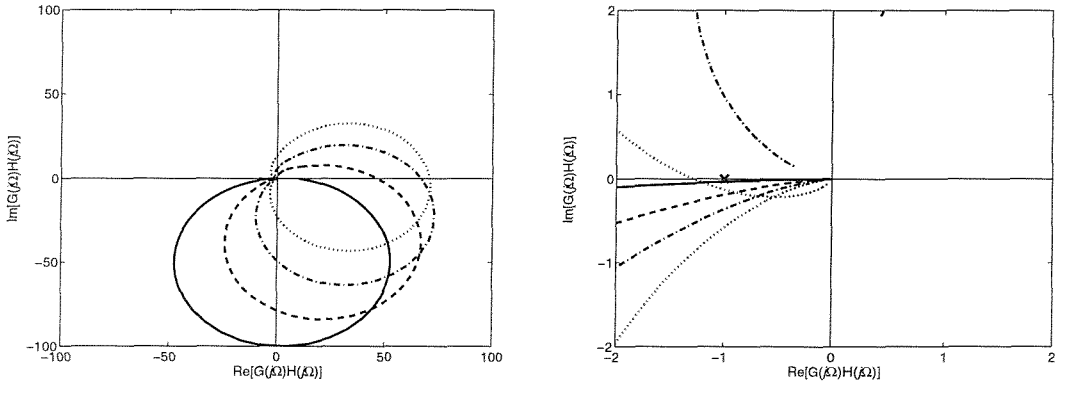

(b) Displacement feedback control (both complete and zoomed in the vicinity of the origin)

Figure 3.5 Open-loop frequency response function with different numbers of first-order high-pass filter components (damping ratio $\zeta = 0.05$, $\alpha = 2$ and non-dimensional gain 5); No high-pass filter:_____, one high- pass filter: ----------, two high-pass filters: -.-.-.-.-.-.-.-.-.-. three high-pass filters: .....

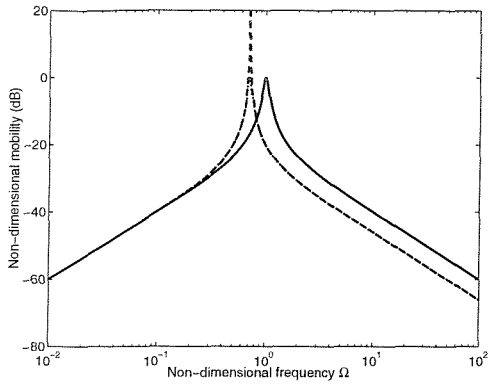

(a) Acceleration feedback with one high-pass filter

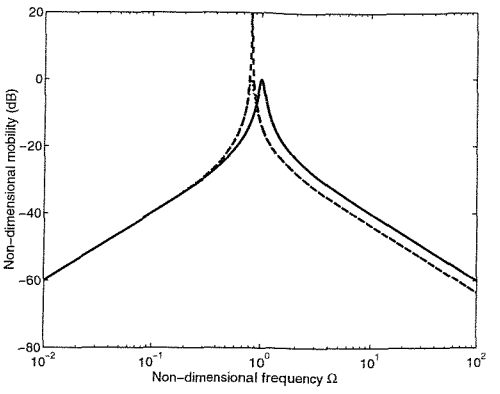

(b) Acceleration feedback with two high-pass filters

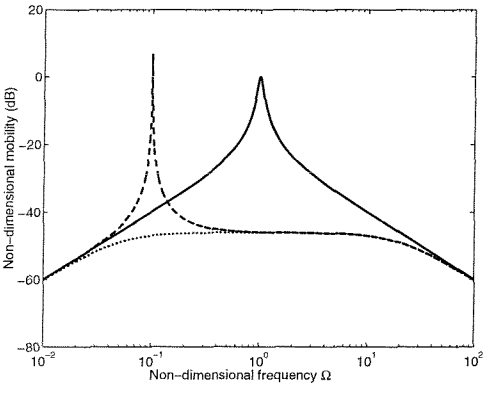

(c) Velocity feedback with two high-pass filters

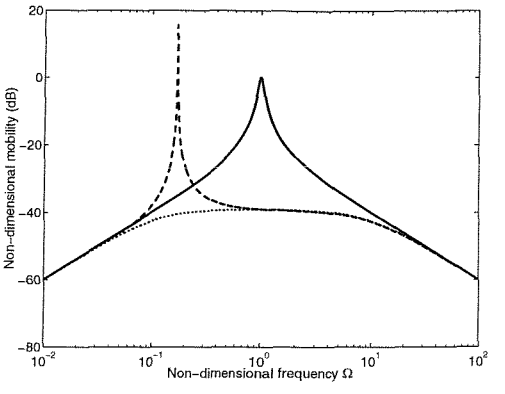

(d) Velocity feedback with three high-pass filters

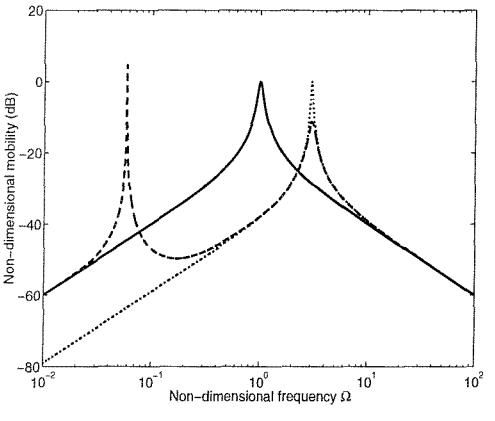

(e) Displacement feedback with three high-pass filters

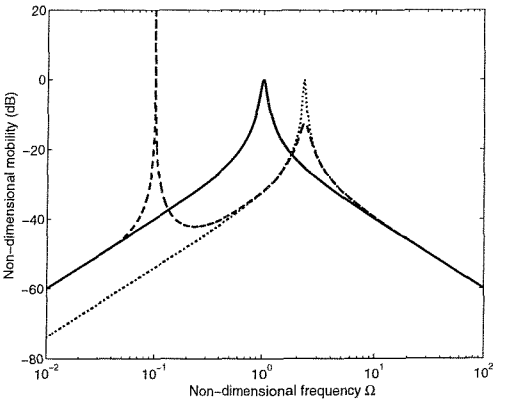

(f) Displacement feedbacks with four high-pass filters

Figure 3.6 Closed-loop response for acceleration, velocity and displacement feedback control with various number of high-pass filters; no control: _____, realistic system, with high-pass filters and gains of 99.9% of the respective maximum: ---------, ideal system with 99.9% of the realistic maximum gain: .....

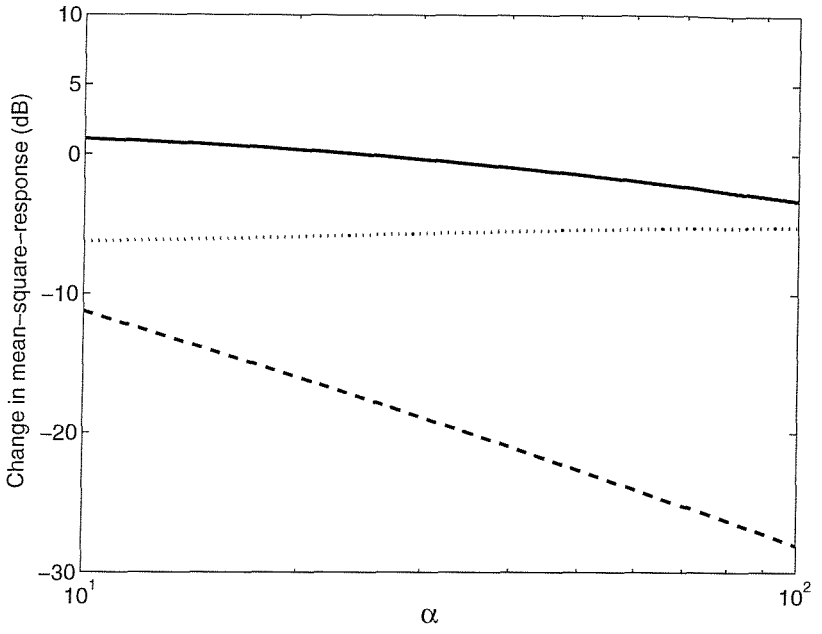

Figure 3.7 Change in mean square response with 99.9% of the respective maximum gain; acceleration feedback with two high-pass filters:_____, velocity feedback with three high-pass filters: ---------- and displacement feedback with four high-pass filters: .....

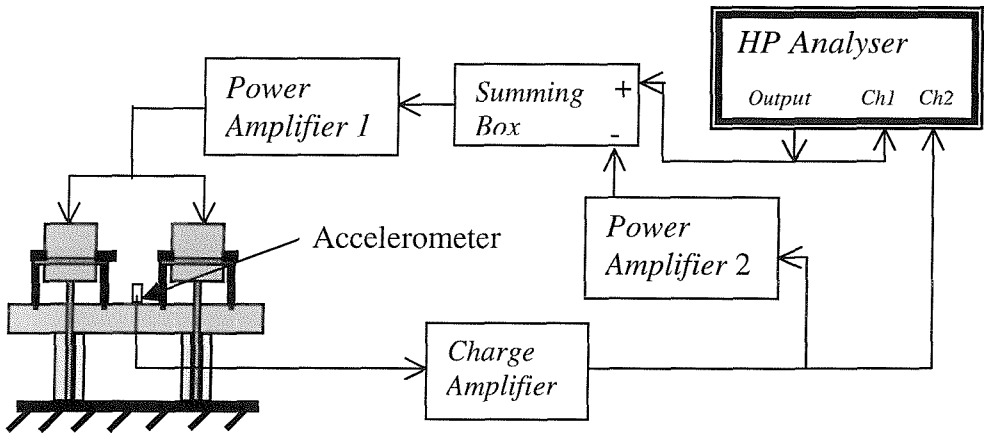

Figure 3.8 Experimental set-up for the feedback control of the single-degree-of-freedom system.

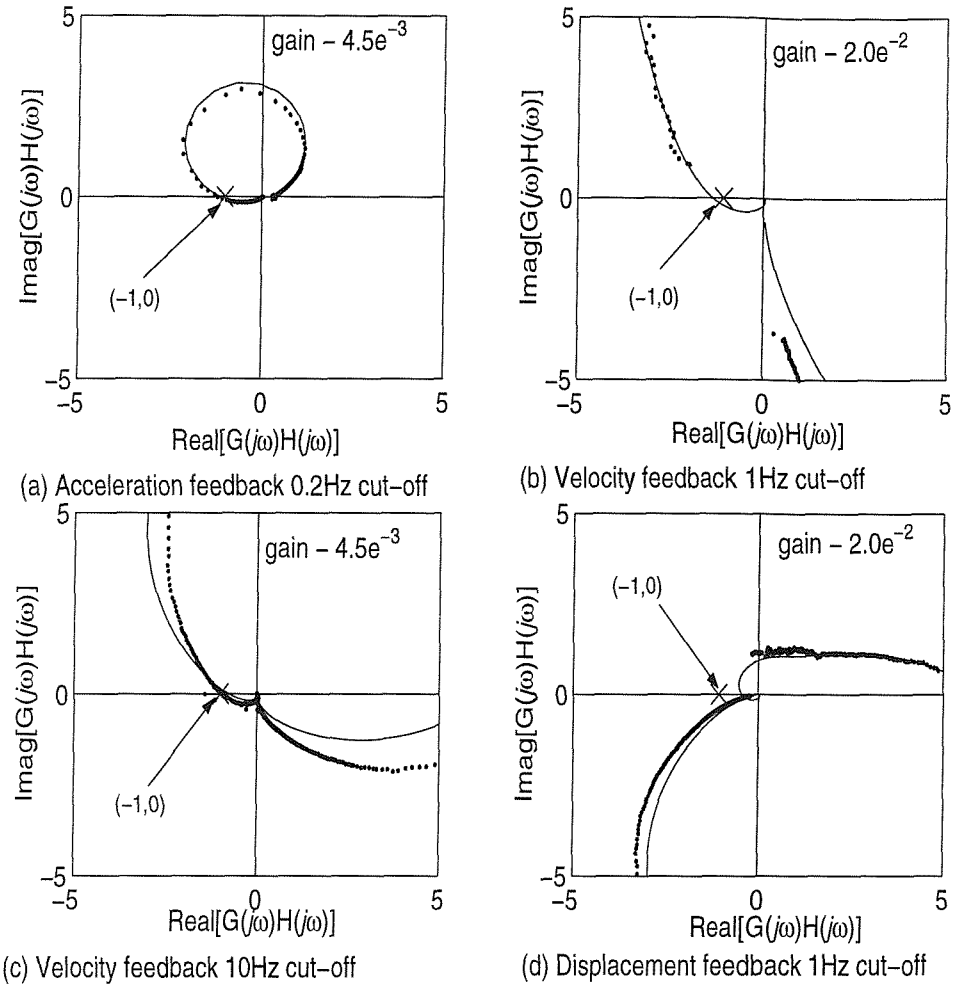

Figure 3.9 Measured and simulated open-loop frequency response function of the single-degree-of-freedom system. Simulations: _____, Experiments:.....

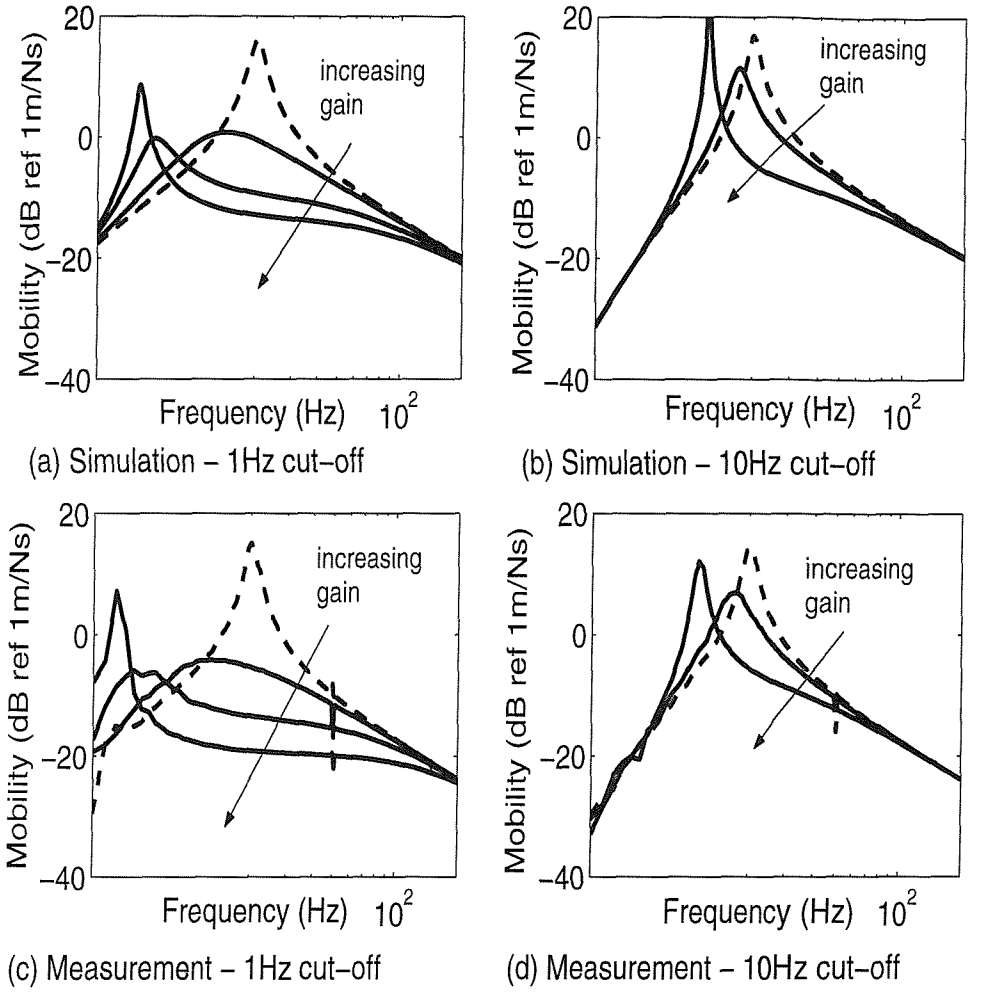

Figure 3.10 Measured and simulated closed-loop frequency response function of the single-degree-of-freedom system (for velocity feedback control). No control: ---------- with control:_____

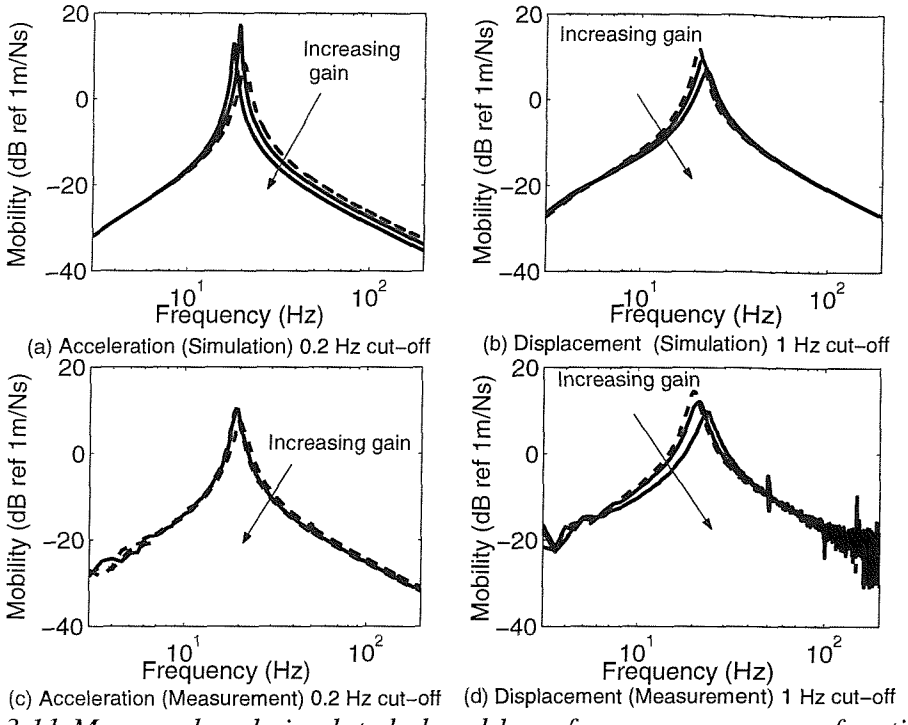

Figure 3.11 Measured and simulated closed loop frequency response function of the single-degree-of-freedom system (for acceleration and displacement feedback control feedback control). No control: ----------, *with control*:_____

Chapter 4

High frequency instabilities in feedback control

4.1 Introduction

In Chapter 3 instabilities that are dominant at low frequencies were discussed. In this Chapter instabilities that are dominant at high frequencies are investigated. It was shown in Chapter 3 that sources of low frequency instability have little or no influence in the high frequency regime. The sources of instabilities that could affect the high frequency regime are (a) time-delay, (b) low-pass filters, (c) secondary or control actuators and (d) sensor dynamics.

Time-delay exists in feedback control loops due to transducers (such as hydraulic actuators) and the computation process in a digital control. Pure time-delay in the frequency domain can be represented by $e^{-j\omega T}$ [13], where T is the delay time. Generally the presence of time-delay affects the feedback frequency response function and hence open and closed-loop frequency response functions. From the model of time-delay considered, it can be seen that it has a magnitude of one $\left(\text{i.e. } \left|e^{-j\omega T}\right|=1\right)$ and has a phase lag of ωT $\left(\text{i.e. } \angle e^{-j\omega T}=-\omega T\right)$. This phase lag, which is a function of frequency, becomes dominant as the frequency is increased. Hence time-delay is generally a high frequency source of instability.

Low-pass filters could be present in the signal conditioning devices such as charge amplifiers to reject the unwanted signals at high frequencies. (Note that a real integrator also takes the form of a low-pass filter. The difference, however, is that a real integrator has a low corner frequency while a low-pass filter has a higher corner frequency) A first order model of a low-pass filter is given by $\frac{1}{1+j\tau_L\omega}$ [89], where τ_L is the time constant. This can be expressed in-terms of its magnitude $\frac{1}{\sqrt{1+\tau_L^2\omega^2}}$ and phase as $\phi=-\tan^{-1}\left(\tau_L\omega\right)$. From the magnitude and phase expressions it can be seen that as frequency tends to zero the

magnitude and phase become one and zero respectively. Similarly as the frequency tends to a large value the magnitude reduces and introduces a phase lag 90-degree. Thus as the frequency is increased the magnitude reduces at the same time as an increasing phase lag, and hence a low-pass filter introduces a high frequency problem.

Actuators are an integral part of active vibration isolation systems. Although there are a variety of actuators such as electromagnetic, hydraulic, piezoelectric, magnetostrictive etc, the type of actuator considered in this thesis is an electromagnetic actuator. Ren et. al. [33] showed that the electrical characteristics of an electromagnetic actuator can be represented by the mathematical model $\frac{g_a}{1+j\tau_a\omega}$ (where g_a is the gain and τ_a is the time constant), which is the same as a first order low-pass filter. Thus an electromagnetic actuator could also cause instabilities at high frequencies.

Sensors are also important components in an active vibration isolation system. Similar to actuators, there are a variety of sensors available as discussed in Chapter 1, however the type of sensor considered in this thesis is an accelerometer. An accelerometer is an electromechanical transducer, which outputs a voltage or charge that is proportional to the acceleration [85] of the object to which it is attached. It is the most widely used vibration measurement transducer due to its small size, range of sensitivities and large working frequency range. An accelerometer can be modelled as a single–degree-of-freedom system, whose resonance frequency is usually very high. It is generally possible to choose an accelerometer whose resonance frequency is well above the frequency range of interest.

The effects of these sources of instabilities on a SDOF system are investigated in the subsequent sections and later generalised to a MIMO system.

4.2 Time-delay

For simplicity the effect of pure time-delay on the feedback control of a single degree of freedom system is considered in this section. The time-delay is represented in the frequency domain as $e^{-j2\pi\Omega}$ where $\Omega=\frac{\omega}{\omega_n}$ (ω_n is the resonance frequency of the SDOF system),

$\tau = \frac{T}{T_n}$ and T_n is the natural period. The method of analysis to determine the critical frequency, at which the system becomes unstable, is similar to the one described in Chapter 3. First consider time-delay introduced into a system with acceleration feedback control.

4.2.1 acceleration feedback control with time-delay

The open-loop frequency response function of an ideal acceleration feedback control system with time-delay can be written as (Note that delay term appears in the open-loop frequency response function given in equation 3.3),

$$G(j\Omega)H(j\Omega) = \left(\frac{g_a}{m}\right)\frac{-\Omega^2 e^{-j2\pi\Omega\tau}}{\left(1-\Omega^2 + j2\zeta\Omega\right)} \tag{4.1}$$

Equation (4.1) can be rearranged in terms of its real and imaginary parts to give,

$$G(j\Omega)H(j\Omega) = \left(-\frac{g_a}{m}\Omega^2\right)\left(\frac{(\Omega^2-1)\cos(2\pi\tau\Omega)-2\zeta\Omega\sin(2\pi\tau\Omega}{4\zeta^2\Omega^2+(\Omega^2-1)^2} + j\frac{(\Omega^2-1)\sin(2\pi\tau\Omega)+2\zeta\Omega\cos(2\pi\tau\Omega)}{4\zeta^2\Omega^2+(\Omega^2-1)^2}\right) \tag{4.2}$$

To determine the relationship between the critical frequency Ω_c at which the system goes unstable, the imaginary part is set to zero which results in $\tan(2\pi\tau\Omega_c) = -\frac{2\zeta\Omega_c}{1-\Omega_c^2}$.

This can be written in alternative form as,

$$f(\Omega_c) = \tan(\pi - 2\pi\tau\Omega_c) = \frac{2\zeta\Omega_c}{1-\Omega_c^2} \tag{4.3}$$

For low damping, i.e. when $\zeta \to 0$; $\tan(\pi - 2\pi\tau\Omega_c) \to 0$ which gives,

$$\Omega_c = \frac{1}{2\tau} \tag{4.4}$$

The Nyquist plot given in Figure 4.1a shows that the critical frequency is the second frequency at which the plot crosses the real axis. This critical frequency depends on the damping ratio ζ and non-dimensional time-delay τ as given in equation (4.3). A graphical representation of solutions to this equation is shown in Figure 4.2a for τ = 0.1. Figure 4.2a shows two solutions of equation (4.3). However the second frequency is of importance in-terms of stability (As mentioned previously when discussing Figure 4.1a). Figure 4.3a shows the critical frequency as a function of damping ratio and non-dimensional time-delay. It is

evident from this figure that the dependence of the critical frequency on the time-delay is much greater than for the damping ratio. Thus for low damping, the approximation given in equation (4.4) can be used. Figure 4.4a shows this approximation graphically together with the numerical solutions to equation (4.3) for damping ratios 0.01, 0.05 and 0.1 respectively (Note that all curves overlay and hence can not be distinguished individually). It can be seen that for a time-delay $0<\tau \leq 0.15$ and damping ratio $0<\zeta \leq 0.1$ the approximation given by equation (4.4) is in good agreement with the numerical solutions.

Substituting the approximate critical frequency given by equation (4.4) into the real part of equation (4.2) and equating to –1 to find the maximum non-dimensional gain $\frac{g_a}{m}$, before the system becomes unstable gives,

$$\frac{g_{a\_\max}}{m} = 1 - 4\tau^2 \tag{4.5}$$

It is evident from equation (4.5) that the maximum attainable non-dimensional gain is less than unity. Figure 4.5a shows the closed-loop performance for the acceleration feedback control strategy. For comparison purposes three graphs are plotted in Figure 4.5a. They are the original system with no control applied, the system that has a non-dimensional time-delay of 0.1 with 99.9% of the corresponding maximum gain and thirdly the system with no time-delay but has 99.9% of the maximum gain, corresponding to a non-dimensional time-delay of 0.1. It can be seen that there are many additional resonance frequencies in the system with acceleration feedback control, making this control system impractical for a system that has a reasonably large time-delay in the control system.

4.2.2 Velocity feedback control with time-delay

The open-loop frequency response function with velocity feedback control given in equation (3.5) could be extended for the velocity feedback system with time-delay. This is given by,

$$G(j\Omega)H(j\Omega) = \left(\frac{g_v}{c}\right)\frac{j2\zeta\Omega e^{-j2\pi\Omega\tau}}{\left(1-\Omega^2+j2\zeta\Omega\right)} \tag{4.6}$$

Equation (4.6) can be rearranged into real and imaginary parts to give,

$$G(j\Omega)H(j\Omega)=\left(\frac{g_v}{c}\right)(2\zeta\Omega)\left(\frac{2\zeta\Omega\cos(2\pi\tau\Omega)-(\Omega^2-1)\sin(2\pi\tau\Omega}{4\zeta^2\Omega^2+(\Omega^2-1)^2}-j\frac{(\Omega^2-1)\cos(2\pi\tau\Omega)+2\zeta\Omega\sin(2\pi\tau\Omega)}{4\zeta^2\Omega^2+(\Omega^2-1)^2}\right) \tag{4.7}$$

To determine the relationship between the critical frequency Ω_c, at which the system goes unstable, and the time-delay, the imaginary part is set to zero. Setting $\mathrm{Im}\{G(j\Omega)H(j\Omega)\}=0$ results in,

$$f(\Omega_c)=\tan(2\pi\tau\Omega_c)=\frac{1-\Omega_c^2}{2\zeta\Omega_c} \tag{4.8}$$

Equation (4.8) can be written in the following form,

$$\tan\left(\frac{\pi}{2}-2\pi\tau\Omega_c\right)=\frac{2\zeta\Omega_c}{1-\Omega_c^2} \tag{4.9}$$

When $\zeta\to 0$, $\tan\left(\frac{\pi}{2}-2\pi\tau\Omega_c\right)\to 0$ which results in,

$$\Omega_c=\frac{1}{4\tau} \tag{4.10}$$

Equation (4.9) shows that the critical frequency for velocity feedback control depends on the non-dimensional time-delay and damping ratio. The open-loop Nyquist plot is given in Figure 4.1b for the velocity feedback control system with a damping ratio 0.05 and non-dimensional gain 1 for various time-delays. The plot shows that the critical frequency for velocity feedback control is the second frequency at which the plot crosses the real axis. A graphical solution for equation (4.8) is shown in Figure 4.2b. In Figure 4.3b the critical frequency as a function of damping ratio and non-dimensional time-delay is shown.

It is seen from Figure 4.3b that the critical frequency is influenced much more by the time-delay than the damping ratio. Figure 4.4b shows the approximate critical frequency given by equation (4.10) and the numerical solutions to equation (4.8) for damping ratios 0.01, 0.05 and 0.1 respectively (Note that all curves overlay and hence can not be distinguished individually). It can be observed that for a time-delay $0<\tau\leq 0.15$ and damping ratio $0<\zeta\leq 0.1$, the approximation given by equation (4.10) is in good agreement with the numerical solutions.

To determine the maximum gain, the real part of the open-loop response function given by equation (4.7) should be set to –1 and the frequency set to the critical frequency. This gives,

$$\frac{g_{v\_max}}{c} = \frac{-\left(4\zeta^2\Omega_c^2 + \left(\Omega_c^2 - 1\right)^2\right)}{2\Omega_c\zeta\left\{2\zeta\Omega_c\cos\left(2\pi\tau\Omega_c\right) + \left(1-\Omega_c^2\right)\sin\left(2\pi\tau\Omega_c\right)\right\}} \tag{4.11}$$

When $\tau \leq 0.15$, $\Omega_c \approx \frac{1}{4\tau}$ and equation (4.11) reduces to

$$\frac{g_{v\_max}}{c} = \frac{-\left(64\tau^2\zeta^2 + \left(16\tau^2 - 1\right)^2\right)}{8\tau\zeta\left(16\tau^2 - 1\right)} \tag{4.12}$$

For $\zeta << 1$ this becomes,

$$\frac{g_{v\_max}}{c} \approx \frac{\left(1-16\tau^2\right)}{8\tau\zeta} \tag{4.13}$$

which for a small time-delay, $\tau << 1$ reduces further to,

$$\frac{g_{v\_max}}{c} = \frac{1}{8\tau\zeta} \tag{4.14}$$

It is evident from equation (4.14) that the maximum attainable non-dimensional gain is reasonably large for small damping and small delay. Figure 4.5b shows the closed-loop performance for the velocity feedback control strategy. For comparison purposes three graphs are plotted in Figure 4.5b. They are the original system with no control applied, system that has a non-dimensional time-delay 0.1 with 99.9% of the corresponding maximum gain and thirdly the system with no time-delay but has 99.9% of the maximum gain corresponding to non-dimensional time-delay of 0.1. It can be seen that the resonance peak appears at higher frequencies while the response at the original resonance frequency reduces considerably. This resonance peak is the undesirable effect of the time-delay. However the effect is less compared to the corresponding case for acceleration feedback control shown in Figure 4.5a.

4.2.3 Displacement feedback control with time-delay

The open-loop frequency response function given in equation (3.7) can be extended to the displacement feedback system with time-delay. It can be written as,

$$G(j\Omega)H(j\Omega) = \left(\frac{g_d}{k}\right)\frac{e^{-j2\pi\Omega\tau}}{\left(1-\Omega^2 + j2\zeta\Omega\right)} \tag{4.15}$$

Equation (4.15) can be rearranged into real and imaginary parts to give,

$$G(j\Omega)H(j\Omega)=\frac{g_d}{k}\left(\frac{(\Omega^2-1)\cos(2\pi\tau\Omega)-2\zeta\Omega\sin(2\pi\tau\Omega}{4\zeta^2\Omega^2+(\Omega^2-1)^2}-j\frac{(\Omega^2-1)\sin(2\pi\tau\Omega)+2\zeta\Omega\cos(2\pi\tau\Omega)}{4\zeta^2\Omega^2+(\Omega^2-1)^2}\right) \tag{4.16}$$

To determine the relationship between the critical frequency Ω_c at which the system goes unstable and the time-delay, the imaginary part is set to zero. Setting $\mathrm{Im}\{G(j\Omega)H(j\Omega)\}=0$, results in,

$$f(\Omega_c)=\tan(2\pi\tau\Omega_c)=-\frac{2\zeta\Omega_c}{1-\Omega_c^2} \tag{4.17}$$

Figure 4.1c shows the open-loop Nyquist plot for displacement feedback control. It should be noted from Figure 4.1c that the critical frequency for displacement feedback control is the first frequency at which Nyquist plot crosses the real axis. This is in contrast to the acceleration and velocity feedback control systems discussed in sections 4.2.1 and 4.2.2. A graphical solution to equation (4.17) is shown in Figure 4.2a with a non-dimensional time-delay of 0.1 and for various damping ratios.

Figure 4.3c shows this critical frequency (first crossing frequency) as a function of time-delay and damping ratio. It can be seen that the critical frequency is influenced much more by the time-delay than the damping ratio. In addition it is also evident that the critical frequency is much lower than for acceleration and velocity feedback control discussed previously. Hence for a small time-delay equation (4.17) can be approximated to,

$$\tan(2\pi\tau\Omega_c)\approx 2\pi\tau\Omega_c=-\frac{2\zeta\Omega_c}{1-\Omega_c^2} \tag{4.18}$$

From equation (4.18) the approximate critical frequency can be written as,

$$\Omega_c^2=1+\frac{\zeta}{\pi\tau} \tag{4.19}$$

Unlike acceleration and velocity feedback control this approximate critical frequency depends on both the time-delay and damping ratio. Figure 4.4c shows the numerical solutions and approximate estimations of critical frequency for damping ratios of 0.01, 0.05 and 0.1 respectively. For time-delay $0<\tau\leq 0.15$ and damping ratio $0<\zeta\leq 0.1$ the approximation given by equation (4.19) is in reasonable agreement with the numerical solutions. Substituting the approximate critical frequency given by equation (4.19) into the

real part of equation (4.16) and equating to –1 the maximum non-dimensional gain $\frac{g_d}{k}$ can be found. This gives,

$$\frac{g_{d\_\max}}{k} = \frac{\zeta}{\pi\tau} \tag{4.20}$$

Figure 4.5c shows the closed-loop performance for the displacement feedback control strategy. For comparison purposes three graphs are plotted in Figure 4.5c. They are the original system with no control applied, the system that has a non-dimensional time-delay of 0.1 with 99.9% of the corresponding maximum gain, and thirdly the system with no time-delay, but has 99.9% of the maximum gain corresponding to a non-dimensional time-delay of 0.1. It is clear that the maximum gain that can be applied with displacement feedback control is very small and hence the benefit of this system is negligible. Therefore displacement feedback control is very sensitive to time-delay.

4.2.4 Summary

It can be seen that there are many additional resonance frequencies in the system with acceleration feedback control, making this control system impractical for reasonably large time-delays in the control system. The velocity feedback control response has similar characteristics to the low frequency instability, but with the critical frequency occurring above the original resonance frequency. Finally it is clear that the maximum gain that can be applied to the displacement feedback system is very small, and hence the benefits of this system are negligible.

4.3 Low-pass filters and control actuators

As mentioned previously, low-pass filters could be present in the signal conditioning devices such as charge amplifiers to reject the unwanted signals at high frequencies. A first order model of low-pass filter is given by $\frac{1}{1+j\tau_L\omega}$ [89]. Similarly actuators, which are used to produce the control force, could also affect the stability, and can also be represented as a first order low-pass filter [33]. Thus in an active isolation system there could be up to two low-pass filters, one each from the signal conditioning equipment and the actuator. However if

either one of them is equivalent to a second order low-pass filter, then the effects can be studied by considering three first order low-pass filters. Thus, an investigation of acceleration, velocity and displacement feedback control systems with up to three low-pass filters, is carried out. This is described in the subsequent sections.

4.3.1 Effect of low-pass filters on acceleration feedback control

With a low-pass filter incorporated the open-loop frequency response function for a SDOF system given in equation (3.9) can be extended to give,

$$G(j\Omega)H(j\Omega)=\left(\frac{g_a}{m}\right)\frac{-\Omega^2}{\left(1-\Omega^2+j2\zeta\Omega\right)}\frac{1}{\left(1+j\beta\Omega\right)} \tag{4.21}$$

where β is the ratio of the natural frequency of the system to the corner frequency of the low-pass filter. Equation (4.21) can be written in terms of its real and imaginary parts as,

$$G(j\Omega)H(j\Omega)=\frac{g_a}{m}\Omega^2\left(\frac{1-\Omega^2-2\zeta\beta\Omega^2}{\left(\left(1-\Omega^2\right)^2+\left(2\zeta\Omega\right)^2\right)\left(1+\beta^2\Omega^2\right)}-j\frac{\Omega\left(2\zeta+\beta\left(1-\Omega^2\right)\right)}{\left(\left(1-\Omega^2\right)^2+\left(2\zeta\Omega\right)^2\right)\left(1+\beta^2\Omega^2\right)}\right) \tag{4.22}$$

Adopting a similar procedure as that described in Chapter 3, when the imaginary part is set to zero the critical frequencies are found to be $\Omega_c=0$ or $\Omega_c^2=1+\frac{2\zeta}{\beta}$ and the corresponding real parts are given by ,

$$\mathrm{Re}\left\{G(j\Omega_c)H(j\Omega_c)\right\}=0 \text{ and } \mathrm{Re}\left\{G(j\Omega_c)H(j\Omega_c)\right\}=\frac{g_a}{m}\frac{2\zeta+\beta}{2\zeta\left(2\beta\zeta+\beta^2+1\right)}.$$

Since the real parts are either zero or positive, the system with a single low-pass filter is *unconditionally stable.*

Maximum gains and corresponding critical frequencies for up-to three low-pass filters are given in Table 4.1 and 4.2 respectively. Figure 4.6a shows how the increasing number of low-pass filters affects the stability of acceleration feedback control system. It can be seen that that acceleration feedback control system becomes unstable with three first order low-pass filters incorporated. The closed-loop performance given in Figure 4.7a shows that with a low-pass filter incorporated, an additional peak appears at a higher frequency. Thus, low-pass filter in the system gives poor performance than the ideal system.

4.3.2 Effect of the low-pass filter on velocity feedback control

With a low-pass filter incorporated the open-loop frequency response function for a SDOF system for velocity feedback control given in equation (3.11) becomes,

$$G(j\Omega)H(j\Omega)=\left(\frac{g_v}{c}\right)\frac{j2\zeta\Omega}{\left(1-\Omega^2+j2\zeta\Omega\right)}\frac{1}{\left(1+j\beta\Omega\right)} \tag{4.23}$$

Equation (4.23) can be written in terms of its real and imaginary parts as,

$$G(j\Omega)H(j\Omega)=\frac{g_v}{c}2\zeta\Omega\left(\frac{\Omega\left(\beta\left(1-\Omega^2\right)+2\zeta\right)}{\left(\left(1-\Omega^2\right)^2+\left(2\zeta\Omega\right)^2\right)\left(1+\beta^2\Omega^2\right)}-j\frac{\left(2\zeta\beta\Omega^2+\left(\Omega^2-1\right)\right)}{\left(\left(1-\Omega^2\right)^2+\left(2\zeta\Omega\right)^2\right)\left(1+\beta^2\Omega^2\right)}\right) \tag{4.24}$$

Applying the Nyquist criterion, when the imaginary part is zero, the critical frequencies are found to be $\Omega_c=0$ or $\Omega_c^2=\frac{1}{1+2\zeta\beta}$ and the corresponding real parts are given by $\mathrm{Re}\{G(j\Omega_c)H(j\Omega_c)\}=0$ or $\mathrm{Re}\{G(j\Omega_c)H(j\Omega_c)\}=\frac{g_v}{c}\frac{1+2\beta\zeta}{\left(1+2\beta\zeta+\beta^2\right)}$. Since the real parts are either zero or positive the velocity feedback control system with a single low-pass filter is *unconditionally stable.*

The maximum gains and corresponding critical frequencies for up-to three low-pass filters are given in Tables 4.1 and 4.2 respectively. Figure 4.6b shows how the increasing number of low-pass filters affects the stability of the velocity feedback control system. It can be seen that the velocity feedback control system becomes unstable with two first order low-pass filters. The closed-loop performance given in Figure 4.7b shows that with a low-pass filter incorporated, a peak appears at a higher frequency. Thus, low-pass filter in the system gives poor performance than the ideal system.

4.3.3 Effect of the low-pass filter on displacement feedback control

With a low-pass filter, the open-loop frequency response function for a SDOF system for displacement feedback control given in equation (3.13) becomes,

$$G(j\Omega)H(j\Omega)=\left(\frac{g_d}{k}\right)\frac{-\Omega^2}{\left(1-\Omega^2+j2\zeta\Omega\right)}\frac{1}{\left(1+j\beta\Omega\right)} \tag{4.25}$$

Equation (4.25) can be written in terms of its real and imaginary parts as,

$$G(j\Omega)H(j\Omega)=\frac{g_d}{k}\left(\frac{1-\Omega^2-2\zeta\beta\Omega^2}{\left(\left(1-\Omega^2\right)^2+\left(2\zeta\Omega\right)^2\right)\left(1+\beta^2\Omega^2\right)}-j\frac{\Omega\left(2\zeta+\beta\left(1-\Omega^2\right)\right)}{\left(\left(1-\Omega^2\right)^2+\left(2\zeta\Omega\right)^2\right)\left(1+\beta^2\Omega^2\right)}\right) \tag{4.26}$$

When the imaginary part is zero as before $\Omega_c=0$ or $\Omega_c^2=1+\frac{2\zeta}{\beta}$ and corresponding real parts are given by

$\mathrm{Re}\{G(j\Omega_c)H(j\Omega_c)\}=1$ or $\mathrm{Re}\{G(j\Omega_c)H(j\Omega_c)\}=-\frac{g_d}{k}\frac{\beta}{2\zeta\left(2\beta\zeta+\beta^2+1\right)}$. This gives,

$$\frac{g_{d\_\max}}{k}=\frac{2\zeta\left(1+2\zeta\beta+\beta^2\right)}{\beta} \tag{4.27}$$

Generally the corner frequency of the low-pass filter is very high and hence $\beta=\frac{\omega_n}{\omega_c}$ is very small. Thus for $\zeta<<1$ and $\beta<<1$ the above equation (4.27) can be simplified to give,

$$\frac{g_{d\_\max}}{k}=\frac{2\zeta}{\beta} \tag{4.28}$$

Thus the displacement feedback control system with a single low-pass filter is only conditionally stable.

The maximum gain and corresponding critical frequencies are given for up to three low-pass filters in Tables 4.1 and 4.2 respectively. Figure 4.6c shows how the increasing number of low-pass filters affects the stability of displacement feedback control system. It can be seen that displacement feedback control system becomes unstable with just one first order low-pass filter. The closed-loop performance given in Figure 4.7c shows that with a low-pass filter incorporated, a strong peak appears at a higher frequency. Thus, low-pass filter in the system gives poor performance than the ideal system.

4.3.4 Summary

Systems with an electromagnetic actuator will effectively have a low-pass filter incorporated into the system. This makes the maximum gain attainable in displacement feedback control small. Thus displacement feedback becomes less attractive compared to acceleration and velocity feedback control. Increasing the number of low-pass filter (or the order of the low-pass filter such as the one in the signal conditioning devices) makes velocity feedback control become conditionally stable rather than unconditionally stable. However the inclusion of the damping ratio in the denominator gives a large gain margin for systems with low damping. The closed-loop performance of the three strategies shows that inclusion of a low-pass filter deteriorates the closed-loop performance from ideal system.

4.4 Effect of sensor dynamics

In this section the effect of sensor dynamics on the stability of the feedback systems is considered. An accelerometer modelled as a single degree of freedom system [85] is shown in Figure 4.8. For vibration isolation systems, it is assumed that the accelerometer has a negligible effect on the system (i.e. the equipment is much heaver than the accelerometer) and hence it does not change the dynamics of the system. The equation describing the motion of the seismic mass (m_a) can be written as,

$$m_a\ddot{y}(t)=k_a\left(x(t)-y(t)\right)+c_a\left(\dot{x}(t)-\dot{y}(t)\right) \tag{4.29}$$

Substituting, $\dot{x}(t)=Ve^{j\omega t}$, $\dot{y}(t)=V_a e^{j\omega t}$, $\omega_a^2=\frac{k_a}{m_a}$ and $\zeta_a=\frac{c}{2\sqrt{k_a m_a}}$ in equation (4.29) and simplifying gives,

$$\frac{V_a}{V}=\frac{1+j2\zeta_a\Omega_a}{\left(1-\Omega_a^2+j2\zeta_a\Omega_a\right)} \tag{4.30}$$

where $\Omega_a=\frac{\omega}{\omega_a}$, which can be written as, $\Omega_a=\frac{\omega}{\omega_n}\frac{\omega_n}{\omega_a}=\frac{\Omega}{p}$, where $p=\frac{\omega_a}{\omega_n}$. From Figure 4. 9 the open-loop frequency response function of the system with accelerometer dynamics can be written as,

$$G_m(j\Omega)H(j\Omega)=G(j\Omega)\frac{1+j2\zeta_a\Omega_a}{\left(1-\Omega_a^2+j2\zeta_a\Omega_a\right)}H(j\Omega) \tag{4.31}$$

where $G_m(j\Omega)$ refers the frequency response function in the forward path of the block diagram shown in Figure 4.9 , which includes the frequency response functions of the plant and accelerometer. Substituting for $G(j\Omega)$ from Chapter 2, equation (2.12), and the appropriate $H(j\Omega)$, the open-loop frequency response functions for acceleration, velocity and displacement feedback control can be obtained.

For velocity feedback control the modified forward path frequency response function is given by (Note that in velocity feedback control, the feedback frequency response function is only a gain and hence does not alter the phase characteristics. Hence it is considered first),

$$G_m(j\Omega) = \frac{j2\zeta\Omega}{\left(1-\Omega^2+j2\zeta\Omega\right)} \times \frac{1+j2\zeta_a\Omega_a}{\left(1-\Omega_a^2+j2\zeta_a\Omega_a\right)} \tag{4.32}$$

The phase range of each function can be written as,

$\frac{\pi}{2} \geq \measuredangle\left(\frac{j2\zeta\Omega}{\left(1-\Omega^2+j2\zeta\Omega\right)}\right) \geq -\frac{\pi}{2}$ and $0 \geq \measuredangle\left(\frac{j2\zeta_a\Omega_a}{\left(1-\Omega_a^2+j2\zeta_a\Omega_a\right)}\right) \geq -\pi$. Thus the phase range of the forward path frequency response function is given by (Note that if the complex numbers are multiplied the phase is added),

$$\frac{\pi}{2} \geq \measuredangle G_m(j\Omega) \geq -\frac{3\pi}{2} \tag{4.33}$$

This phase range shows that the forward path frequency response function includes the negative real axis. The feedback frequency response function for acceleration feedback control is given by, $H(j\Omega) = j\Omega\frac{g_a}{m}\frac{1}{2\zeta}$. This adds a phase of $\frac{\pi}{2}$ to the open-loop frequency response characteristic of the velocity feedback. Thus considering equation (4.33), the phase range for acceleration feedback control is given by,

$$\pi \geq \measuredangle G_m(j\Omega)H(j\Omega) \geq -\pi \tag{4.34}$$

This suggests that the accelerometer dynamics does not cause any instability in acceleration feedback control. The feedback frequency response function for displacement feedback control is given by, $H(j\Omega) = \frac{1}{j\Omega}\frac{g_d}{k}\frac{1}{2\zeta}$. This adds a phase of $-\frac{\pi}{2}$ to the open-loop frequency response characteristic of velocity feedback. Thus considering equation (4.33), the phase range for displacement feedback control is given by,

$$0 \geq \measuredangle G_m(j\Omega)H(j\Omega) \geq -2\pi \tag{4.35}$$

This suggests that the accelerometer dynamics does affect the stability of displacement feedback control.

For systems, which have high frequency roll-off characteristics such as the single-degree-of-freedom-system considered, the effect of accelerometer dynamics would be minimal. This is because a high frequency roll-off characteristic gives the system a large gain margin provided that the natural frequency of the accelerometer is much greater than the natural frequency of the plant.

In summary, from the analysis presented above, the accelerometer causes instability in velocity and displacement feedback control systems. The acceleration feedback control system is less susceptible to instability problems due to sensor dynamics.

4.5 Multi-input-multi-output system

For a decentralised feedback control system with equal gains in each loop and identical instruments, the feedback frequency response matrix in terms of non-dimensional frequency takes the form $\mathbf{H}(j\Omega)=H(j\Omega)\mathbf{I}$. Here $H(j\Omega)$ is same as that in the single degree of freedom system considered previously. Thus, the sources of instabilities at high frequencies affect the MIMO system in a similar manner to that discussed for low frequency instabilities in Chapter 3. Hence applying the same principle to that in Chapter 3, the analysis presented for a SDOF system can be applied readily to a MIMO system provided collocated decentralised feedback control techniques are applied.

It is shown in appendix F that the MIMO system considered in Chapter 3 is unconditionally stable. Thus the eigenvalue plots of the open-loop response matrix are entirely on the right half of the Nyquist plane. This means that the phase range of eigenvalues can be written as $\frac{\pi}{2} \geq \measuredangle eig\left(\mathbf{G}(j\Omega)\right) \geq -\frac{\pi}{2}$. Considering the forward path frequency response function similar to the one given in equation (4.32), it can be shown that the forward path frequency response function for the MIMO system with velocity feedback control has a phase range $\frac{\pi}{2} \geq \measuredangle eig\left(\mathbf{G}_m(j\Omega)\right) \geq -\frac{3\pi}{2}$. This shows that the accelerometer affects the stability of a MIMO system similar to the SDOF system discussed previously. In a similar manner

described previously for the SDOF system, the argument can be extended to acceleration and displacement feedback control strategies.

4.6 Conclusions

The sources of high frequency instabilities have been investigated in this chapter. It has been shown that although the displacement feedback control strategy exhibits good low frequency stability, with time-delay and low-pass filters in the feedback loop, it exhibits poor robustness. It has also been shown that among the three strategies the acceleration feedback control system gives excellent stability characteristics. However the closed-loop performance of the acceleration feedback control system with time-delay gives poor performance. Thus, considering the high frequency stability and performance characteristics, velocity feedback control is the most attractive strategy.

Order of first order low-pass filter	Acceleration feedback	Velocity feedback	Displacement feedback
0	*Unconditionally stable*	*Unconditionally stable*	*Unconditionally stable*
1	*Unconditionally stable*	*Unconditionally stable*	$\frac{g_{d\_\max}}{k} \approx \frac{2\zeta}{\beta}$
2	*Unconditionally stable*	$\frac{g_{v\_\max}}{c} \approx \frac{9}{16\zeta\beta}$	$\frac{g_{d\_\max}}{k} \approx \frac{\zeta}{\beta}$
3	$\frac{g_{a\_\max}}{m} \approx 8$	$\frac{g_{v\_\max}}{c} \approx \frac{4}{9\zeta\beta}$	$\frac{g_{d\_\max}}{k} \approx \frac{2\zeta}{3\beta}$

Table 4. 1. Non-dimensional maximum gains for different numbers of low-pass filters $\beta << 1$ & $\zeta << 1$

Order of first order low-pass filter	Acceleration feedback	Velocity feedback	Displacement feedback
0	*Unconditionally stable*	*Unconditionally stable*	*Unconditionally stable*
1	*Unconditionally stable*	*Unconditionally stable*	$\Omega_c = \sqrt{1+\frac{2\zeta}{\beta}}$
2	*Unconditionally stable*	$\Omega_c \approx \frac{1}{\sqrt{2}\beta}$	$\Omega_c = \sqrt{1+\frac{\zeta}{\beta}}$
3	$\Omega_c \approx \frac{\sqrt{3}}{\beta}$	$\Omega_c \approx \frac{1}{\sqrt{3}\beta}$	$\Omega_c = \sqrt{1+\frac{2\zeta}{3\beta}}$

Table 4.2. Non-dimensional critical frequencies for different numbers of low-pass filters $\beta << 1$ & $\zeta << 1$

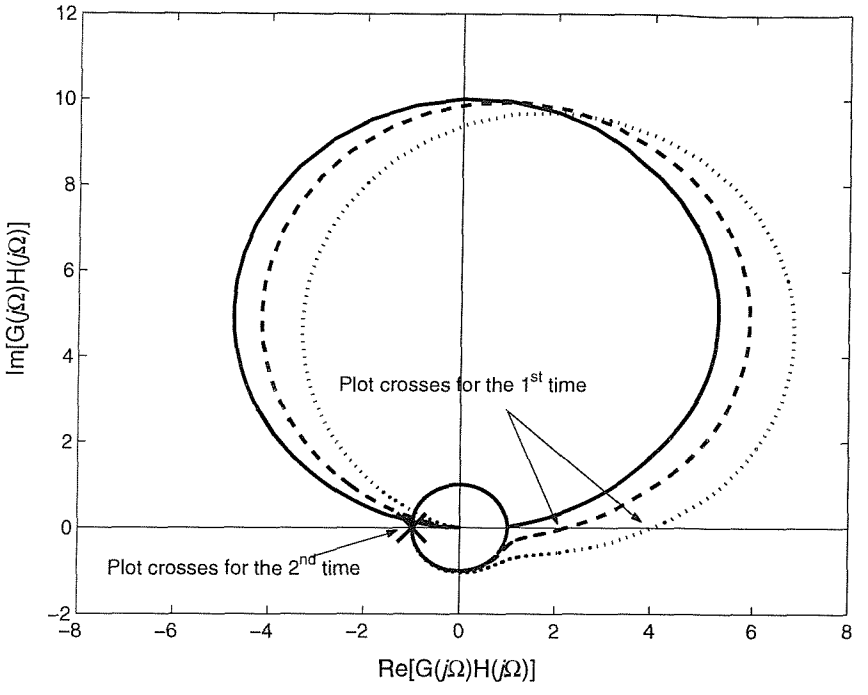

(a) *Acceleration feedback control* $\frac{g_a}{m}=1$ *and* $\zeta=0.05$. *No time- delay:* _____, *Non-dimensional time- delay* 0.05*:* --------, *Non-dimensional time- delay* 0.1*:* ..... *and X:* (-1,0) *point.*

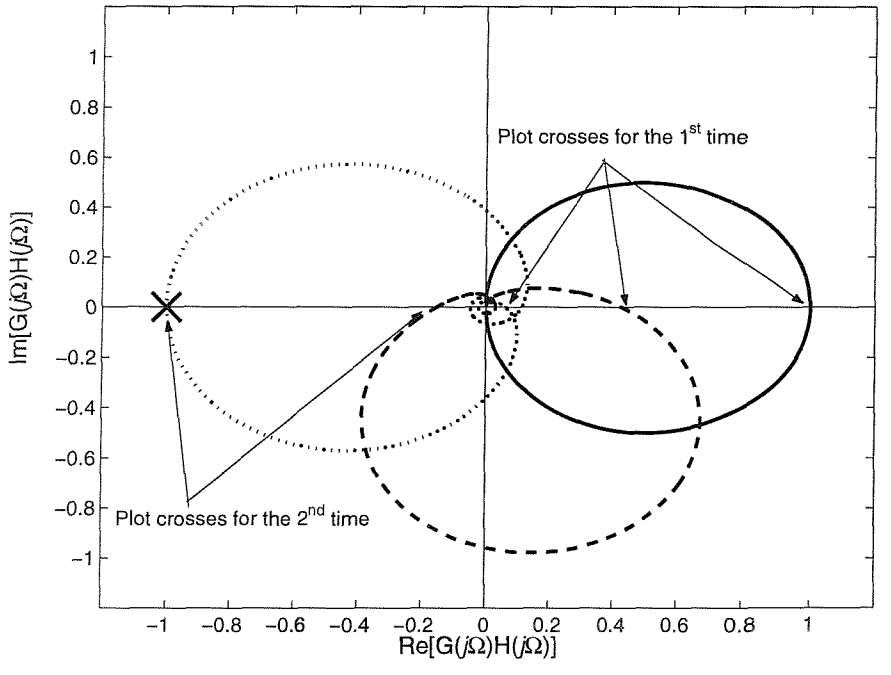

(b) Velocity feedback control $\frac{g_v}{c}=1$ *and* $\zeta=0.05$ *No time- delay:* _____, *Non-dimensional time-delay* 0.1*:* --------, *Non-dimensional time-delay* 0.2*:*.....*and X:* (-1,0) *point*

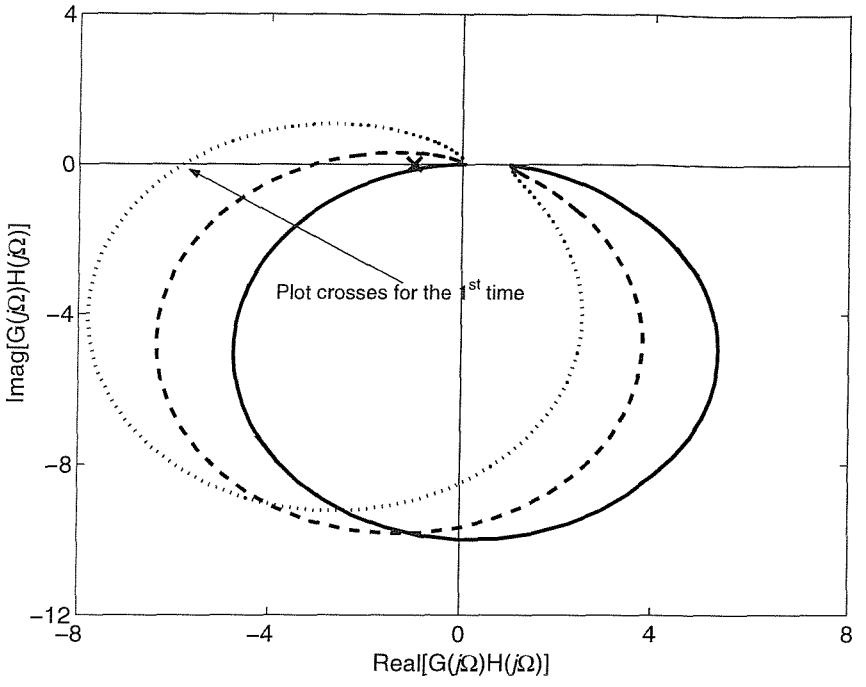

(c) Displacement feedback control $\frac{g_d}{k}=1$ *and* $\zeta=0.05$ *No time-delay:* _____, *Non-dimensional time-delay* 0.05*:* --------, *Non-dimensional time-delay* 0.1*:*..... *and X:* (-1,0) *point*

Figure 4.1 the Nyquist plot of the open-loop frequency response functions for different time-delay with acceleration, velocity and displacement feedback control.

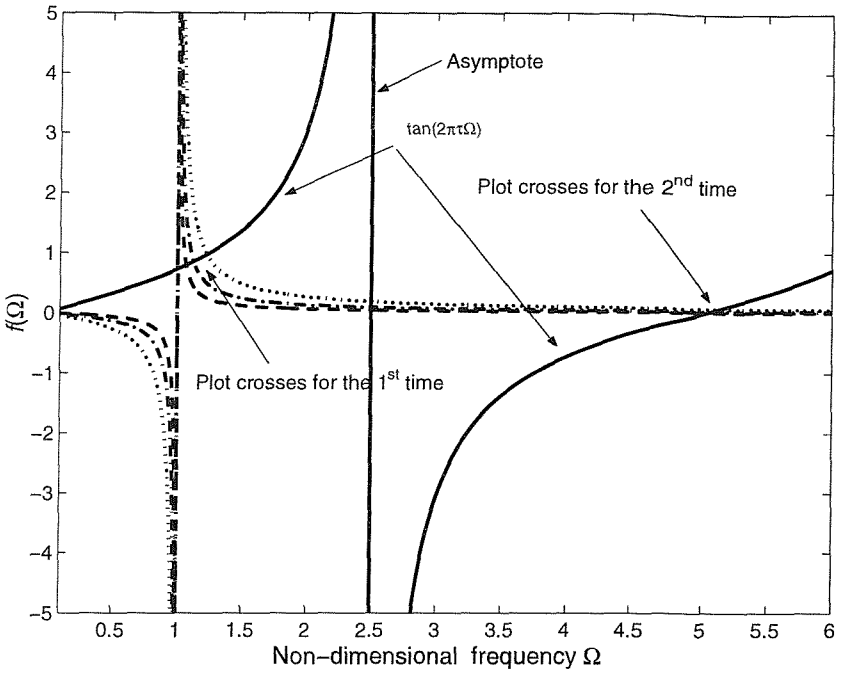

(a) Acceleration and displacement feedback control

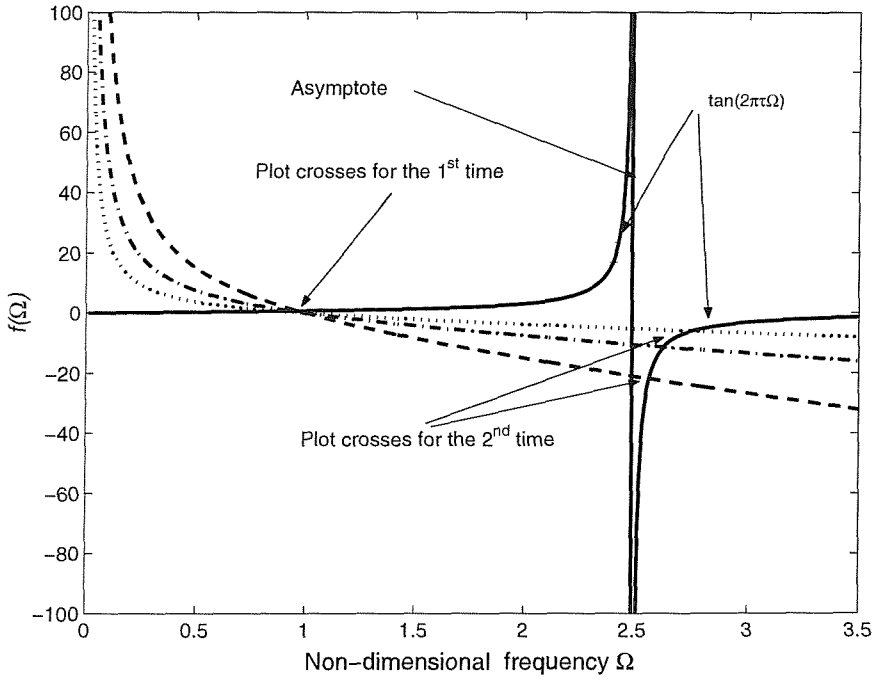

(b) Velocity feedback control

Figure 4.2 Graphical representations of the solutions for the equation of critical frequency (non-dimensional time-delay $\tau = 0.1$*)* $\tan(2\pi\tau\Omega)$*: _____, damping ratio 0.05: ---------, damping ratio 0.1: -.-.-.-.-.-., damping ratio:.....*

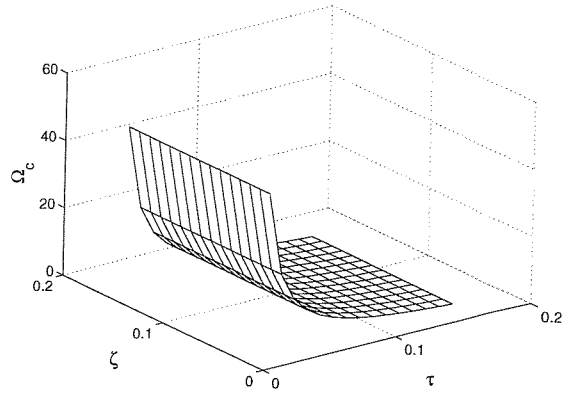

(a) Acceleration feedback control

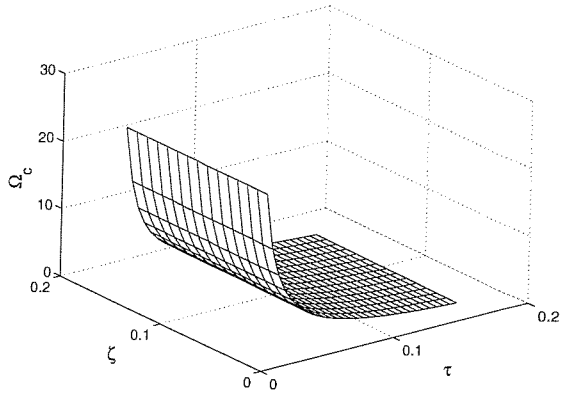

(b) Velocity feedback control

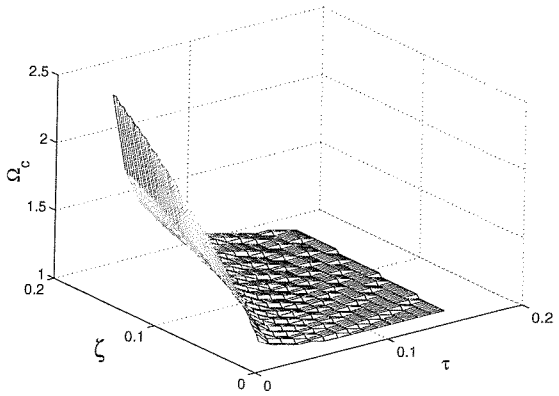

(c) Displacement feedback control

Figure 4.3 Critical frequencies as a function of non-dimensional time-delay and damping ratio.

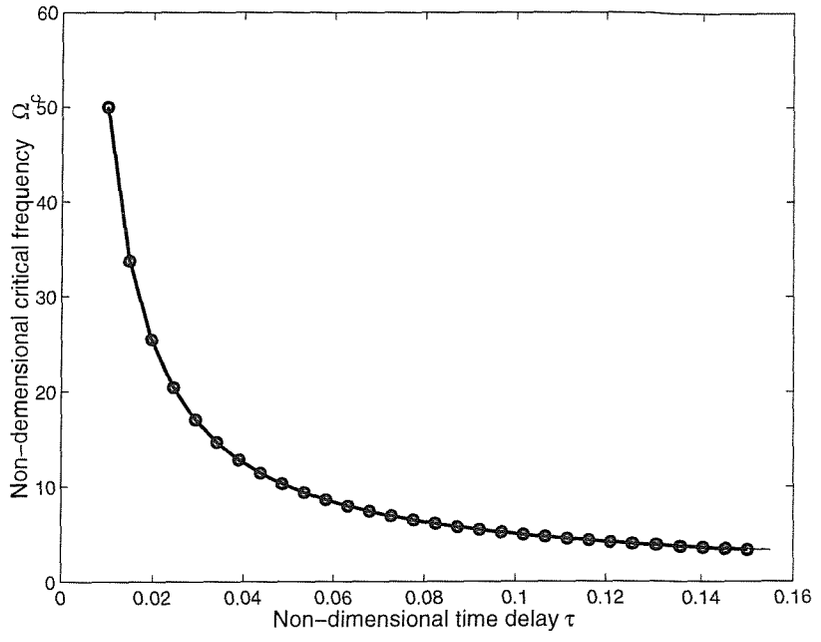

(a) Acceleration feedback control. Damping ratio 0.01:_____, *Damping ratio* 0.05:----------, *Damping ratio* 0.1:....., $\Omega_c = 1/2\tau$: —⊖—

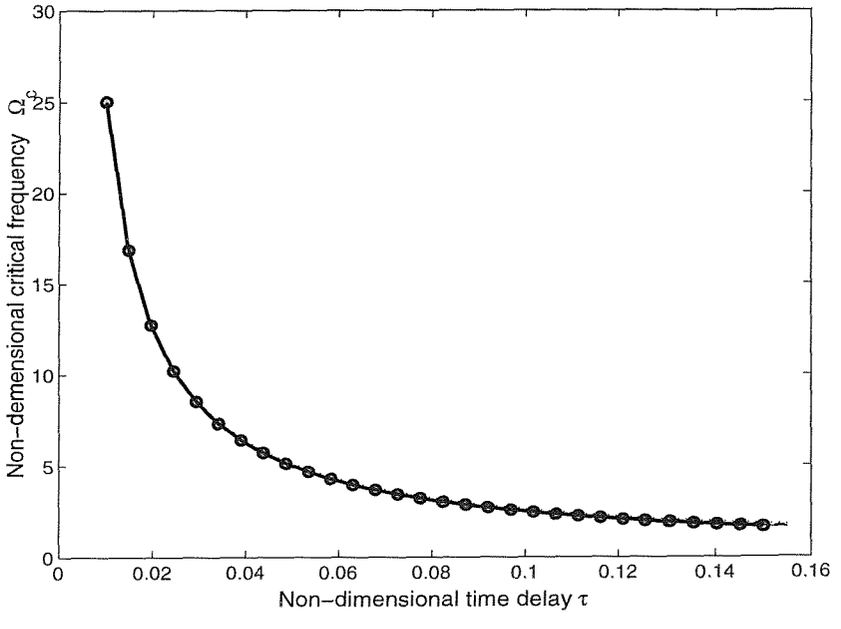

(b) Velocity feedback control. Damping ratio 0.01:_____, *Damping ratio* 0.05:----------, *Damping ratio* 0.1:....., $\Omega_c = 1/4\tau$: —⊖—

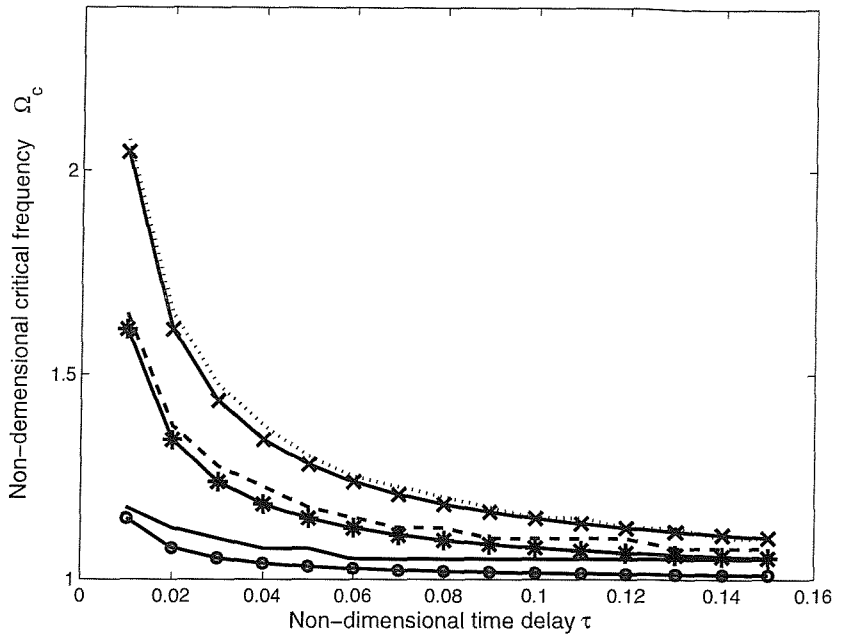

(c)Displacement feedback control Damping ratio 0.01:_____, *Damping ratio* 0.05:----- , *Damping ratio* 0.1:..... $\Omega_c = \sqrt{1+\zeta/\pi\tau}$ & ζ=0.01 —⊖—

$\Omega_c = \sqrt{1+\zeta/\pi\tau}$ & ζ=0.05 —✳— $\Omega_c = \sqrt{1+\zeta/\pi\tau}$ & ζ=0.1 —×—

Figure 4.4 Critical frequencies as a function of time-delay for selected damping ratios (with approximate models)

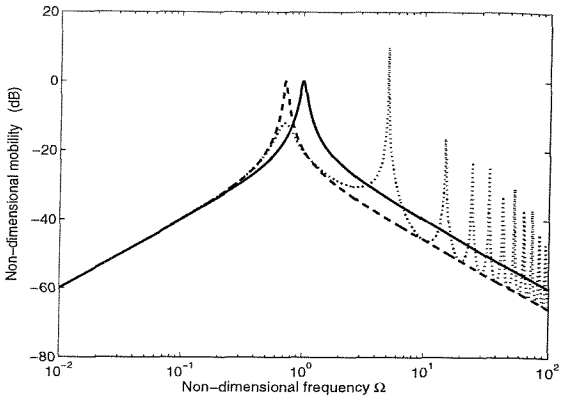

(a) Acceleration feedback control $\left(\frac{g_{a\_\max}}{m} = 1 - 4\tau^2\right)$

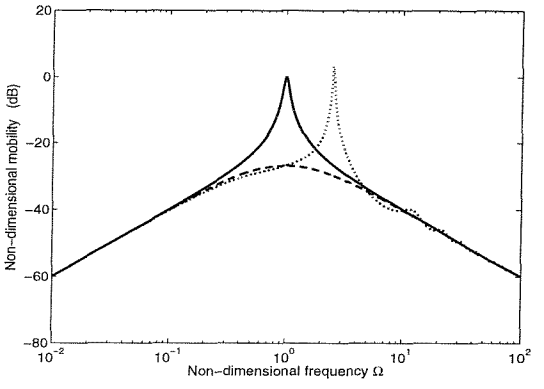

(b) Velocity feedback control $\left(\frac{g_{v\_\max}}{c} = \frac{1}{8\tau\zeta}\right)$

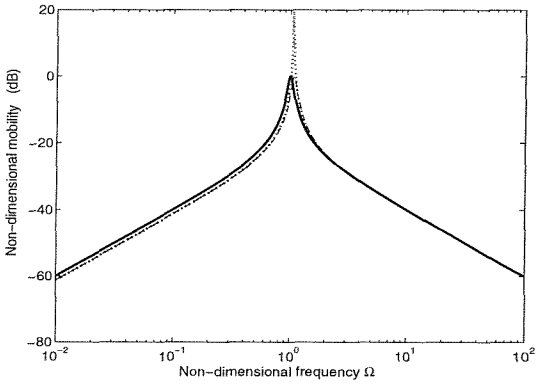

(c) Displacement feedback control $\left(\frac{g_{d\_\max}}{k} = \frac{\zeta}{\pi\tau}\right)$

Figure 4.5 Closed-loop response - effect of time-delay, $\zeta = 0.05$ *No control:*_____, *ideal system:----------, System with 99.9% of the respective maximum gain and delay* $\tau = 0.1$*:.....*

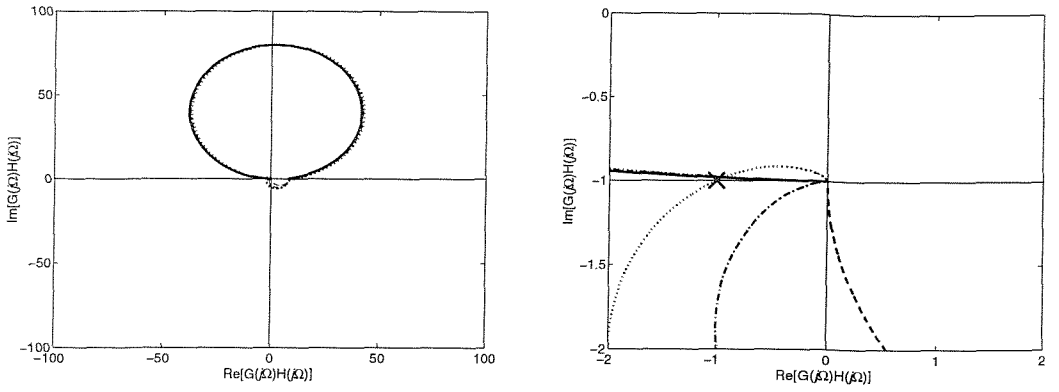

(a) Acceleration feedback control (also given – zoomed in the vicinity of the origin)

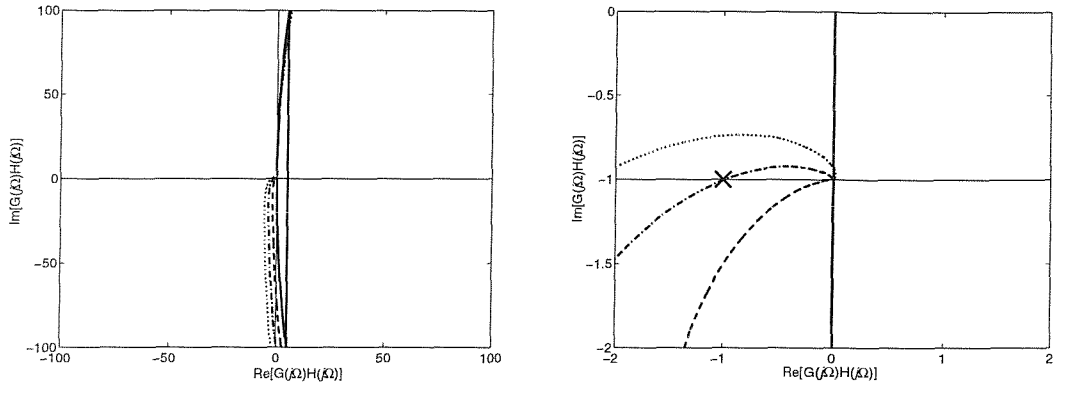

(b) Velocity feedback control (also given – zoomed in the vicinity of the origin)

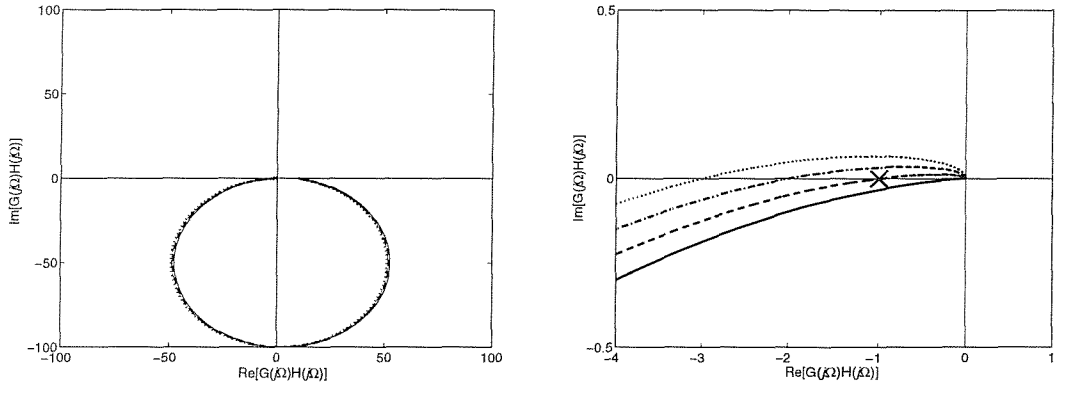

(a) Displacement feedback control (also given – zoomed in the vicinity of the origin)

Figure 4.6 Open-loop frequency response function with various number of first order low-pass filter components $(\beta = 0.01)$*; No low-pass filter:*_____*, one low-pass filter:*------*, two low-pass filters:*-.-.-.-.-.-.-.-.-.*, three low-pass filters:*.....

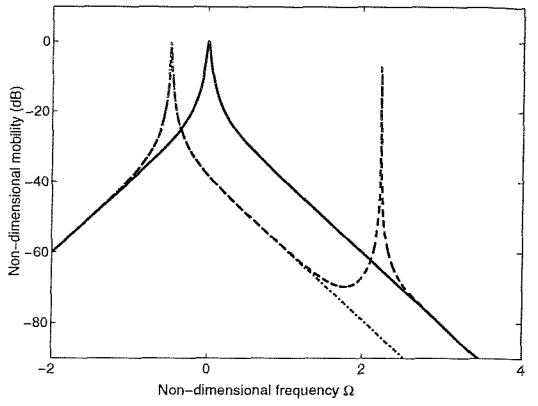

(a) Acceleration feedback control system with three low-pass filters

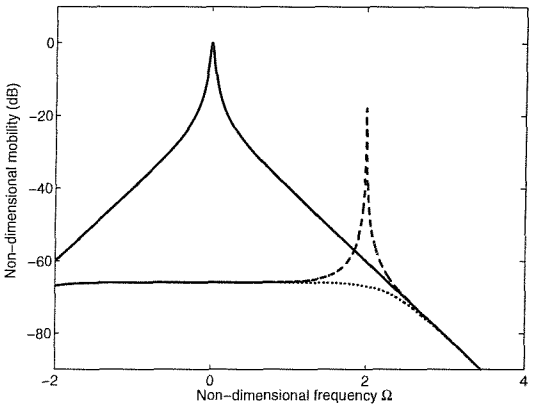

(b) Velocity feedback control system with two low-pass filters

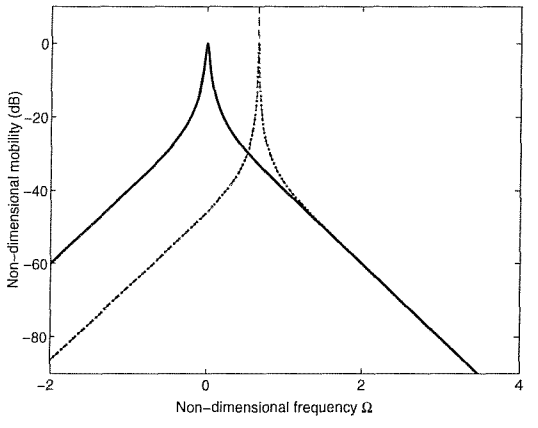

(c) Displacement feedback control system with one low-pass filter

Figure 4.7 Closed-loop frequency response for acceleration, velocity and displacement feedback control with various number of low-pass filters; no control:_____, realistic system with lo- pass filters and gains of 99.9% of the respective maximum:----------, ideal system with 99.9% of the realistic maximum gain:.....

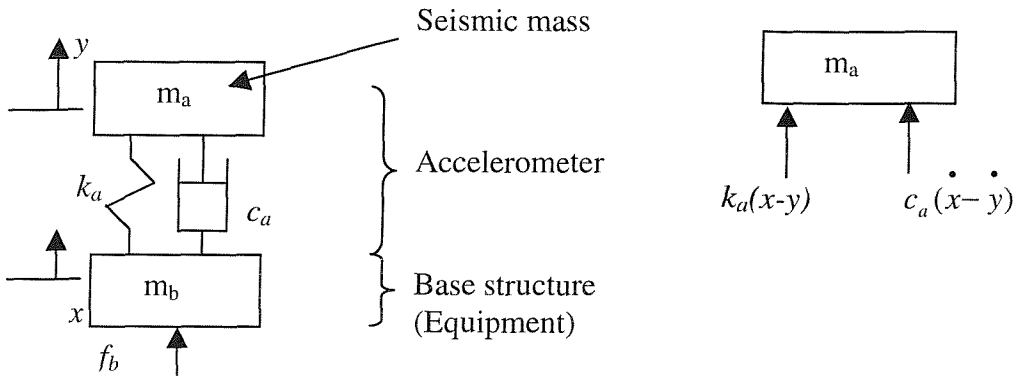

(a) Schematic diagram *(b) Free-body diagram*

Figure 4.8 Accelerometer model

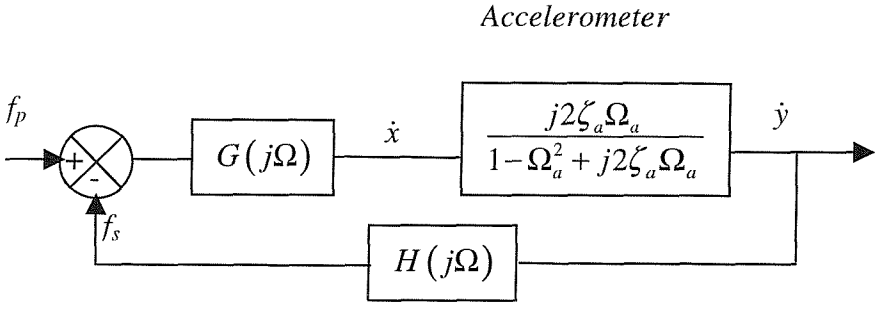

Figure 4.9 Block diagram representation of the system with accelerometer

Chapter 5

Performance of a two-channel feedback control system with the failure of a single channel

5.1 Introduction

The effects on the stability and performance of a feedback control system of signal conditioning devices, actuator and sensor dynamics at low and high frequencies were discussed in Chapters 3 and 4 respectively. Velocity feedback control was found to be more attractive as it is more robust to low and high frequency instabilities. However the stability of a perfectly working system is not the only concern when it comes to robustness. Other considerations include sensor and actuator failures, uncertainties (disturbance as well as model uncertainties), etc. In this chapter the effect of losing control of a channel (sensor or actuator failure) is considered. An analytical study of a two-channel feedback control system is conducted and supported by some experimental work.

5.2 Problem formulation

The same two-mount system considered in Chapter 2 is used for the analysis and subsequent experimental work. A description of the system is given in this section for convenience. Consider a two-degree of freedom system (2DOF) modelled as a lumped mass-spring-damper system with two-channel decentralised feedback control applied as shown in Figure 2.3a. Two passive mounts with equal stiffness k and damping coefficient c support a rigid plate (representing some equipment) of mass m_p and length l_p (the distance between the mounts is l). Two shakers are also installed directly on top of the mounts, and each produces a control force between the base and the rigid plate. Small masses can be lumped on top of the shakers so that the mass centre can be moved from the centre of the plate. The combined mass of the shaker at mount1 and the mass lumped on top of that shaker is m_1, and similarly

the total mass at mount2 is m_2 as shown in Figure 2.3a. The masses are chosen such that $m_m = m_1 + m_2$. The total mass of the system is $m = m_m + m_p$ and is assumed to be unchanged throughout the analysis in this chapter. It is also assumed that the masses m_1 and m_2 are point masses. Thus the system inertia properties can be described by its total mass m and moment of inertia J about its mass centre. If the distance between mount1 and the mass centre is rl, then the distance between mount2 and the mass centre is consequently $r(1-l)$, where $r = \dfrac{2m_2 + m_p}{2\left(m_p + m_m\right)}$ (Derivation is given in appendix C).

The two-control forces f_{c1} and f_{c2} act between the plate and the base in parallel with the passive mounts. The control system is a decentralised direct negative velocity feedback control such that the signal measured by each sensor mounted on the plate is used to produce a control force at that mount location. These forces are produced via the controllers, which have equal gain and are proportional to velocities at the mount locations. The system, where both controllers are working and set to produce control forces proportional to the corresponding velocities, is referred to as the perfectly working system. The system where one of the controllers, actuators, sensors or any other component in a single feedback loop fails to work is referred to as the defective system or system with failure. In this chapter the performance of this system is investigated. As before, two situations are considered, namely the two-mount system (a) on a moving inelastic-base and (b) on a flexible base. For simplicity only ideal situations are considered i.e. the electrical instrumentation is considered to be perfect with no unintentional phase shift, if it is working.

5.3 Two-mount system on a moving inelastic-base

Figure 5.1 shows the impedance representation of the physical system shown in Figure 2.1. From equation (2.24) the vector of equipment velocities at the mount location is given by,

$$\mathbf{v}_e = \left[\mathbf{I} + \mathbf{G}(j\omega)\mathbf{H}(j\omega)\right]^{-1} \mathbf{G}(j\omega)\mathbf{Z}_m \mathbf{v}_b \qquad (5.1)$$

where, $\mathbf{G}(j\omega)=[\mathbf{Z}_e+\mathbf{Z}_m]^{-1}$, $\mathbf{Z}_m=\begin{bmatrix} Z_m & 0 \\ 0 & Z_m \end{bmatrix}$, $Z_m=\frac{k}{j\omega}+c$, (From Appendix C)

$\mathbf{Z}_e = j\omega\begin{bmatrix} m(1-r)^2+\frac{J}{l^2} & mr(1-r)-\frac{J}{l^2} \\ mr(1-r)-\frac{J}{l^2} & mr^2+\frac{J}{l^2} \end{bmatrix}$, $\mathbf{H}(j\omega)=c\begin{bmatrix} \frac{g}{c} & 0 \\ 0 & \frac{g}{c} \end{bmatrix}=c\begin{bmatrix} g_{nv} & 0 \\ 0 & g_{nv} \end{bmatrix}$ and g_{nv} is non-dimensional gain.

The translational and rotational velocities at the mass centre of the plate are given by v and $\dot{\theta}$ as described in appendix C. The velocity vector at the mass centre is $\mathbf{a}=\begin{bmatrix} v \\ l\dot{\theta} \end{bmatrix}$ and $\mathbf{Q}$ is the transformation matrix, which transforms the velocity vector at the mount locations to the velocity vector at the mass centre. The elements of $\mathbf{Q}$ are given in appendix C. The velocity vector at the mount location can be related to the velocity vector at the mass centre by equation (2.26b). Combining equations (5.1) and (2.26b) and substituting $\mathbf{v}_b=[1 \quad 1]^T v_b$ the mass centre velocity vector can be written as,

$$\frac{\mathbf{a}}{v_b}=\mathbf{Q}^{-1}\left[\mathbf{I}+\mathbf{G}(j\omega)\mathbf{H}(j\omega)\right]^{-1}\mathbf{G}(j\omega)\mathbf{Z}_m[1 \quad 1]^T \qquad (5.2)$$

Equation (5.2) gives the mass centre velocity vector **a** when both the active mounts are working. When one of the active mounts fails (mount 2 for example), the control force produced at that mount becomes zero, which gives $\mathbf{H}_f(j\omega)=c\begin{bmatrix} g_{nv} & 0 \\ 0 & 0 \end{bmatrix}$. By substituting $\mathbf{H}_f(j\omega)$ into equation (5.2) the mass centre velocity vector corresponding to the system with single channel failure can be found.

As discussed in chapter 2 the total kinetic energy of the equipment is used as the performance measure. In addition the change in the total kinetic energy is also considered as an overall performance measure, which is used to judge the effectiveness of the control system over the frequency bandwidth considered (e.g. $0 \le freq \le 250$ Hz). The first performance measure can be used to judge the performance of an active isolation system at troublesome frequencies, while the other is used to judge the system over a frequency band.

From equations (2.27) and (2.28) the total kinetic energy is given by,

$$E_k = \frac{1}{2}\mathbf{a}^{\mathrm{H}}\mathbf{J}\mathbf{a} = \frac{1}{2}\left(m|v|^2 + J|l\dot{\theta}|^2\right) \tag{5.3}$$

Note that J is the moment of inertia of the equipment and attached masses about the mass centre of the system and m is the total mass of the system. The moment of inertia is derived in appendix C and is given by,

$$J = J_{pg} + J_m \tag{5.4}$$

where, $J_{pg} = \frac{m_p l_p^2}{12} + m_p\left(\frac{(1-2r)l}{2}\right)^2$, $J_m = m_1 r^2 l^2 + m_2(1-r)^2 l^2$.

In the system with a single channel failure (failure in the active part of mount2), if the gain of the working mount is increased to a sufficiently large value (say to infinity), then the corresponding mount can be considered to be a pinned support. The system with zero gain (ie there are only passive mounts) and the system with a pinned support can be considered limiting cases of performance of the system with a single channel failure. Figure 5.2 shows the later case. The kinetic energy of this system is given by,

$$E_f = \frac{1}{2}J_{pin}\dot{\theta}^2 \tag{5.5}$$

where $J_{pin} = \frac{m_p l_p^2}{12} + m_p\left(\frac{l}{2}\right)^2 + m_2 l^2$ (applying the parallel axis theorem to the plate and the moment of inertia of mass m_2 about the pinned end) Considering the dynamic moment balance about the pinned mount (i.e. Mount1) gives,

$$J_{pin}\ddot{\theta}(t) + c\left(l\dot{\theta}(t) - \dot{x}_b(t)\right)l + k\left(l\theta(t) - x_b(t)\right)l = 0 \tag{5.6}$$

where $x_b(t)$ is the displacement of the base at mount2. Assuming simple harmonic motion equation (5.6) can be simplified to give,

$$\frac{\dot{\theta}}{v_b} = \frac{kl + j\omega cl}{kl^2 - J_{pin}\omega^2 + j\omega cl^2} \tag{5.7}$$

where it can be seen that the resulting system has a resonance frequency at $f_{np} = \frac{1}{2\pi}\sqrt{\frac{kl^2}{J_{pin}}}$.

In the following section simulations are presented on a practical system and experimentally validated in the subsequent section.

5.3.1 Simulations

In this section simulations performed on a two-mount system set on a moving inelastic-base are presented. The performance measure used is total kinetic energy calculated using closed-loop velocity per unit base velocity as given in equation (5.3). The properties of the system considered for simulations and subsequent experiments are given in Table 5.1.
The simulations are done for the following purposes,

1. To compare the performance of a system with single channel failure with the corresponding perfectly working system.
2. To study the relative importance of the working actuators in a two-mount system, where the system is not necessarily symmetric.

Three cases of differing mass centre of the system shown in Figure 2.3a are considered, which are the mass centre (a) at the geometric centre of the equipment (i.e. mass centre at $0.5l$), (b) at $0.404l$ from left hand end of the mount (i.e. from mount 1 in Figure 2.1) and (c) at $0.596l$ from left hand end of the mount. These mass centres are chosen for convenience. Although under perfectly working conditions, both $0.404l$ and $0.596l$ mass centre cases give the same behaviour they are helpful in the investigation of the relative importance of working actuator when one of them fails. In addition a general system could be either symmetric or asymmetric, thus the three cases considered cover a general system. Both a perfectly working system and a system with a single channel failure are compared. The total kinetic energy plots for all three differing mass centre cases are given in Figure 5.3 for both perfectly working and single channel failure conditions. For convenience, simulations are performed for non-dimensional gains 0, 20, 30 and 50. The total kinetic energy can be considered as the sum of kinetic energies of translational motion and rotational motion at mass centre.

In appendix I the kinetic energy plots for translational and rotational motion at the mass centre are given. For the symmetric system (i.e. mass centre is at $0.5l$), it should be noted that only translational motion is excited at the mass centre and hence the total kinetic energy is equal to the kinetic energy in translational motion at the mass centre (Figure I1a in appendix I). However when the system is non-symmetric both translational and rotational motion are excited at the mass centre (Figures I1c and I1d in appendix I).

Only one peak can be seen for the symmetric system i.e. mass centre - $0.5l$ (Figure 5.3a) and two peaks can be seen for asymmetric system i.e. mass centre - $0.404l$ or $0.596l$ (Figure 5.3b or 5.3c). Figures 5.3a, and 5.3b (or 5.3c) show that the active part of the mounts effectively isolates the system as the gain is increased. The magnitudes of the peaks are reduced because of the 'skyhook' damping effect in velocity feedback control [6,29]. Figures 5.3a and 5.3b (or 5.3c) show that the system is controllable at both resonance peaks irrespective of the position of the mass centre.

Figures 5.3d, 5.3e and 5.3f show the total kinetic energy of the system when the active part of mount2 has failed for differing mass centre cases $0.5l$, $0.404l$ and $0.596l$ respectively. In a symmetric system when one of the active channels fails, it becomes asymmetric and hence rotational motion also presents [Figure I1c - Appendix I, it should be noted that there is no line corresponding to zero gain in Figure I1c]. In these systems (i.e. with failure), as the gain corresponding to the working active mount is increased, the equipment becomes virtually pinned at this position. Figures 5.3d, 5.3e and 5.3f also show the infinite gain cases (or pinned cases). The passive system (zero gain in both channels), and pinned system (i.e. infinite gain) can be considered as the limiting cases of performance measure for a system with single channel failure. It can be noted from Figures 5.3d, 5.3e and 5.3f that between these limiting cases only a small reduction in the peak response is achievable.

It is interesting to note from Figures 5.3e and 5.3f that in an asymmetric system with failure, as the gain is increased there is a considerable reduction in one of the peaks while the other peak largely remains unaffected. These two figures show that as the gain is increased the system changes from a 2DOF system to a SDOF system. It should be noted that when the mass centre is closer to the working mount it is the first peak that is controlled while it is the second peak when the mass centre is further away from working mount. When the system is transformed from a 2DOF system to a SDOF system, the translational movement at the working mount (i.e. mount1 in this case) is gradually being reduced. When the mass centre is closer to the working mount this has a considerable influence in the heave mode, while it has less influence when it is further away from the working mount.

The uncontrollable mode is determined by the SDOF system whose resonance frequency is given by $f_{np} = \frac{1}{2\pi}\sqrt{\frac{kl^2}{J_{pin}}}$, i.e. when the system changes from a 2DOF to SDOF the uncontrollable mode is the natural frequency closer to the pinned SDOF mode.

It can be seen from Figure 5.3 that when both active mounts are working the system effectively controls both peaks and loses control over a peak when one of the channels fail. In addition, the common feature in Figures 5.3d, 5.3e and 5.3f is that as one of the loops fails the reduction in peak kinetic energy falls considerably even in the peak that is controlled. Systems with very large gain (a non-dimensional gain of 5000 is used) is also plotted in Figures 5.3d, 5.3e and 5.3f.

Figure 5.4 shows the change in total kinetic energy in a given frequency band as a function of gain. The frequency band considered is $0 \leq freq \leq 250\text{Hz}$, where *freq* denotes the frequency. Three cases with mass centres at $0.5l$, $0.404l$ and $0.596l$ are shown in Figures 5.4(i), 5.4(ii) and 5.4(iii) respectively. In each case both perfectly working and single channel failure cases are shown. In the perfectly working system, it can be seen that as the overall performance (Figures 5.4(i)a, 5.4(ii)a and 5.4(iii)a) of the system continues to improve under active control. In the system with single channel failure, this improvement in performance is very poor as seen in Figures 5.4(i)b, 5.4(ii)b and 5.4(iii)b. It can be seen that as the gain is increased the kinetic energy reduces until a certain gain is reached. This is because as the gain is increased the system changes from a 2DOF system to a SDOF system and the performance that can be achieved between these limiting cases is poor as discussed previously. The initial reduction in the change in total kinetic energy of the system with failure is attributed to the reduction in one of the peaks in total kinetic energy as discussed previously.

In Figures 5.4(i)b, 5.4(ii)b and 5.4(iii)b the change in translational and rotational kinetic energies are also shown together with the total kinetic energy. It can be seen that while translational kinetic energy reduces, the rotational kinetic energy increase. This is because as, the failure occurs the system becomes more asymmetric where rotational motion becomes dominant (Also refer Figures I1c, I2e, I3e in Appendix I).

In summary, the simulations carried out in this section reveal two things, which are (a) when one of the active mounts fails, the overall performance of the system degrades and (b) this does not improve even if the gain is increased to infinity in the working active mount. In addition, when the gain is increased from zero to infinity the system changes from a 2DOF system to a SDOF system, meaning that while one of the peaks is effectively controlled the

other peak remains largely unaffected. Some experiments were carried out to support these findings and are described in the next section.

5.3.2 Experiments

Figure 2.13 shows a schematic diagram of the experimental set-up of the active isolation system on a moving inelastic base. The decentralised control arrangements are also shown in Figure 2.13. Two accelerometers (B&K type 4375) were attached on the top surface of the equipment plate close to the centre of each mount location. Measured acceleration signals from the accelerometers were integrated and conditioned to give velocity signals by charge amplifiers (B&K type 2635). The output of each of the charge amplifiers was fed into a two-channel power amplifier (type V200 Mos-Fet) and to a Hewlett Packard (HP) analyser for data collection (velocities v_{e1} and v_{e2} mentioned in section 5.3). The power amplifier outputs were fedback into the corresponding control shakers to produce the necessary control forces. Accelerometer signals were fed back to the control shakers on the same side as the accelerometer, and hence decentralised feedback control was achieved. A 180° phase change at the output of the power amplifier was introduced so that negative feedback control was applied to the system.

An accelerometer was attached on the moving inelastic base between the mounts. This signal was also converted into velocity signal by means of a charge amplifier and was used as a reference signal to the analyser (velocity v_b mentioned section 5.3).

A large rigid plate attached to a large shaker was considered in the experiment as the moving inelastic base. A two-mount system designed by Gardonio [4] was used for the experimental work. This isolation system on a rigid plate attached to a shaker is shown in Figure 2.12. The large shaker was excited by a broadband random signal from the analyzer (Not shown in Figure 2.13) and thus the motion of the inelastic base was achieved. A list of the instruments used in the experimental work is given in Table 2.3.

The measurements give the velocities at the mounts with reference to the base velocity $\left(\text{i.e. } \frac{\mathbf{v}_e}{v_b}\right)$. Applying equation (2.26b), the corresponding mass centre velocities can be found. These mass centre velocities and equation (5.3) can be used to calculate the measured total kinetic energy. The values of m and J as well as the matrix $\mathbf{Q}$ were the same as those

used in the simulations. The information given in the calibration chart of accelerometers was assumed to be true. This means that the accelerometers have a flat frequency response up to 10kHz. In addition no phase shift is introduced by the accelerometers within this frequency range.

Figures 5.5a and 5.5b (or 5.5c) show the symmetric (i.e. mass centre is at $0.5l$) and asymmetric systems (i.e. mass centre is at $0.404l$ or $0.596l$) when both the cannels are working perfectly. The measurements are shown for power amplifier gains 0, 0.02, 0.06 and 0.12. In the control system the power amplifier provides variable gain, but the charge amplifier and the shakers are also provide gains (which are fixed). Letting the charge amplifier, shaker and the power amplifier gains be g_c, g_s and g_p then the normalised experimental gain g_e is given by $g_e = \frac{g_c g_s g_p}{c}$. (The purpose of these experiments was to qualitatively support the theoretical simulations; the corresponding normalised gains are given by 0, 0.748, 2.43, 8.1 and 15.46.)

Figures 5.5a and 5.5b (or 5.5c) show that when both shakers work the total kinetic energy in system is reduced considerably (approximately 15 dB at the peak). Similarly when one of the channels fail (i.e. second channel), the attenuation achieved reduces considerably. In addition, as predicted theoretically, in a system with single channel failure, there is only a reasonable control of one of the peaks. From Figures 5.5e and 5.5f it can be seen that when the mass centre is closer to the working mount only one peak is controlled and there is little or no control in the other peak. The total kinetic energy plots for a perfectly working system and a system with failure show that in general there is reasonable agreement with the simulations.

In Figures 5.6a, 5.6b and 5.6c the changes in total kinetic energy are shown for system with mass centre at $0.5l$, $0.404l$ and $0.596l$ respectively. These figures show that for a perfectly working system as the gain is increased the change in total kinetic energy reduces considerably and hence the overall performance improves. However with a single channel failure the rate of reduction falls considerably. This confirms the theoretical predictions.

5.3.3 Summary

Simulations and experiments performed on a two-mount system have shown that when a single channel failure occurs the performance of the active isolation system deteriorates. The overall performance also deteriorates considerably. Considering the original passive system and the pinned case (or the system with large gain), between the limiting cases (i.e. no gain and infinite gain) there is only a small improvement in the performance.

5.4 Two-mount system on a flexible base

The active vibration isolation of a two-mount system from a moving inelastic base described in section 5.3, does not include the base dynamics in the analysis. However most of the isolation problems are strongly influenced by the base dynamics, which is included in the plant frequency response function/matrix [88]. As discussed in Chapter 2 a simple flexible clamped-free-clamped-free (CFCF) base is considered for the investigation of the influence of the base structure. The stability of this system has been discussed in Chapter 2. A CFCF base is relatively easy to realise in practice and the analysis can be readily verified [2].

The impedance representation of a two-mount system on a flexible base is given in Figure 2.3b. The plant (the term plant represents the frequency response function or matrix of the mechanical system when excited only by the secondary forces [4]) frequency response matrix for flexible base excited system is given by (From equation (2.24)),

$$\mathbf{G}(j\omega)=\left[\mathbf{Z}_e+\mathbf{Z}_m+\mathbf{Z}_m\mathbf{Y}_b\mathbf{Z}_e\right]^{-1} \tag{5.8}$$

The feedback frequency response matrix is given by, $\mathbf{H}(j\omega)=cg_{nv}\mathbf{I}$, where $\mathbf{I}$ is the identity matrix of size (2 x 2). The closed-loop vector of equipment velocities $\mathbf{v}_e$ (i.e. velocity in the presence of primary disturbance) can be written as (From equation 2.25)),

$$\mathbf{v}_e=\left(1+\mathbf{G}(j\omega)\mathbf{H}(j\omega)\right)^{-1}\mathbf{G}(j\omega)\mathbf{f}_{pm} \tag{5.9}$$

where the vector $\mathbf{f}_{pm}$ is the collocated vector of primary disturbances/excitation on the base. Applying equation (2.17b) the mass centre velocity vector can be found and is given by,

$$\mathbf{a}=\mathbf{Q}^{-1}\left(1+\mathbf{G}(j\omega)\mathbf{H}(j\omega)\right)^{-1}\mathbf{G}(j\omega)\mathbf{f}_{pm} \tag{5.10}$$

where $\mathbf{f}_{pm}$ can be written in terms of disturbance forces vector $\mathbf{f}_p$ on the base structure as,

$$\mathbf{f}_{pm}=\mathbf{Z}_b\mathbf{Y}_{bp}\mathbf{f}_p \tag{5.11}$$

where $\mathbf{Y}_{bp}$ is the mobility matrix of the uncoupled base due to the primary force vector $\mathbf{f}_p$. Thus the velocity vector at the mass centre can be found, provided $\mathbf{Z}_e$, $\mathbf{Z}_m$, $\mathbf{Y}_b$ and $\mathbf{Q}$ are known. Substituting equation (5.11) in equation (5.3) the total kinetic energy can be found. The model of a simple clamped-free-clamped-free (CFCF) base structure discussed in Chapter 2 is used for simulations.

5.4.1 Simulations

Simulations for active vibration isolation from a CFCF flexible base are discussed in this section. Location of mounts and excitation on the plate with respect to the coordinate system considered are given in Figure 2.8. The same three different equipment structures with differing mass centres at $0.5l$, $0.404l$ and $0.596l$ from left hand end of the mount are considered. The total kinetic energy plots for these systems are shown in Figures 5.7a, 5.7b and 5.7c. It can be seen from these that the active isolation system is as effective as in the corresponding moving inelastic base cases. It can also be seen that in comparisons with Figures 5.3a, 5.3b and 5.3c that apart from first two peaks all others correspond to the dynamics of the base structure.

When one of the active mounts fails (mount2) the performance deteriorates, similar to the moving inelastic-base cases. These are shown in Figures 5.7d, 5.7e and 5.7f. It was observed in the moving inelastic base cases (with a single channel failure) that as the gain of the working mount is increased the system performs better than the corresponding passive system at any frequency. Due to the closeness of the system resonance frequency and the first resonance frequency of the base (it is at 42.11 Hz Table E1 in Appendix E), it exhibits worse behaviour between these frequencies (Figures 5.7d, 5.7e and 5.7f).

Figures 5.7d, 5.7e and 5.7f also show the total kinetic energy for the system with large gain (a non-dimensional gain of 5000 is used) in the working mount. It can be seen from these figures that although there are some improvements at the original resonance frequency, the peak appears elsewhere. This gives a poor performance of the system. For the limiting cases (i.e. the system with no control and system with pinned end or infinite gain) only a small improvement can be seen.

The change in kinetic energy plots for the three cases considered are given in Figures 5.8(i), 5.8(ii) and 5.8(iii) for a frequency band $0 \leq freq \leq 250\text{Hz}$. Both perfectly working and

system with single channel failure are shown in these figures. The overall performance of the system on the flexible base also improves as the gain is increased. However when one of the channels fail the system becomes largely ineffective as shown in Figures 5.8(i)b, 5.8(ii)b and 5.8(iii)b apart from a small improvement at low gains. Some experiments were conducted to support the flexible base cases and are described in the next section.

5.4.2 Experiments

Experiments were conducted to support the theoretical predictions and are described in this section. Figure 2.18 shows a schematic diagram of the experimental set-up, which is similar to the one described for the moving inelastic base. In the inelastic base case, the prescribed velocity of the base was considered as the reference signal, which eliminates the base dynamics from the plant response. However in the flexible base case the base velocity is dependent on the location and is hence unsuitable for a reference. Here the primary force applied to the base structure is used as the reference, which was measured by a force gauge. From the measurements total kinetic energy was calculated in a similar manner to that described in section 5.3.2.

The primary excitation and mount positions are given in Table 2.2 and in Figure 2.8 respectively. Instruments used for the measurements are tabulated in Table 2.3. A primary shaker placed at the excitation point, (the coordinates are given in Table 2.2) excited the base structure. Two accelerometers measured the acceleration at the top of the equipment plate, one each close to each mount centre. Outputs of the accelerometers were conditioned and integrated by charge amplifiers to produce velocity signals. These velocity signals were then passed through a two-channel power amplifier and fed into the control shakers. The velocity signals were also fed into the input terminal of HP analyser for data collection.

Figure 5.9 shows the isolation system and the base structure used for the experimental work. Two additional mass of equal weight shown in Figure 5.9 were used to change the mass centre by placing them on the control shakers. When both weights are on the left shaker the mass centre is at $0.404l$, and both are on right the shaker the mass centre is at $0.596l$.

Figures 5.10a, 5.10b and 5.10c show the plots of total kinetic energy for a perfectly working system. It can be seen that under perfectly working conditions a reduction of total kinetic energy greater than 15 dB at the first peak can be obtained for all three cases. In summary the results show a good agreement with theoretical predictions.

However when one of the channels fails as seen in Figures 5.10d, 5.10e and 5.10f only a small reduction in kinetic energy is achieved. Although, as predicted in the simulations, the degradation in overall performance of the isolation system at some frequencies is not clearly visible, the measured performance shows that the system becomes less effective.

Figures 5.11a, 5.11b and 5.11c show that the change in total kinetic energy for systems with mass centres at $0.5l$, $0.404l$ and $0.596l$ respectively. It can be seen that as the gain is increased the overall performance reduces to about half the performance of a perfectly working system. This implies that the system becomes less effective when one of the active mounts fails.

5.4.3 Summary

Simulations and experiments performed on a two-mount system on a CFCF flexible base show that when a single channel failure occurs the performance deteriorates (i.e. the attenuation on total kinetic energy is small). The overall performance (i.e. change in kinetic energy) also deteriorates considerably. Considering the original passive system and the pinned case (or system with large gain), between the limiting cases there is only a small improvement in its performance (i.e. attenuation in kinetic energy) as seen when the moving base was inelastic.

5.5 A general two-mount system

The general agreement between the simulations and experiments motivates a further study of the system. In the system considered so far, the shaker masses are considerably large compared to the mass of the equipment. Thus it is possible that the shaker masses dominate the system behaviour giving two nearly SDOF systems weakly coupled by a beam. Thus in this section a system with dominant equipment mass as described in Appendix C is considered. Similar to previous cases three differing mass centre cases are considered.

Figure 5.12 shows total kinetic energy of the two-mount system on a moving inelastic base. Three differing mass centres of the system are considered similar to the previous cases. Figures 5.12d, 5.12e and 5.12f show that the behaviour deteriorates when one of the channels

fails. The improvement between the limiting cases (i.e. the original passive system and the system when the gain is increased to a very large value in working mount and other being failed) is very poor. The overall performance shown in Figure 5.13 reveals that the overall improvement of a system with failure is very poor and similar to the previous cases. Figures 5.14 and 5.15 show the corresponding cases for the system on a CFCF base structure. They also support the main finding of the corresponding cases considered previously.

5.6 Conclusions

A perfectly working two-mount active isolation system and a two-mount isolation system with single channel failure has been investigated in this Chapter. A moving inelastic base and a CFCF flexible base were considered. The first does not include the base dynamics in the analysis or experiments and hence helps to identify weaknesses of the system alone when a failure occurs. The latter helps to confirm the findings and to draw general conclusions.

The simulations and experiments carried out on a moving inelastic base show that,

- The perfectly working system controls both resonance peaks of the system and gives a better overall performance.
- The perfectly working system also improves (i.e. the resonance peaks corresponding to the system continue to reduce) as the gain is increased.
- When one of the channels fails, the system loses control over one of the resonance peaks. The uncontrollable peaks depend on the closeness of the working mount to the mass centre.
- In addition, when one of the channels fails, after a certain small value of gain the overall performance of the system does not improve.
- The improvement in the performance of the system is poor even if the gain is increased to infinity in a system with single channel failure.

The simulations and experiments carried out with a two-mount system on a CFCF flexible base structure supports most of the findings of the moving inelastic base cases. As the gain of a two-mount system with single channel failure is increased from zero to infinity the two-mount system becomes a 2DOF system to a SDOF system. When one of the channels fails, the performance of the two-mount system does not improve considerably from its passive behaviour as the gain is increased.

Masses (kg)	$r = 0.404$	$m_1 = 1.6$	$m_2 = 0.91$	$m_p = 1.08$	$m = 3.59$
	$r = 0.50$	$m_1 = 1.255$	$m_2 = 1.255$	$m_p = 1.08$	$m = 3.59$
	$r = 0.596$	$m_1 = 0.91$	$m_2 = 1.6$	$m_p = 1.08$	$m = 3.59$
Moment of Inertia (kgm^2) $J = J_{pg} + J_m$	$r = 0.404$	$J_m = 0.0105$	$J_{pg} = 0.0038$	$J = 0.0143$	$J_{pin} = 0.0248$
	$r = 0.50$	$J_m = 0.0062$	$J_{pg} = 0.0036$	$J = 0.0098$	$J_{pin} = 0.0259$
	$r = 0.596$	$J_m = 0.0105$	$J_{pg} = 0.0038$	$J = 0.0143$	$J_{pin} = 0.0372$
Plate length l_p (mm)		200			
Distance between mounts l (mm)		134			

Table 5.1 Geometric and physical properties of system

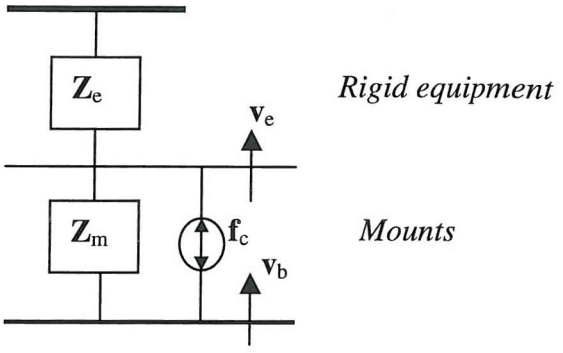

Figure 5.1 Impedance representation of the two-mount system on a moving inelastic base

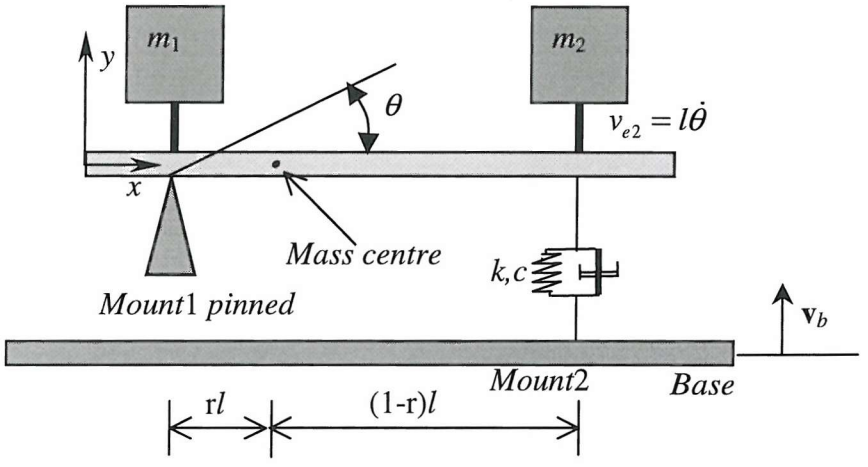

Figure 5.2 Two-mount system with active mount 2 failed and mount 1 pinned (infinite gain)

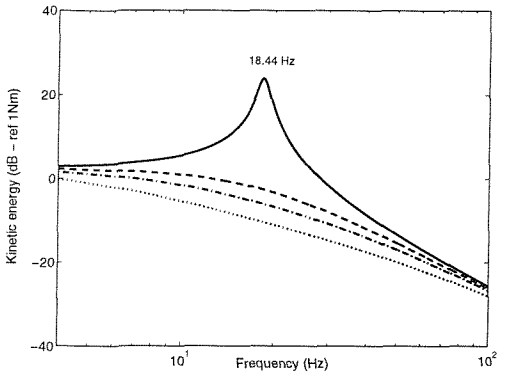

(a) Perfectly working system Mass centre - 0.5l

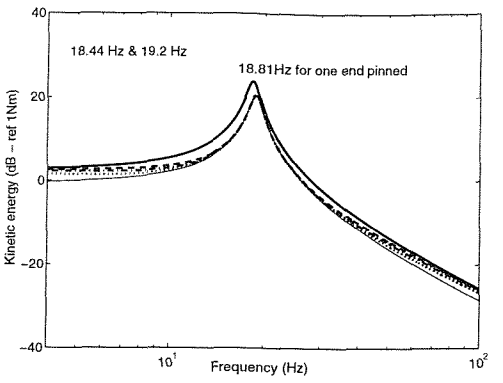

(d) System with single channel failure Mass centre – 0.5l

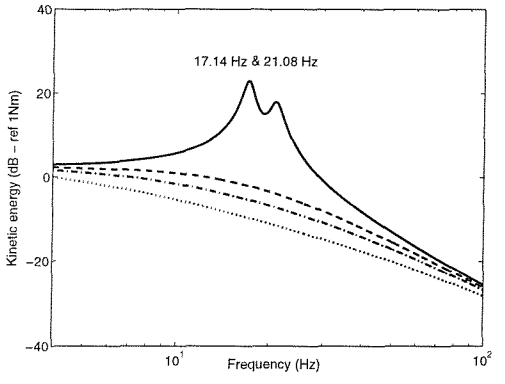

(b) Perfectly working system Mass centre - 0.404l

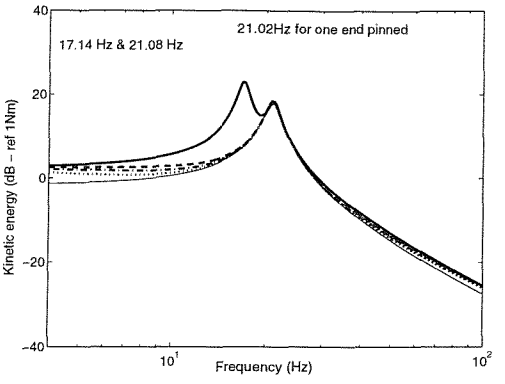

(e) System with single channel failure Mass centre – 0.404l

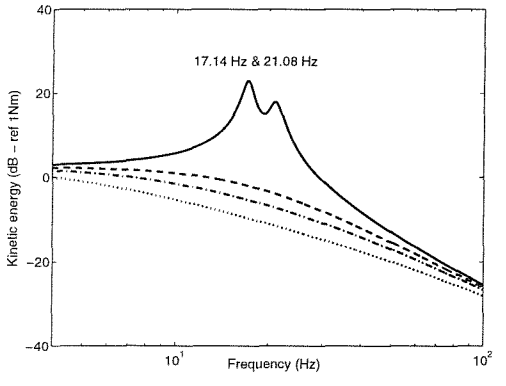

(c) Perfectly working system Mass centre - 0.596l

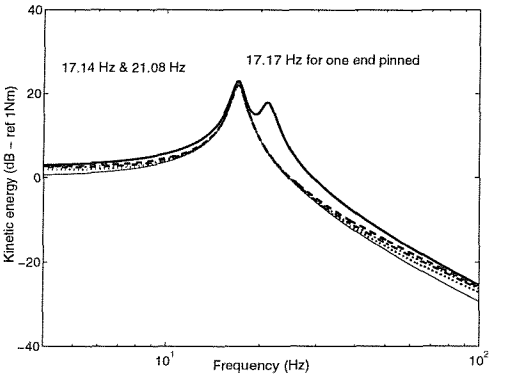

(f) System with single channel failure Mass centre – 0.596l

Figure 5.3 Total kinetic energy plots for a system on a moving inelastic base (Simulations). Non-dimensional gain 0: _____, non-dimensional gain 20: --------, non-dimensional gain 30: -.-.-.-.-., non-dimensional gain 50: ....., infinite gain:_____

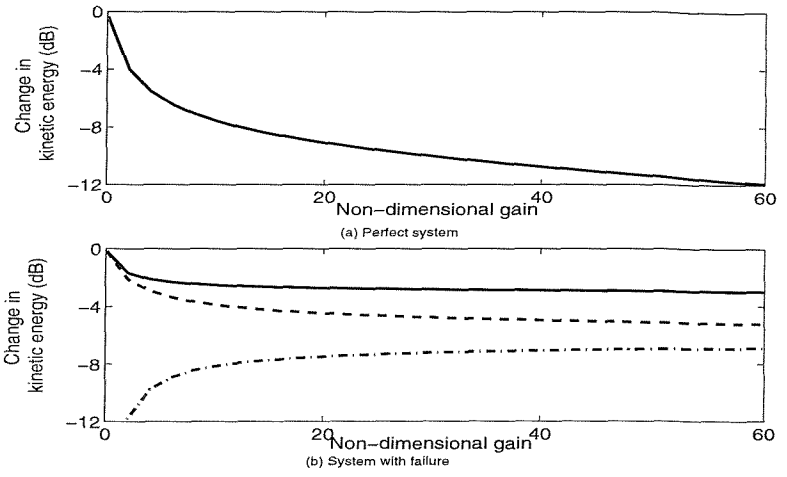

(i) Mass centre is at 0.5l

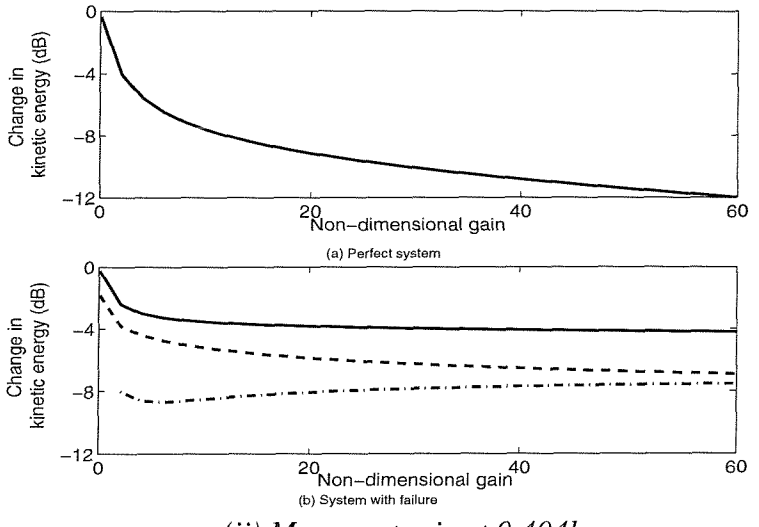

(ii) Mass centre is at 0.404l

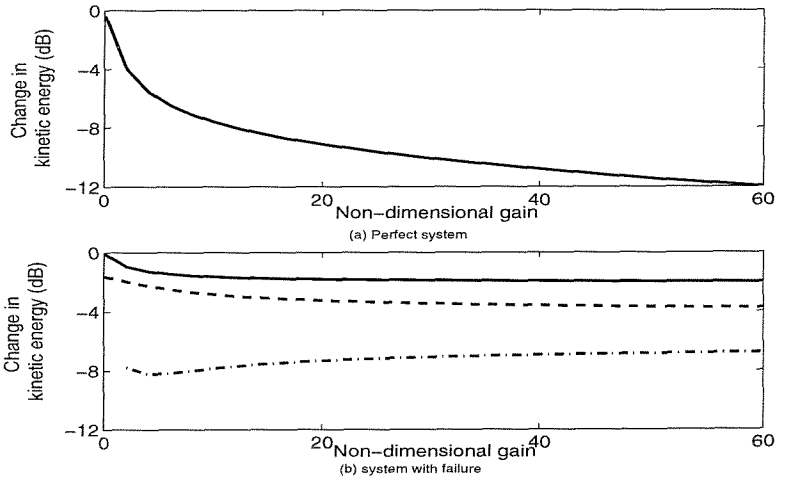

(iii) Mass centre is at 0.596l

Figure 5.4 Change in kinetic energy of the two-mount system $(0 \leq freq \leq 250\ \text{Hz})$ *Total kinetic energy: _____, translational kinetic energy: - - - - - - - - -, Rotational kinetic energy:-.-.-.-.-.-*

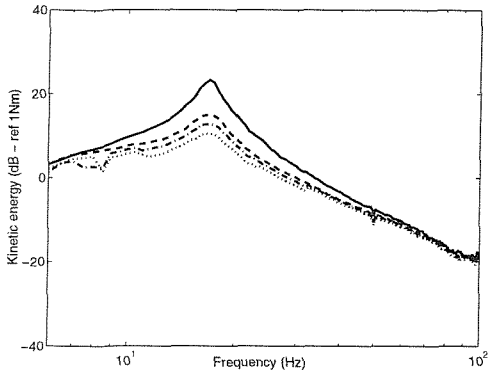

(a) Perfectly working system Mass centre - 0.5l

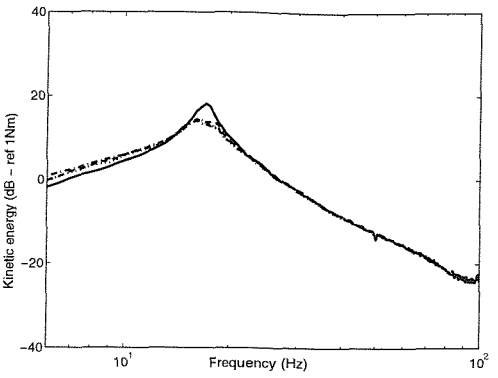

(d) System with single channel failure Mass centre – 0.5l

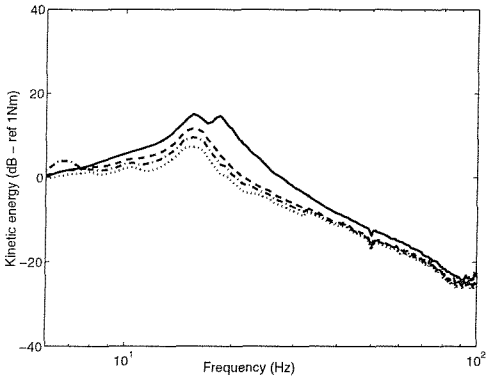

(b) Perfectly working system Mass centre - 0.404l

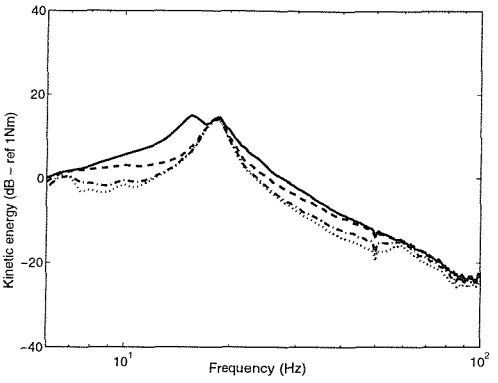

(e) System with single channel failure Mass centre – 0.404l

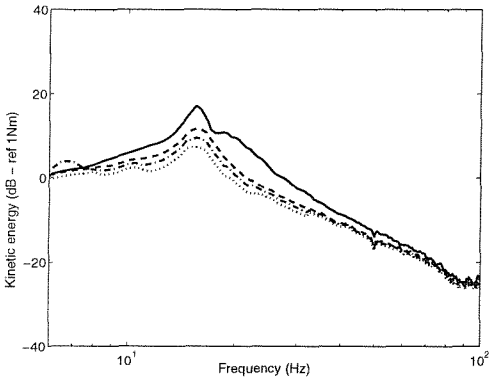

(c) Perfectly working system Mass centre - 0.596l

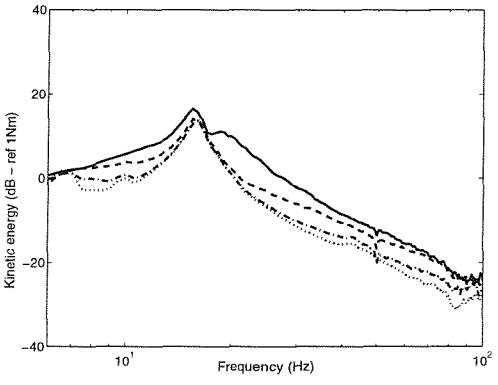

(f) System with single channel failure Mass centre – 0.596l

Figure 5.5 Total kinetic energy plots for a system on a moving inelastic base (Measurement). Power amplifier gain 0: _____, power amplifier gain 0.02: --------, power amplifier gain 0.06: -.-.-.-.-., power amplifier gain 0.12: .....

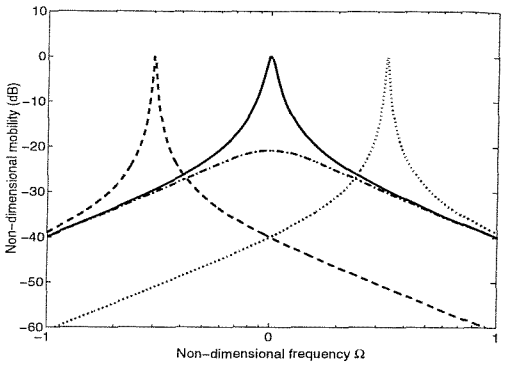

(a) Closed-loop frequency response (Non-dimensional gain 10 *and damping ratio* $\zeta = 0.05$ *) No control: _____, acceleration feedback: ----------, velocity feedback: -.-.-.-.-.-.-.-.-, displacement feedback:.....*

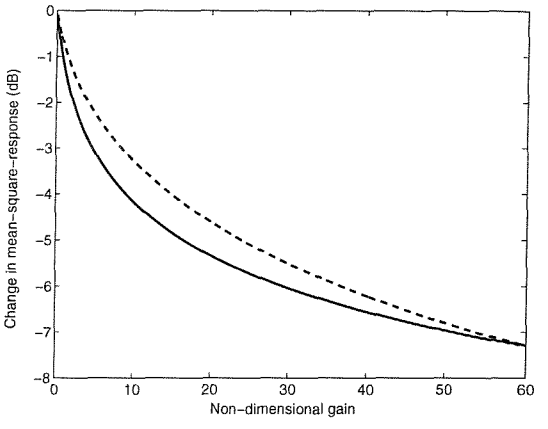

(b) Change in mean square response in the frequency range $0.01 \leq \Omega \leq 100$ *; (damping ratio* $\zeta = 0.05$ *) velocity feedback: ----------, acceleration and displacement feedback:_____*

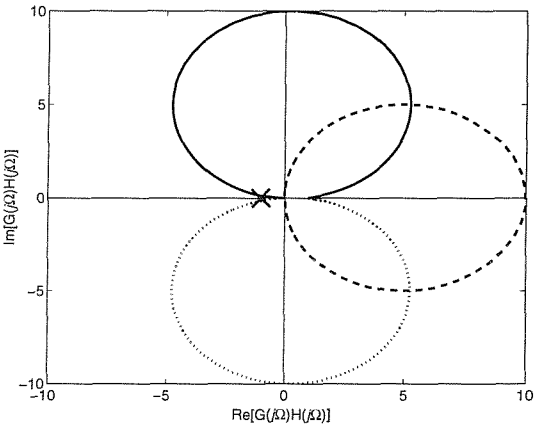

(c) Open-loop frequency response (damping ratio $\zeta = 0.05$ *); acceleration feedback:_____, velocity feedback:----------, displacement feedback:.....*

Figure 3.2 Ideal SDOF system response with acceleration, velocity and displacement feedback control.

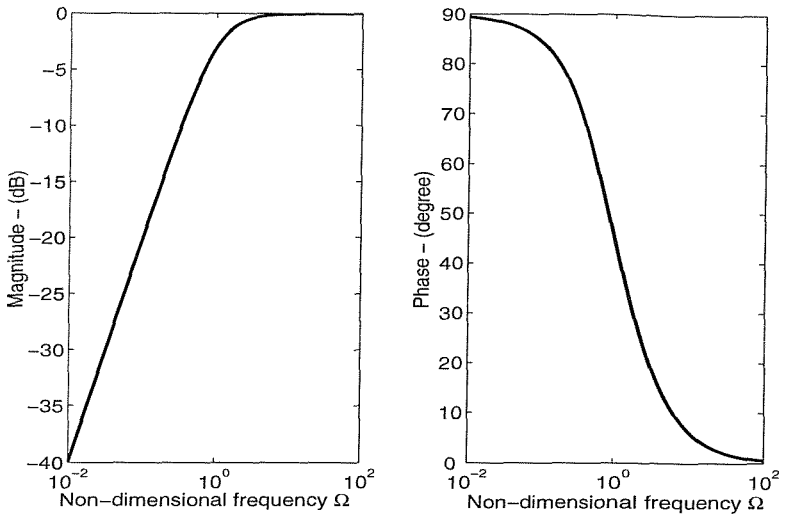

(a) The characteristics of a high pass filter (for $\alpha = 1$)

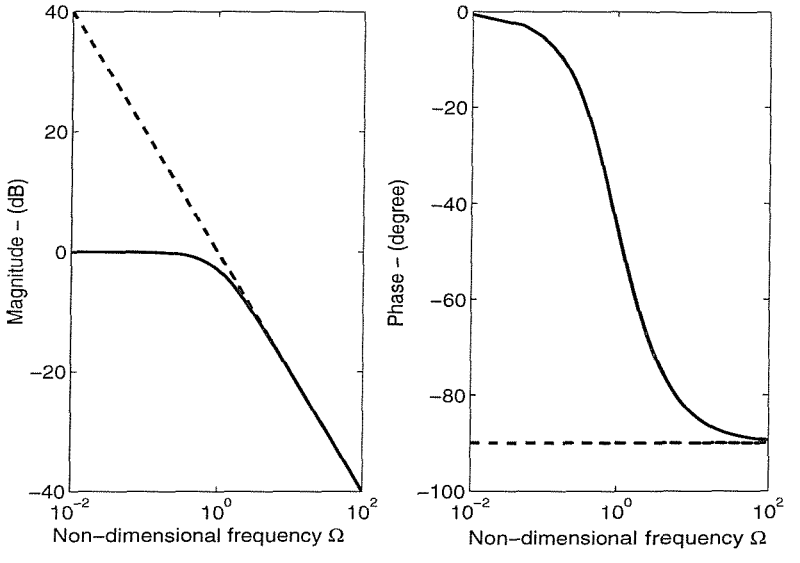

(b) The characteristics of an electronic integrator (for $\beta = 1$) ideal integrator:----------, real integrator:_____

Figure 3.3 Frequency response characteristics of electronic components in the feedback loop

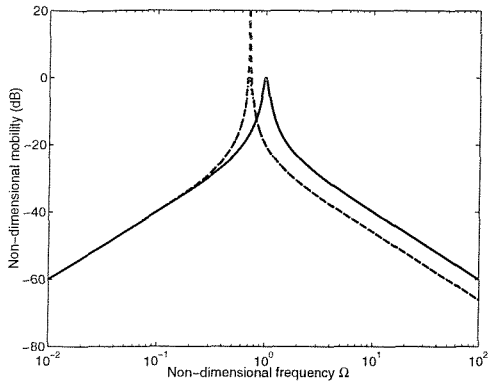

(a) Acceleration feedback with one high-pass filter

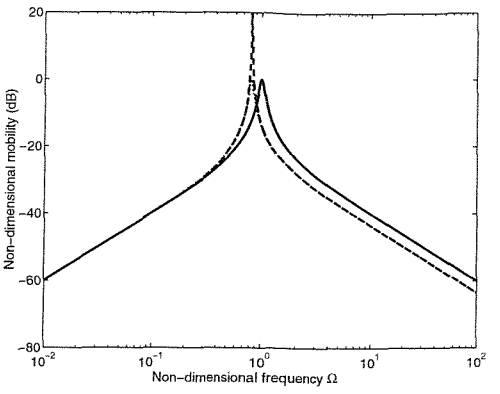

(b) Acceleration feedback with two high-pass filters

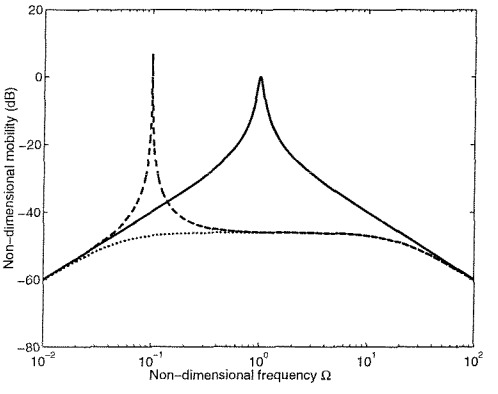

(c) Velocity feedback with two high-pass filters

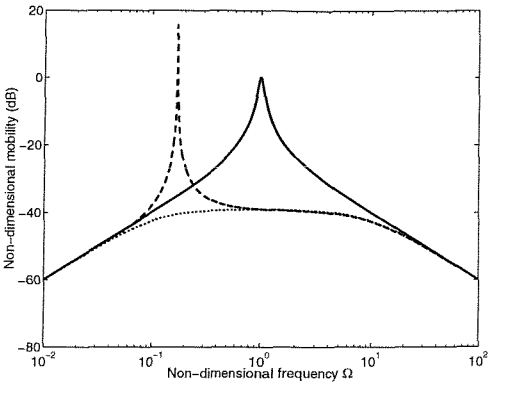

(d) Velocity feedback with three high-pass filters

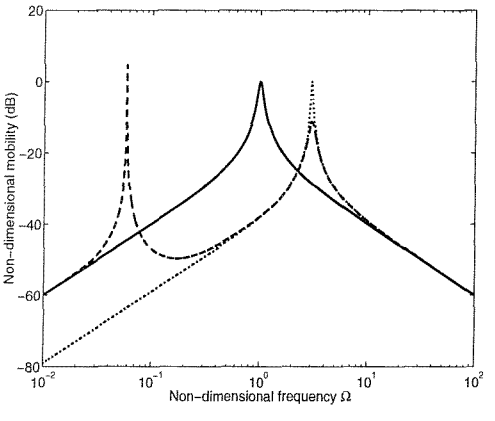

(e) Displacement feedback with three high-pass filters

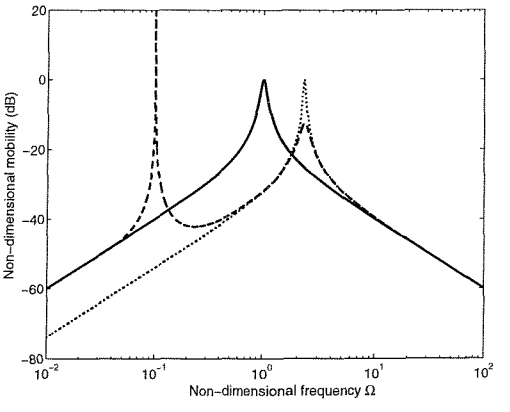

(f) Displacement feedbacks with four high-pass filters

Figure 3.6 Closed-loop response for acceleration, velocity and displacement feedback control with various number of high-pass filters; no control: _____, realistic system, with high-pass filters and gains of 99.9% of the respective maximum: ---------, ideal system with 99.9% of the realistic maximum gain: .....

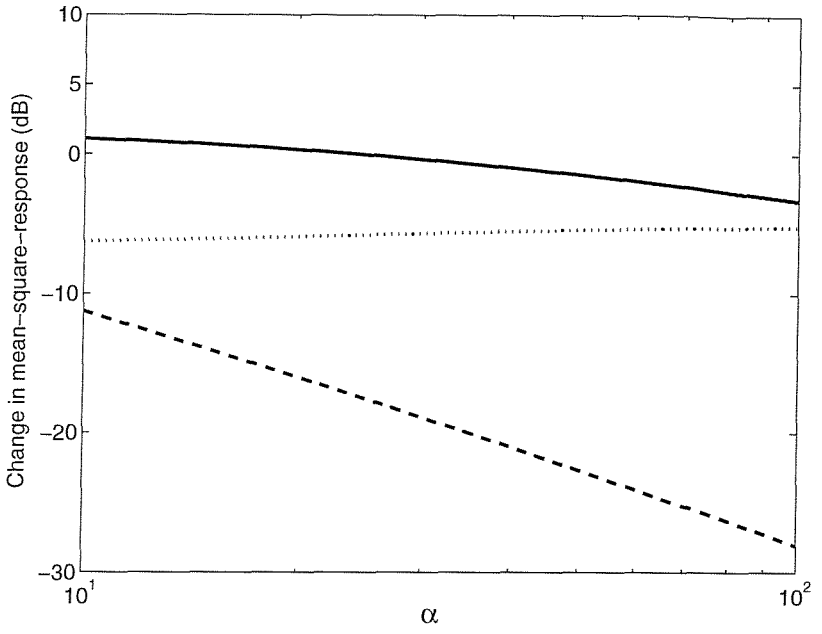

Figure 3.7 Change in mean square response with 99.9% of the respective maximum gain; acceleration feedback with two high-pass filters:_____, velocity feedback with three high-pass filters: ---------- and displacement feedback with four high-pass filters: .....

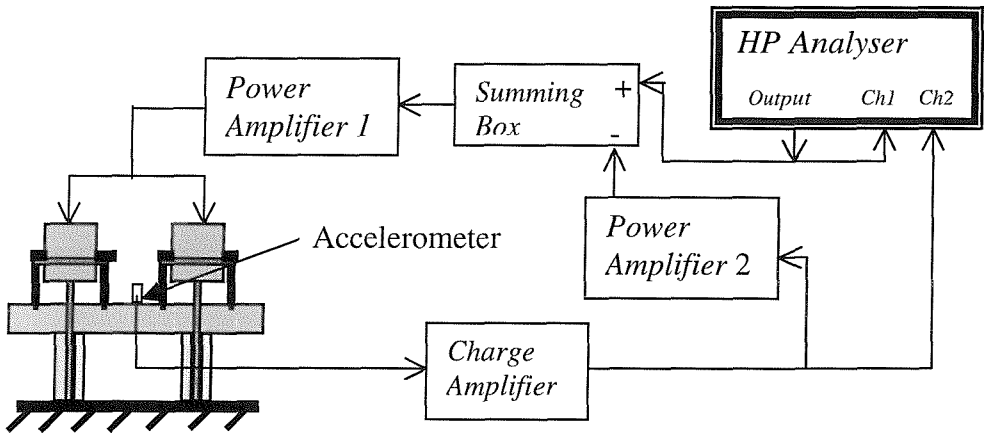

Figure 3.8 Experimental set-up for the feedback control of the single-degree-of-freedom system.

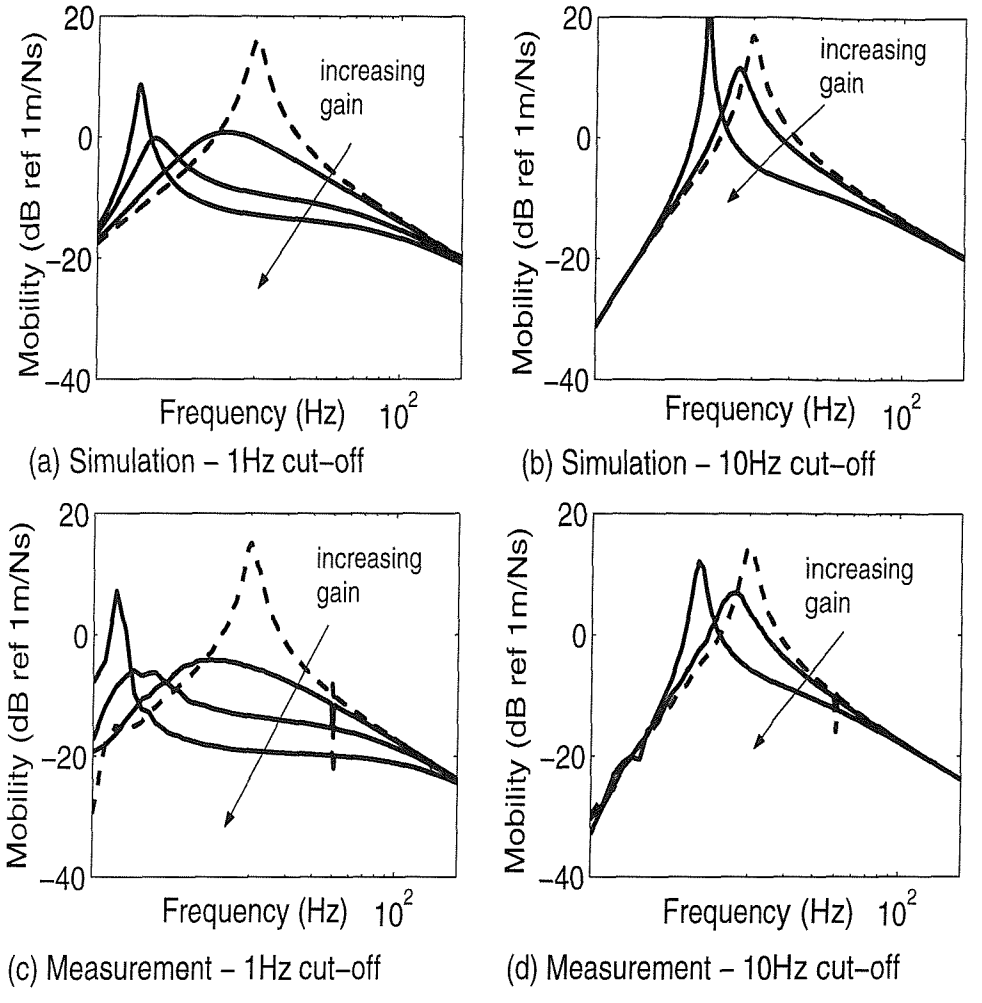

Figure 3.10 Measured and simulated closed-loop frequency response function of the single-degree-of-freedom system (for velocity feedback control). No control: ---------- with control:_____

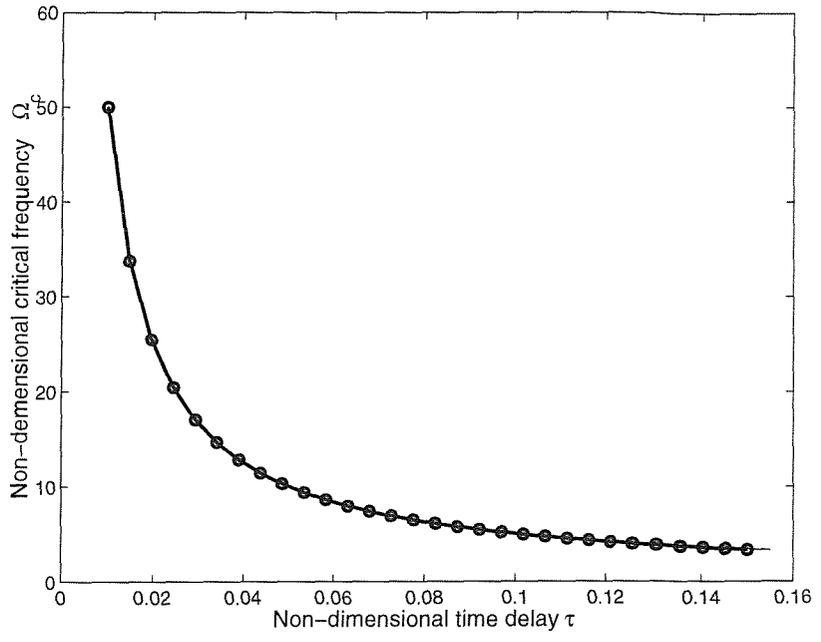

(a) Acceleration feedback control. Damping ratio 0.01:_____, *Damping ratio* 0.05:----------, *Damping ratio* 0.1:....., $\Omega_c = 1/2\tau$: —⊖—

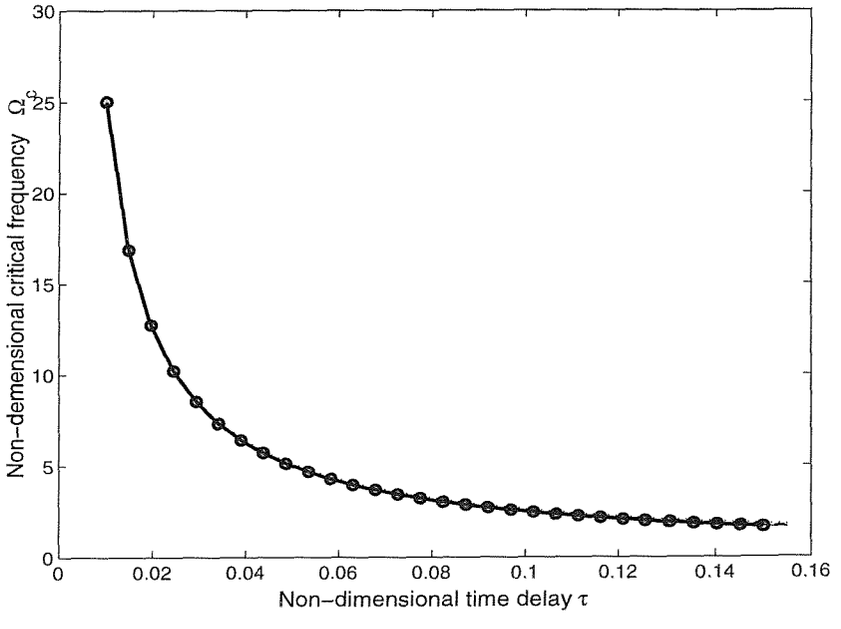

(b) Velocity feedback control. Damping ratio 0.01:_____, *Damping ratio* 0.05:----------, *Damping ratio* 0.1:....., $\Omega_c = 1/4\tau$: —⊖—

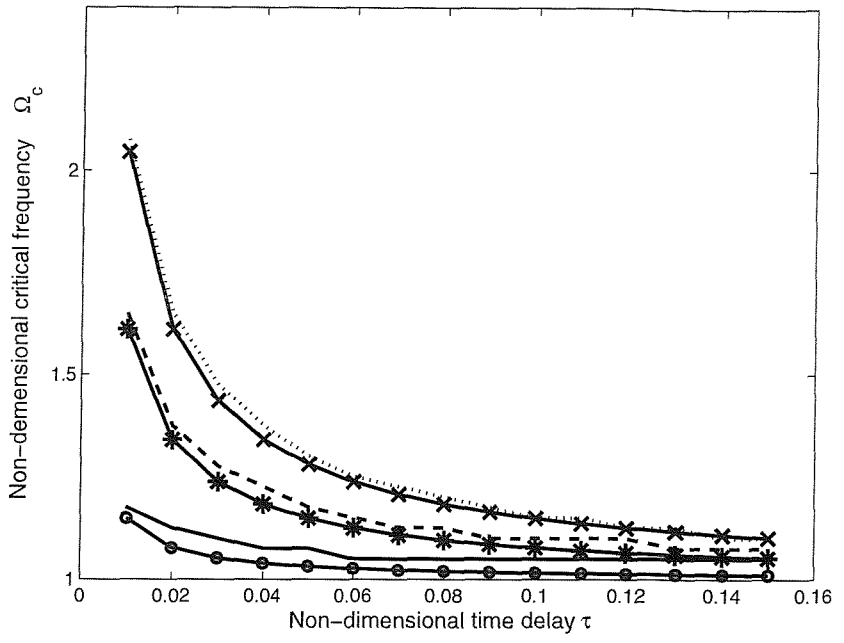

(c)Displacement feedback control Damping ratio 0.01:_____, *Damping ratio* 0.05:----- , *Damping ratio* 0.1:..... $\Omega_c = \sqrt{1+\zeta/\pi\tau}$ & ζ=0.01 —⊖—

$\Omega_c = \sqrt{1+\zeta/\pi\tau}$ & ζ=0.05 —✳— $\Omega_c = \sqrt{1+\zeta/\pi\tau}$ & ζ=0.1 —×—

Figure 4.4 Critical frequencies as a function of time-delay for selected damping ratios (with approximate models)

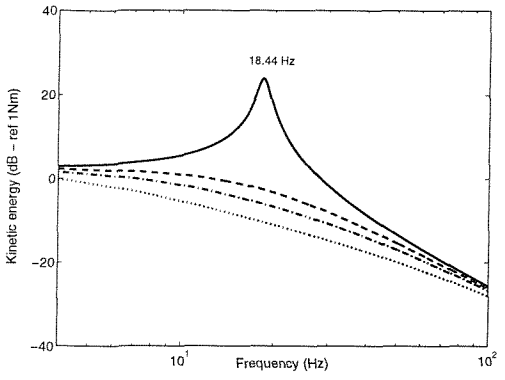

(a) Perfectly working system Mass centre - 0.5l

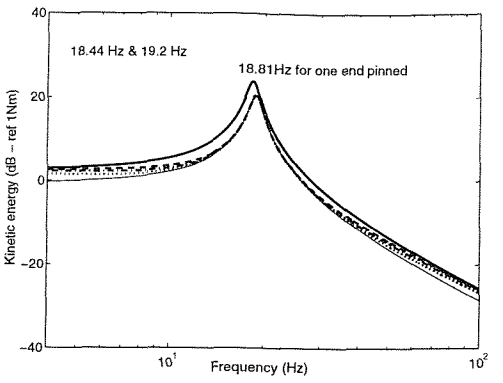

(d) System with single channel failure Mass centre – 0.5l

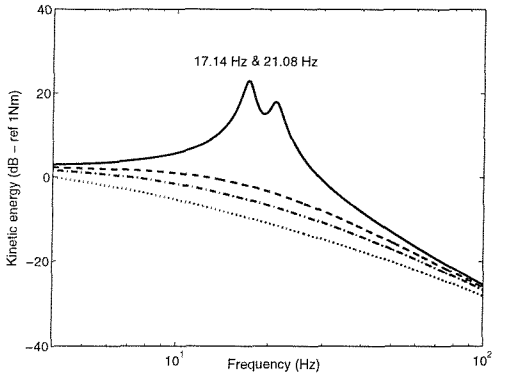

(b) Perfectly working system Mass centre - 0.404l

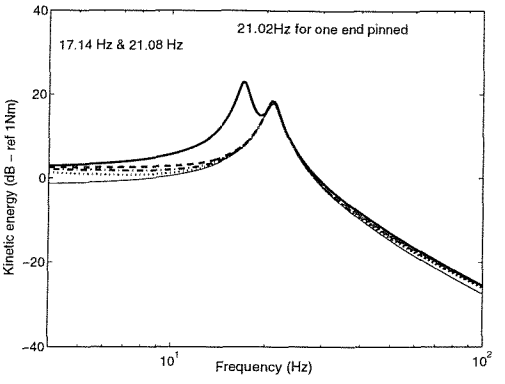

(e) System with single channel failure Mass centre – 0.404l

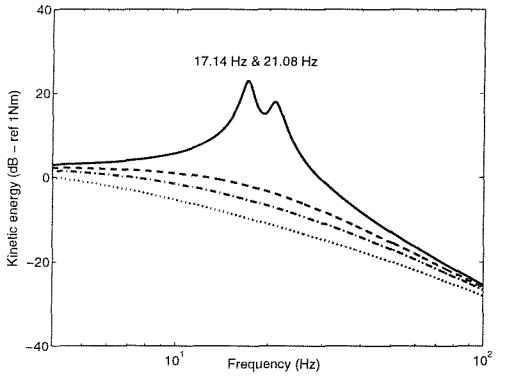

(c) Perfectly working system Mass centre - 0.596l

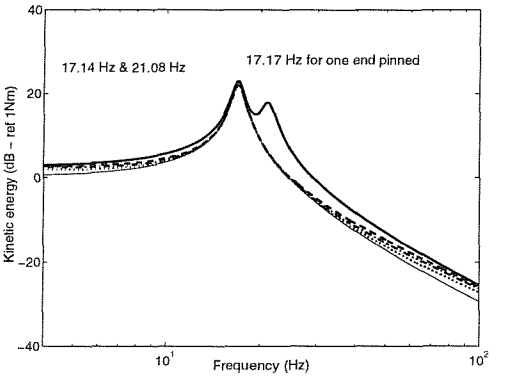

(f) System with single channel failure Mass centre – 0.596l

Figure 5.3 Total kinetic energy plots for a system on a moving inelastic base (Simulations). Non-dimensional gain 0: _____, non-dimensional gain 20: --------, non-dimensional gain 30: -.-.-.-.-., non-dimensional gain 50: ....., infinite gain:_____

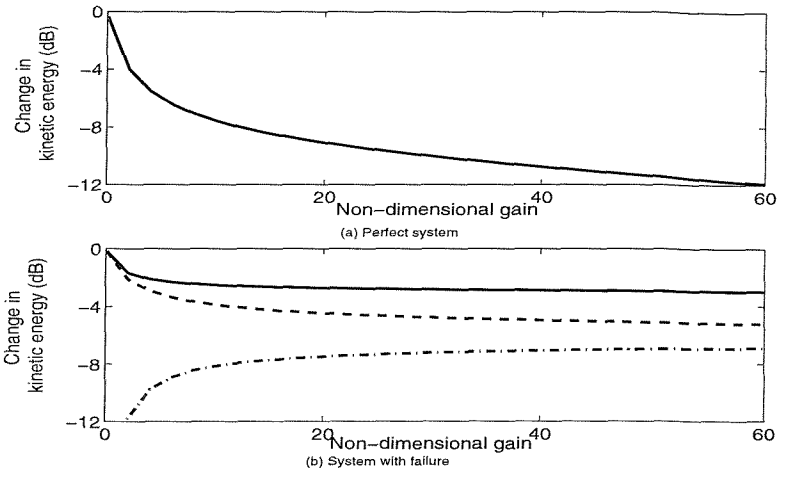

(i) Mass centre is at 0.5l

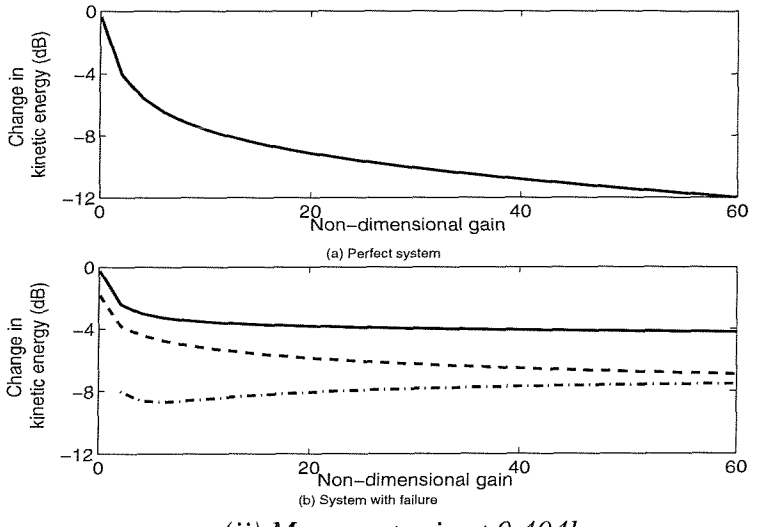

(ii) Mass centre is at 0.404l

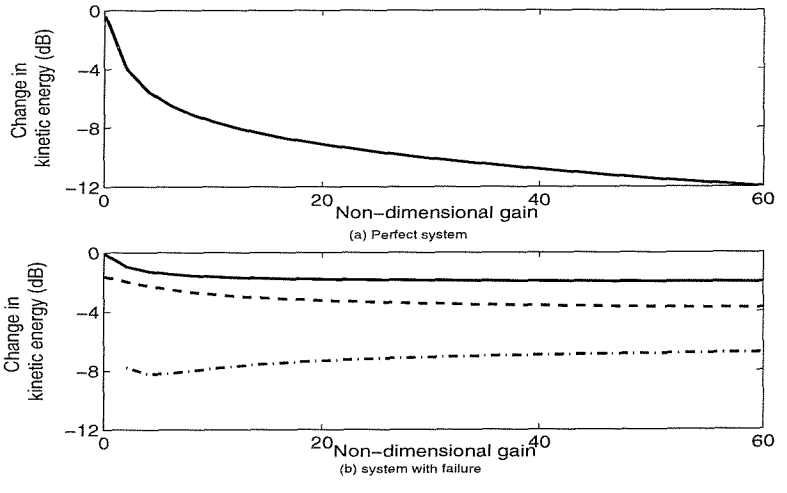

(iii) Mass centre is at 0.596l

Figure 5.4 Change in kinetic energy of the two-mount system $(0 \leq freq \leq 250\ \text{Hz})$ *Total kinetic energy: _____, translational kinetic energy: - - - - - - - - -, Rotational kinetic energy:-.-.-.-.-.-*

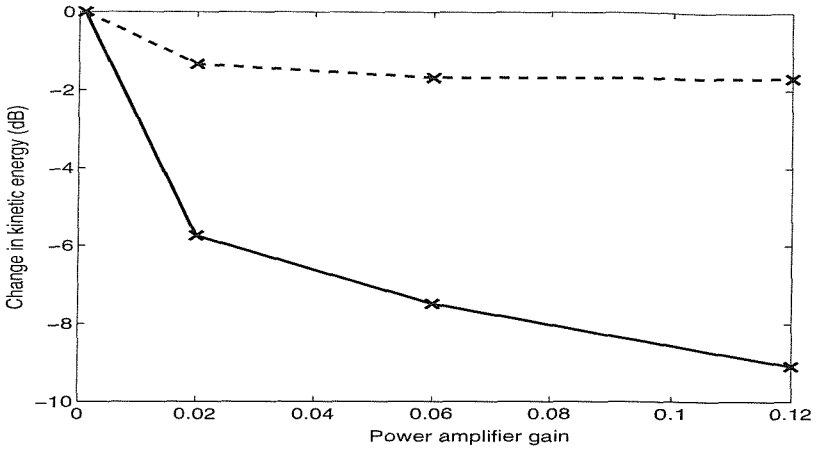

(a) Mass centre is at 0.5l

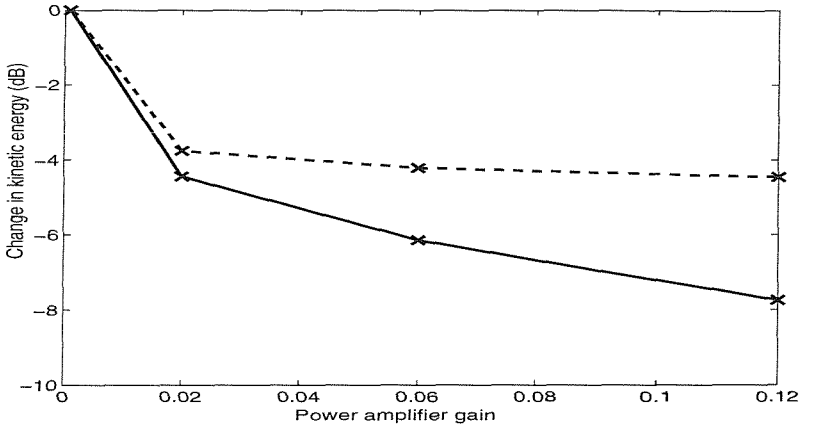

(b) Mass centre is at 0.404l

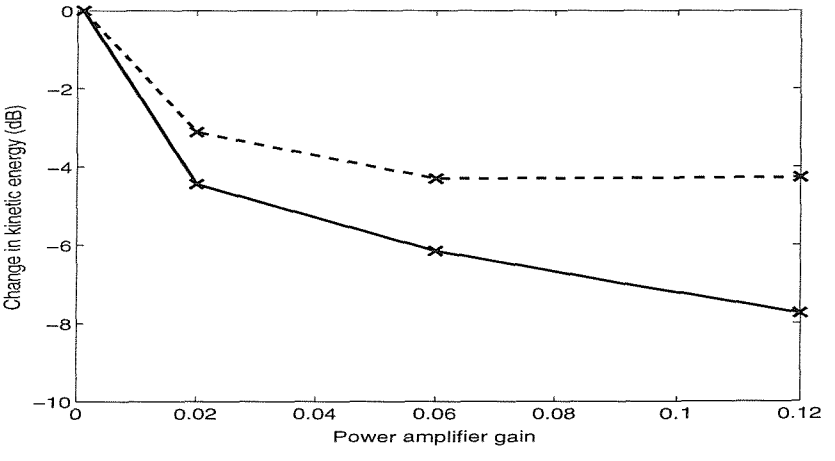

(c) Mass centre is at 0.596l

Figure 5.6 Change in total kinetic energy of the two-mount system on a moving inelastic base (Measurement bandwidth $(0 \leq freq \leq 200\ \text{Hz})$ *) Perfectly working system: _____, system with single channel failure: .....*

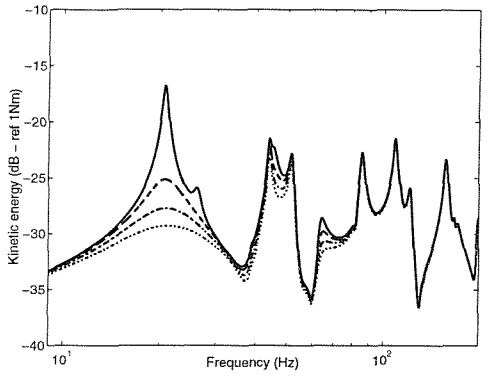

(a) Perfectly working system Mass centre - 0.5l

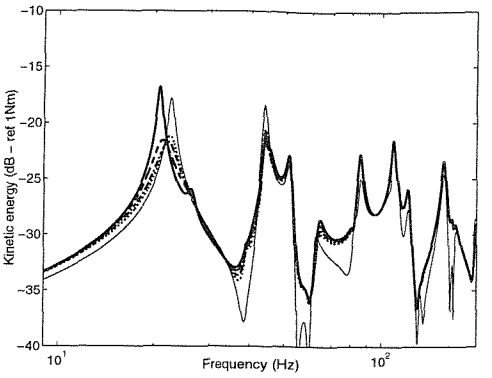

(d) System with single channel failure Mass centre – 0.5l

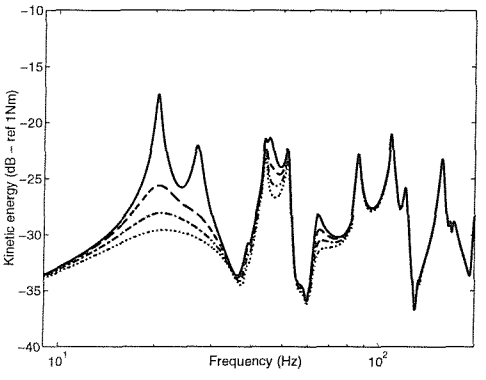

(b) Perfectly working system Mass centre - 0.404l

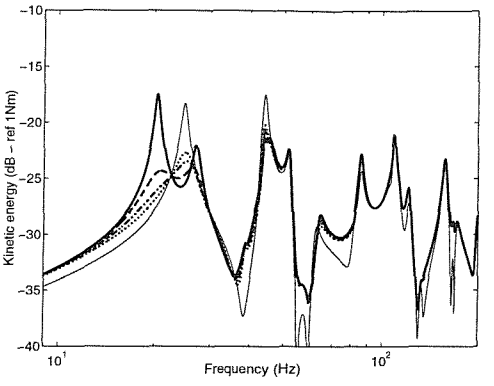

(e) System with single channel failure Mass centre – 0.404l

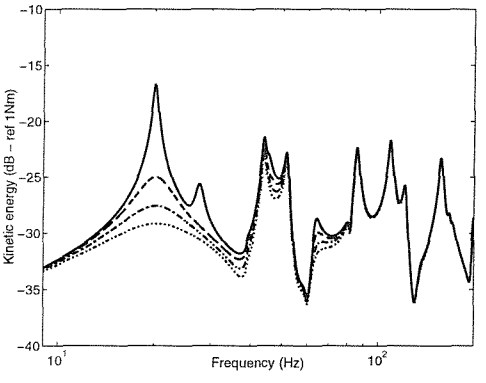

(c) Perfectly working system Mass centre - 0.596l

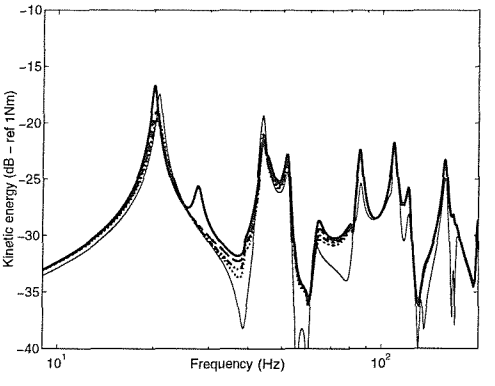

(f) System with single channel failure Mass centre – 0.596l

Figure 5.7 Total kinetic energy plots for a system on flexible CFCF base (Simulations). Non-dimensional gain 0: _____, non-dimensional gain 5: --------, non-dimensional gain 10: -.-.-.-.-., non-dimensional gain 15: .....infinite gain:_____

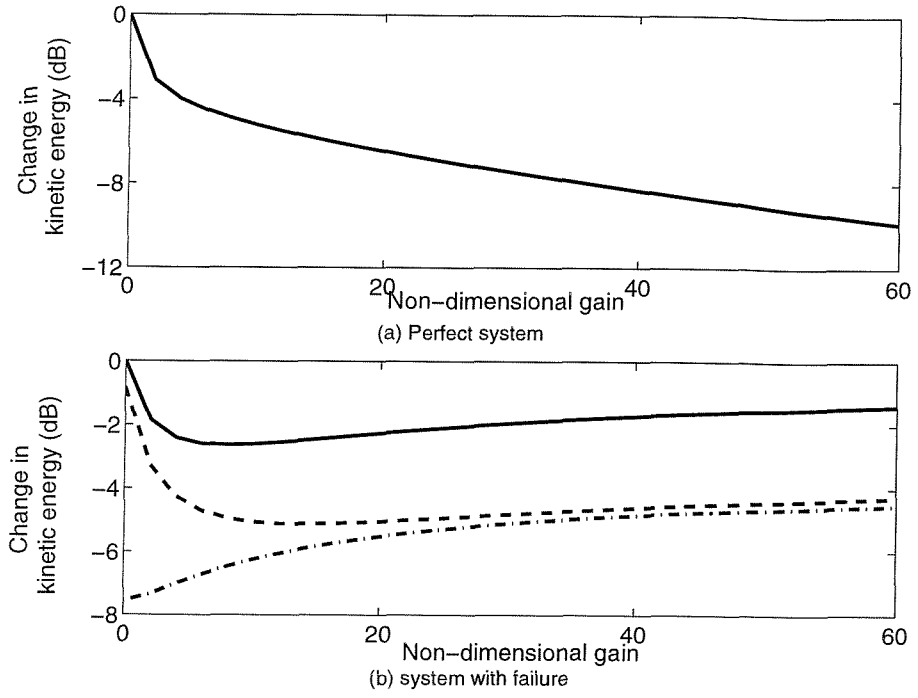

(i) Mass centre is at 0.5l

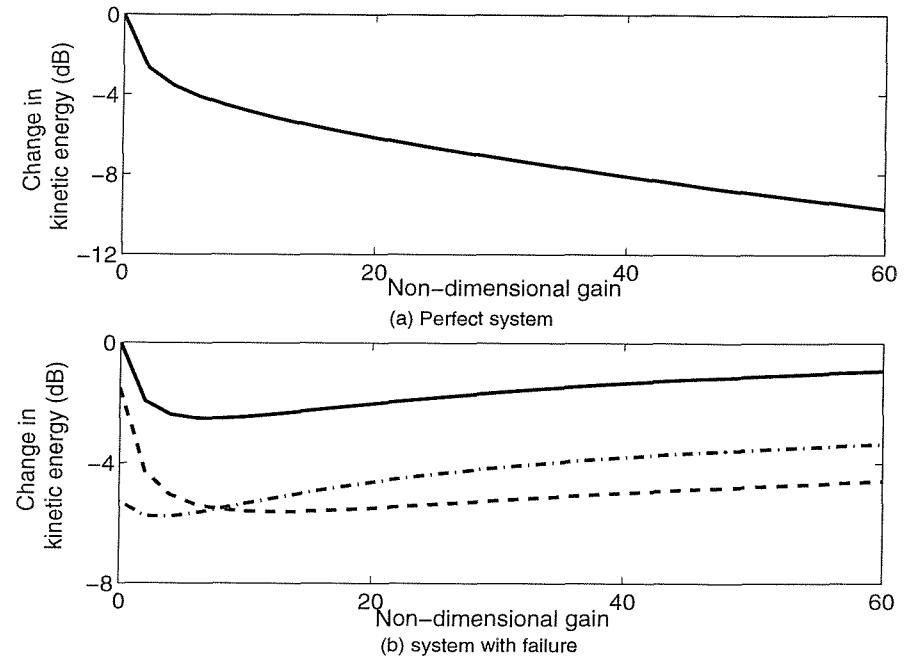

(ii) Mass centre is at 0.404l

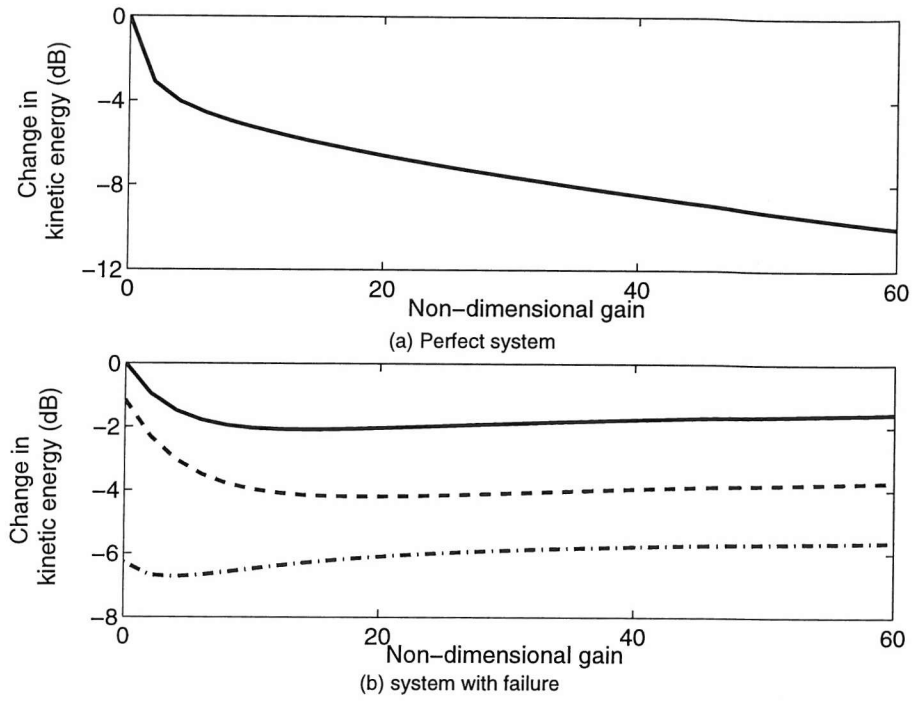

(iii) Mass centre is at 0.596l

Figure 5.8 Change in kinetic energy of the two-mount system Total kinetic energy: _____, translational kinetic energy: ----------, Rotational kinetic energy: -.-.-.-.-.-

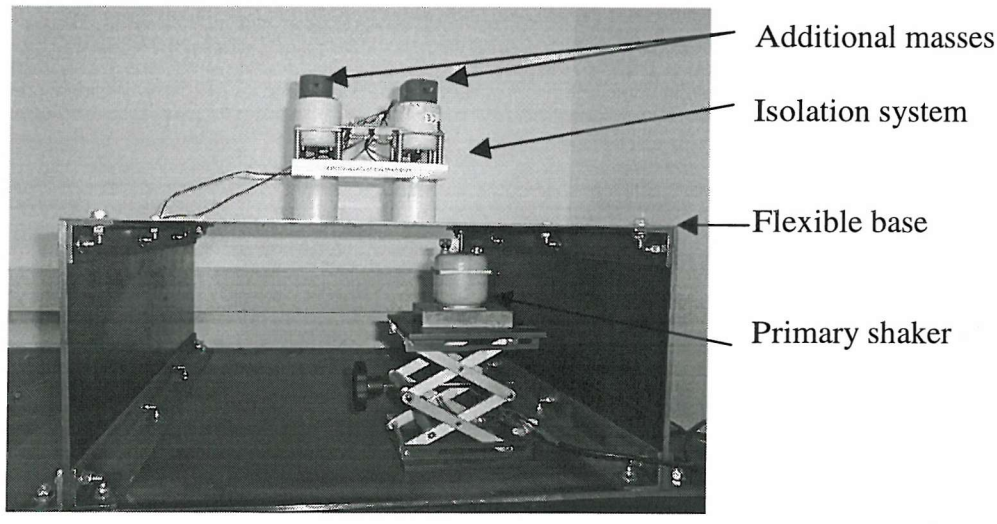

Figure 5.9 Two-mount isolation system with additional masses on CFCF flexible base structure

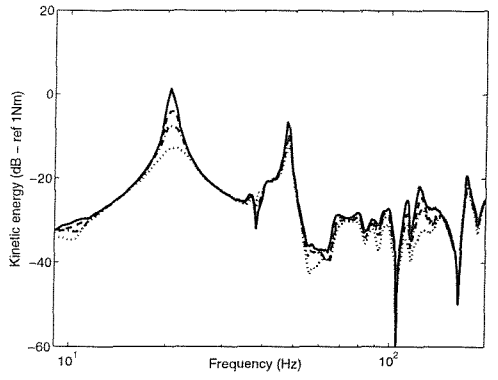

(a) Perfectly working system Mass centre - 0.5l

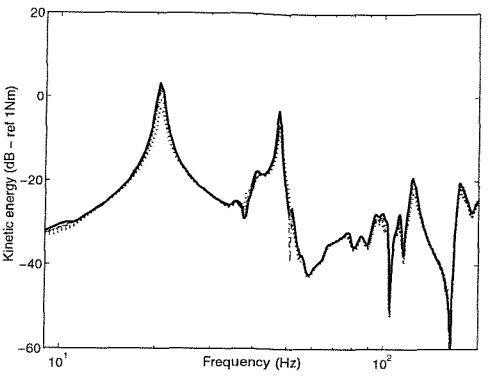

(d) System with single channel failure Mass centre – 0.5l

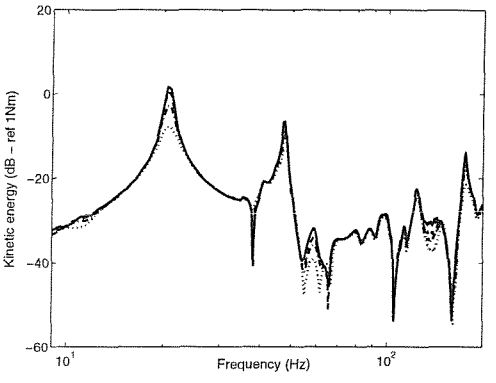

(b) Perfectly working system Mass centre - 0.404l

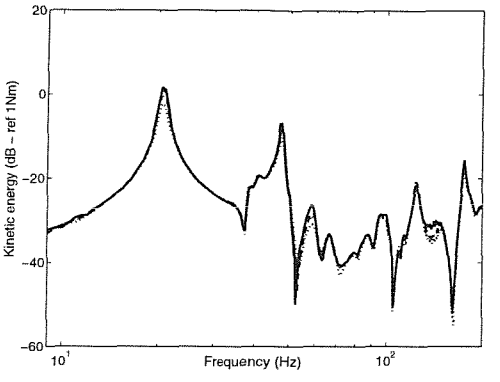

(f) System with single channel failure Mass centre – 0.404l

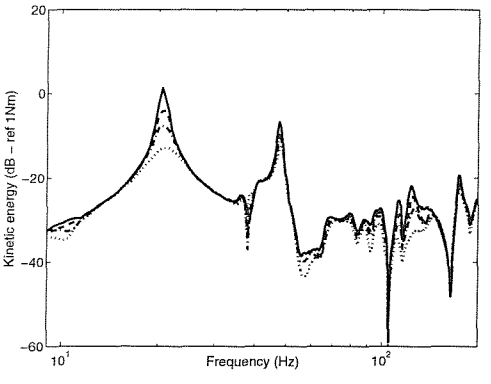

(c) Perfectly working system Mass centre - 0.596l

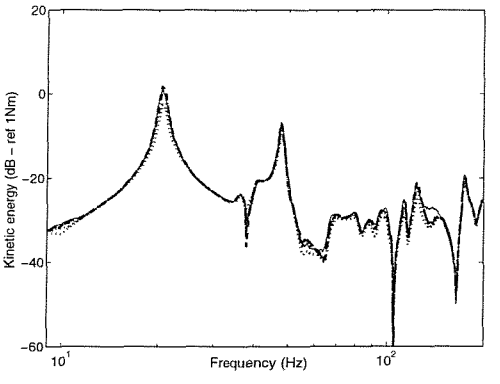

(f) System with single channel failure Mass centre – 0.596l

Figure 5.10 Total kinetic energy plots for a system on a moving inelastic base (Measurement). Power amplifier gain 0: _____, power amplifier gain 0.06: --------, power amplifier gain 0.12: -.-.-.-.-., power amplifier gain 0.25: .....

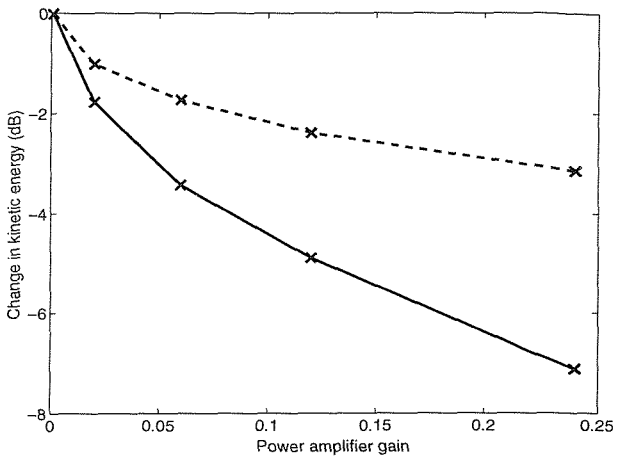

(a) Mass centre is at 0.5l

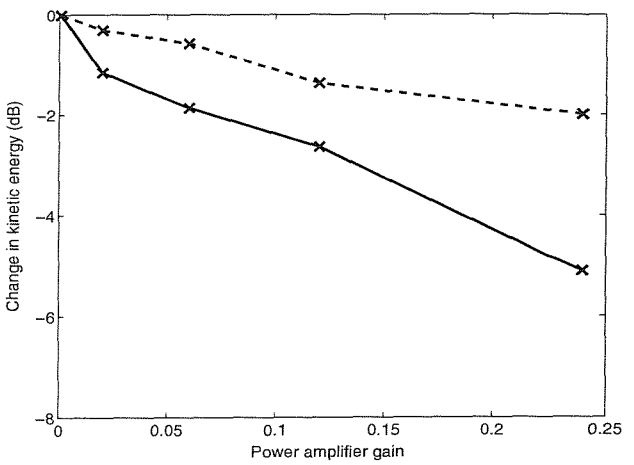

(b) Mass centre is at 0.404l

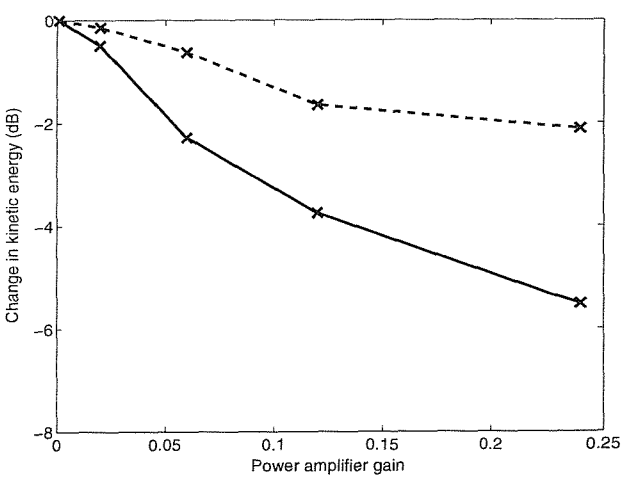

(c) Mass centre is at 0.596l

Figure 5.11 Change in total kinetic energy of the two-mount system on a moving inelastic base (Measurement) Perfectly working system: _____, system with single channel failure: --------.

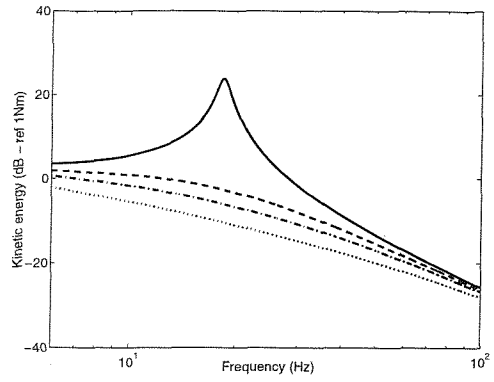

(a) Perfectly working system
Mass centre - 0.5l

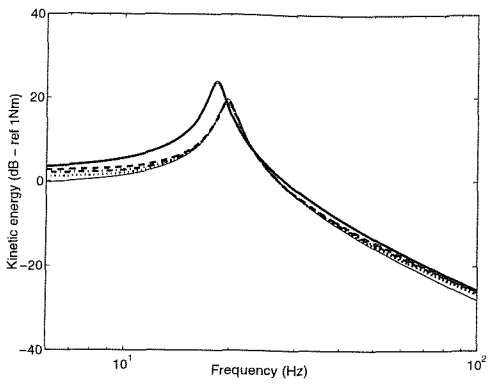

(d) System with single channel failure
Mass centre – 0.5l

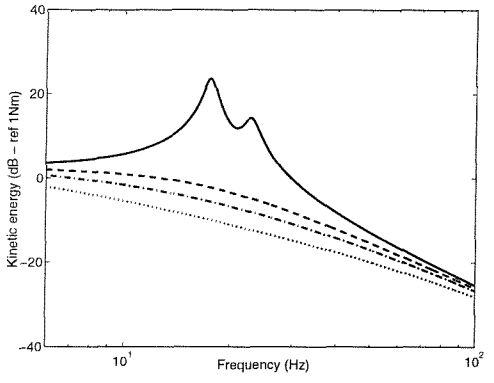

(b) Perfectly working system
Mass centre - 0.404l

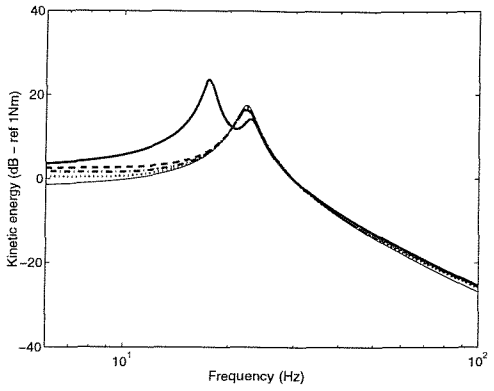

(e) System with single channel failure
Mass centre – 0.596l

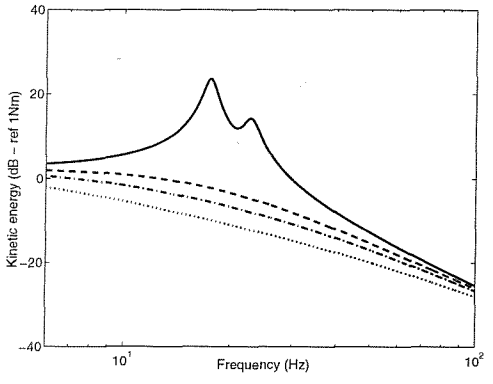

(c) Perfectly working system
Mass centre - 0.596l

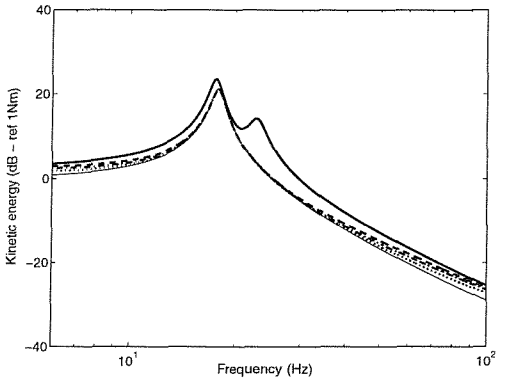

(f) System with single channel failure
Mass centre – 0.596l

Figure 5.12 Total kinetic energy plots of the two-mount system on a moving inelastic base (Simulations). Non-dimensional gain 0: _____, non-dimensional gain 20: --------, non-dimensional gain 30: -.-.-.-.-., non-dimensional gain 50: ....., infinite gain / large gain:_____

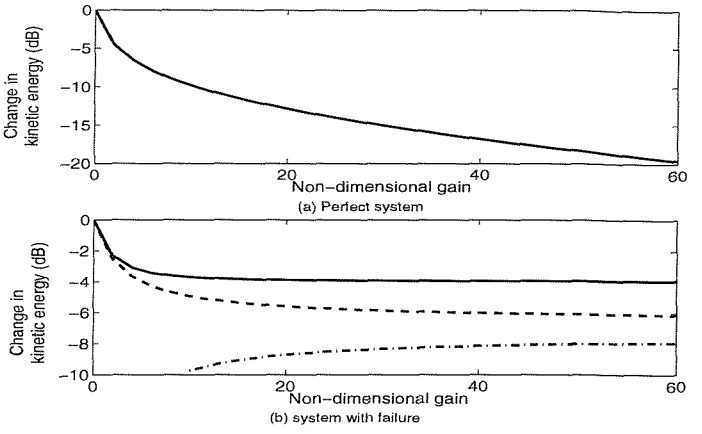

(i) Mass centre is at 0.5l

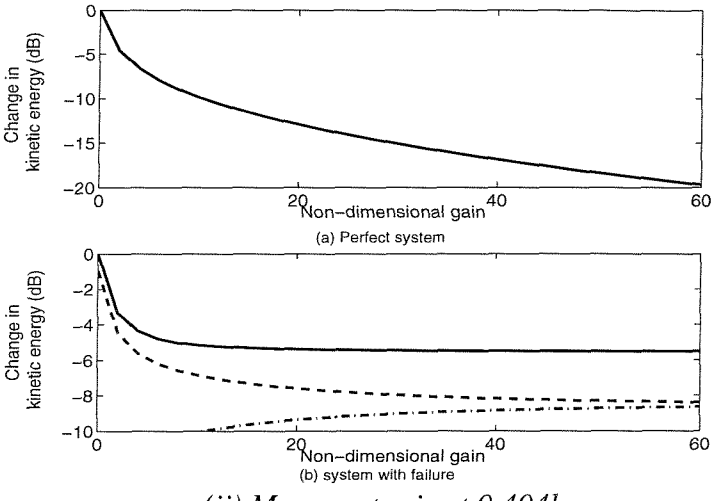

(ii) Mass centre is at 0.404l

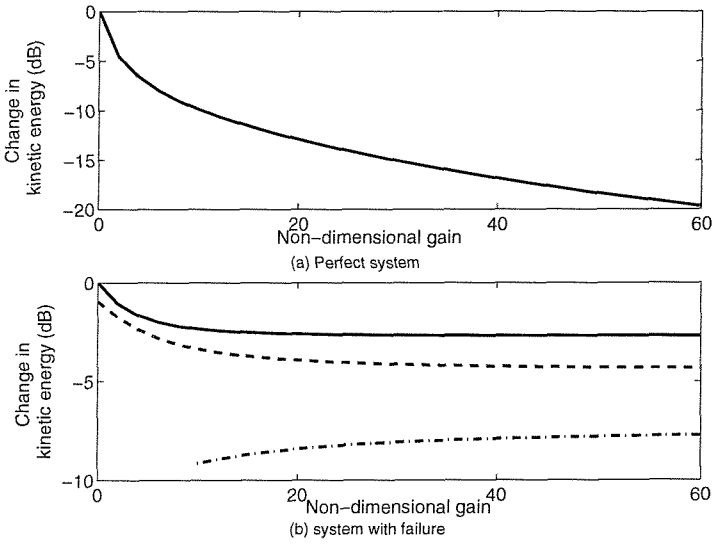

(iii) Mass centre is at 0.596l

Figure 5.13 Change in kinetic energy of the two-mount system. Total kinetic energy: _____, translational kinetic energy: - - - - - - - - -, Rotational kinetic energy:-.-.-.-.-.

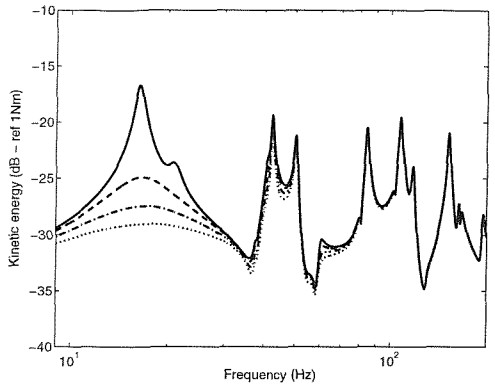

(a) Perfectly working system
Mass centre - 0.5l

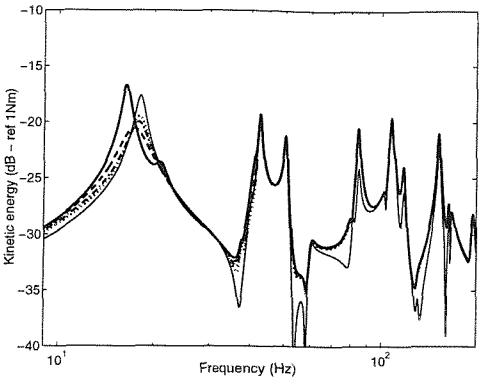

(d) System with single channel failure
Mass centre – 0.5l

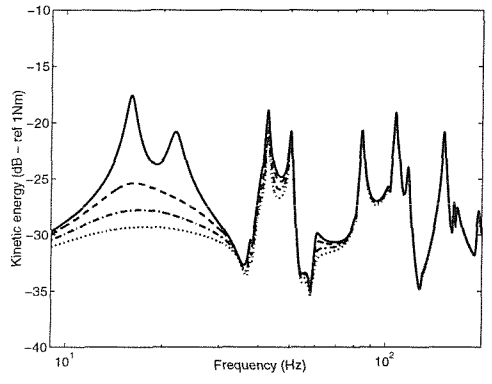

(b) Perfectly working system
Mass centre - 0.404l

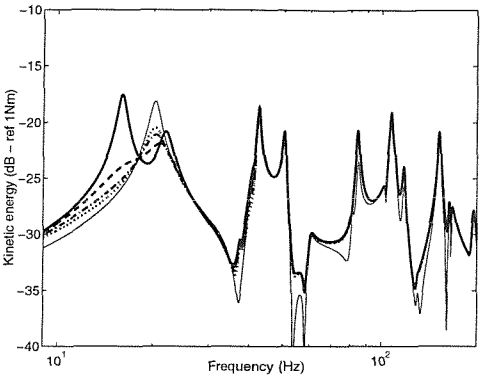

(e) System with single channel failure
Mass centre – 0.404l

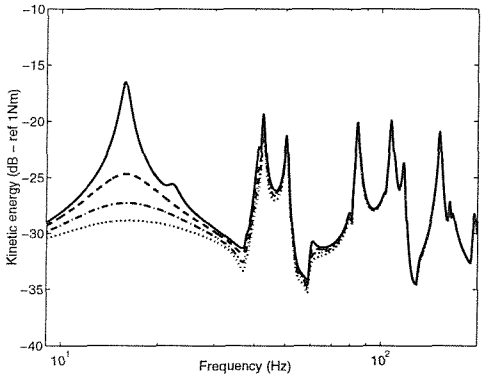

(c) Perfectly working system
Mass centre - 0.596l

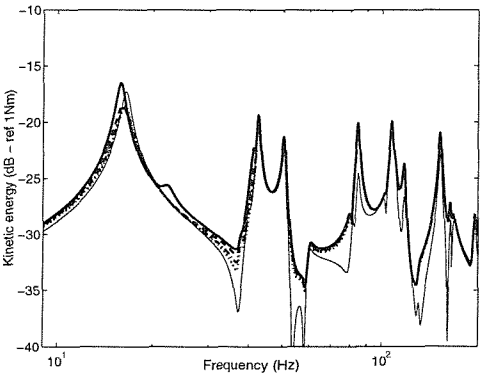

(f) System with single channel failure
Mass centre – 0.596l

Figure 5.14 Total kinetic energy plots for a system on a moving inelastic base (Simulations). Non-dimensional gain 0: _____, non-dimensional gain 5: --------, non-dimensional gain 10: -.-.-.-.-., non-dimensional gain 15: .....infinite gain:_____

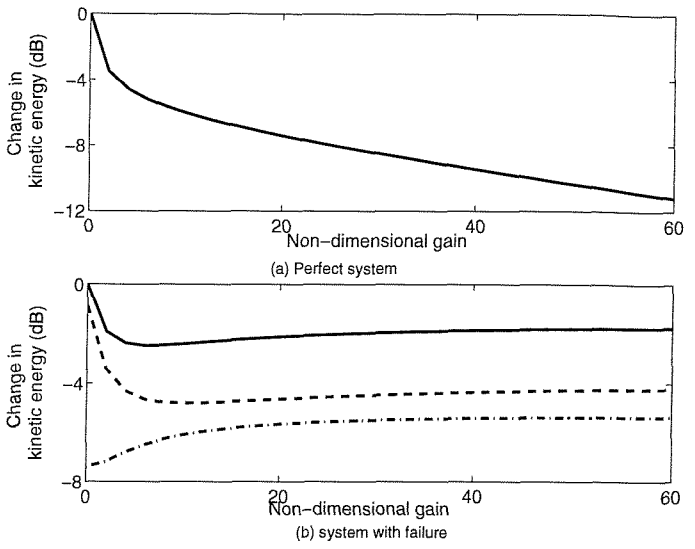

(i) Mass centre is at 0.5l

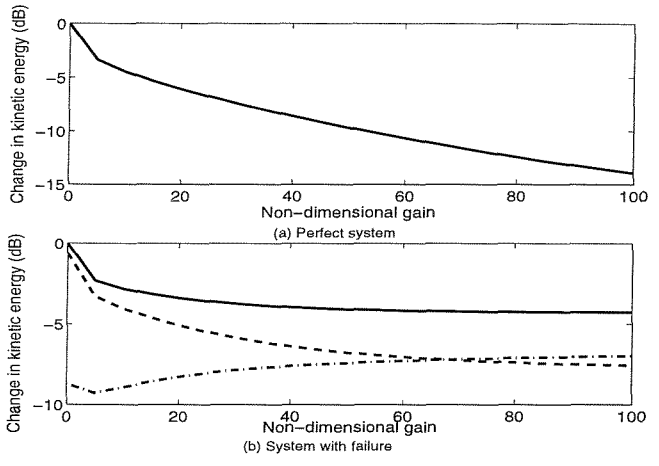

(ii) Mass centre is at 0.404l

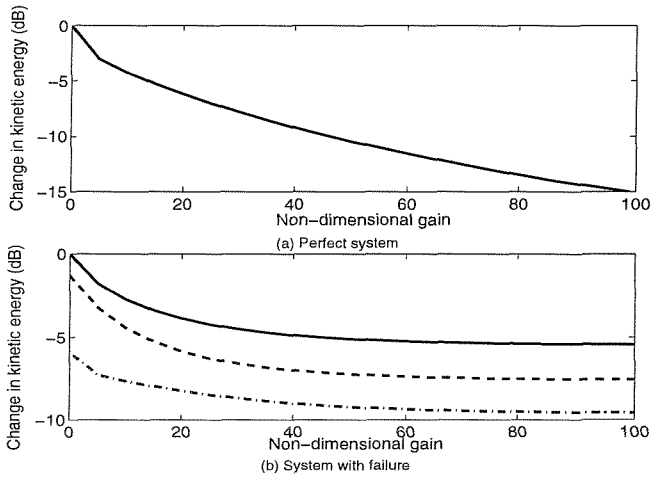

(iii) Mass centre is at 0.596l

Figure 5.15 Change in kinetic energy of the two-mount system Total kinetic energy: _____, translational kinetic energy: - - - - - - - - -, Rotational kinetic energy:-.-.-.-.-.

Chapter 6

Conclusions and recommendations for further work

This thesis has described an investigation carried out on the *stability and performance of active vibration isolation systems* using acceleration, velocity and displacement feedback control with a decentralised control strategy. This chapter summarises the conclusions of this thesis and suggests some areas of further research on this topic.

6.1 Conclusions

The concept of active vibration isolation was described in Chapter 2 using a SDOF system. This concept was applied to a two-mount system with decentralised feedback control strategies. Simulations and measurements were conducted using this two-mount system. Although, the simulations presented in Chapter 2 showed that all three strategies provide a stable system with a better performance than the original passive system the measurements showed that all three strategies are only conditionally stable in practice. It was shown that this discrepancy between the simulations and the measurements in terms of stability and performance is due to instrumentation.

In Chapter 3 the sources of instability (that causes the discrepancy) at low frequencies have been investigated. It was shown that low frequency sources of instability could be treated as high-pass filters. Considering the three configurations, the acceleration feedback control system exhibited the lowest maximum allowable gain. The velocity feedback control system is unconditionally stable with one high-pass filter (or with a real integrator) and displacement feedback control system is unconditionally stable for up to two high-pass filters. Some simple formulae for the maximum allowable gains for these systems and corresponding frequencies at which these systems become unstable (critical frequencies) were derived. It was shown that although displacement feedback gives better stability at low frequencies, its closed-loop performance is poor.

On the other hand, however, velocity feedback control system gives a stable system with better closed-loop performance.

In chapter 4 the sources of high frequency instabilities were investigated. It was shown that although the displacement feedback control strategy exhibited good low frequency stability, with time-delay and low-pass filters in the feedback loop, it exhibits poor stability characteristics. It was also shown that among the three strategies the acceleration feedback control system has excellent high frequency stability characteristics. However the acceleration feedback control system with time-delay gives poor closed-loop performance. Thus considering the high frequency stability and performance characteristics together, velocity feedback control is the most attractive control strategy. Simple formulae were derived for the maximum allowable gain with high frequency sources of instabilities for all three strategies.

Considering low and high frequency sources of instabilities, velocity feedback control strategy was thus established as be more robust and hence most attractive for vibration isolation. Based on this conclusion the two-mount system with velocity feedback control was further investigated for the uncertainty due to component failure in Chapter 5. It was found that that the failure does not affect the stability of the system (Appendix F) but it does deteriorate the performances significantly. It was observed that in a two-mount system with a single channel failure only a small improvement in performance is possible when the gain in the working mount is increased from zero to infinity (a large gain).

Thus, overall, this thesis has presented an investigated the *stability and performance of active vibration isolation systems* integrating (a) structural dynamics (b) signal conditioning devices and (c) actuators and sensors. Further it also has investigated into the uncertainty due to component failure.

6.2 Design Guidelines

A velocity feedback control system exhibits better stability than either a displacement or acceleration feedback system at both low and high frequencies, and hence is recommended as the most attractive control system for vibration isolation applications. An acceleration feedback system has a maximum gain proportional to the damping ratio in the mount due low frequency instabilities (Table 3.1, page 81), and hence may have only a small maximum gain. Similarly the maximum gain for displacement feedback control is proportional to the damping ratio in the mount due to high frequency instabilities (Table 4.1, page 108), and hence may also have only a small maximum gain. The maximum feedback gain for velocity feedback is however proportional to the inverse of the damping factor for both low and high frequency instabilities, and so this can be large if the system is lightly damped before control.

For a velocity feedback control system, lowering the cut-off frequency of the real integrator (and high-pass filters) improves the stability. However most piezoelectric accelerometers are not capable of a true DC response and can only produce a charge when acted upon by dynamic forces. In addition to obtain a low sensitivity of the accelerometer to environmental effects also demands a reasonable cut-off frequency of the integrator. Thus the choice of cut-off frequency is always a compromise between the stability of the system and the sensitivity of the accelerometer.

With present technology it is easy to measure acceleration response. Velocity and displacement signals can be obtained by integration. An ideal integrator has a frequency response given by $\frac{1}{j\omega}$ and hence at zero frequency (and near zero frequencies) it would give unacceptably high velocity (or displacement) signals. Thus it is essential to have a reasonable cut-off frequency of the integrator. It is therefore recommended that the characteristics of accelerometer and the importance of low frequency response should be considered in the design of the feedback controller.

Amplifiers and practical dynamics of integrators act as high-pass filters. It was shown in this thesis that increasing the number of high-pass filters reduces the maximum

gain available. It is therefore recommended that the number of high-pass filters should be minimised and the cut-ff frequency also should be kept as low as possible.

The accelerometer should also be selected in such a way that the accelerometer resonance frequency is well above that of the frequency range of interest. The number of low-pass filters in the control system should also be reduced for high frequency stability. For improved stability the cut-off frequency of the low-pass filters should be set well above the system resonance frequency. Another important factor is the time delay in the system, which causes high frequency instability. To maintain reasonable stability, steps must be taken to reduce the time-delay in the system.

6.3 Recommendations for further work

The work presented in this thesis considers active vibration isolation from random base vibration. However isolation of a piece of equipment from shock, which is a transient excitation is an important area. Although this transient will die out eventually, the piece of equipment may be damaged (or malfunction) due to shock. Thus the stability and performance of the active vibration isolation systems considered here should be investigated for shock.

The investigation carried out assumes that the base is not moving in space significantly but has a random vibration. It is possible to have a vibrating base, which moves in space. Dynamically decoupling delicate equipment from such a moving base some times must be accomplished under the restriction of suspension rattle space. Even if the delicate equipment is actively isolated, damage can occur due to the base movement. Thus the limitations, stability and performance of the active vibration isolation systems considered here should be investigated for this case accomplishing the restriction of suspension rattle space.

References

1. M. Serrand 2000 *Direct velocity feedback control of equipment vibration.* MPhil thesis, ISVR, University of Southampton.
2. S.M. Kim, S.J. Elliott, and M.J. Brennan 2001 *IEEE Transactions on control systems technology* **9**(1), 93-100. Decentralized control for Multichannel active vibration isolation.
3. C.E. Crede and J.E. Ruzicka 1996 *Shock and vibration handbook,* Chapter 30 Theory of vibration isolation, editor. C.M.Harris McGraw-Hill.
4. M. Serrand 1998 *Active isolation of base vibration.* MSc Dissertation, ISVR, University of Southampton
5. D.J. Mead 1999 *Passive vibration control.* John Wiley & Sons Ltd.
6. M. Serrand and S.J. Elliott 2000 *Journal of sound and vibration* **234**(4), 681-704. Multichannel feedback control for the isolation of base-excited vibration.
7. G.W.V Santen 1958 *Mechanical vibration* Cleaver-Hume Press, London.
8. K.N. Tong 1960 *Theory of mechanical vibration* John Wiley and Sons, New York.
9. F. Tse, I. Morse, and R.Hinkle 1978 *Mechanical vibrations -Theory and applications.* Second edition. Prentice - Hall, London.
10. W.T. Thomson 1973 *Theory of vibration (with applications)* Prentice-Hall, New Jersey.
11. M. Lalanne, P. Berthier and J.D. Hagopian 1983 *Mechanical vibrations for engineers.* John Wiley and Sons.
12. D.A. Bies and C.H. Hansen 1988 *Engineering noise control.* Unwin Hyman, London.
13. C.R. Fuller, S.J.Elliott, and P.A. Nelson 1996 *Active control of vibration.* Academic Press, London.
14. S. A Collins and A.H.Von Flotow 1991 *Proceedings of the 42nd Congress of the International Astronautical Federation*, Montreal, Canada. Active isolation for spacecraft.
15. M.J. Brennan, J. Garcia-Bonito, S.J.Elliott, A. David, R.J. Pinnington 1999 *Smart Mater. Struct* **8,** 145-153. Experimental investigation of different actuator technologies for active vibration control.
16. S.A. Collins, D.W. Miller, and A.H.V. Flotow 1994 *Journal of sound and vibration* **173**(4), 471-501. Distributed sensors as spatial filters in active structural control.

17. J. D'azzo, J. and C.H. Houpis 1995 *Linear control system analysis and design.* McGraw-Hill Inc.
18. K. Ogata 1970 *Modern control engineering.* Prentice-Hall.
19. T.J. Sutton, S.J. Elliott, D.A.C. Jessop, M.J. Brennan and K.H. Heron 1997 *Journal of sound and vibration* **205**(1), 81-101. Active isolation of multiple structural waves on a helicopter gearbox support strut.
20. G. Housner, L. Bergman, T. Caughey, A. Chassiakos, R. Claus R. Skelton, S. Masri, T. Soong, B. Spencer and J. Yao 1997 *Journal of engineering mechanics* **123,** 897-947. Structural control: Past present and future.
21. M.A. Franchek, M.W. Runn, and R.J. Bernhard 1995 *Journal of sound and vibration* **189,** 565-585. Adaptive passive vibration control.
22. E.E Ungar, 1992 Vibration *isolation- Noise and vibration control engineering.* Editors L Beranek and I.L. Ver. Wiley, Chichester.
23. M.R.F. Kidner 1999 *An active vibration neutraliser.* PhD thesis, ISVR, University of Southampton.
24. K.J. Kitching, D.J. Cole and D. Cebon 2000 *Journal of dynamic systems measurement and control* **122,** 498-506. Performance of a semi-active damper for heavy vehicles.
25. K. Yi and B.S. Song 1999 *Proceedings of Institution of the Mechanical engineers* **213**(Part D), 293-303. A new adaptive sky-hook control of vehicle semi-active suspensions.
26. M. Ahmadian 1999 *Journal of vibration and control* **5,** 217-232. On the isolation properties of semi-active dampers.
27. E.M. Elbeheiry 1998 *Journal of sound and vibration* **214**(2), 269-283. A method for preview vibration control of systems having forcing inputs and rapidly switched dampers.
28. N. Jalili 2000 *Journal of sound and vibration* **238**(3), 481-494. A new perspective for semi-automated structural vibration control.
29. D. Karnopp, M.J. Crosby, and R.A. Harwood 1974 *Journal of engineering for industry* 619-626. Vibration control using semi-active force generators.
30. M.K. Kwak and D. Sciulli 1996 *Journal of sound and vibration* **191**(1), 15-28. Fuzzy-logic based vibration suppression control experiments on active structures.
31. S. Skogestad and I. Postlethwaite 1996 *Multivariable feedback control: Analysis and design.* John Wiley & Sons, Inc.

32. D.L. Hall and A.B. Flatau 1998 *Journal of sound and vibration* **211**(3), 481-494. On analog feedback control for magnetostrictive transducer linearization.
33. M.Z. Ren, K. Seto, and F. Doi 1997 *Journal of sound and vibration* **205**(1), 57-80 Feedback structure-borne sound control of a flexible plate with an electromagnetic actuator: the phase lag problem.
34. M.J. Brennan and S.M. Kim 2001 *Journal of sound and vibration* **246(2),** 281-296. Feed forward and feedback control of sound and vibration - a Wiener filter approach.
35. N. Sungsoo and L. Librescu 1998 *Smart Mater. Struct.* **7,** 833-845. Oscillation control of cantilevers via smart materials technology and optimal feedback control: actuator location and power consumption issues.
36. Y.A. Khulief 2001 *Journal of sound and vibration* **242**(4), 681-699. Vibration suppression in rotating beams using active modal control.
37. C.J. Damaren and L. Le-Ngoc 2000 *Transactions of the ASME Journal of vibration and acoustics* **122,** 69-76. Robust active vibration control of a band-saw blade.
38. S.H. Chen, Z.D. Wang, and X.H. Liu 1997 *Journal of sound and vibration* **200**(2), 167-177. Active vibration control and suppression for intelligent structures.
39. A. Hac 1986 *Journal of guidance and control, Transactions of the ASME* **108,** 106-110. Stochastic optimal control of vehicles with elastic body and active suspension.
40. D. Hrovat and M. Hubbard 1981 *Journal of guidance and control, Transactions of the ASME* **103,** 228-236. Optimal vehicle suspensions minimizing RMS rattle space, sprung-mass acceleration and jerk.
41. M.J. Balas 1979 *Journal Guidance and control* **2**(3), 252-253. Direct velocity feedback control of large space structures.
42. X. Huang, S.J. Elliott, and M.J. Brennan 2001 *ISVR Technical Memorandum No* 866, Active isolation of flexible equipment structure on a rigid base.
43. S.M. Joshi 1986 *Journal of guidance and control* **9**, 85-91. Robustness properties of collocated controllers for flexible spacecraft.
44. M. Morari and E. Zafiriou 1989 *Robust process control.* Prentice - Hall, Inc.
45. M.I Friswell and D.J Inman 1999 *Smart Mater. Struct.* **8,** 285-291. The relationship between positive position feedback and output feedback controllers.
46. J. L. Fanson and T.K. Caughey 1990 *AIAA Journal* **28**(4), 717-724. Positive position feedback for large space structures.
47. C. J. Goh and T. K. Caughey 1985 *International Journal of Control* **41**(3), 787-802. On the stability problem caused by finite actuator dynamics in the control of large space structures.

48. A. Preumont 1997 *Vibration control of active structures – An introduction.* Kluwer Academic publishers.

49. J.T. Pearson, R.M. Gooddall, and I. Lyndon 1994 *Computing and control engineering journal* **5**(6), 277-284. Active control of helicopter vibration.

50. R. Maier, M. Pucher, and W. Gembler 1999 Proceedings *of Active 99: The international symposium on active control of sound and vibration.* Helicopter interior noise reduction by active vibration isolation with smart gearbox struts.

51. S.D. Gennaro 1998 *Journal of Guidance control and dynamics* **21**(3), 400-408. Active vibration suppression in flexible spacecraft attitude tracking.

52. L. Vaillon, B. Petitjean, B. Frapard and D. Lebihan 1999 *Smart Mater. Struct.* **8,** 781-790. Active isolation in space truss structures: from concept to implementation.

53. E. Esmailzadeh and F. Fahimi 1997 *Vehicle system dynamics* **27**(2), 89-107. Optimal adaptive active suspensions for a full car model.

54. M. Ramsbottom, D.A. Crolla, and A.R. Plummer 1999 *Proceedings of Institution of Mechanical Engineers* **213**(Part D) 1-17. Robust adaptive control of an active vehicle suspension system.

55. M. Winberg, S. Johansson and I. Claesson 1999 *Proceedings of Active 99: The international symposium on active control of sound and vibration.* Active vibration isolation in ships: An ASAC (active structure acoustic control) approach.

56. M.D. Jenkins, P.A. Nelson, R.J. Pinnington and S.J.Elliott 1993 *Journal of sound and vibration* **166**(1), 117-140. Active isolation of periodic machinery vibrations.

57. K. Nevala and M. Jarviluoma 1997 *Proceedings of the 4th annual conference on mechatronics and machine vision in practice.* An active vibration damping system of a driver's seat for off-road vehicles.

58. C. Erin and B. Wilson 1998 *Journal of sound and vibration* **218**(1), 81-101. An improved model of a pneumatic vibration isolator: Theory and experiment

59. R.C. Dorf 1967 *Modern control systems.* Addison Wesley publishing company.

60. D.K. Anthony and S.J.Elliott 2000 *Journal of sound and vibration* **237**(2), 223-244. Comparison of the effectiveness of minimizing cost function parameters for active control of vibrational energy transmission in a lightly damped structure.

61. A. Baz and S. Poh 1988 *Journal of sound and vibration* **126**(2), 327-343. Performance of an active control system with piezoelectric actuators.

62. J.Q. Pan and C.H. Hansen 1993 *Journal of Acoustical society of America* **93,** 1947-1953. Active control of vibrational power flow from a vibrating rigid body to a flexible panel through two active isolators.

63. C.Q. Howard, S.D. Snyder, and C.H. Hansen 2000 *Journal of sound and vibration* **233**(4), 573-585. Calculation of vibratory power transmission for use in active vibration control.

64. M.J. Brennan, S.J.Elliott, and R.J. Pinnington 1995 *Journal of sound and vibration* **186**(4), 657-688. Strategies for the active control of flexural vibration on a beam.

65. B.R. Mace 1987 *Journal of sound and vibration* **114**(2), 253-270. Active control of flexural vibrations.

66. X. Huang, S.J.Elliott, and M.J. Brennan 2001 *ISVR Technical Memorandum No* 879. Active vibration isolation of a flexible equipment structure on a flexible base.

67. S.J.Elliott, M. Serrand, and P. Gardonio 2001 *Transactions of the ASME Journal of vibration and acoustics* **123,** 250-261. Feedback stability limits for active isolation systems with reactive and inertial actuators.

68. J. Tang and K.W. Wang 2001 *Smart Mater. Struct* **10,** 794-806. Active-passive hybrid piezoelectric networks for vibration control: comparisons and improvement.

69. A.H. Von Flotow 1988 *Proceedings of the 27th conference on decision and control, Austin, Texas.* An expository overview of active control of machinery mounts.

70. P. Gardonio, S.J.Elliott, and R.J. Pinnington 1997 *Journal of sound and vibration* **207**(1), 95-121. Active isolation of structural vibration on a multiple- degree - of - freedom system, Part II: Effectiveness of active control strategies.

71. Z.H. Wang and H.Y.Hu 1999 *Journal of sound and vibration* **226**(1), 57-81. Delay-independent stability of retarded dynamic systems of multiple degrees of freedom.

72. D. Karnopp 1995 *ASME Journal of Mech Des.* **117,** 177-185. Active and semi-active vibration isolation.

73. G.J. Balas and P.M. Young 1999 *IEEE transactions on control systems technology* **7**(6), 692-705. Sensor selection via closed-loop control objectives.

74. R. Kashani, S. Kiriczi 1992 *vehicle system dynamics* **21**(6), 361-384. Robust stability analysis of LQG-controlled active suspension with model uncertainty using structured singular value, mu, method.

75. S. Arusawatwung 1996 *International journal of control* **65,** 347-367. Stability of retarded delay differential systems.

76. J. Garcia-Bonito, M.J. Brennan, S.J.Elliott, A. David and R.J. Pinnington 1997 *Smart Mater. Struct.* **7,** 31-42. A novel high-displacement actuator for active vibration control.

77. S.Y. Yang and W.H. Huang 1998 *Journal of sound and vibration* **216**(3), 529-538. Is a collocated piezoelectric sensor/actuator pair feasible for an intelligent beam?

78. M. Malowicki and D.J. Leo 2001 *shock and vibration* **8**(5), 271-285. Active vibration isolation using an induced strain actuator with application to automotive seat suspension
79. G. Bohannan, H. Schmidt, D. Brandt and M. Mooibroek 1999 *Ferroelectrics* **224**(1-4), 639-645. Piezoelectric polymer actuators for active vibration isolation in space applications.
80. Jae-Hung Han, Keun-Ho Rew, and In Lee 1997 *Smart Mater. Struct* **6,** 549-558. An experimental study of active vibration control of composite structures with a piezo-ceramic actuator and a piezo-film sensor.
81. K.A. Stroud, 1995 *Engineering Mathematics*. 4th edition, Macmillan press ltd.
82. G.B. Warburton, 1951 *Proceedings of the institute of Mechanical Engineering* **168**, 371-384. The vibration of rectangular plates.
83. P. Gardonio and M. J. Brennan, 2002 *Journal of sound and vibration* **249**(3), 557-573, On the origins and development of mobility and impedance methods in structural dynamics.
84. K.A. Ananthaganeshan, M.J. Brennan and S.J. Elliott 2001 *ISVR Technical Memorandum No* 870, Low and high frequency instabilities in feedback control of a vibrating single degree of freedom system.
85. K.G. McConnell, 1995 *Vibration testing: Theory and Practice*, John Wiley & Sons Inc.
86. M. Serridge, T.R Licht, 1986, *Piezoelectric accelerometer and vibration preamplifier Handbook*, B&K.
87. W. Bolton, 1996 *Measurement and instrumentation systems*, Newnes An imprint of Butter Worth-Heinemann
88. S.M. Kim, S.J. Elliott, and M.J. Brennan 1999 *ISVR Technical Memorandum No* 845, Active vibration isolation of a 3-Dimensional structure using velocity feedback control
89. R. J. Higgins, 1983 *Electronics with digital and analog integrated circuits*, Prentice-hall, Inc.
90. G.H. Golub and C. F Van Loan 1983 *Matrix computations* North Oxford Academic, Oxford.
91. W.W. Bell 1975 *Matrices for scientists and engineers*, Van Nostrand Reinhold Company.
92. P. Gardonio, E. Bianchi, and Stephen J. Elliott 2002 Proceedings *of Active 2002: The international symposium on active control of sound and vibration.* Smart panel with

multiple decentralized units for the control of sound transmission. Part II: Design of the decentralized control units.

93. L. Cremer, M. Heckl and E.E. Ungar 1988 *Structure-Borne Sound.* Berlin: Springer-Verlag.

Appendix A

Commercial active vibration isolation solution providers

In this appendix a brief survey of commercial active vibration isolation equipment manufactures and solution providers are given base on an Internet search. The corresponding Internet address is given in parenthesis.

Technical Manufacturing Corporation (TMC™) produces active vibration isolation tables (http://www.techmfg.com/Products/LabTables_TableTops/20SERIES.htm) for general purpose high precision applications such as (a) Atomic Force Microscopes, (b) Scanning Probe Microscopes, (c) Commercial Interferometers, (d) Electro-Physiology Recording and (d) Semiconductor Inspection Equipment. They use a tailor made actuator unit (STACIS™ 2000 – US Patent No 5660255), which is essentially an active/passive mount and is mounted in each leg of the table. These piezoelectric actuators receive information on disturbances through absolute velocity sensors. This information from the sensors causes the actuators to expand or contract as demanded by a feed-forward controller.

Lord Corporation use active engine mounts in-order to isolate the engine of a rotary-wing aircraft developed by Bell™/Agusta Aerospace Company from the rest of the structure and thus reduce the cabin noise and vibration. (http://www.lord.com/news/2001/lord_corporation_selected_to_provide_active_vibration_control.htm). The active/passive mounts, consisting of actuators, are driven by small power amplifiers in response to an adaptive control system in order to dynamically decouple the engine from airframe.

Planning system incorporated- Melbourne controls Group, have produced an active isolation fitting (AIF), which is essentially an actuator with a controller. The Controller works on a feedback control technique with non-adjustable (or pre assigned) gain. This product hence requires an external sensor. It is claimed that it provides $20-30$ dB of wide band vibration

isolation (http://www.psi-controls.com/aif.htm) and could be used for precision pointing devices.

Herzan (http://www.herzan.com/herz15.htm) introduces active vibration isolation technology (they call it the AVI series) that senses vibration levels and counteracts them via an inertial feedback technique. The potential applications include: (a) measuring equipment mounts (b) microscope mounts (c) mounts for inspection stations etc. A similar product is manufactured by CSA Engineering, Inc (http://www.csaengineering.com/semicon/elite.shtml) for original equipment manufacturer (OEM) products and they call it ELITE-3. It works at 1 Hz, which is the resonance frequency of the table. A feedback control loop works on digital control principles of activates piezoelectric actuators. Electrodynamic inertial sensors are used as sensors.

Although the number of commercial companies given above is few, it can be seen that there is a wide range of vibration isolation applications for which active isolation techniques are used.

Appendix B

Stability of a base excited single-degree-of-freedom (SDOF) system

B1 Plant frequency response

From equation (2.6) (in Chapter 2) the plant frequency response function of a base excited SDOF system can be written as,

$$G(j\omega)=\frac{1}{Z_e+Z_m+Z_mY_bZ_e} \qquad \text{(B1)}$$

where $Z_m=\frac{k}{j\omega}+c$ is the impedance of a single mount. The mobility of the base and the impedance of the equipment are Y_b and Z_e respectively. Expanding the equipment impedance and base mobility in terms of their real and imaginary components gives,

$$Z_e=Z_{er}+jZ_{ei} \text{ and } Y_b=Y_{br}+jY_{bi} \qquad \text{(B2, B3)}$$

where Z_{er}, and Z_{ei}, are the real and imaginary parts of the equipment impedance respectively, and Y_{br} and Y_{bi} are the real and imaginary parts of the base mobility respectively. The terms Z_{er} and Y_{br} are always positive or zero [3,93]. Substituting equations (B2) and (B3) into equation (B1) gives,

$$G(j\omega)=\frac{1}{(Z_{er}+jZ_{ei})+\left(\frac{k}{j\omega}+c\right)\left(1+(Y_{br}+jY_{bi})(Z_{er}+jZ_{ei})\right)} \qquad \text{(B4)}$$

Letting $A+jB=(Y_{br}+jY_{bi})(Z_{er}+jZ_{ei})$, where $A=(Y_{br}Z_{er}-Y_{bi}Z_{ei})$, $B=(Y_{br}Z_{ei}+Y_{bi}Z_{er})$, equation (B4) can be written as,

$$G(j\omega)=\frac{1}{(Z_{er}+jZ_{ei})+\left(\frac{k}{j\omega}+c\right)(1+A+jB)} \qquad \text{(B5)}$$

Letting,

$$G(j\omega)=\frac{1}{(P_r+jP_i)} \tag{B6}$$

where $P_r=\left(c(1+A)+\frac{kB}{\omega}+Z_{er}\right)$ and $P_i=\left(cB-\frac{k(1+A)}{\omega}+Z_{ei}\right)$, equation (B6) can be rewritten in terms of its real and imaginary parts to give,

$$G(j\omega)=\frac{P_r}{P_r^2+P_i^2}-j\frac{P_i}{P_r^2+P_i^2} \tag{B7}$$

B2 Acceleration feedback control

The feedback frequency response function of an ideal system with acceleration feedback control is given by $H(j\omega)=j\omega g_a$. Thus the open-loop frequency response function can be written as,

$$G(j\omega)H(j\omega)=\frac{\omega g_a P_i}{P_r^2+P_i^2}+\frac{j\omega g_a P_r}{P_r^2+P_i^2} \tag{B8}$$

Applying the Nyquist criterion gives $\omega=0$ or $P_r=0$. (The imaginary part of equation (B8) is equated to zero and the resulting condition is substituted into the real part of the equation (B8). If the real part is positive then the system is unconditionally stable. If it is negative the real part is equated to –1 and solved for the maximum gain.)

Thus, when the imaginary part of the equation (B8) is zero, $\omega=0$ or $P_r=0$. When $\omega=0$ the real part is also zero. Letting the frequency at which $P_r=0$ be ω_c (i.e. critical frequency), then the real part of the open-loop frequency response function can be written as (i.e. substituting for $P_r=0$ and $\omega=\omega_c$ in equation (B8)),

$$Re\left(G(j\omega_c)H(j\omega_c)\right)=\frac{\omega_c g_a}{P_i} \tag{B9}$$

Equation (B9) can be written as,

$$Re\left(G(j\omega_c)H(j\omega_c)\right)=\frac{\omega_c g_a}{\left(cB-\frac{k(1+A)}{\omega_c}+Z_{ei}\right)} \tag{B10}$$

Substituting for $A=(Y_{br}Z_{er}-Y_{bi}Z_{ei})$ and $B=(Y_{br}Z_{ei}+Y_{bi}Z_{er})$ in equation (B10) gives,

$$Re\left(G(j\omega_c)H(j\omega_c)\right)=\frac{g_a\omega_c}{c\left(Y_{br}Z_{ei}+Y_{bi}Z_{er}\right)-\frac{k}{\omega_c}\left(1+Y_{br}Z_{er}-Y_{bi}Z_{ei}\right)+Z_{ei}} \quad \text{(B11)}$$

Case 1: The equipment is mass-like

If the equipment is mass-like then $Z_e = j\omega m_e$ and hence $Z_{er}=0$ & $Z_{ei}=\omega m_e$. Substituting these quantities in equation (B11) gives,

$$Re\left(G(j\omega_c)H(j\omega_c)\right)=\frac{g_a\omega_c}{c\omega_c m_e Y_{br}-\frac{k}{\omega_c}\left(1-\omega_c m_e Y_{bi}\right)+\omega_c m_e} \quad \text{(B12)}$$

Now considering $P_r=\left(c(1+A)+\frac{kB}{\omega_c}+Z_{er}\right)=0$ at $\omega=\omega_c$ and substituting for A and B gives,

$$c\left(1+Y_{br}Z_{er}-Y_{bi}Z_{ei}\right)+\frac{k}{\omega_c}\left(Y_{br}Z_{ei}+Y_{bi}Z_{er}\right)+Z_{ei}=0 \quad \text{(B13)}$$

Substituting for $Z_{er}=0$ & $Z_{ei}=\omega m_e$ in equation (b13) and rearranging gives,

$$\left(1-\omega_c m_e Y_{bi}\right)=-\frac{k}{c}m_e Y_{br} \quad \text{(B14)}$$

Substituting (B14) in equation (B12) gives,

$$Re\left(G(j\omega_c)H(j\omega_c)\right)=\frac{g_a\omega_c}{\left(c+\frac{k^2}{c\omega_c^2}\right)\left(Y_{br}\omega_c m\right)+\omega_c m} \quad \text{(B15)}$$

Since $Y_{br}\geq 0$[3,93] and all other parameters such as g_a, k, c, ω_c etc (in equation (B15)) are also greater than zero the real part of the open loop frequency response is positive when the open-loop frequency response plot crosses the real axis. Hence the system is unconditionally stable irrespective of the nature of the base mobility.

Case 2: The equipment is stiffness-like

If the equipment is stiffness-like then $Z_e=-j\frac{k_e}{\omega}$, and hence $Z_{er}=0$ and $Z_{ei}=-\frac{k_e}{\omega}$

Substituting these quantities in equation (B11) gives,

$$Re\left(G\left(j\omega_c\right)H\left(j\omega_c\right)\right)=\frac{-g_a\omega_c}{\frac{k_e}{\omega_c}cY_{br}+\frac{k}{\omega_c}\left(1+\frac{k_e}{\omega_c}Y_{bi}\right)+\frac{k_e}{\omega_c}} \tag{B16}$$

Now substituting for $Z_{er}=0$ and $Z_{ei}=-\frac{k_e}{\omega}$ in equation (B13) and rearranging gives,

$$\left(1+\frac{k_e}{\omega_c}Y_{bi}\right)=\frac{kk_e}{c\omega_c^2}Y_{br} \tag{B17}$$

Substituting (B17) in (B16) gives,

$$Re\left(G\left(j\omega_c\right)H\left(j\omega_c\right)\right)=\frac{-g_a\omega_c}{\left(c+\frac{k^2}{c\omega_c^2}\right)\left(Y_{br}\frac{k_e}{\omega_c}\right)+\frac{k_e}{\omega_c}} \tag{B18}$$

Since $Y_{br}\geq 0$[3,93] and all other parameters are positive, the real part is always negative irrespective of the nature of the base mobility. The maximum gain can be obtained by equating the real part to –1. This gives,

$$g_{a\_\max}=\frac{1}{\omega_c}\left(\left(c+\frac{k^2}{c^2\omega_c^2}\right)\left(Y_{br}\frac{k_e}{\omega_c}\right)+\frac{k_e}{\omega_c}\right) \tag{B19}$$

(Note that if the system critical frequency is small then it has a large gain margin)

Special case 1: Base is either mass-like or stiffness-like

This gives $Y_b=-j\frac{1}{m_b\omega}$ or $Y_b=j\frac{\omega}{k_b}$ where m_b and k_b are mass and the stiffness of the base.

For both of these cases $Y_{br}=0$ and from equation (B19)

$$g_{a\_\max}=\frac{k_e}{\omega_c^2} \tag{B20}$$

Equation (B20) gives the maximum gain when the base behaves as either a stiffness or a mass and the equipment behaves as a stiffness.

B3 Velocity feedback control

The feedback frequency response function of an ideal system with velocity feedback control is given by $H\left(j\omega\right)=g_v$. Thus the open loop frequency response function can be written as,

$$G(j\omega)H(j\omega)=\frac{g_v P_r}{P_r^2+jP_i^2}-j\frac{g_v P_i}{P_r^2+jP_i^2} \qquad \text{(B21)}$$

Applying the Nyquist criterion gives $P_i=0$, (The imaginary part of equation (B21) is equated to zero and the resulting condition is substituted into the real part of the equation (B21). If the real part is positive then the system is unconditionally stable. If it is negative the real part is equated to –1 and solved for the maximum gain.)

From equation (B21) when $P_i = 0$ the real part of open-loop frequency response function becomes,

$$Re\left(G(j\omega_c)H(j\omega_c)\right)=\frac{g_v}{P_r} \qquad \text{(B22)}$$

Using $P_r=\left(c(1+A)+\frac{kB}{\omega}+Z_{er}\right)$ and substituting for $A=(Y_{br}Z_{er}-Y_{bi}Z_{ei})$ and $B=(Y_{br}Z_{ei}+Y_{bi}Z_{er})$ equation (B22) can be written as,

$$Re\left(G(j\omega_c)H(j\omega_c)\right)=\frac{g_v}{c(1+Y_{br}Z_{er}-Y_{bi}Z_{ei})+\frac{k}{\omega_c}(Y_{br}Z_{ei}+Y_{bi}Z_{er})+Z_{er}} \qquad \text{(B23)}$$

Now consider the following cases,

Case 1: The equipment is mass-like

When the equipment behaves as a mass (i.e. $Z_e = j\omega m$, thus $Z_{er}=0$ and $Z_{ei}=\omega m$) equation (B23) reduces to,

$$Re\left(G(j\omega_c)H(j\omega_c)\right)=\frac{g_v}{c(1-Y_{bi}Z_{ei})+\frac{k}{\omega_c}Y_{br}Z_{ei}} \qquad \text{(B24)}$$

Now considering $P_i=\left(cB-\frac{k(1+A)}{\omega}+Z_{ei}\right)=0$, substituting for A, B & $Z_{er}=0$ and $Z_{ei}=\omega m$ and rearranging gives,

$$1-Y_{bi}m_e\omega_c=\frac{m_e\omega_c^2}{k}(1+cY_{br}) \qquad \text{(B25)}$$

Substituting equation (B25) in equation (B24) gives,

$$Re\left(G(j\omega_c)H(j\omega_c)\right)=\frac{g_v}{\frac{cm_e\omega_c^2}{k}(1+cY_{br})+km_eY_{br}} \qquad \text{(B26)}$$

Since $Y_{br} \geq 0$ for any base mobility [3,93], the real part of the open-loop frequency response function given in equation (B26) is positive when it crosses the negative real axis. Hence the isolation system with velocity feedback control is unconditionally stable irrespective of the base mobility.

Case 2: The equipment is stiffness-like

When the equipment behaves as a stiffness (i.e. $Z_e=-j\frac{k_e}{\omega}$, thus $Z_{er}=0$ and $Z_{ei}=-\frac{k_e}{\omega}$) equation (B22) reduces to,

$$Re\left(G(j\omega_c)H(j\omega_c)\right)=\frac{g_v}{c\left(1+Y_{bi}\frac{k_e}{\omega_c}\right)-\left(\frac{kk_e}{\omega_c^2}Y_{br}\right)} \qquad \text{(B27)}$$

Now if the base is also stiffness-like then $Y_b=\frac{j\omega}{k_b}$ and hence $Y_{br}=0$ and $Y_{bi}=\frac{\omega}{k_b}$. Substituting these quantities in equation (B27) gives,

$$Re\left(G(j\omega_c)H(j\omega_c)\right)=\frac{g_v}{c\left(1+\frac{k_e}{k_b}\right)} \qquad \text{(B28)}$$

Thus if the base also behaves as a stiffness then the system is unconditionally stable.

If the base is mass-like then $Y_b=\frac{1}{j\omega m_b}$ and hence $Y_{br}=0$ and $Y_{bi}=-\frac{1}{\omega_c m_b}$. Substituting these quantities in equation (B27) gives,

$$Re\left(G(j\omega_c)H(j\omega_c)\right)=\frac{g_v}{c\left(1-\frac{k_e}{m_b\omega_c^2}\right)} \qquad \text{(B29)}$$

Thus if the base behaves as a mass then the system is only conditionally stable.

B4 Displacement feedback control

The feedback frequency response function of an ideal displacement feedback control system is given by $H(j\omega)=\frac{1}{j\omega}g_d$. The open loop frequency response function can be written as,

$$G(j\omega)H(j\omega)=-\left(\frac{g_d P_i}{\omega\left(P_r^2+P_i^2\right)}+\frac{jg_d P_r}{\omega\left(P_r^2+P_i^2\right)}\right) \qquad \text{(B30)}$$

As before when the imaginary part is zero $P_r=0$ and the corresponding real part can be written as,

$$Re\left(G(j\omega_c)H(j\omega_c)\right)=\frac{g_d}{\omega_c P_i} \qquad \text{(B31)}$$

Using $P_i=\left(cB-\frac{k(1+A)}{\omega}+Z_{ei}\right)$ and substituting for A and B the equation (B31) can be written as,

$$Re\left(G(j\omega_c)H(j\omega_c)\right)=\frac{g_d}{\omega_c\left(c\left(Y_{br}Z_{ei}+Y_{bi}Z_{er}\right)-\frac{k}{\omega_c}\left(1+Y_{br}Z_{er}-Y_{bi}Z_{ei}\right)+Z_{ei}\right)} \qquad \text{(B32)}$$

Case 1: The equipment is mass-like

If the equipment is mass-like then $Z_e=j\omega m_e$ and hence $Z_{er}=0$ & $Z_{ei}=\omega m_e$ Substituting these quantities in equation (B11) gives,

$$Re\left(G(j\omega_c)H(j\omega_c)\right)=\frac{g_d}{\omega_c\left(c\omega_c m_e Y_{br}-\frac{k}{\omega_c}\left(1-\omega_c m_e Y_{bi}\right)+\omega_c m_e\right)} \qquad \text{(B33)}$$

Substituting from equation (B14) for $\left(1-\omega_c m_e Y_{bi}\right)=-\frac{k}{c}m_e Y_{br}$ in equation (B33) gives,

$$Re\left(G(j\omega_c)H(j\omega_c)\right)=\left(\frac{1}{\omega_c}\right)\frac{g_d}{\left(c+\frac{k^2}{c\omega_c^2}\right)\left(Y_{br}\omega_c m\right)+\omega_c m} \qquad \text{(B34)}$$

Since $Y_{br}\geq 0$ and all other parameters such as g_a, k, c, ω_c etc (in equation (B34)) are also greater than zero the real part of the open-loop frequency response is positive when the open-

loop frequency response plot crosses the real axis. Hence the system is unconditionally stable irrespective of the nature of the base mobility.

Case 2: The equipment is stiffness-like

If the equipment is stiffness-like then. $Z_e = -j\frac{k_e}{\omega}$, and hence $Z_{er} = 0$ and $Z_{ei} = -\frac{k_e}{\omega}$

Substituting these quantities in equation (B32) gives,

$$Re\left(G(j\omega_c)H(j\omega_c)\right) = \frac{1}{\omega_c}\frac{-g_d}{\left(\frac{k_e}{\omega_c}cY_{br} + \frac{k}{\omega_c}\left(1+\frac{k_e}{\omega_c}Y_{bi}\right)+\frac{k_e}{\omega_c}\right)} \qquad \text{(B35)}$$

Now substituting (B17) in equation (B35) gives,

$$Re\left(G(j\omega_c)H(j\omega_c)\right) = \frac{-g_d}{k_e\left(1+cY_{br}+\frac{k^2}{c\omega_c^2}Y_{br}\right)} \qquad \text{(B36)}$$

Since $Y_{br} \geq 0$ [3,93], the real part is always positive irrespective of the nature of the base mobility. The maximum gain can be obtained by equating the real part to –1. This gives,

$$g_{d\_\max} = k_e\left(1+cY_{br}+\frac{k^2}{c\omega_c^2}Y_{br}\right) \qquad \text{(B37)}$$

(Note that if the system critical frequency is small then it has a large gain margin)

Special case 1: Base is either mass-like or stiffness-like

This gives $Y_b = -j\frac{1}{m_b\omega}$ or $Y_b = j\frac{\omega}{k_b}$ and for both of these cases $Y_{br} = 0$ and from equation (B37)

$$g_{d\_\max} = k_e \qquad \text{(B38)}$$

Equation (B38) gives the maximum gain when the base behaves as either a stiffness or a mass and the equipment behaves as a stiffness.

Appendix C

Formulation of transformation matrix, equipment impedance and moment of inertia

In this Appendix the transformation matrix $\mathbf{Q}$, equipment impedance matrix $\mathbf{Z}_e$ and moment of inertia of the equipment about it mass centre J, which are required to analysis the two-mount system considered in chapters 2 and 5 are derived.

C1 Transformation matrices

From Figure 2.2a mass centre velocities $\mathbf{a} = \begin{bmatrix} v \\ l\dot{\theta} \end{bmatrix}$ are related to the mount location velocities v_{e1} and v_{e2} by,

$$v_{e1} = v - rl\dot{\theta} \qquad \text{(C1)}$$

$$v_{e2} = v + (1-r)l\dot{\theta} \qquad \text{(C2)}$$

where l is the distance between the mounts and r is the ratio of the distance between the left hand mount and the mass centre to the distance between the mounts. Equations (C1) and (C2) can be written in matrix form to give,

$$\begin{bmatrix} v_{e1} \\ v_{e2} \end{bmatrix} = \begin{bmatrix} 1 & -r \\ 1 & 1-r \end{bmatrix} \begin{bmatrix} v \\ l\dot{\theta} \end{bmatrix} \qquad \text{(C3)}$$

Thus the transformation matrix $\mathbf{Q}$ that relates the vector of velocities at the mass centre to the vector of velocities at the mount positions is given by,

$$\mathbf{Q} = \begin{bmatrix} 1 & -r \\ 1 & 1-r \end{bmatrix} \text{ and hence } \mathbf{Q}^{-1} = \begin{bmatrix} 1-r & r \\ -1 & 1 \end{bmatrix} \qquad \text{(C4, C5)}$$

C2 Equipment impedance matrix

Letting the mount forces on the equipment at locations 1 and 2 in Figure 2.2a be f_{m1} and f_{m2} respectively, then the equations of motion in the frequency domain can be written as,

$$f_{m1} + f_{m2} = j\omega m v \tag{C6}$$

$$-rlf_{m1} + (1-r)rlf_{m2} = j\omega J\dot{\theta} \tag{C7}$$

where J is the moment of inertia of the equipment about its mass centre.

Equations (C6) and (C7) can be rearranged to give the matrix equation,

$$\begin{bmatrix} f_{m1} \\ f_{m2} \end{bmatrix} = j\omega \begin{bmatrix} m(1-r) & -\frac{J}{l^2} \\ mr & \frac{J}{l^2} \end{bmatrix} \begin{bmatrix} v \\ l\dot{\theta} \end{bmatrix} \tag{C8}$$

Equations (C3) and (C8) can be combined to give, $\mathbf{f}_m = \mathbf{Z}_e \mathbf{v}_e$,

where, $\mathbf{v}_e = \begin{bmatrix} v_{e1} \\ v_{e2} \end{bmatrix}$, $\mathbf{f}_m = \begin{bmatrix} f_{m1} \\ f_{m2} \end{bmatrix}$ and $\mathbf{Z}_e$ is given by,

$$\mathbf{Z}_e = j\omega \begin{bmatrix} (1-r)^2 m + \frac{J}{l^2} & mr(1-r) - \frac{J}{l^2} \\ mr(1-r) - \frac{J}{l^2} & mr^2 + \frac{J}{l^2} \end{bmatrix} \tag{C9}$$

Since the mounts are assumed to have equal properties, the impedance matrix of the mounts can be written as,

$$\mathbf{Z}_m = \begin{bmatrix} Z_m & 0 \\ 0 & Z_m \end{bmatrix} \tag{C10}$$

where $Z_m = \frac{k}{j\omega} + c$.

C3 Approximate method of finding the equipment moment of inertia

For the system discussed in chapters 2 and 5, the total mass m and length between mounts l is assumed to be constant, but the centre of gravity is at position rl from the left hand end of the mount. The system used in the experimental work in Chapter 5 consists of an aluminium plate with two shakers and movable masses, which can be lumped on shakers so as to move the mass centre. A schematic diagram is shown in Figure C1. The masses m_1 and m_2

represent the masses of control shakers and any additional masses lumped on them. It is assumed that masses m_1 and m_2 are point masses and hence the moment of inertia of these point masses about the neutral axis trough mass centre of the system is negligible.

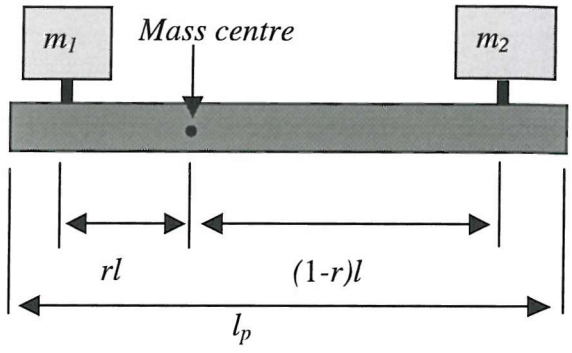

Figure C1 Schematic diagram of the system with shakers and additional masses.

The plate is assumed to be symmetric and the moment of inertia about its centre of gravity is given by $J_p = \frac{m_p l_p^2}{12}$ where J_p , m_p and l_p are the moment of inertia, the mass and the length of the plate respectively.

Using the parallel axis theorem the moment of inertia of the plate about the mass centre of the system can be written as [81],

$$J_{pg} = \frac{m_p l_p^2}{12} + m_p \left(\frac{(1-2r)l}{2} \right)^2 \qquad \text{(C11)}$$

where J_{pg} is the moment of inertia of the plate about the mass centre of the system.
Now the moment of inertia of the masses with respect to the mass centre of the system can be written to give,

$$J_m = m_1 r^2 l^2 + m_2 (1-r)^2 l^2 \qquad \text{(C12)}$$

The total moment of inertia is the sum of moment of inertias given in (C11) and (C12) and is given by,

$$J = J_{pg} + J_m \qquad \text{(C13)}$$

Letting $m_m = m_1 + m_2$ and taking moments about the mass centre gives,

$$m_1 rl = m_p \left(\frac{l}{2} - rl \right) + m_2 (1-r)l \qquad \text{(C14)}$$

From equation (C14), the ratio r as a function of the masses is given by $r = \dfrac{2m_2 + m_p}{2(m_p + m_m)}$.

C4 Approximate model of the system considered in Chapter 5

In-order to represent a system with dominant equipment mass, which is also consistent with the experimental work and simulations in pervious Chapters, the total mass m, length between mounts l are assumed to be constant. Hence for analytical purpose the actuators are assumed to be mass less. Similar to the previous cases the mass centre is considered to be at rl from the left-hand mount. Mass of the equipment to the left of the mass centre is m_1 and to the right of the mass centre is m_2.

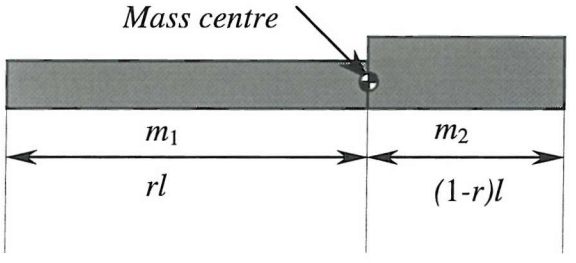

Figure C2 Schematic diagram of the distributed system

Considering total the mass and moment about its mass centre, masses m_1 and m_2 can be written as, $m_1 = (1-r)m$ and $m_2 = rm$. Two plates can be combined to represent an off mass centre equipment. Thus moment of inertia about the mass centre of the equipment can be written as,

$$J = \left(m_1 \frac{(rl)^2}{12} + m_1 \left(\frac{rl}{2} \right)^2 \right) + \left(m_2 \frac{((1-r)l)^2}{12} + m_2 \left(\frac{(1-r)l}{2} \right)^2 \right) \qquad \text{(C15)}$$

This can be simplified to give,

$$J = \frac{m}{3} r(1-r)l^2 \qquad \text{(C16)}$$

Appendix D

Input and transfer mobilities of a clamped free clamped free (CFCF) base

In-order to study the effectiveness of active control of a base excited system, a CFCF base structure was chosen as a flexible base. A CFCF boundary conditions of a base structure is relatively easy to realise in practice. Figure D1 shows a layout of a CFCF base structure and the physical co-ordinate system. Thin plate theory in conjunction with Warburton's method [82] is used to describe the dynamics of the CFCF base structure.

The governing equation for undamped plate vibration [9] is given by,

$$D\nabla^4 w(x,y,t) + \rho h \frac{\partial^2 w(x,y,t)}{\partial t^2} = f_0(x,y,t) \qquad \text{(D1)}$$

Where $D = \frac{Eh^3}{12(1-\nu^2)}$, E is Young's modulus, h is the thickness of the plate, ν is Poisson's ratio and $\nabla^2 = \frac{\partial^2}{\partial x^2} + \frac{\partial^2}{\partial y^2}$.

Letting $w(x,y,t) = W(x,y)e^{i\omega t}$ and $f_0(x,y,t) = F(x,y)e^{j\omega t}$ and substituting in equation (D1) gives,

$$\nabla^4 W(x,y) - k_1^4 W(x,y) = \frac{F(x,y)}{D} \qquad \text{(D2)}$$

Where $k_1^4 = \frac{\rho h \omega^2}{D}$.

Applying Warburton's method [82] where beam functions are used to describe the plate modes *(m, n),* the amplitude of the out-of-plane displacement *W(x,y)* can be represented as a sum of an infinite number of structural modes.

$$W(x,y) = \sum_{m=2}^{\infty} \sum_{n=o}^{\infty} B_{mn} \theta_m(x) \phi_n(y) \qquad \text{(D3)}$$

where $\theta(x)$ and $\phi(y)$ are the characteristic beam mode shapes in the x and y direction respectively which are chosen to satisfy the plate boundary conditions in the direction they represent and B_{mn} is the complex amplitude of the mn^{th} mode. Since the clamped boundary conditions are regarded as modal lines m ≥ 2 is assumed. Although there are an infinite number of modes, which contribute to the vibration response of a plate, in practice a finite number of modes must be used, and equation (D3) can be written as,

$$W(x,y)=\sum_{m=2}^{M}\sum_{n=o}^{N}B_{mn}\psi_{mn}(x,y) \qquad \text{(D4)}$$

where $\psi_{mn}(x,y)=\theta_m(x)\phi_n(y)$

Multiplying both side of equation (D2) by $\psi_{pq}(x,y)$ and integrating over the whole area of the plate gives,

$$\int_0^a\int_0^b[\nabla^4W(x,y)-k^4W(x,y)]\psi_{pq}(x,y)dxdy=\frac{1}{D}\int_0^a\int_0^b F(x,y)\psi_{pq}(x,y)dxdy \qquad \text{(D5)}$$

where a,b are the length and width of the plate (in the x and y direction respectively)

The orthogonality of any two modes gives,

$$\int_0^a\int_0^b\psi_{mn}(x,y)\psi_{pq}(x,y)dxdy=0 \quad \text{for } mn\neq pq$$

$$=N_{mn} \text{ for } mn=pq$$

where N_{mn} is called a normalising factor.

Because of the orthogonality conditions, equation (D5) reduces to,

$$\int_0^a\int_0^b\nabla^4W(x,y)\psi_{pq}(x,y)dxdy-\frac{\rho hB_{mn}\omega^2N_{mn}}{D}=\frac{1}{D}\int_0^a\int_0^b F(x,y)\psi_{pq}(x,y)dxdy \qquad \text{(D6)}$$

The natural frequencies are obtained by solving equation (D6) after setting the force component to zero. (Since the natural frequencies correspond to the modes m, n, they are denoted by ω_{mn}.)

$$\int_0^a\int_0^b\nabla^4W(x,y)\psi_{pq}(x,y)dxdy-\frac{\rho hB_{mn}\omega_{mn}{}^2N_{mn}}{D}=0 \qquad \text{(D7)}$$

From equations (D6) and (D7),

$$B_{mn}=\frac{\int_0^a\int_0^b F(x,y)\psi_{mn}(x,y)dxdy}{\rho hN_{mn}(\omega_{mn}^2-\omega^2)} \qquad \text{(D8)}$$

For a point force excitation (such as that generated by a shaker) the forcing function can be represented using the delta function [8]. If the force is applied at position (x_j,y_j) then,

$$F(x,y) = F_0\delta(x-x_j)\delta(y-y_j) \tag{D9}$$

The RHS of equation (D6) then becomes,

$$\int_0^a\int_0^b F(x,y)\psi_{pq}(x,y)dxdy = F_0\psi_{pq}(x_j,y_j) \tag{D10}$$

From equations (D10), (D8), (D4), substituting for $\psi_{pq}(x_0,y_0)$ and including the damping coefficient ζ_{mn} gives,

$$w(x,y) = \frac{F_0}{\rho h}\sum_{m=2}^{M}\sum_{n=0}^{N}\frac{\theta_m(x_j)\phi_n(y_j)\theta_m(x)\phi_n(y)}{N_{mn}(\omega_{mn}^2-\omega^2+j2\zeta_{mn}\omega_{mn}\omega)} \tag{D11}$$

It is now possible to calculate the mobility at a point (x_i,y_i) due to the force applied at (x_j,y_j). This is given by the following equation.

$$Y_{ij} = \frac{V(x_i,y_i)}{F(x_j,y_j)} = \frac{j\omega}{\rho h}\sum_{m=2}^{M}\sum_{n=0}^{N}\frac{\theta_m(x_i)\phi_n(y_i)\theta_m(x_j)\phi_n(y_j)}{N_{mn}(\omega_{mn}^2-\omega^2+j2\zeta\omega_{mn}\omega)} \tag{D12}$$

The relevant beam functions are given by the following equations,

- Free-free beam,

  $\theta(x)$= 1 for m=0;

  $\theta(x) = \left[1-\frac{2x}{a}\right]$ For m=1;

  $\theta(x) = \cos\gamma\left(\frac{x}{a}-\frac{1}{2}\right)+k_1\cosh\gamma\left(\frac{x}{a}-\frac{1}{2}\right)$ For m=2,4,6...

  Where $k_1 = -\frac{\sin(\gamma/2)}{\sinh(\gamma/2)}$ and $\tan(\gamma/2)+\tanh(\gamma/2)=0.$

  $\theta(x) = \sin\gamma'\left(\frac{x}{a}-\frac{1}{2}\right)+k_1'\sinh\gamma'\left(\frac{x}{a}-\frac{1}{2}\right)$ For m=3,5,7...

  Where $k_1' = \frac{\sin(\gamma'/2)}{\sinh(\gamma'/2)}$ and $\tan(\gamma'/2)-\tanh(\gamma'/2)=0$ (D13)

- Clamped-clamped beam

  $\phi(y) = \cos\gamma\left(\frac{y}{b}-\frac{1}{2}\right)+k_2\cosh\gamma\left(\frac{y}{b}-\frac{1}{2}\right)$ For m=2,4,6...

  Where $k_2 = \frac{\sin(\gamma/2)}{\sinh(\gamma/2)}$ and $\tan(\gamma/2)+\tanh(\gamma/2)=0$

$$\phi(y) = \sin\gamma'\left(\frac{y}{b}-\frac{1}{2}\right)+k_2'\sinh\gamma'\left(\frac{y}{b}-\frac{1}{2}\right) \text{ For m=3,5,7...}$$

$$\text{Where } k_2' = -\frac{\sin(\gamma'/2)}{\sinh(\gamma'/2)} \text{ and } \tan(\gamma'/2)-\tanh(\gamma'/2)=0 \qquad \text{(D14)}$$

Equation (D12) can be used to calculate the theoretical mobility, provided the natural frequencies and beam mode functions for free- free and clamped-clamped conditions are known. The natural frequencies are given by [82],

$$\omega_{mn} = \frac{2\lambda_{mn}h\pi^2}{a^2}\left[\frac{E}{48\rho(1-\nu^2)}\right]^{\frac{1}{2}} \qquad \text{(D15)}$$

where λ_{mn} is given by [82],

$$\lambda_{mn}^2 = G_x^4 + G_y^4\left[\frac{a^4}{b^4}\right]+\frac{2a^2}{b^2}\left[\nu H_x H_y + (1-\nu)J_x J_y\right] \qquad \text{(D16)}$$

Where G_x, H_x, J_x, G_y, H_y & J_y for a non-square plate with clamped-free-clamped-free boundary conditions are given in Table D1 [82]

m or n	0	1	2	3,4,5...
G_x	-	-	*1.506*	*(m-0.5)*
H_x	-	-	*1.248*	$(m-0.5)^2[1-2/\{(m-0.5)\pi\}]$
J_x	-	-	*1.248*	$(m-0.5)^2[1-2/\{(m-0.5)\pi\}]$
G_y	*0*	*0*	*1.506*	*(n-0.5)*
H_y	*0*	*0*	*1.248*	$(n-0.5)^2[1-2/\{(n-0.5)\pi\}]$
J_y	*0*	$12/\pi^2$	*5.017*	$(n-0.5)^2[1+6/\{(n-0.5)\pi\}]$

Table D1 Coefficients of parameters in equation (D19)

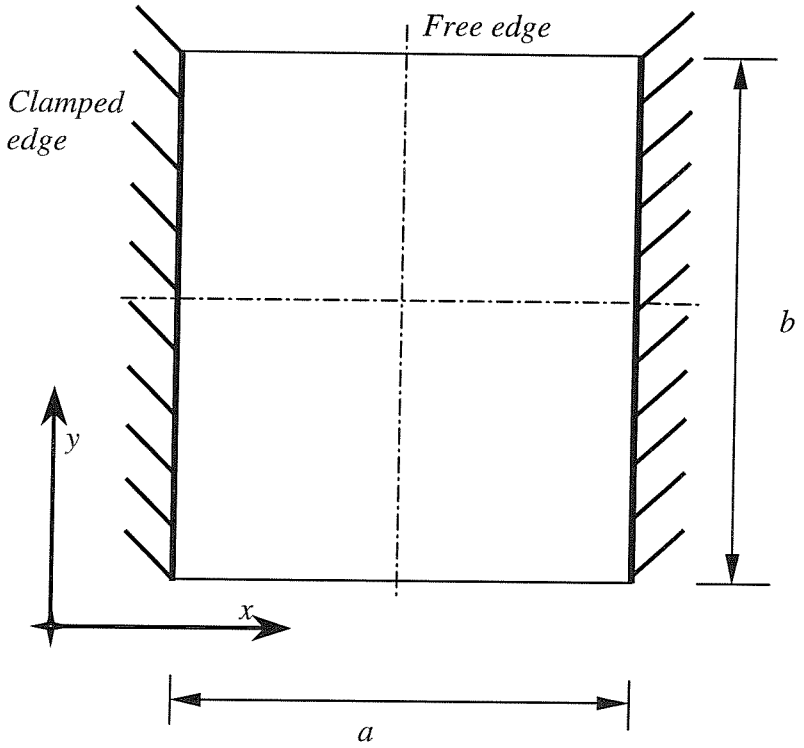

Figure D1 Schematic diagram of the base structure

Appendix E

Clamped-free-clamped-free (CFCF) base structure model validation

The agreement between the simulation and experimental results for the CFCF base structure presented in Chapter 2 depends on the validity of the model of the base structure. Thus it is useful to check on the validity of the model of the base structure. Three checks were performed for this purpose.

1. Comparison of receptance (stiffness) with a beam model.
2. Comparison of calculated and measured accelerance.
3. Comparison of resonant frequencies and mode shapes with measurements.

In the following sections these are discussed.

E1 Comparison of receptance with a beam model

Figure E1 shows the point receptance of the base CFCF base structure calculated at the centre of the plate (x=*260 mm* and y=*350 mm* - with reference to Figure 2.7). Equation (D12) (in appendix D) gives the mobility of a CFCF base structure. The receptance can be found from the mobility by considering the relationship $Y_{ij} = j\omega R_{ij}$, where R_{ij} denotes the receptance at (x_i,y_i) due to a force at (x_j,y_j). The beam functions and modal frequencies required to calculate the receptance of the CFCF base structure are given in equations (D13), (D14), (D15) and (D16). From Figure E1, the receptance at low frequency (which is approximately constant) is given by, 103.8 dB (dB ref 1m/N), which is $6.457e^{-6}$ m/N. The stiffness is given by 1/Receptance and so the stiffness is $1.55e5$ N/m.

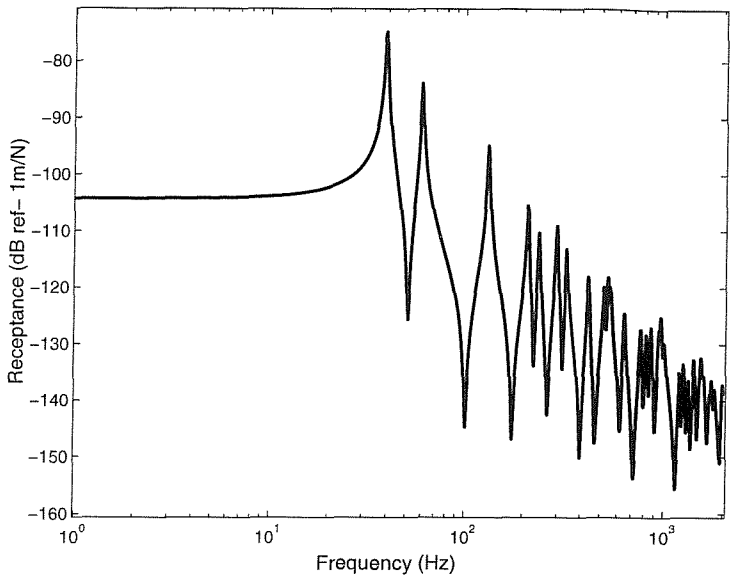

Figure E1 Receptance plot of the CFCF base structure (simulation)

The stiffness obtained from the simulations was compared with a beam of clamped-clamped boundaries to confirm the order of magnitude of stiffness. The stiffness at the mid span of a clamped-clamped beam with length l is given by [9],

Stiffness $= 192EI / l^3$ (E1)

Where E is the Young's modulus and I is the second moment of area of the cross section of the beam about its neutral axis. It is given by $I = \frac{bt^3}{12}$. Where b and t are the width and the thickness of the beam respectively. A beam of length 0.52 m, width 0.7 m and thickness 1.9 mm with Young modulus 2.06e11 Pa, the stiffness is given by,

Stiffness $= 1.27\ e5$ N/m.

Although there is reasonable agreement with the beam model, the actual magnitudes differ from each other. This is because of the beam model assumes that the thickness and width are small in comparison with the length. But here the width is greater than the length.

Note that the stiffness of a plate is given by $\frac{192Et^3}{12(1-\nu^2)}$, which does not inlude the boundary conditions. Hence for comparison a beam model is chosen which reflects the bounday conditions.

E2 Comparison of calculated accelerance with measurement

Equation (D12) gives the mobility of the CFCF base structure at (x_i, y_i) for a unit excitation at (x_j, y_j). The accelerance can be calculated from mobility using $j\omega Y_{ij}$. Figure E2 shows simulated accelerance calculated at the centre of the base plate. Similarly accelerance can be obtained by measuring acceleration at the centre of the base structure per unit excitation at the centre of the base structure.

Figure E2 shows the simulated and measured accelerance of the CFCF base structure. It can be seen that, although they do not match exactly, there is reasonable general agreement. At low frequencies the simulation shows the first peak at a higher frequency than that of the measured accelerance. One possible reason is that the simulation considers perfectly clamped-clamped boundary conditions for one pair of edges while it is only bolted at equal spacing in the real base used. This means that the base is predicted to be stiffer than it actually is.

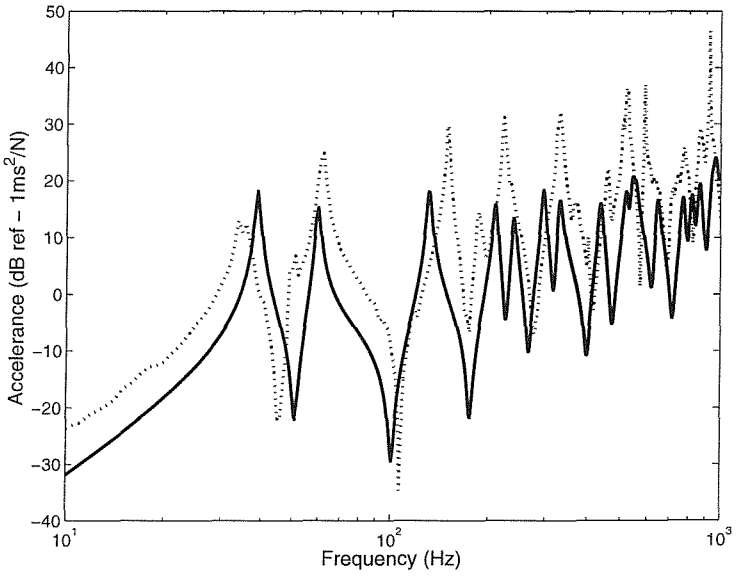

Figure E2 Accelerance of the CFCF base. Simulation:_____, Measurement:.....

E3 Comparison of resonant frequencies and mode shapes with measurements

A comparison of the measured and predicted first six natural frequencies of the CFCF base structure is given in Table E1. Natural frequencies can be calculated using equation (D15) given in Appendix D. Measured natural frequency given in Table E1 was extracted from the measured accelerance given in Figure E2.

Mode	*Calculated Frequency* (Hz)	*Measured Frequency* (Hz)
2,0	42.11	32.5
2,1	46.33	37.0
2,2	62.77	62.0
2,3	84.33	93.0
3,0	116.04	116.0
3,1	121.9	121.0

Table E1 Predicted and measured natural frequencies of the CFCF base structure.

A comparison of mode shape was also made. Dividing the mobility given in equation (D12) gives the receptance of the base structure. For each natural frequency receptance can be calculated at various points of the base structure. For first four natural frequencies, receptance was calculated at a 30 x 20 grid points and mode shape were plotted from magnitude and phase information, which are given in Figures E3a, E3c, E3e and E3g.

A 10 x 7 grid was marked on the CFCF base structure. The receptance at these positions was measured by placing an accelerometer on each grid point on the base structure for a broadband excitation at the centre of the base. The required magnitude and phase information for each mode was then extracted and the mode shapes were plotted. It can be seen from Figure E3 that the first four measured and simulated mode shapes are generally in good agreement.

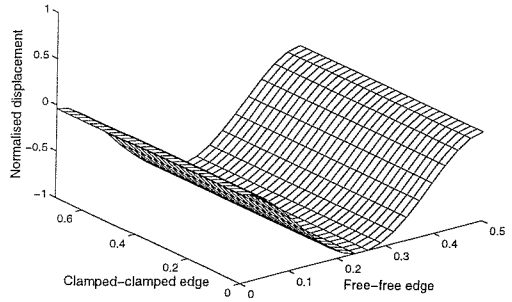

(a) Mode (2,0)- Simulation

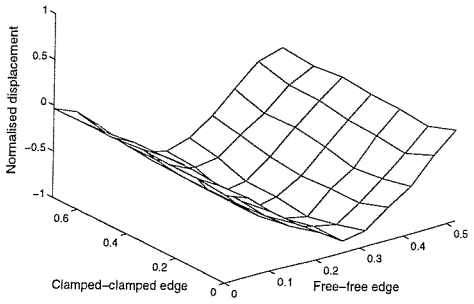

(b) Mode (2,0)- Measured

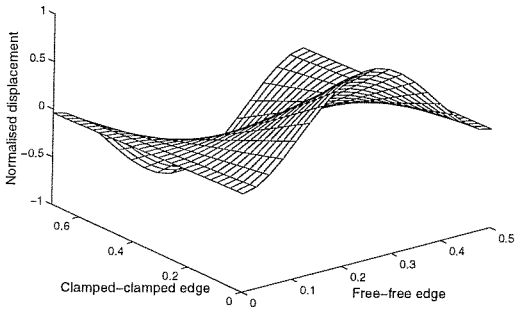

(c) Mode (2,1)- Simulation

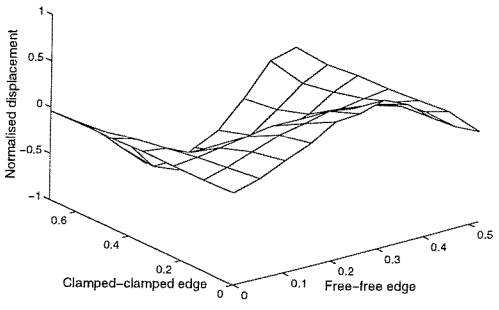

(d) Mode (2,1)- Measured

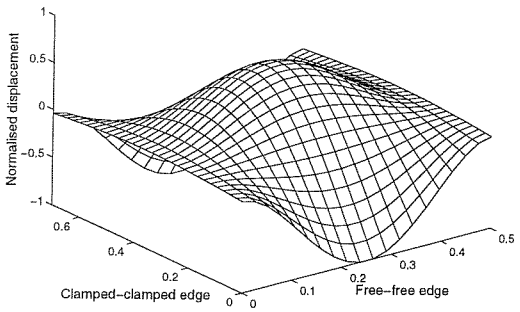

(e) Mode (2,2)- Simulation

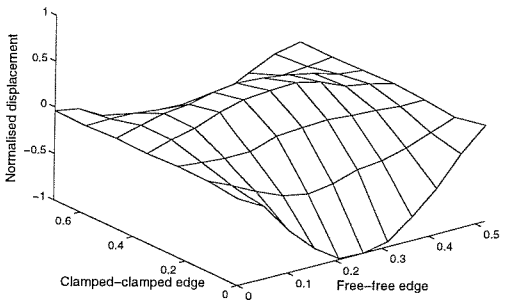

(f) Mode (2,2)- Measured

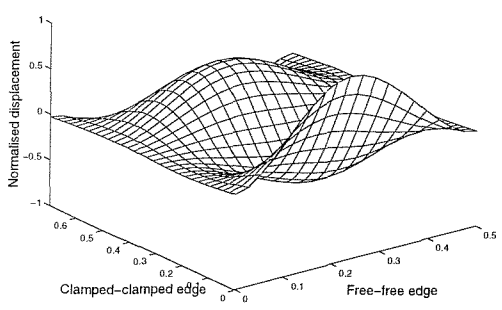

(g) Mode (2,3)- Simulation

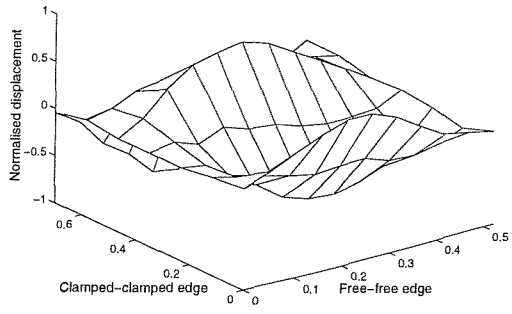

(h) Mode (2,3)- Measured

Figure E3 Simulated and measured mode shapes of the CFCF base structure.

E4 Concluding remarks

The first method described in section E1 is a simple check for low frequency behaviour of the physical and the mathematical model. The second check given in section E2 compares the two (the physical and the mathematical model) over a band of frequency. In addition, it can be used to compare the agreement between damping used for the mathematical model and the damping present in the physical model. First two methods are based on a single point on the base structure and the third method includes entire surface of the base structure. All these three methods show that the mathematical model is generally in good agreement with the physical model.

Appendix F

Stability of a multi-input-multi-output (MIMO) system on a rigid foundation

In this appendix proof of the unconditional stability of a MIMO vibration isolation system on a rigid foundation is presented. Figure F1 shows a multi-input (n secondary forces or control forces) and multi-output (n co-located equipment velocities) system in the form of a block diagram. From Chapter 2 it can be seen that the plant response matrix is the mobility matrix of the system when excited by the vector of control forces in the absence of the primary disturbance.

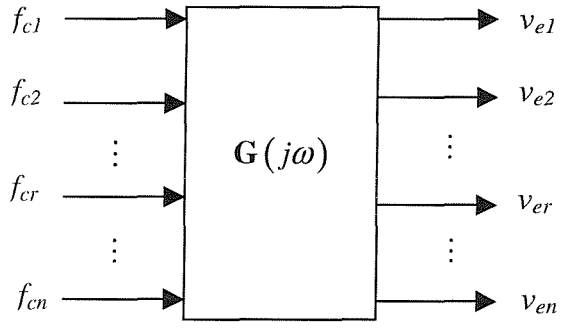

Figure F1 Block diagram representation of an MIMO system

The output velocity vector is related to the input control force vector through mobility matrix by,

$$\mathbf{v}_e = \mathbf{Y}\mathbf{f}_c \qquad \text{(F1)}$$

where $\mathbf{v}_e$, $\mathbf{f}_c$ and $\mathbf{G}(j\omega)=\mathbf{Y}$ denote the velocity vector, control force vector and mobility matrix respectively. The concept used to prove unconditional stability is briefly stated below. The stability criterion for an MIMO system states that the system is stable if and only if none of the of the open-loop eigenvalue plots includes the critical (-1,0) point of the Nyquist plane [31]. In other words the system is stable when the imaginary parts of the eigenvalues are zero and the real parts are greater than –1. The system is unconditionally stable if the real parts of the eigenvalues are greater than zero (i.e. $\mathrm{Re}\{eig(\mathbf{Y})\}\geq 0$).

According to Maxwell's reciprocity theorem $\mathbf{Y} = \mathbf{Y}^{T}$ (So the mobility matrix is symmetric). Applying the Schur decomposition [90] of $\mathbf{Y}$ gives,

$$\mathbf{Y} = \mathbf{Q}_s^{H}\mathbf{T}\mathbf{Q}_s \tag{F2}$$

where $\mathbf{T} = \mathbf{\Lambda}_m + \mathbf{N}$ and $\mathbf{\Lambda}_m = \mathrm{diag}(\lambda_{m1} \cdots\cdots \lambda_{mn})$ are the eigenvalues of **Y,** and **N** is strictly upper triangular and $\mathbf{Q}_s$ is the transformation matrix which can be chosen so that eigenvalues λ_{mi} appear in any order along the diagonal $\mathbf{\Lambda}_m$ [90]. The superscript H denotes the conjugate transpose.

The power supplied to the system by the control actuators Π is given by [93],

$$\Pi = \frac{1}{2}\mathrm{Re}\{\mathbf{f}_c^{H}\mathbf{v}_e\} = \frac{1}{2}\mathrm{Re}\{\mathbf{f}_c^{H}\mathbf{Y}\mathbf{f}_c\} \tag{F3}$$

Substituting for $\mathbf{Y}$ from equation (F2) into equation (F3) gives,

$$\Pi = \frac{1}{2}\mathrm{Re}\{\mathbf{f}_c^{H}\mathbf{Q}_s^{H}\mathbf{T}\mathbf{Q}_s\mathbf{f}_c\} \tag{F4}$$

Letting $\mathbf{p} = \mathbf{Q}_s\mathbf{f}_c$, equation (F4) can be written as,

$$\Pi = \frac{1}{2}\mathrm{Re}\{\mathbf{p}^{H}\mathbf{T}\mathbf{p}\} = \frac{1}{2}\sum_{i=1}^{n}|p_i|^2\,\mathrm{Re}\{\lambda_{mi}\} + \frac{1}{2}\mathrm{Re}\{\mathbf{p}^{H}\mathbf{N}\mathbf{p}\} \tag{F5}$$

Equation (F5) can be written to give,

$$\Pi = \frac{1}{2}\sum_{i=1}^{n}|p_i|^2\,\mathrm{Re}\{\lambda_{mi}\} + \frac{1}{4}\mathrm{Re}\left\{(\mathbf{p}^{H}\mathbf{N}\mathbf{p}) + (\mathbf{p}^{H}\mathbf{N}\mathbf{p})^{H}\right\} \tag{F6}$$

which can also be written as,

$$\Pi = \frac{1}{2}\sum_{i=1}^{n}|p_i|^2\,\mathrm{Re}\{\lambda_{mi}\} + \frac{1}{2}\mathbf{p}^{H}\mathbf{D}\mathbf{p} \tag{F7}$$

where $\mathbf{D} = \dfrac{\mathbf{N} + \mathbf{N}^{H}}{2}$. Since **D** is a Hermitian matrix it can be diagonalised to give, $\mathbf{D} = \mathbf{Q}_N^{H}\mathbf{\Lambda}_d\mathbf{Q}_N$, where $\mathbf{\Lambda}_d = \mathrm{diag}(\lambda_{d1}, \lambda_{d2} \cdots\cdots \lambda_{dn})$ and $\mathbf{Q}_N$ is the transformation matrix. Also letting $\mathbf{s} = \mathbf{Q}_N\mathbf{p}$, equation (F7) can be written to give,

$$\Pi = \frac{1}{2}\sum_{i=1}^{n}|p_i|^2\,\mathrm{Re}\{\lambda_{mi}\} + \frac{1}{2}\mathbf{s}^{H}\mathbf{\Lambda}_d\mathbf{s} \tag{F8}$$

Equation (F8) can be written as,

$$\Pi = \frac{1}{2}\sum_{i=1}^{n}|p_i|^2\,\mathrm{Re}\{\lambda_{mi}\} + \frac{1}{2}\sum_{i=1}^{n}|s_i|^2\,(\lambda_{di}) \tag{F9}$$

Since **D** is a Hermitian matrix, the eigenvalues of **D** are real (but not necessarily positive). Since the power supplied must be equal to or greater than zero for all frequencies, equation

(F9) must hold for all frequencies so, $\mathrm{Re}(\lambda_{mi}) \geq 0$. Thus the system is unconditionally stable with velocity feedback control.

Since acceleration or displacement feedback control system only add a 90-degree phase advance or lag to the above system, they are also stable.

Appendix G

Analysis of maximum gain of a SDOF system

In Chapter 3 maximum gain corresponding to different number of high-pass filters are derived. Acceleration, velocity and displacement feedback control system with no high-pass filter (ideal system) and one high-pass filter are discussed in Chapter 3.

Consider an acceleration feedback control system with two first order high-pass filters. The open-loop frequency response function is given by,

$$G(j\Omega)H(j\Omega)=\frac{g_a}{m}\left(\frac{-\Omega^2}{(1-\Omega^2)+j2\zeta\Omega}\right)\left(\frac{j\alpha\Omega}{1+j\alpha\Omega}\right)^2 \tag{G1}$$

Equation (G1) can be arranged into real and imaginary parts as follows,

$$\mathrm{Re}\{G(j\Omega)H(j\Omega)\}=\frac{g_a}{m}\frac{\Omega^4\alpha^2\left(4\zeta\alpha\Omega^2+(1-\Omega^2)(\alpha^2\Omega^2-1)\right)}{\left((1-\Omega^2)^2+(2\zeta\Omega)^2\right)(1+\alpha^2\Omega^2)^2} \tag{G2}$$

$$\mathrm{Im}\{G(j\Omega)H(j\Omega)\}=\frac{g_a}{m}\frac{2\alpha^2\Omega^5\left(\zeta(\alpha^2\Omega^2-1)+\alpha(1-\Omega^2)\right)}{\left((1-\Omega^2)^2+(2\zeta\Omega)^2\right)(1+\alpha^2\Omega^2)^2} \tag{G3}$$

Applying the Nyquist criterion as described in Chapter 3 gives,

$$\Omega_c^2=\frac{\alpha+\zeta}{\alpha(\alpha\zeta+1)} \tag{G4}$$

For systems with $\alpha >> 1$ and $\zeta << 1$, the critical frequency is given by,

$$\Omega_c \approx \frac{1}{\sqrt{1+\alpha\zeta}} \tag{G5}$$

Substituting the critical frequency into the real part of the open-loop frequency response function given by equation (2) and equation to -1 gives the maximum gain as,

$$\frac{g_{a\_\max}}{m}\approx\alpha\zeta \tag{G6}$$

Now consider velocity feedback control system with two high-pass filters. The open-loop frequency response function is given by,

$$G(j\Omega)H(j\Omega)=\frac{2\zeta g_v}{c}\left(\frac{j\Omega}{(1-\Omega^2)+j2\zeta\Omega}\right)\left(\frac{j\alpha\Omega}{1+j\alpha\Omega}\right)^2 \tag{G7}$$

Equation (G7) can be arranged into real and imaginary parts as follows,

$$\mathrm{Re}\{G(j\Omega)H(j\Omega)\}=\left(\frac{2\zeta g_v\alpha^2}{c}\right)\frac{2\Omega^4\left(\zeta\left(\alpha^2\Omega^2-1\right)+\alpha\left(\Omega^2-1\right)\right)}{\left(\left(1-\Omega^2\right)^2+\left(2\zeta\Omega\right)^2\right)\left(1+\alpha^2\Omega^2\right)^2} \tag{G8}$$

$$\mathrm{Im}\{G(j\Omega)H(j\Omega)\}=\left(\frac{2\zeta g_v\alpha^2}{c}\right)\frac{\Omega^3\left(4\alpha\zeta\Omega^2+\left(1-\Omega^2\right)\left(\alpha^2\Omega^2-1\right)\right)}{\left(\left(1-\Omega^2\right)^2+\left(2\zeta\Omega\right)^2\right)\left(1+\alpha^2\Omega^2\right)^2} \tag{G9}$$

Applying the Nyquist criterion and considering $\alpha >> 1$ and $\zeta << 1$ gives the critical frequency as,

$$\Omega_c \approx \frac{1}{\alpha} \tag{G10}$$

Substituting the critical frequency into the real part of the open-loop frequency response function given by equation (G8) gives (for $\alpha >> 1$ and $\zeta << 1$),

$$\frac{g_{v\_\max}}{c} \approx \frac{\alpha}{\zeta} \tag{G11}$$

Now consider velocity feedback control system with three first order high-pass filters. The open-loop frequency response function is given by,

$$G(j\Omega)H(j\Omega)=\frac{2\zeta g_v}{c}\left(\frac{j\Omega}{(1-\Omega^2)+j2\zeta\Omega}\right)\left(\frac{j\alpha\Omega}{1+j\alpha\Omega}\right)^3 \tag{G12}$$

Equation (G12) can be arranged into real and imaginary parts to give,

$$\mathrm{Re}\{G(j\Omega)H(j\Omega)\}=\left(\frac{2\zeta g_v\alpha^3}{c}\right)\frac{\Omega^4\left(2\zeta\alpha\Omega^2\left(\alpha^2\Omega^2-3\right)+\left(\Omega^2-1\right)\left(3\alpha^2\Omega^2-1\right)\right)}{\left(\left(1-\Omega^2\right)^2+\left(2\zeta\Omega\right)^2\right)\left(1+\alpha^2\Omega^2\right)^3} \tag{G13}$$

$$\mathrm{Im}\{G(j\Omega)H(j\Omega)\}=\left(\frac{2\zeta g_v\alpha^3}{c}\right)\frac{\Omega^5\left(2\zeta\left(3\alpha^2\Omega^2-1\right)+\alpha\left(1-\Omega^2\right)\left(\alpha^2\Omega^2-3\right)\right)}{\left(\left(1-\Omega^2\right)^2+\left(2\zeta\Omega\right)^2\right)\left(1+\alpha^2\Omega^2\right)^3} \tag{G14}$$

Applying the Nyquist criterion and considering $\alpha >> 1$ and $\zeta << 1$ gives the critical frequency as,

$$\Omega_c \approx \frac{\sqrt{3}}{\alpha} \tag{G15}$$

Substituting the critical frequency into the real part of the open-loop frequency response function given by equation (G13) gives (for $\alpha >> 1$ and $\zeta << 1$),

$$\frac{g_{c\_\max}}{c} \approx \frac{4\alpha}{9\zeta} \tag{G16}$$

Now consider displacement feedback control system with two first order high-pass filters. The open-loop frequency response function is given by,

$$G(j\Omega)H(j\Omega) = \frac{g_d}{k}\left(\frac{1}{(1-\Omega^2)+j2\zeta\Omega}\right)\left(\frac{j\alpha\Omega}{1+j\alpha\Omega}\right)^2 \tag{G17}$$

Equation (G17) can be arranged into real and imaginary parts as follows,

$$\mathrm{Re}\{G(j\Omega)H(j\Omega)\} = \left(\frac{g_d\alpha^2}{k}\right)\frac{\Omega^2\left(4\zeta\alpha\Omega^2+\left(1-\Omega^2\right)\left(\alpha^2\Omega^2-1\right)\right)}{\left(\left(1-\Omega^2\right)^2+\left(2\zeta\Omega\right)^2\right)\left(1+\alpha^2\Omega^2\right)^2} \tag{G18}$$

$$\mathrm{Im}\{G(j\Omega)H(j\Omega)\} = -\left(\frac{g_d\alpha^2}{k}\right)\frac{2\Omega^3\left(\zeta\left(\alpha^2\Omega^2-1\right)+\alpha\left(\Omega^2-1\right)\right)}{\left(\left(1-\Omega^2\right)^2+\left(2\zeta\Omega\right)^2\right)\left(1+\alpha^2\Omega^2\right)^2} \tag{G19}$$

Applying the Nyquist criterion and considering $\alpha >> 1$ and $\zeta << 1$ gives the critical frequency as,

$$\Omega_c \approx \frac{1}{\sqrt{1+\zeta\alpha}} \tag{G20}$$

Substituting the critical frequency into the real part of the open-loop frequency response function given by equation (G18) gives,

$$\mathrm{Re}\{G(j\Omega)H(j\Omega)\} = \left(\frac{g_d\alpha^2}{k}\right)\frac{(\zeta\alpha+1)(\alpha+\zeta)}{\zeta\left(4\alpha^2\zeta^2+4\zeta\alpha\left(\alpha^2+1\right)+\left(\alpha^2+1\right)\right)} \tag{G21}$$

Which is positive and hence the system is *unconditionally stable*.

Now consider displacement feedback control system with three first order high-pass filters. The open-loop frequency response function is given by,

$$G(j\Omega)H(j\Omega) = \frac{g_d}{k}\left(\frac{1}{(1-\Omega^2)+j2\zeta\Omega}\right)\left(\frac{j\alpha\Omega}{1+j\alpha\Omega}\right)^3 \tag{G22}$$

Equation (G22) can be arranged into real and imaginary parts as follows,

$$\mathrm{Re}\left\{G(j\Omega)H(j\Omega)\right\}=\left(\frac{g_d\alpha^3}{k}\right)\frac{\Omega^4\left(2\zeta\left(3\alpha^2\Omega^2-1\right)+\alpha\left(\Omega^2-1\right)\left(\alpha^2\Omega^2-3\right)\right)}{\left(\left(1-\Omega^2\right)^2+\left(2\zeta\Omega\right)^2\right)\left(1+\alpha^2\Omega^2\right)^3} \quad \text{(G23)}$$

$$\mathrm{Im}\left\{G(j\Omega)H(j\Omega)\right\}=\left(\frac{g_d\alpha^3}{k}\right)\frac{\Omega^3\left(2\alpha\zeta\Omega^2\left(\alpha^2\Omega^2-3\right)+\left(1-\Omega^2\right)\left(3\alpha^2\Omega^2-1\right)\right)}{\left(\left(1-\Omega^2\right)^2+\left(2\zeta\Omega\right)^2\right)\left(1+\alpha^2\Omega^2\right)^3} \quad \text{(G24)}$$

Applying the Nyquist criterion and considering $\alpha >> 1$ and $\zeta << 1$ gives the critical frequency as,

$$\Omega_c \approx \frac{1}{\sqrt{3}\alpha} \quad \text{(G25)}$$

Substituting the critical frequency into the real part of the open-loop frequency response function given by equation (G23) gives (for $\alpha >> 1$ and $\zeta << 1$),

$$\frac{g_{d\_\max}}{k} \approx 8 \quad \text{(G26)}$$

Now consider displacement feedback control system with four high-pass filters. The open-loop frequency response function is given by,

$$G(j\Omega)H(j\Omega)=\frac{g_d}{k}\left(\frac{1}{\left(1-\Omega^2\right)+j2\zeta\Omega}\right)\left(\frac{j\alpha\Omega}{1+j\alpha\Omega}\right)^4 \quad \text{(G27)}$$

Equation (G27) can be arranged into real and imaginary parts as follows,

$$\mathrm{Re}\left\{G(j\Omega)H(j\Omega)\right\}=\frac{g_d\alpha^4}{k}\frac{\Omega^4\left(8\zeta\alpha\Omega^2\left(\alpha^2\Omega^2-1\right)+\left(\Omega^2-1\right)\left(\alpha^4\Omega^4-6\alpha^2\Omega^2+1\right)\right)}{\left(\left(1-\Omega^2\right)^2+\left(2\zeta\Omega\right)^2\right)\left(1+\alpha^2\Omega^2\right)^4} \quad \text{(G28)}$$

$$\mathrm{Im}\left\{G(j\Omega)H(j\Omega)\right\}=-\left(\frac{g_d\alpha^4}{k}\right)\frac{2\Omega^5\left(\zeta\left(\alpha^4\Omega^4-6\alpha^2\Omega^2+1\right)+2\alpha\left(1-\Omega^2\right)\left(\alpha^2\Omega^2-1\right)\right)}{\left(\left(1-\Omega^2\right)^2+\left(2\zeta\Omega\right)^2\right)\left(1+\alpha^2\Omega^2\right)^3} \quad \text{(G29)}$$

Applying the Nyquist criterion and considering $\alpha >> 1$ and $\zeta << 1$ gives the critical frequency as,

$$\Omega_c \approx \frac{1}{\alpha} \quad \text{(G30)}$$

Substituting the critical frequency into the real part of the open-loop frequency response function given by equation (G28) gives (for $\alpha >> 1$ and $\zeta << 1$),

$$\frac{g_{d\_\max}}{k} \approx 4 \quad \text{(G31)}$$

Appendix H

Analysis of instruments used in active control

An attempt was made to study the characteristics of each instrument used in this project and to mathematically model their characteristics that were obtained experimentally.

H1 Power Amplifiers

A simple experiment, as depicted in figure H1, was conducted to measure the frequency response of the power amplifiers. White noise from a Hewlett Packard analyser C (Type 35650 serial No 2911A02485) was fed into the power amplifier and the output was normalised by the input white noise signal. Figure H2 shows the measured characteristic of power amplifier 1 (H/H electronic TPA 50-D, S.No 14415), which was used in the experiment discussed in Chapter 3.

It can be seen that the phase of the system tends to zero above 100 Hz. In addition at low frequencies the phase trends to 90 degrees. It suggests that the power amplifier contains a high-pass filter of first order, and a mathematical model can take the following form in the frequency domain.

$\frac{jg_{p1}\omega}{(1+j\tau_{p1}\omega)}$, where g_{p1} is the gain of power amplifier 1 and τ_{p1} is the time constant.

This function can be expressed as magnitude and phase. The magnitude is $PA1 = \frac{g_{p1}\omega}{\sqrt{(1+\tau_{p1}^2\omega^2}}$ and the phase is $\phi = 90 - \tan^{-1}(\tau_{p1}\omega)$.

From measurement of power amplifier characteristics, the phase angle ϕ_i and the magnitude $PA1_i$ are known for each frequency points f_i in the range 0~200 Hz. Where i goes from 1 to the number of frequency lines in the measurements n. Using the

phase relationship above, the time constant τ_{p1i} can be calculated for each frequency point f_i. . τ_{p1i} becomes,

$$\tau_{p1i} = \frac{\tan(90-\phi_i)}{\omega_i} \tag{H1}$$

Now using magnitude relationship and equation (H1), the coefficient g_{p1i} can be calculated for each frequency point. It becomes,

$$g_{p1i} = \frac{PA1_i\sqrt{(1+\tau_{p1i}^2\omega_i^2}}{\omega_i} \tag{H2}$$

An estimate of the time constant τ_{p1} and gain g_{p1} are the average of τ_{p1i} and g_{p1i} over the frequency range. Since it takes into account the measurement over the frequency range considered, they are considered to be reasonable estimate. They can be expressed as follows,

$$\tau_{p1} = \frac{\sum_{i=1}^{n}\tau_{p1i}}{n} \tag{H3}$$

$$g_{p1} = \frac{\sum_{i=1}^{n} g_{p1i}}{n} \tag{H4}$$

The frequency response function of the power amplifier 1 then becomes,

$$Pow\_amp1 = \frac{j0.2775\omega}{(1+j0.0633\omega)} \tag{H5}$$

Figure A2.2 also shows the Bode magnitude plot and phase plot for this model. It can be seen that this plot is in good agreement with the measured characteristic of power amplifier 1.

Since power amplifier 2 (H/H electronic TPA 100-D, S.No 15397) was used as a controller all available gains were measure and are shown in Figure H3. The phase difference between the low and high frequency of the power amplifier characteristics suggests that it contains a high-pass filter of order 2. Hence the frequency response function can be written as,

$$Pow\_amp2 = \frac{-g_{p2}\omega^2}{(1+j\tau_{p2}\omega)^2} \tag{H6}$$

where g_{p2} is the gain and τ_{p2} is the time constant of power amplifier 2. Similar to power amplifier 1, equation (H6) can be simplified to obtain the time constant τ_{p2} and the gain g_{p2}.

From the phase relationship the coefficient τ_{p2i} at each frequency point becomes,

$$\tau_{p2_i} = \frac{\tan\left(90 - \frac{\phi_i}{2}\right)}{\omega_i} \tag{H7}$$

Now using magnitude relationship,

$$g_{p2i} = \frac{PA2_i(1+\tau_{p2i}^2\omega_i^2)}{\omega_i^2} \tag{H8}$$

where $PA2_i$ and ϕ_i are measured magnitude and phase at each frequency points.

Now the time constant τ_{p2} and gain g_{p2} can be calculated using equations (H3) and (H4) with appropriate modifications. Repeating the procedure for each gain settings, g_{p2} for each gain can be found. The frequency response function for the power amplifier 2 then becomes,

$$Pow\_amp2 = \frac{-g_{p2}\omega^2}{(1+j0.0633\omega)^2} \tag{H9}$$

Where g_{p2} = [0.002, 0.0045, 0.0075, 0.0131, 0.0162, 0.020].

The mathematical model is plotted in the form of Bode magnitude plot and phase plot as shown in Figure H3. It can be seen that these plots are in good agreement with the measured characteristic of the power amplifier. Due to poor quality of the measurement at very low frequencies, the measurement of power amplifier 1 and 2 is not shown at very low frequencies. It is also interesting to note that the phase is independent of gain. This is because the characteristics of power amplifier are linear. Small peaks at frequencies 50 Hz and 150 Hz are due to the line effect.

H2 Charge Amplifier with integrator module

As discussed in Chapter 3, a charge amplifier was used to integrate the accelerometer output so that the output is proportional to the velocity or displacement. Hence velocity or displacement feedback control can also be studied. Kim et el. [88] measured the characteristic of a single integrator of charge amplifier using the following approach.

In the frequency domain acceleration and velocity are related by,

$$\ddot{X} = j\omega\dot{X}$$

This can be rearranged to give,

$$\frac{\dot{X}}{\ddot{X}} = \frac{1}{j\omega}$$

Where $\ddot{X}$ and $\dot{X}$ denote acceleration and velocity respectively. Therefore dividing the velocity response measured at a point by acceleration response measured at the same point.

gives the integrator characteristics. Similarly dividing the displacement response measured at a point by acceleration response measured at the same point gives characteristics of the double integrator.

The B&K (type 2635) charge amplifier was used for this purpose. It contains a high-pass filter and an integrator module. For velocity and displacement response the high-pass filter can be set to a cut-off frequency of 1Hz or 10Hz. Signal from an accelerometer (B&K type 4375, S. No- 987173) attached to large shaker was fed into the channel 2 of Hewlett Packard analyser as shown in Figure H4. A random signal from the analyser, which was amplified by a power amplifier (H/H electronic TPA 50-D S.No 14415) excited the large shaker as shown in Figure H4.

The measured characteristic of single integrator is shown in Figure H5. Due to the low sensitivity of the actuator and sensor at low frequencies, the responses at low frequencies are not shown. Even with a 1Hz cut off frequency there is a small phase advance at very low frequencies. However the phase approximately tends to -90 degree at high frequencies.

The integrator module in the charge amplifier performs integrations of the filtered signals electronically. It is assumed that the integrator module and high-pass filter can be represented separately in a mathematical model.

Therefore the charge amplifier together with its high pass filter can be modelled as,

$$cha\_amp1 = \frac{jg_c\omega}{(1+j\tau_c\omega)} \frac{1}{(1+j\tau_i\omega)} \tag{H10}$$

where g_c is the gain of the charge amplifier and $1/\tau_c$ and $1/\tau_i$ are the corner frequency of the high pass filter and integrator respectively.

There are three unknown in equation (H10), only two can be found using magnitude and phase information. Hence one of the coefficients has to be fixed to a suitable value. The most appropriate is to fix the time constant τ_c to the setting of the charge amplifier cut-off frequency. The time constant τ_c can be related to the cut-off frequency of the charge amplifier by $\tau_c = \frac{1}{2\pi f_c}$, where f_c is the cut-off frequency. For 1 Hz and 10 Hz cut-off frequencies τ_c is 0.159 and 0.0159 respectively.

Therefore the overall mathematical model of the charge amplifier becomes,

$$Cha\_amp1 = \frac{jg_{c1}\omega}{(1+j0.159\omega)} \times \frac{1}{(1+j\tau_{i1}\omega)} \tag{H11}$$

$$Cha\_amp10 = \frac{jg_{c2}\omega}{(1+j0.0159\omega)} \times \frac{1}{(1+j\tau_{i2}\omega)} \tag{H12}$$

Using a similar approach to the power amplifier, the charge amplifier characteristics can be written as,

At cut-off frequency 1 Hz

$$Cha\_amp1 = \frac{j4.1539\omega}{(1+j0.159\omega)} \times \frac{1}{(1+j0.251\omega)} \tag{H13}$$

At cut-off frequency 10 Hz

$$Cha\_amp10 = \frac{j0.0567\omega}{(1+j0.0159\omega)} \times \frac{1}{(1+j0.0333\omega)} \tag{H14}$$

H3. Charge Amplifier with double integrator module

Figure H6 shows the charge amplifier characteristic at double integration. A cut-off frequency of 1 Hz was used. Therefore, it can be assumed that the high-pass model in equation (H11) is unchanged. Thus, a mathematical model for the charge amplifier at double integration can be written as,

$$Cha\_amp\_double = \frac{jg_{dc}}{(1+j0.159\omega)} \times \frac{1}{(1+j\tau_{id}\omega)^2} \qquad \text{(H15)}$$

Using the phase and magnitude relationship and applying a similar argument presented for power amplifier, the double integration model can be expressed as,

$$Cha\_amp\_double = \frac{j5.0752\omega}{(1+j0.159\omega)} \times \frac{1}{(1+j0.1757\omega)^2} \qquad \text{(H16)}$$

Figure H5 also shows the Bode plot of this mathematical model. It can be seen that the representation up to about 3Hz does not reflect the measured characteristic exactly. However apart from that it is a reasonable representation. One reason may be the inaccuracy of the measured response at low frequency. As mentioned above at low frequencies the accelerometer has low sensitivity.

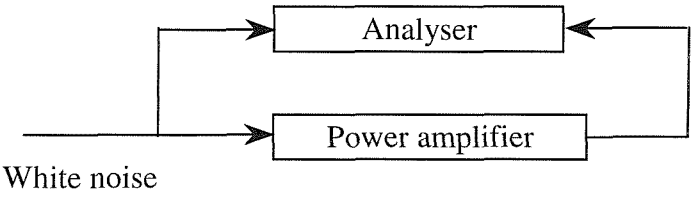

Figure H1 the arrangement for measuring frequency response function of Power amplifier

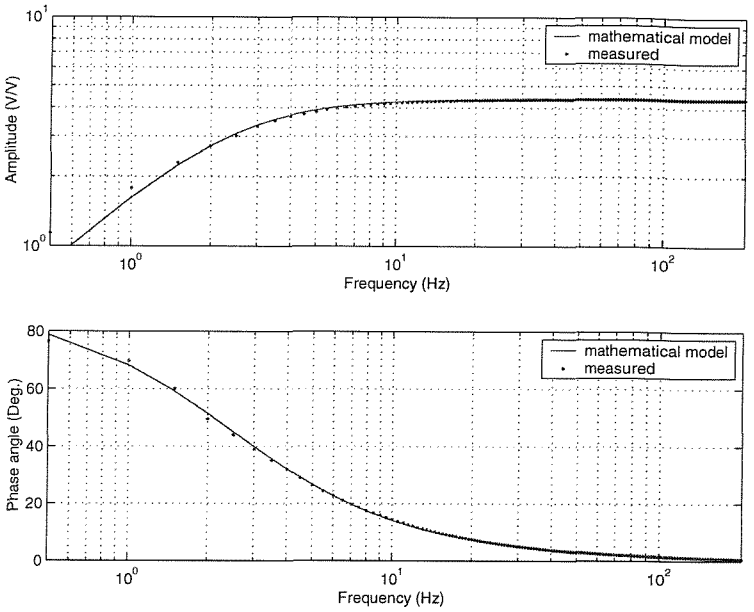

Figure H2 Measured and mathematical model of the characteristic of power amplifier 1

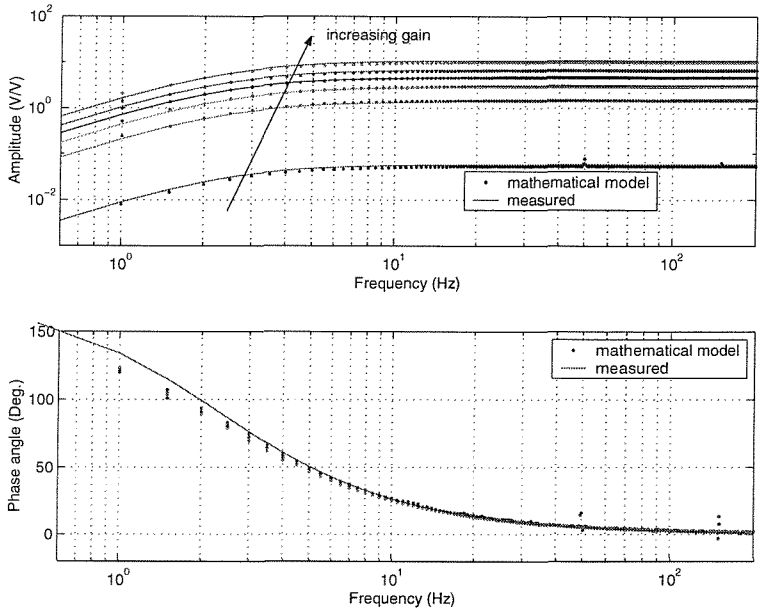

Figure H3 Measured and mathematical model of the characteristic of power amplifier 2

(Each curve in the magnitude plot corresponds to the gain settings in the power amplifier from its lowest position. As the gain increased the plots shifts upwards in the direction shown. Corresponding gains are [0.002, 0.0045, 0.0075, 0.0131, 0.0162, 0.020])

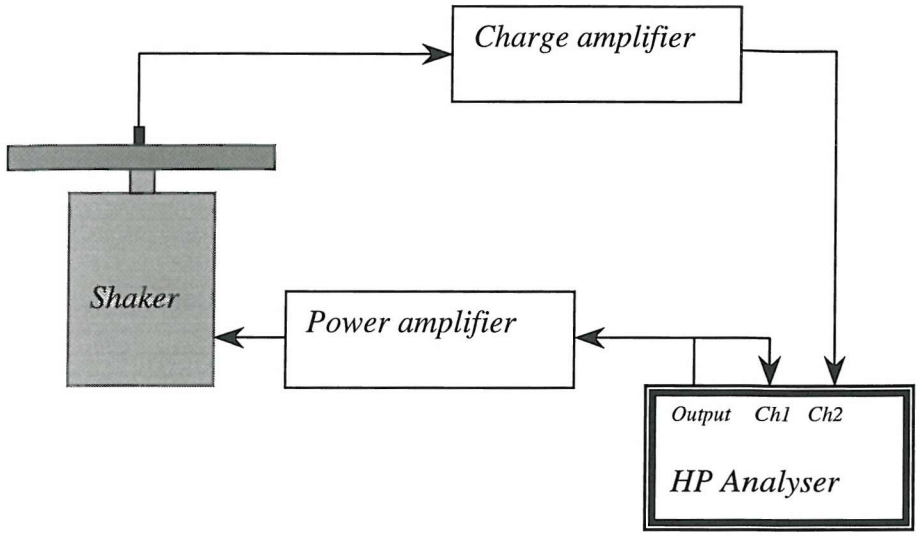

Figure H4 the arrangement for measuring frequency response function of charge amplifier.

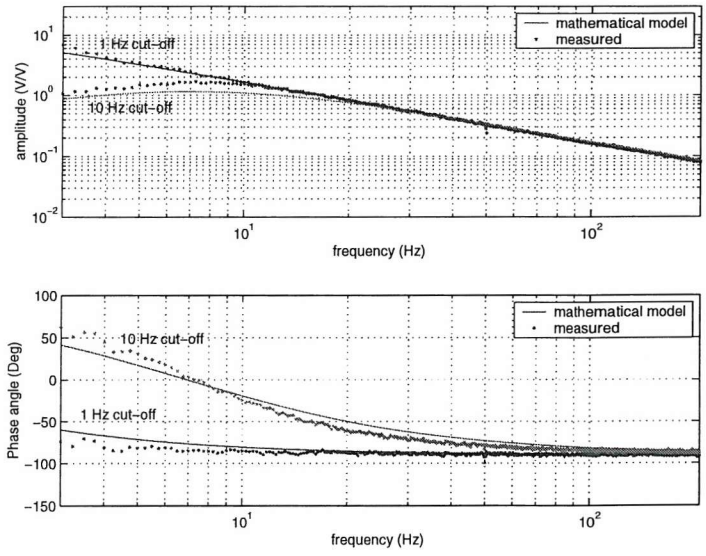

Figure H5 Measured and mathematical model of charge amplifier characteristics at 1 Hz and 10 Hz cut-off frequencies.

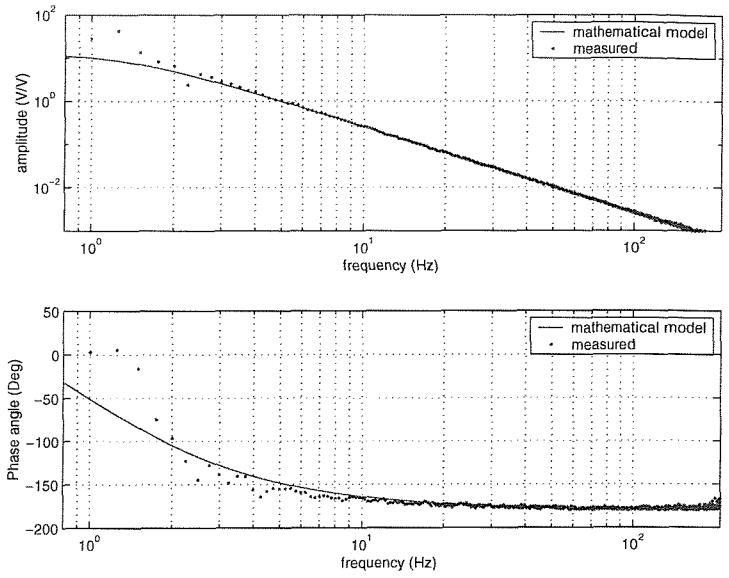

Figure H6 Measured and mathematical model of Charge Amplifier characteristic at double integration

Appendix I

Simulated and experimental results of a perfectly working system and a system with failure

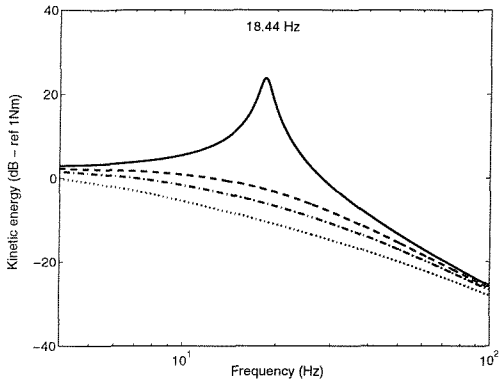

(a) Total kinetic energy (Perfectly working system)

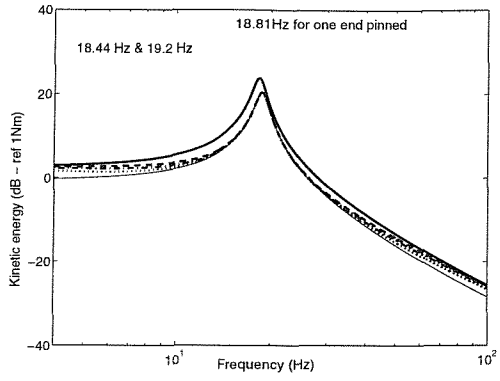

(b) Total kinetic energy (System with single channel failure)

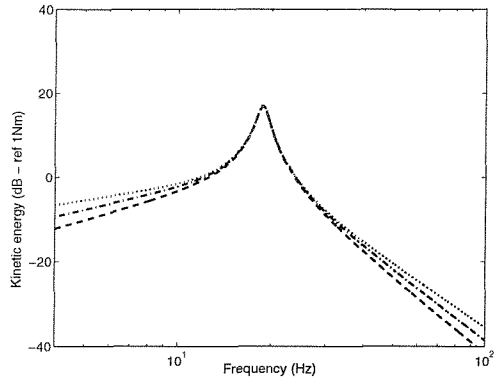

(c) Rotational motion at mass centre (System with single channel failure)

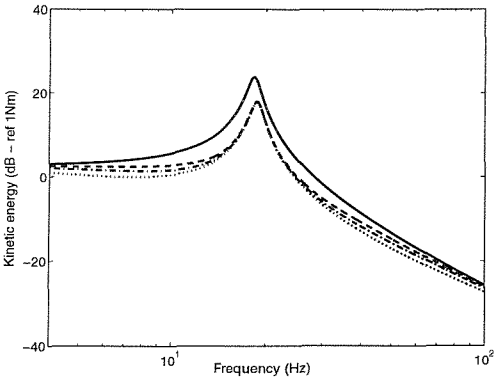

(d) Translational motion at mass centre (System with single channel failure)

Figure I1 Kinetic energy plots for the two-mount system on a moving inelastic base - mass centre is at 0.5l (simulations). Non-dimensional gain 0: _____ non-dimensional gain 20: -- --------, non-dimensional gain 30: -.-.-.-.-.-., non-dimensional gain 50: ..... infinite gain:_____

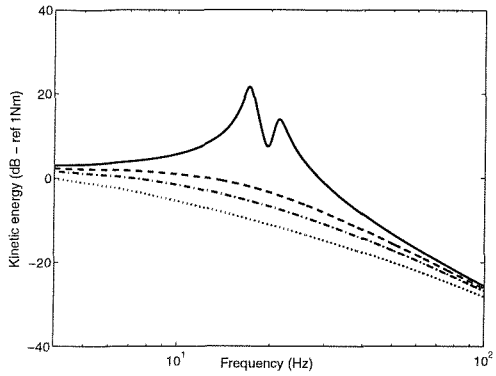

(a) Perfectly working system

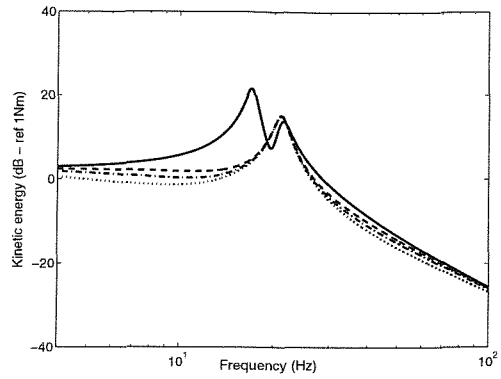

(d) System with single channel failure (Translational motion at mass centre)

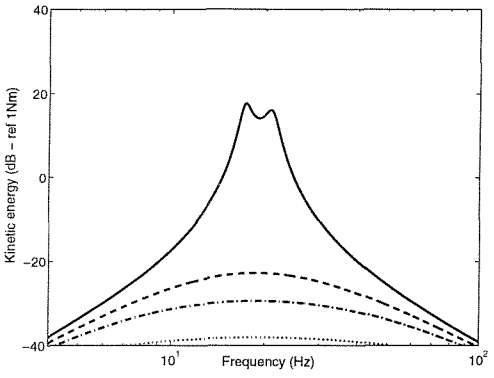

(b) Perfectly working system

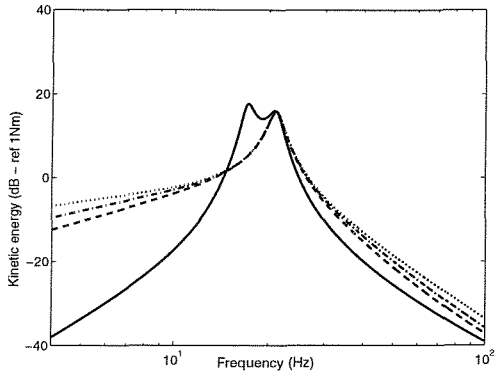

(e) System with single channel failure (Rotational motion at mass centre)

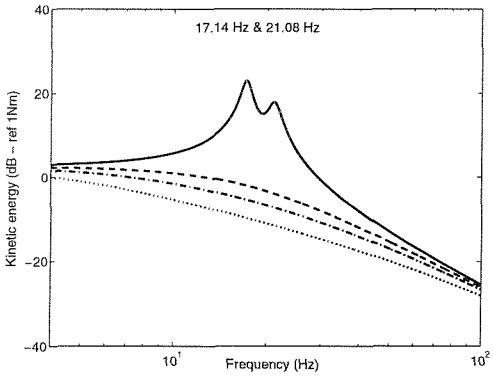

(c) Perfectly working system

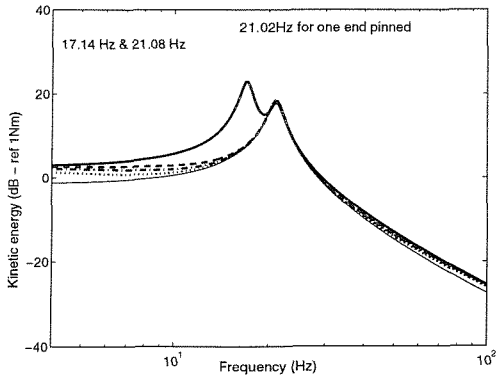

(f) System with single channel failure (Total kinetic energy)

Figure I2 Kinetic energy plots for the two-mount system on a moving inelastic base - mass centre is at 0.404l (simulations). Non-dimensional gain 0: _____ non-dimensional gain 20: ----------, non-dimensional gain 30: -.-.-.-.-.-., non-dimensional gain 50: ..... infinite gain:_____

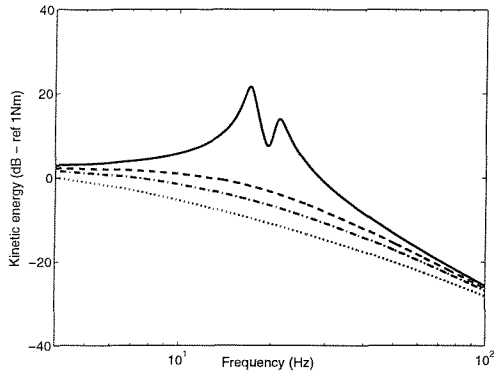

(a) Perfectly working system

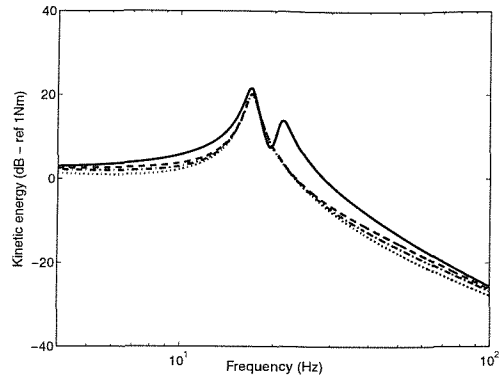

(d) System with single channel failure (Translational motion at mass centre)

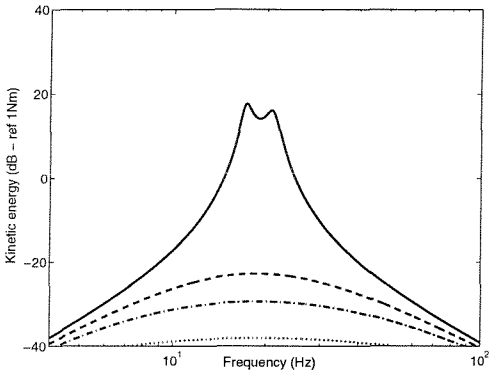

(b) Perfectly working system

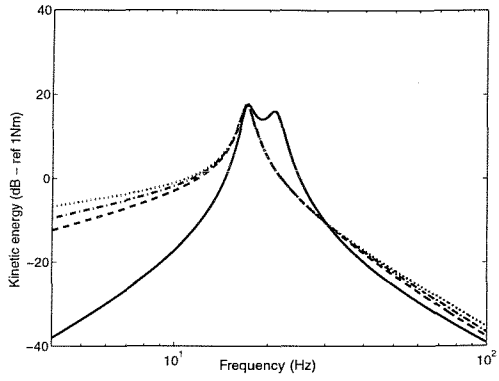

(e) System with single channel failure (Rotational motion at mass centre)

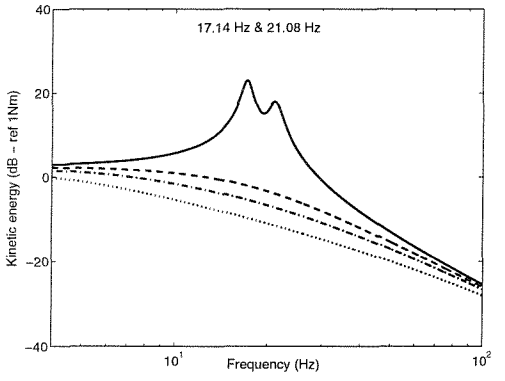

(c) Perfectly working system

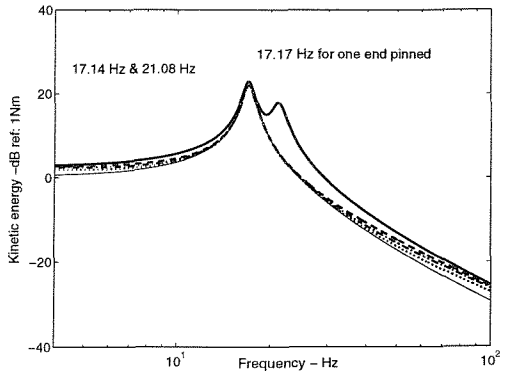

(f) System with single channel failure (Total kinetic energy)

Figure I3 Kinetic energy plots for the two-mount system on a moving inelastic base - mass centre is at 0.596l (simulations). Non-dimensional gain 0: _____ non-dimensional gain 20: ----------, non-dimensional gain 30: -.-.-.-.-.-., non-dimensional gain 50: ..... infinite gain:_____

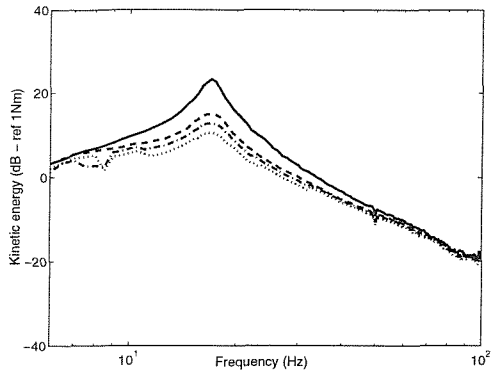

(a) Total kinetic energy (Perfectly working system)

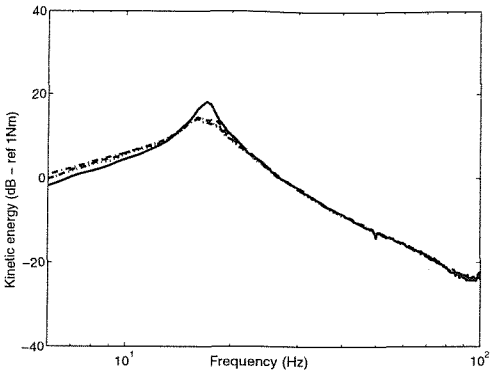

(b) Total kinetic energy (System with single channel failure)

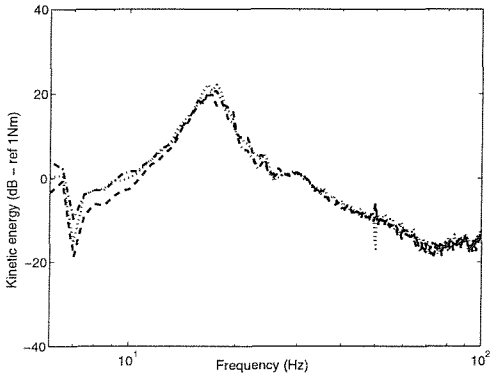

(c) Rotational motion at mass centre (System with single channel failure)

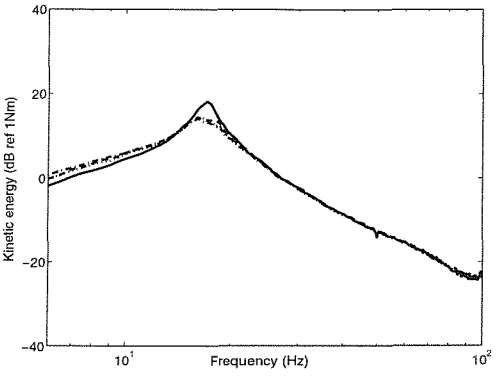

(d) Translational motion at mass centre (System with single channel failure)

Figure I4 Kinetic energy plots for the two-mount system on a moving inelastic base - mass centre is at 0.5l (Measurement). Power amplifier gain 0: _____ power amplifier gain 0.02: ----------, power amplifier gain 0.06: -.-.-.-.-.-., power amplifier gain 0.12: .....

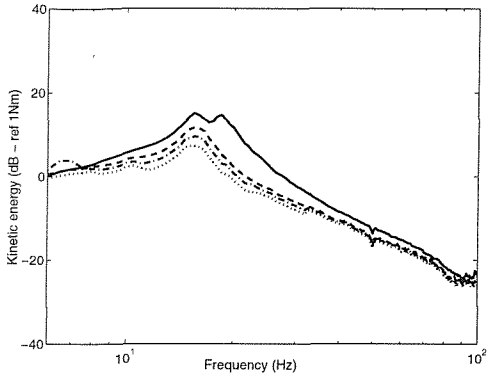

(a) Perfectly working system

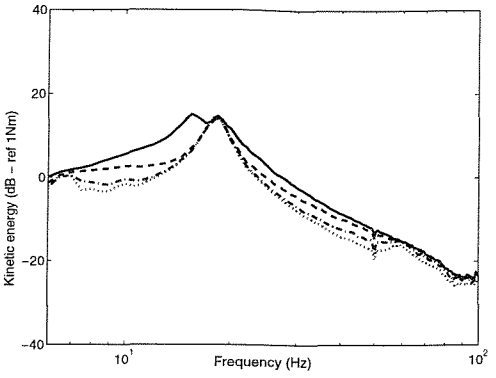

(d) System with single channel failure (Translational motion at mass centre)

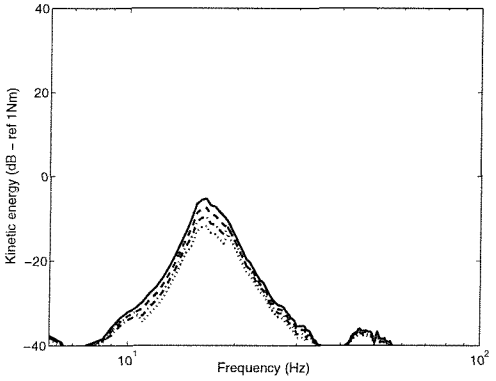

(b) Perfectly working system

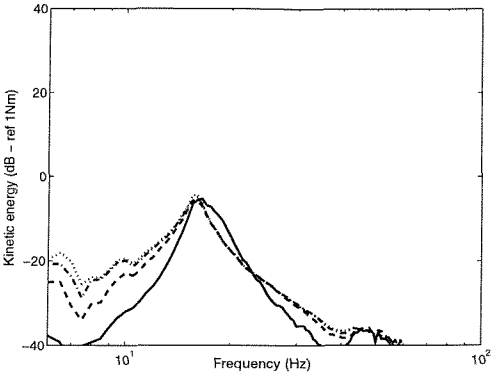

(e) System with single channel failure (Rotational motion at mass centre)

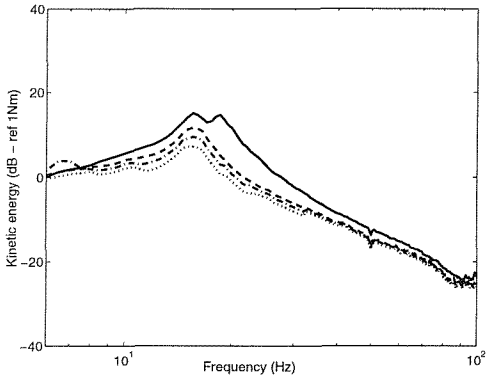

(c) Perfectly working system

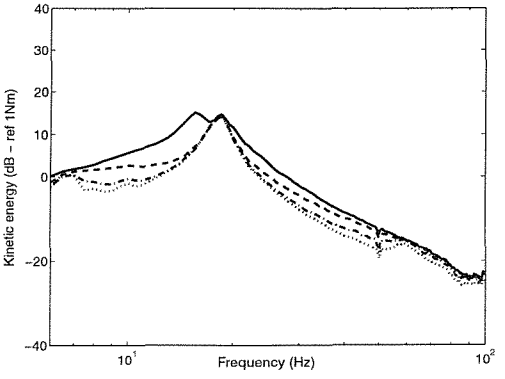

(f) System with single channel failure (Total kinetic energy)

Figure I5 Kinetic energy plots for the two-mount system on a moving inelastic base - mass centre is at 0.404l (Measurement). Power amplifier gain 0: _____ power amplifier gain 0.02: ----------, power amplifier gain 0.06: -.-.-.-.-.-., power amplifier gain 0.12: .....

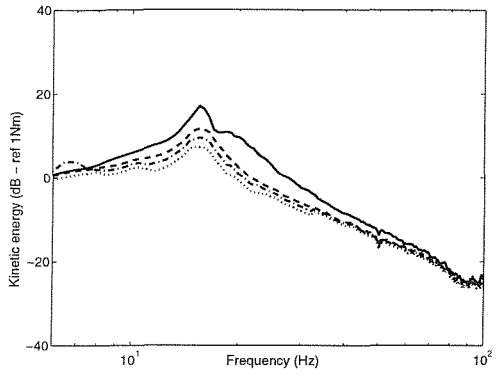

(a) Perfectly working system

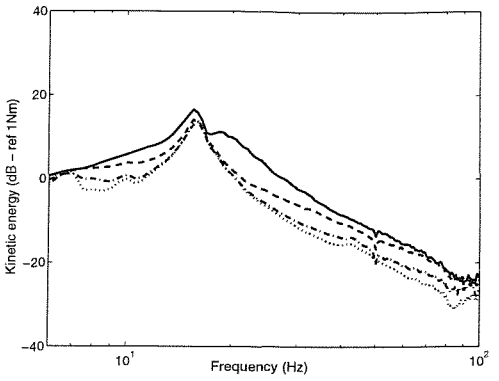

(d) System with single channel failure (Translational motion at mass centre)

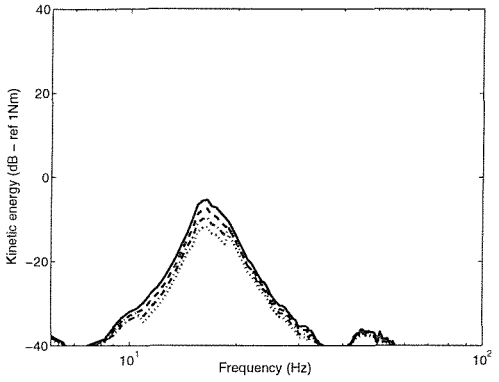

(b) Perfectly working system

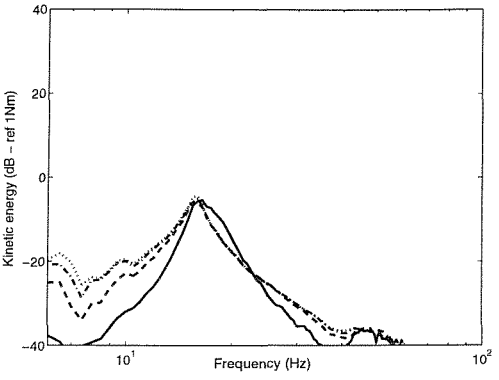

(e) System with single channel failure (Rotational motion at mass centre)

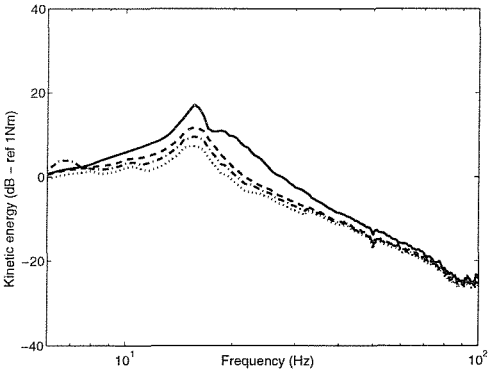

(c) Perfectly working system

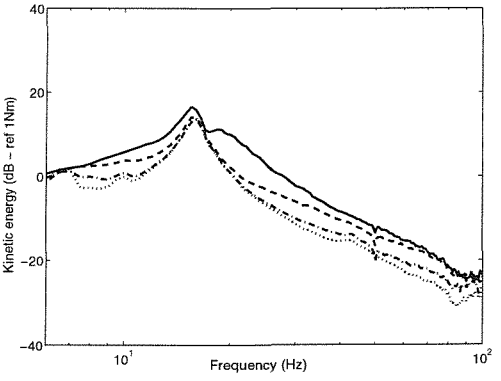

(f) System with single channel failure (Total kinetic energy)

Figure I6 Kinetic energy plots for the two-mount system on a moving inelastic base - mass centre is at 0.596l (Measurement). Power amplifier gain 0: _____ power amplifier gain 0.02: ----------, power amplifier gain 0.06: -.-.-.-.-.-., power amplifier gain 0.12: .....

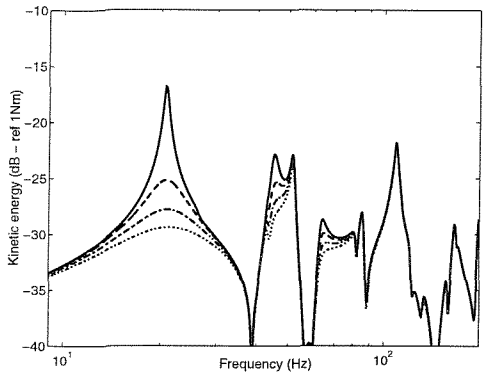

(a) Perfectly working system

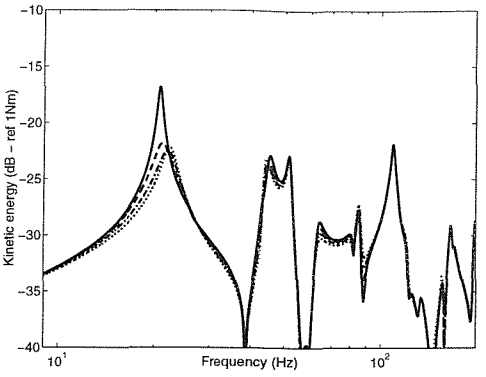

(d) System with single channel failure (Translational motion at mass centre)

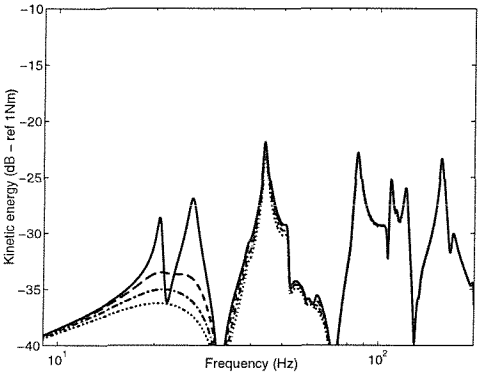

(b) Perfectly working system

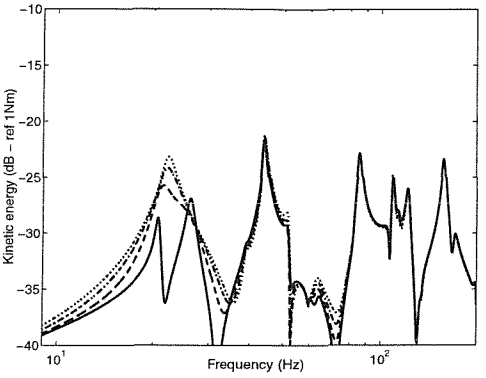

(e) System with single channel failure (Rotational motion at mass centre)

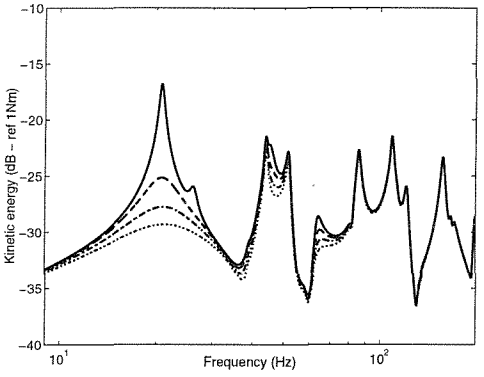

(c) Perfectly working system

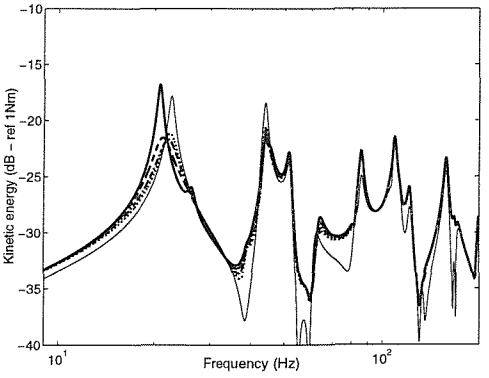

(f) System with single channel failure (Total kinetic energy)

Figure I7 Kinetic energy plots for the two-mount system on a CFCF flexible base - mass centre is at 0.5l (simulations). Non-dimensional gain 0: _____ non-dimensional gain 5: ----------, non-dimensional gain 10: -.-.-.-.-.-., non-dimensional gain 15: ..... non-dimensional gain 5000:_____

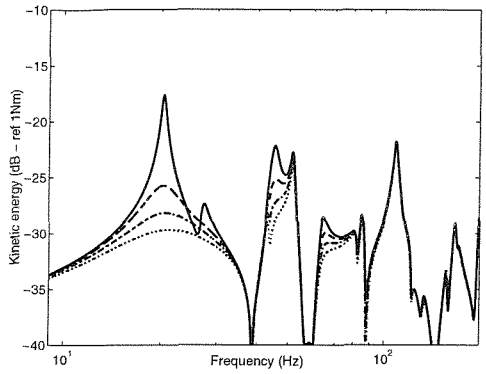

(a) Perfectly working system

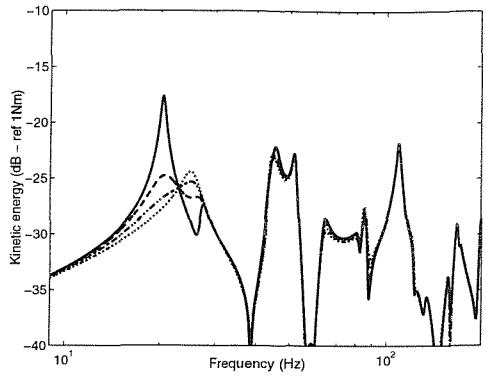

(d) System with single channel failure (Translational motion at mass centre)

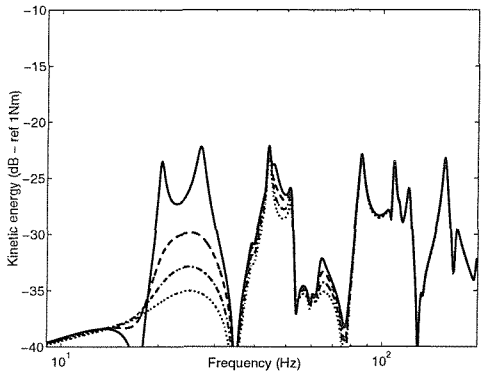

(b) Perfectly working system

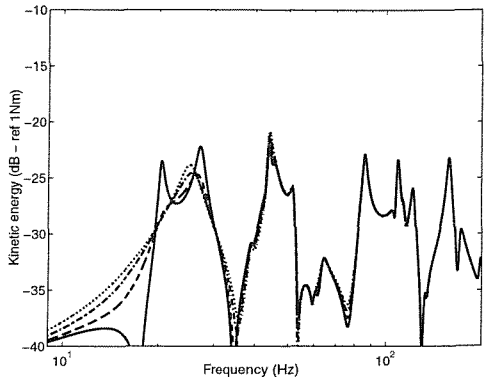

(e) System with single channel failure (Rotational motion at mass centre)

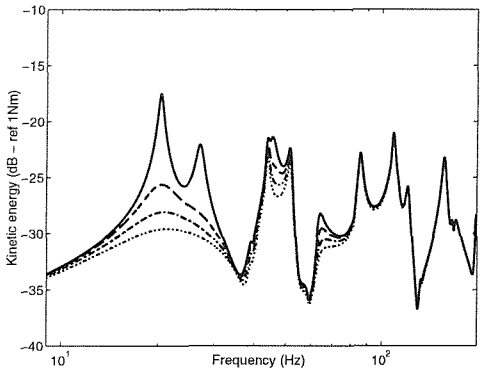

(c) Perfectly working system

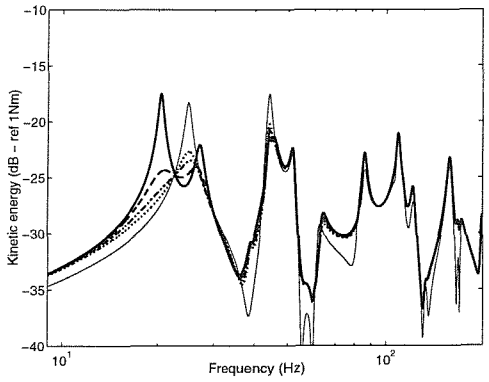

(f) System with single channel failure (Total kinetic energy)

Figure I8 Kinetic energy plots for the two-mount system on a CFCF flexible base - mass centre is at 0.404l (simulations). Non-dimensional gain 0: _____ non-dimensional gain 5: ----------, non-dimensional gain 10: -.-.-.-.-.-., non-dimensional gain 15: ..... non-dimensional gain 5000:_____

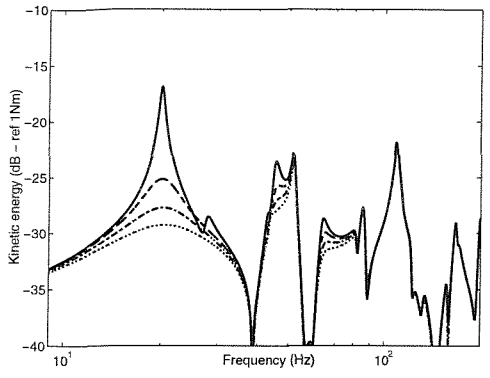

(a) Perfectly working system

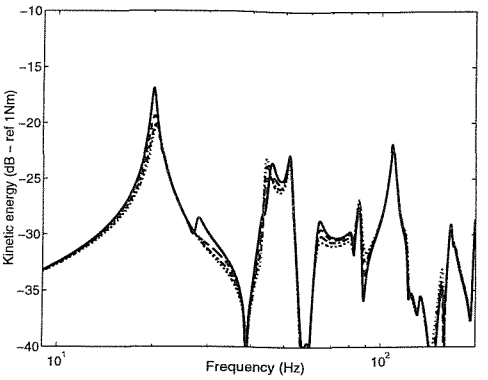

(d) System with single channel failure (Translational motion at mass centre)

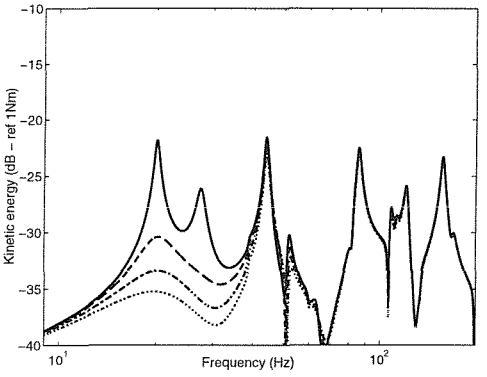

(b) Perfectly working system

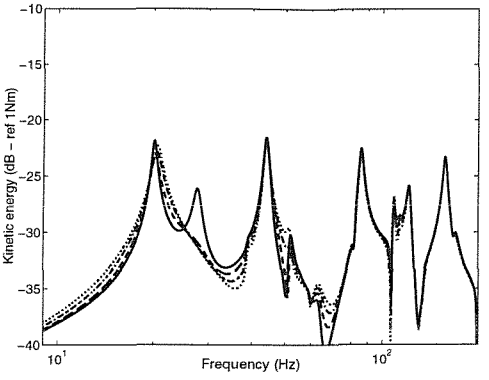

(e) System with single channel failure (Rotational motion at mass centre)

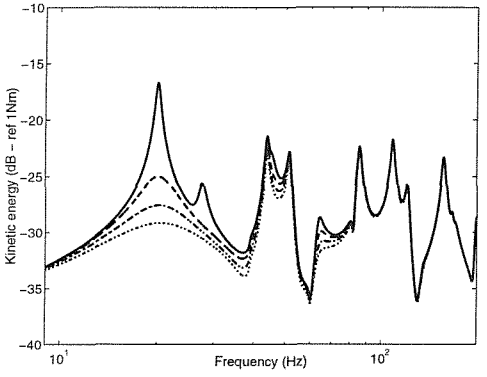

(c) Perfectly working system

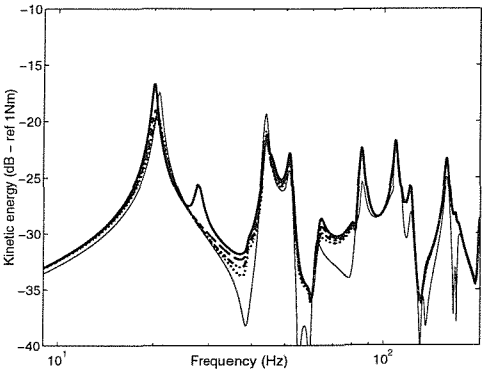

(f) System with single channel failure (Total kinetic energy)

Figure I9 Kinetic energy plots for the two-mount system on a CFCF flexible base - mass centre is at 0.596l (simulations). Non-dimensional gain 0: _____ non-dimensional gain 5: ----------, non-dimensional gain 10: -.-.-.-.-.-., non-dimensional gain 15: ..... non-dimensional gain 5000:_____

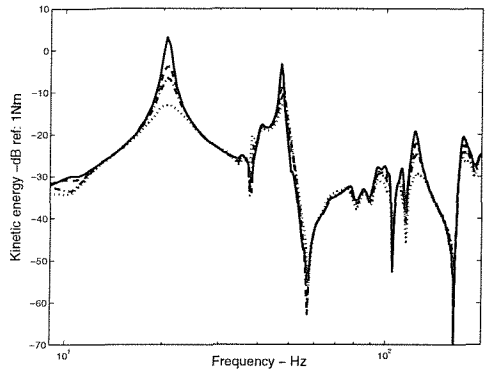

(a) Perfectly working system

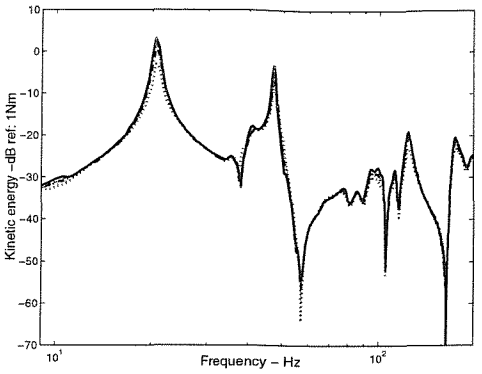

(d) System with single channel failure (Translational motion at mass centre)

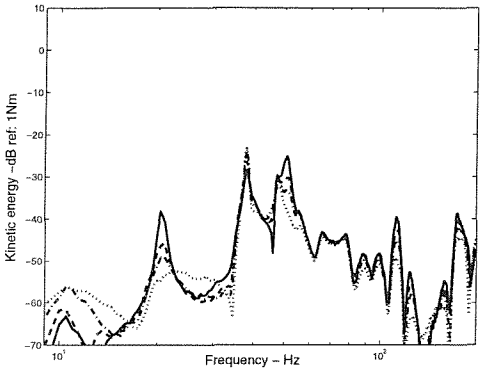

(b) Perfectly working system

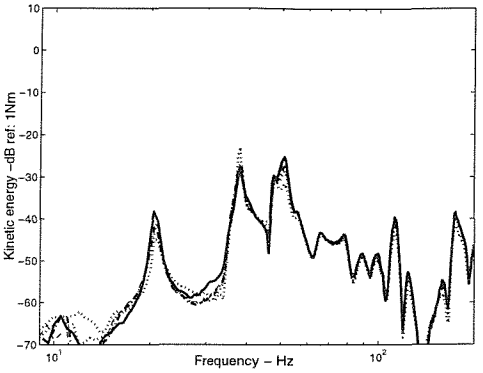

(e) System with single channel failure (Rotational motion at mass centre)

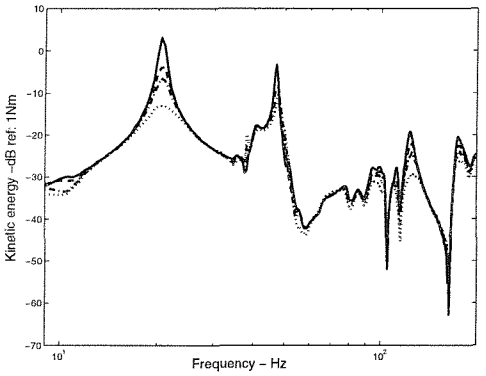

(c) Perfectly working system

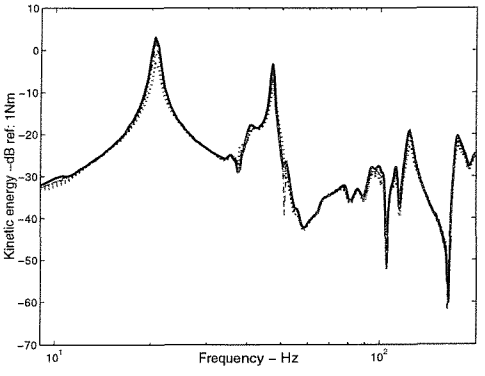

(f) System with single channel failure (Total kinetic energy)

Figure I10 Kinetic energy plots for the two-mount system on a CFCF flexible base - mass centre is at 0.5l (Measurement). power amplifier gain 0: _____ power amplifier gain 0.06: ----------, power amplifier gain 0.12: -.-.-.-.-.-., power amplifier gain 0.25: .....

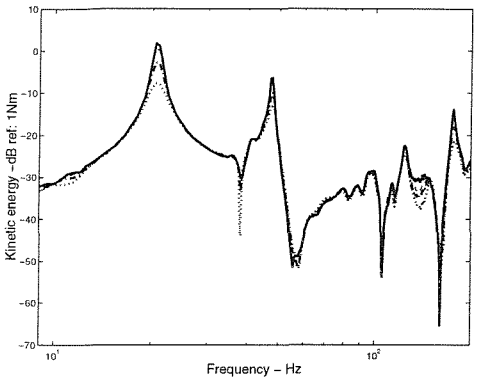

(a) Perfectly working system

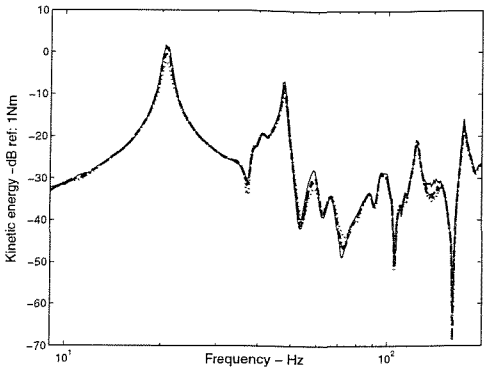

(d) System with single channel failure (Translational motion at mass centre)

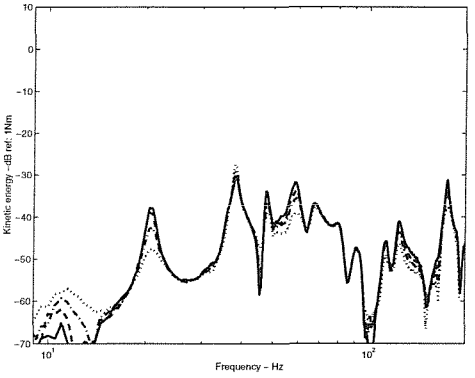

(b) Perfectly working system

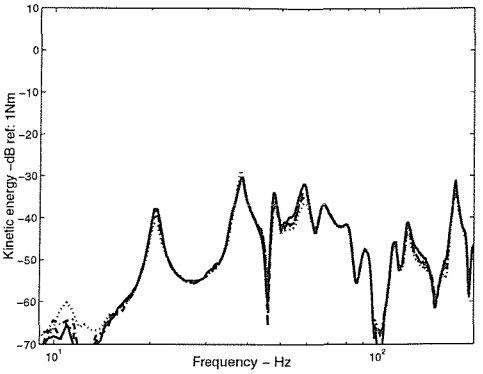

(e) System with single channel failure (Rotational motion at mass centre)

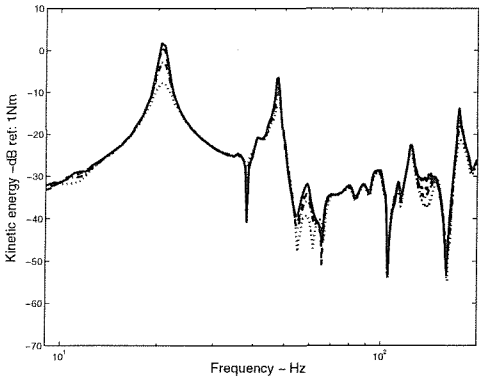

(c) Perfectly working system

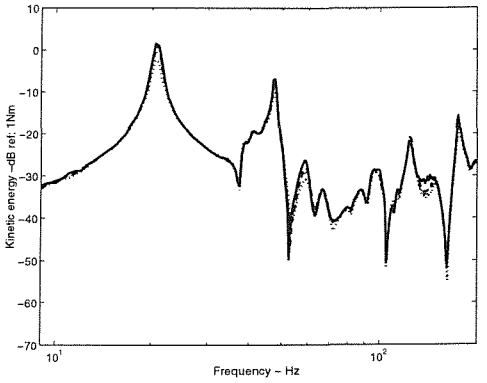

(f) System with single channel failure (Total kinetic energy)

Figure I11 Kinetic energy plots for the two-mount system on a CFCF flexible base - mass centre is at 0.404l (Measurement). power amplifier gain 0: _____ power amplifier gain 0.06: ----------, power amplifier gain 0.12: -.-.-.-.-.-., power amplifier gain 0.25: .....

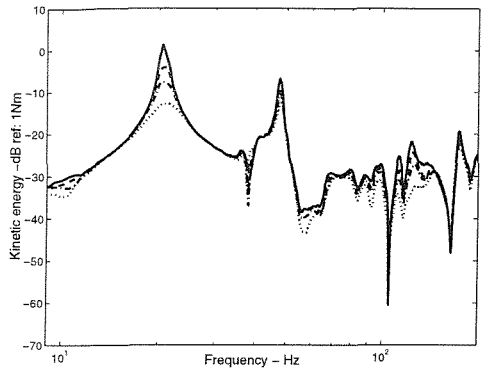

(a) Perfectly working system

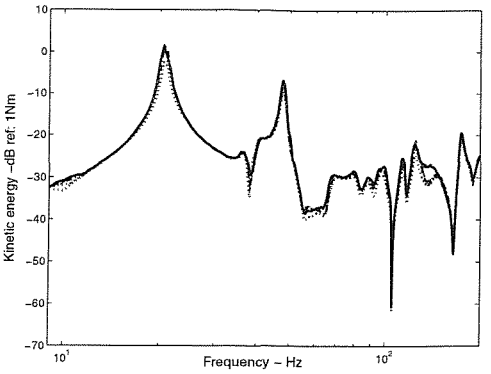

(d) System with single channel failure (Translational motion at mass centre)

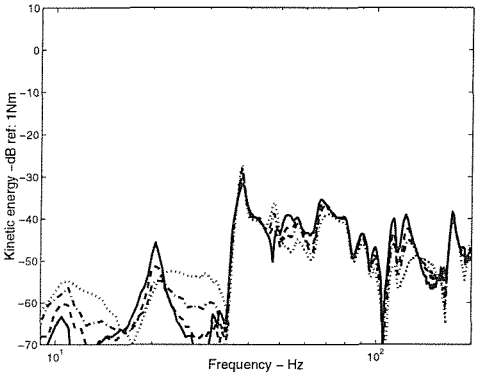

(b) Perfectly working system

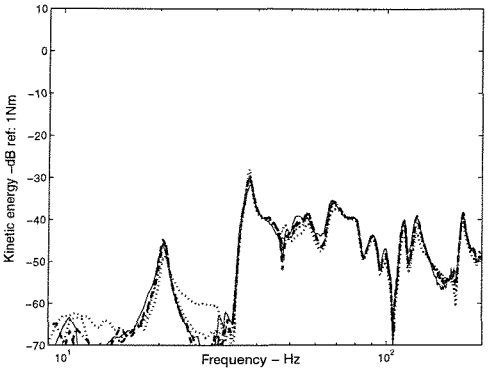

(e) System with single channel failure (Rotational motion at mass centre)

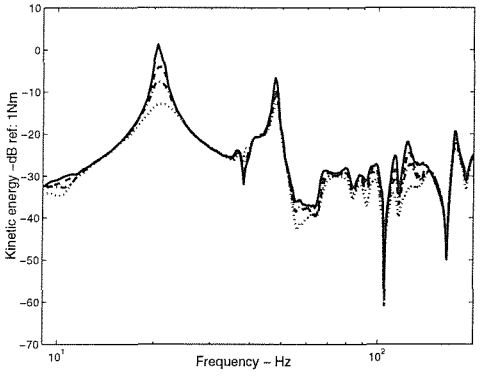

(c) Perfectly working system

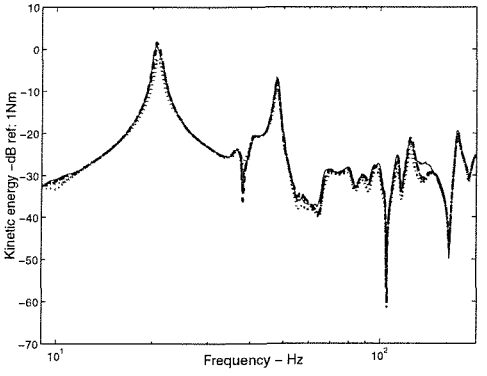

(f) System with single channel failure (Total kinetic energy)

Figure I12 Kinetic energy plots for a system on a CFCF flexible base - mass centre is at 0.596l (Measurement). power amplifier gain 0: _____ power amplifier gain 0.06: ---------, power amplifier gain 0.12: -.-.-.-.-.-., power amplifier gain 0.25: .....